Newcastle University
School of Engineering

The role of molten-salt distribution in dual-phase ceramic molten-salt membranes

by Maria Kazakli

A thesis submitted for the degree of Doctor of Philosophy

July 2020

Declaration of originality

I hereby declare that the contents and experimental results presented in this thesis have been collected and composed entirely by myself unless clearly stated otherwise. The information sources in the review sections are indicated in the text and are appropriately referenced within this thesis. Experimental work conducted outside Newcastle University has also been appropriately acknowledged.

Maria Kazakli

Newcastle University
December 2019

Abstract

Dual-phase ceramic molten-salt membranes offer high permselectivity for carbon dioxide at high temperature (> 400 °C) under continuous operation and offer a reduced environmental footprint compared to current carbon dioxide separation technologies. However, these membranes have not been developed with consideration to controlling the distribution of the molten carbonate phase within their ceramic supports, which can decrease molten carbonate effective thickness and increase surface area for carbon dioxide desorption and feasibly improve flux. Furthermore, the highly wetting nature of molten salts on ceramic supports could be exploited to spread and self-heal cracks developed during long-term operation attributed to the brittle nature of ceramic supports.

Here, carbon dioxide permeation was initially investigated in a model dual-phase membrane, where the support did not contribute to the permeation mechanism so that the permeation of carbon dioxide was restricted to the molten phase alone. Surface-exchange reactions were found to be rate-limiting on carbon dioxide flux between 450 – 750 °C, whereas bulk-diffusion limitations occurred above 750 °C. Thus, carbon dioxide flux can be increased in the surface-exchange-limited region by increasing the available surface area for carbon dioxide desorption (chapter 4).

Subsequently, an asymmetric hollow fibre with high and tailorable surface area for carbon dioxide desorption was used as the membrane support. Asymmetric hollow-fibre supports (widely used in polymeric and ceramic membrane systems) comprise two distinct porosity domains: micro-channels, conically shaped with an open entrance on the lumen/permeate-side surface (pore size: 2 – 30 μm), and a porous micro-structured packed-pore network (pore size: 0.05 – 0.5 μm), located between micro-channels and at the shell/feed-side surface of the hollow-fibre supports. Hence, the permeate-side surface area of the hollow fibre supports consists of the projected surface areas of the micro-channels and the areas between them, whereas the feed-side surface is the projected surface area of a cylinder. So far, the molten phase has been infiltrated into both porosity domains of the hollow fibre supports in an uncontrolled way, sacrificing gaseous mass transfer advantages of the micro-channels and decreasing the available interfacial area between gaseous carbon dioxide and molten carbonate from the projected surface areas of the micro-channels and the areas between them to that of a cylinder. A new carbonate infiltration method was developed in this work, aiming to control the incorporation and distribution of the molten

phase inside the packed-pore network of the hollow-fibre supports alone. As the infiltration targeted the incorporation of the carbonates in the packed-pore network alone, leaving the micro-channels unblocked, the interfacial area between molten carbonate and carbon dioxide increased (chapter 3).

In the controlled-infiltrated hollow-fibre membranes the porous micro-channels remained unblocked, increasing the surface area for carbon dioxide desorption to that of the sum of the micro-channels surface areas. In the uncontrolled-infiltrated membranes the surface area for carbon dioxide desorption was ~5 times smaller as the surface area of the micro-channels was blocked. The increase in surface area in the membranes developed by the controlled-infiltration method showed an 8-fold flux improvement (0.036 ml min^{-1} cm^{-2}) at 600 °C compared to membranes where the molten-salt distribution, and available surface area, was uncontrolled (0.004 ml min^{-1} cm^{-2}) (chapter 4).

Finally, molten carbonate wetting on the ceramic surface, was exploited to self-heal cracks in membrane supports. A membrane system with an incorporated sacrificial crack-inducing material demonstrated that the molten phase can spread and self-heal the catastrophic crack created upon removal of the crack-inducing material. The permselectivity of the membrane was restored after self-healing occurred, demonstrating the first autonomous and intrinsic self-healing membrane (chapter 5).

Dedicated to my family.

Acknowledgments

Upon conclusion of my research I would like to express my gratitude to the people and academics who have supported me throughout the entire research programme. First, I would like to give my sincere thanks to Prof. Ian S. Metcalfe for his guidance, objective advice and for sharing his in-depth knowledge on membrane science. His supervision and suggestions formed this doctoral thesis and were crucial to my development as a researcher. I will forever be grateful for the opportunity to work with him and receive his unlimited support and funding for this project. I would also like to thank Prof. Kang Li, Dr Bo Wang and Dr Tao Li of Imperial college for their collaboration and advice and for providing the ceramic hollow-fibre support precursors used in this research project.

Additionally, I would like to express my sincerest gratitude to my co-supervisors for sharing their knowledge, spending countless hours teaching and guiding me and supporting me with my research during times when the research obstacles seemed insurmountable and the research objectives seemed unachievable. I would particularly like to thank Dr Ana Gouveia Gil for teaching me everything she knows about hollow fibres and becoming a mentor and most importantly a friend. I would also like to thank Dr Georgio Triantafyllou for his knowledge on materials science without which I would have never overcome the set-up difficulties of the experimental apparatus. Last but not least, I would like to thank Dr Greg A. Mutch whose maddening attention to detail and push for excellence have helped me achieve all the things I have done with this research today, as well as the most trivial things, such as learning how to hyphenate.

A special thanks to Dr Liu Qu, who even though was never in my official supervisory list, helped me with the self-healing work in this thesis more than I would have hoped for. Her crucial advice, ideas and hard work were what made this work possible. I would also like to thank the rest of the academic members of the group, Dr Evangelos I. Papaioannou, Dr Wenting Hu, Dr Dragos Neagu, Dr Kelly Kousi, and Dr Richard Court, as well as previous members of the group, Dr Guangru Zhang, Dr Nisa Ramli, Danny Mak and Sotiria Tsochataridou, for being happy to help me whenever I needed help. I would also like to express my infinite and eternal gratitude to my co-PhD students, or ‘people in the office’, Selim Ungut, Yuhao Ji, Chengyang Tang, Sahr Sana, Leonidas Bekris, Liam McNeil, Stephen Johnston and Chris de Leeuwe, for making these four years better than I could have hoped for. Leonidas, Liam, Stephen and Chris especially for keeping me straight and narrow, providing a pleasant work environment, listening

to my worries and problems and actively contributing in solving them and overall, being true friends.

I would also like to acknowledge the financial support provided by ESPRC in the United Kingdom (Grant no: EP/M01486X/1) and Newcastle University as well as the people behind the scenes: the lab technicians, IT and administrative staff of the school that have helped all the academics and myself with their hard work. Especially Justine McGruther for her patience, tremendous help and always treating PhD students with a smile. A big thank you to my friends outside of the university supporting me every step of the way, and to the people that doubted me throughout my life as they were the reason for trying harder and the reason for pushing myself more.

I would finally like to express how grateful I am for the support I have received from my family in this demanding endeavour and for all the patience they showed while I was away from them throughout the PhD. Without my mother, father, παππού (grandpa) and γιαγιά (grandma) and the people in our wider family, I would have never grown up to be the person I am today. Thank you for being there when I needed you and providing me with the tools I needed to succeed in life. You mean the world to me and I could never show the depth of my appreciation in words. A special thanks to my partner, Joe, for teaching me how to find work-life balance and sharing his PhD journey with me. Thank you for being there on the good days and the bad, being my greatest supporter and believing in my abilities. Without all of you holding my ground I would not have the strength, courage and resilience to make it this far.

Table of Contents

List of figures

List of tables

List of acronyms and abbreviations

AGR – Acid gas removal

ALD – Atomic layer deposition

Al_2O_3 – Aluminium oxide

atm – Atmosphere

Barrer – 1 barrer= 3.35×10^{-15} mol m^{-1} s^{-1} Pa^{-1}

BET – Brunauer - Emmett - Teller

BYS – $Bi_{1.5}Y_{0.3}Sm_{0.2}O_{3-\delta}$

CCS – Carbon dioxide capture and sequestration

CGO – $Ce_{0.9}Gd_{0.1}O_{1.95}$

CMS – Carbon molecular sieve

cP – Centipoise, 1 cP = 1 mPa s

CVD – Chemical vapor deposition

DAC – Direct air capture

DI – Deionised

DMSO – Dimethyl sulfoxide

DPHFM – Dual-phase hollow-fibre membrane

EDX – Energy-dispersive X-ray spectroscopy

HFCs – hydrofluorocarbons

HTS – High temperature shift

ID – Inner diameter

IL – Ionic liquid

IGCC – Integrated gasification combined cycle

LTS – Low temperature shift

LSCF – $La_{0.6}Sr_{0.4}Co_{0.8}Fe_{0.2}O_{2-\delta}$

MAX – $M_{n+1}AX_n$, where M is an early transition metal, A is an A-group element and X is either carbon or nitrogen

MEA – Monoethanolamine

MIEC – Mixed ionic and electronic conductors

MIP – Mercury intrusion porosimetry

MMM – Mixed matrix membrane

MOF – Metal organic framework

Mt_{CO2} – Metric tons of carbon dioxide equivalent

MW – Megawatt

MWe – Megawatts electric

MWth – Megawatts thermal

NGCC – Natural gas combined cycle

NMP – n-methyl-2-pyrrolidone

OD – Outer diameter

PESf – Polyethersulfone

PFCs – Perfluorocarbons

PMMA – Poly(methyl methacrylate)

pts – Energy penalty

rpm – Rounds per minute

SDC – $Ce_{0.8}Sm_{0.2}O_{1.9}$

SEM – Scanning electron microscopy

SF6 – Sulphurhexafluoride

SFN – $SrFe_{0.8}Nb_{0.2}O_{3-\delta}$

SLM – Supported liquid membrane

STA – Simultaneous thermal analysis

TPB – Triple-phase boundary

WGS – Water-gas-shift

XRD – X-ray powder diffraction

YSZ – Yttria stabilised zirconia

A_s – Outer lateral membrane surface area (m^2)

C_{CO2} – Concentration of carbon dioxide (mol m^{-3})

D – Diffusivity coefficient (m^2 s^{-1})

D_i – Inner diameter of the hollow fibre (m)

D_o – Outer diameter of the hollow fibre (m)

F – Faraday's constant (9.649×10^4 C mol^{-1})

F – Force (N)

i – permeant

j – non-permeant

J_{CO2} – Carbon dioxide flux (ml min^{-1} cm^{-2})

k_H – Henry's constant (mol m^{-1} atm^{-1})

L – Membrane thickness (m)

L_c – Critical thickness (m)

P_c – Capillary pressure (atm)

pCO_2, P_{CO2} – Partial pressure of carbon dioxide (atm)

pO_2, P_{O2} – Partial pressure of oxygen (atm)

P – Permeability (mol m^{-1} s^{-1} Pa^{-1})

$\mathcal{P}$ – Permeance (mol s^{-1} m^{-2} Pa^{-1})

r – Pore radius (m)

R_0 – Outer radius of the hollow fibre (m)

R – Ideal gas constant (J mol^{-1} K^{-1})

S – Solubility coefficient (mol m^{-3} Pa)

S – Spreading coefficient (J m^{-2}) (chapter 2)

T – Temperature (°C)

V – Volume of cylindrical container (m^3)

$\dot{V}$ – Volumetric flow rate on the permeate side (ml min^{-1})

α – Selectivity (chapter 1)

α – Permeance coefficient of total conductance for a dual-phase membrane (chapter 2)

γ – Surface tension (J m^{-2})

ε – Porosity

η – Viscosity (Pa s^{-1})

θ – Contact angle (°)

λ – Mean free path (m)

ρ – Density (g cm^{-3})

σ – Conductivity (Ω^{-1} m^{-1})

τ – Tortuosity

φ_{CO_2} – Volume fraction of carbon dioxide in the permeate-side outlet

Chapter 1

Introduction

1.1 Research background

Carbon dioxide (CO_2) is the most widely produced greenhouse gas as a result of fossil-fuel combustion (coal, natural gas, and oil) and its increasing release in the atmosphere during the 21st century is a growing global environmental issue [1]. Carbon dioxide is the most important greenhouse gas because it remains in the atmosphere for an extended period of time. Whereas other major greenhouse gases, such as methane (CH_4), nitrous oxide (N_2O), hydrofluorocarbons (HFCs), perfluorocarbons (PFCs) and sulphurhexafluoride (SF_6) will leave the atmosphere after 12 (CH_4) to 270 (HFCs) years, carbon dioxide will leave the atmosphere after anywhere between 20 years to tens of thousands of years [2]. The majority of carbon dioxide emissions related to human activities are generated during the combustion of fossil fuels in power plants to cover electricity and heat generation needs (40 – 45% of global carbon dioxide emissions). Together with the emissions related to transportation, they constitute ~75% of today's global carbon dioxide emissions. The rest of the emissions are attributed to the industrial sector (manufacturing, mining, construction sites and agriculture) [3,4]. The continuous increase of carbon dioxide concentration in the atmosphere, has led to global warming and climate change, with the average global temperature increasing by 1 °C since 1880, 60% of which was the increase from the end of the 20th century onwards [1]. Global warming and climate change mitigation depends heavily on advances related with the use of low carbon fuels, the replacement of fossil fuels by renewable energy, global energy conservation, energy efficiency and the use of carbon dioxide capture and sequestration technologies (CCS). Climate change targets (<2 °C within this century) can be met by reducing the produced carbon dioxide and by improving the CCS technologies and capturing more carbon dioxide, *i.e.* removing carbon dioxide from flue gases chemical reactions and straight from the atmosphere (air, negative emission technologies).

There are three main capture systems for carbon dioxide emissions generated in power plants due to the combustion of fossil fuels: pre-combustion, post-combustion and oxy-fuel combustion. Pre-combustion decarbonisation relies on carbon dioxide

removal from the fuel prior to its combustion and is typically achieved with integrated gasification combined cycles (IGCC) (Figure 1.1a). Initially, the solid, liquid or gas fuel goes through gasification or a reforming process followed by a water gas shift (WGS) reaction. The WGS reaction uses steam to convert the carbon monoxide produced by the gasification process into carbon dioxide and hydrogen at temperatures between 185 and 500 °C, depending on the activity of the catalyst used for the conversion [5]. Traditionally, carbon dioxide is separated and captured in pre-combustion decarbonisation by chemical (solvent absorption) or physical (pressure swing adsorption) processes. In post-combustion decarbonisation, carbon dioxide is separated from the gas stream that derives after the combustion of the fuel [6]. After combustion, which is usually performed with the use of air, the resulting driving force for carbon dioxide separation in the flue gas is low (<0.15 atm) and the pressure of the flue gas is atmospheric (Figure 1.1b). Traditionally, chemical absorption is used for carbon dioxide capture post-combustion. Finally, in oxy-fuel combustion a 95% oxygen-carbon dioxide mixture is used for combustion instead of air which produces a carbon dioxide-rich fuel gas (Figure 1.1c). Carbon dioxide can then be easily recovered after water has been condensed from the stream and additional impurities have been removed [6]. Absorption and adsorption-based CCS technologies (used in pre- and post-combustion decarbonisation) are quite attractive for carbon dioxide separation as they can be integrated in already existing plants. Their application worldwide however has been insufficient, and the United Nations are not on track to meet the climate change goals of the Paris Agreement [7]. The high commercial and technical risks of developing large scale CCS projects has outweighed their potential contribution in carbon dioxide capture, thus a total of 12 CCS projects planned to be operational in the European Union in 2015 were all abandoned. Two more CCS procurement projects that have previously been operational in the UK and the clean coal component of an IGCC project in the US have also been abandoned due to technical issues and over-budget expenses [8].

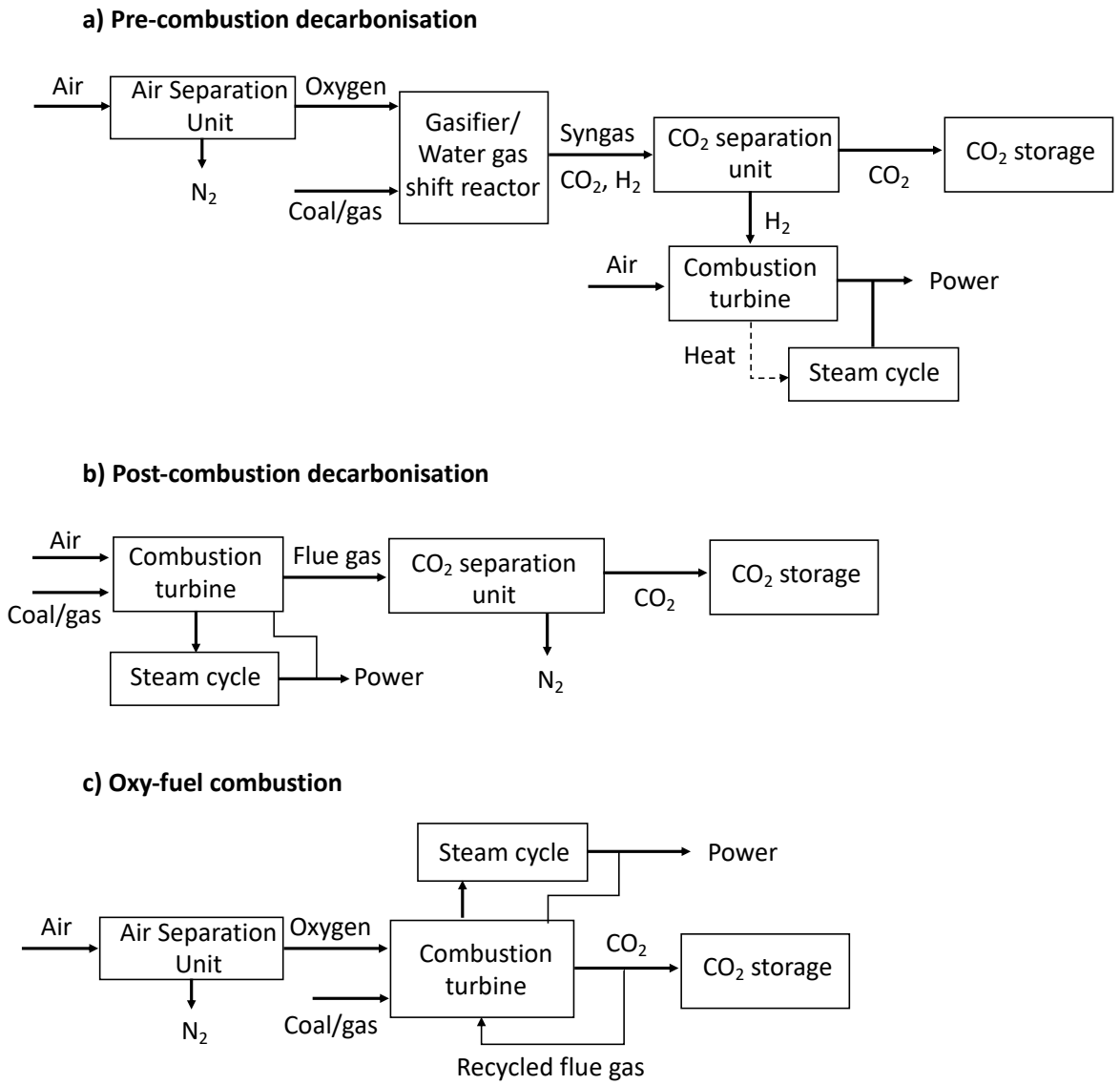

Figure 1.1: Pre-combustion decarbonisation (a), post-combustion decarbonisation (b) and oxy-fuel combustion capture (c) for carbon dioxide emissions generated in power plants [5,6].

CCS technologies are used to sequester carbon dioxide at a commercial scale, at 17 operational CCS large-scale projects world-wide, capturing between 0.7 and 8.4 Mt_{CO2} per year. The sequestration of carbon dioxide in these projects is usually realised by absorption and stripping with an aqueous absorbent technology, where carbon dioxide from the flue or combustion gas is absorbed into an aqueous amine solution [9]. During the absorption process, the use of amine-based solvents, mainly monoethanolamine (MEA), has a high energy demand and incurs high capital costs for solvent regeneration [10,11]. The environmental fate and the toxicity of the MEA solvent are also points for concern in its application, which raise the need for cleaner alternatives. Ammonia, aqueous ammine solution, slurries of oxide/hydroxide, other amines and their blends, ionic liquids and amino acids have all been investigated as alternatives to

the use of MEA solvent [12]. However, these alternatives, with the exception of ionic liquids, have not shown long-term stability, there are high emissions associated with their production or they show degradation during operation [12].

Ionic liquids (ILs) are composed of ions that have exceptionally low vapour pressure. They have a melting point below 100 °C, show thermal (up to 300 °C) and chemical stability for carbon dioxide capture applications and their properties can be easily customised by synthetically altering the ion they are made of. Ionic liquids could have potential for carbon dioxide CCS technologies after addressing issues with their high viscosity (66 to 1100 cP from 20 – 25 °C, viscosity of water 1 cP at 20 °C) which reduces their gas solubility and gas uptake and does not make them competitive with the already existing MEA solvent technology [13,14]. Solid adsorbents have also been considered for CCS but they in turn suffer from capacity degradation and slow adsorption kinetics [15]. The need for next generation adsorbents has turned the scientific interest to metal organic framework (MOF) adsorbents [16,17], zeolites [18], metal oxides [19], activated carbon [20] and hydrotalcites [21]. A promising technology for carbon dioxide separation is calcium looping, which exploits the reversible reaction between carbon dioxide in the gas phase and a solid calcium oxide-based sorbent to remove carbon dioxide from flue gas [22]. Recently, a direct air capture (DAC) plant started its operation in Switzerland, using a solid-supported amine filter for carbon dioxide adsorption [23] and a number of calcium-looping pilot plants are already in operation demonstrating >90% carbon dioxide capture efficiency in a MWth scale (up to 1.9 MWth) and for more than 600 h of operation [16,24–26].

The need for carbon dioxide separation at a large scale in a continuous, cost-effective, environmentally friendly and robust process has been a catalyst for the development of ‘next generation’ carbon dioxide separation technologies. In addition to chemical looping and ionic liquids, membranes are a promising second generation technology for carbon dioxide separation. As a technology for carbon dioxide separation, membranes offer high modularity; as they can be easily integrated in the plant process, flexibility, continuous operation and lower energy penalties compared to adsorption and absorption processes [27]. Membranes for carbon dioxide separation have already been industrially applied in natural gas sweetening processes (carbon dioxide and hydrogen sulphide removal from natural gas aiming for cost-reductions in the natural gas purification process) [28,29] and for carbon dioxide separation from syngas (polymeric Polaris membranes) [30]. Membranes could be potentially used in all major

CCS technologies: pre-combustion, post-combustion and oxy-fuel combustion, depending on membrane material, permeability and separation efficiency. Despite their promising potential, membranes have not been widely used in commercial scale for carbon dioxide separation as they still need to showcase their long-term stability and functionality in large-scale processes under realistic operating conditions [8]. They have however been the focus of many experimental and process simulation studies that have tried to address a number of their operating issues, pushing this technology forward and developing numerous interesting combinations for membrane materials. This thesis focuses on increasing the understanding and application challenges of dual-phase ceramic molten-salt membranes (a class of membranes consisting of a molten carbonate phase infiltrated into a porous solid) in the scope of carbon dioxide separation, for which they are showing promising results.

1.2 Membranes and their application in gas separation

1.2.1 Membranes in gas separation

Membranes are selective barriers used for solute separation that results in the separation, concentration or purification of a mixture [31]. The feed stream is separated into two effluent streams, the permeate and the retentate which should contain high and low concentrations of the desired component, respectively, for the separation to be effective (Figure 1.2). Transport through a membrane is the result of a driving force, *i.e*. chemical or electrical potential difference, on the individual system components. A pressure, temperature, concentration, or electrical potential difference results in a difference in potential between the two sides of the membrane, which subsequently drives transport [32]. For gas separation membranes the driving force is typically the partial pressure difference between the feed and permeate side of the membrane. The gas species for which a partial pressure difference applies permeates from the high partial pressure side (P_f: feed side) to the low partial pressure side of the membrane (P_p: permeate side) resulting in its separation (Figure 1.2).

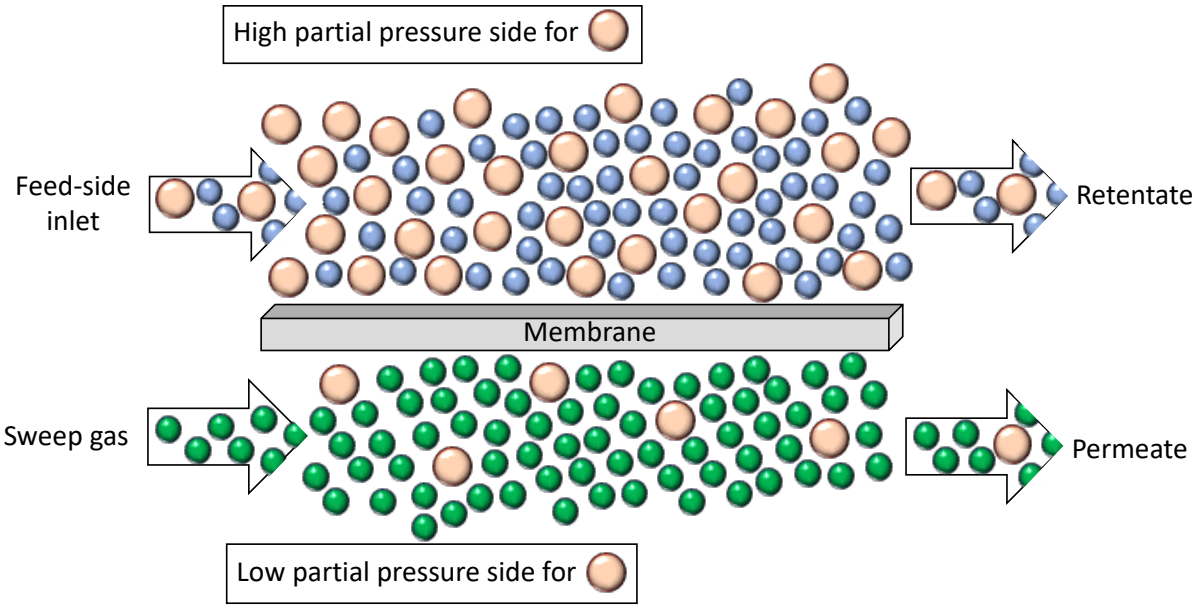

Figure 1.2: Schematic of a membrane for a gas separation process where partial pressure difference is the driving force for separation. Feed-side inlet stream is separated into the retentate and the permeate.

1.2.2 Mechanisms for gas separation membranes

The prevailing mechanisms for gas separation membranes are shown in Figure 1.3 and they include Knudsen diffusion (Figure 1.3a), surface diffusion (Figure 1.3b), capillary condensation (Figure 1.3c), molecular sieving (Figure 1.3d), solution diffusion (Figure 1.3e) and facilitated transport (Figure 1.3f). The above permeation

mechanisms can be differentiated depending on whether the membrane is porous or dense. Knudsen diffusion, surface diffusion, capillary condensation and molecular sieving only apply in porous membranes, whereas the solution diffusion mechanism, only takes place in dense membranes. A facilitated-transport mechanism on the other hand can be introduced in both porous and dense membranes. More specifically, Knudsen diffusion occurs when the ratio of the pore radius (r) over the mean free path (λ) of the gas molecules is a lot less than one. In that case the collisions of the gas molecules with the porous walls of the membrane are more frequent than the collisions in-between the gas molecules (kinetic diameter of the molecule). Hence, the gas molecules develop different speed that leads to their separation [33]. In surface diffusion, the gas molecules are adsorbed and diffused on the porous walls due to active sites available in the membrane. The activation energy required for the diffusion of molecules from one active site to another depends on the heat of adsorption, which determines the bond strength between the diffused molecules and the membrane's active sites. Molecules that are strongly adsorbed on the membrane active sites are not as mobile as molecules that are weakly adsorbed on the membrane active sites. Surface diffusion follows an exponential relationship with $-\Delta H_f/kT$, as described by Bonzel [34] where ΔH_f is the formation enthalpy of the molecule-active site bond, k is Boltzmann's constant and T is the operating temperature. Therefore, surface diffusion has been found to be the dominant permeation mechanism at low temperatures, as suggested by the above exponential relationship (when the pore diameter is less than 2 nm), with the contribution of Knudsen diffusion becoming the dominant permeation mechanism at high temperatures [35]. Capillary condensation in a gas separation membrane is the phenomenon of a gas molecule condensing in the membrane pores due to capillary forces. This mechanism is favoured in small pores ($D< 5$ nm), where capillary forces are stronger, and at low temperatures [36]. Molecular sieving is another mechanism occurring in porous membranes with particularly small pores ($D< 0.5$ nm). For a membrane to act as a molecular sieve the membrane pores should have a diameter in-between the size of the gas molecules that are required to be separated, hence separation can be achieved by molecular size exclusion [37]. In the solution diffusion mechanism, occurring in dense membranes only, the gas molecules, driven by a concentration gradient on the feed and permeate side of the membrane, first dissolve and then diffuse through the membrane material [38]. Finally, for facilitated transport to take place in the membrane the gas separation needs to be mediated by a carrier that aims to increase the rate of transport in the membrane. For

the separation to be possible the carrier needs to react in a reversible way with the gas targeted for separation. In porous membranes, the carriers are fixed inside the membrane network and have the ability to react with the gas desired for separation. In dense membranes, such as polymeric membranes or dense membranes comprised of two phases; a solid and a liquid, the carrier can be mobile. Mobile carriers in the liquid phase, react with the permeating species dissolved in the membrane and the created complex diffuses across to the feed side of the membrane. The permeant is then released in the permeate gas stream, while the released carrier diffuses back to the feed side of the membrane to recycle the same process [39].

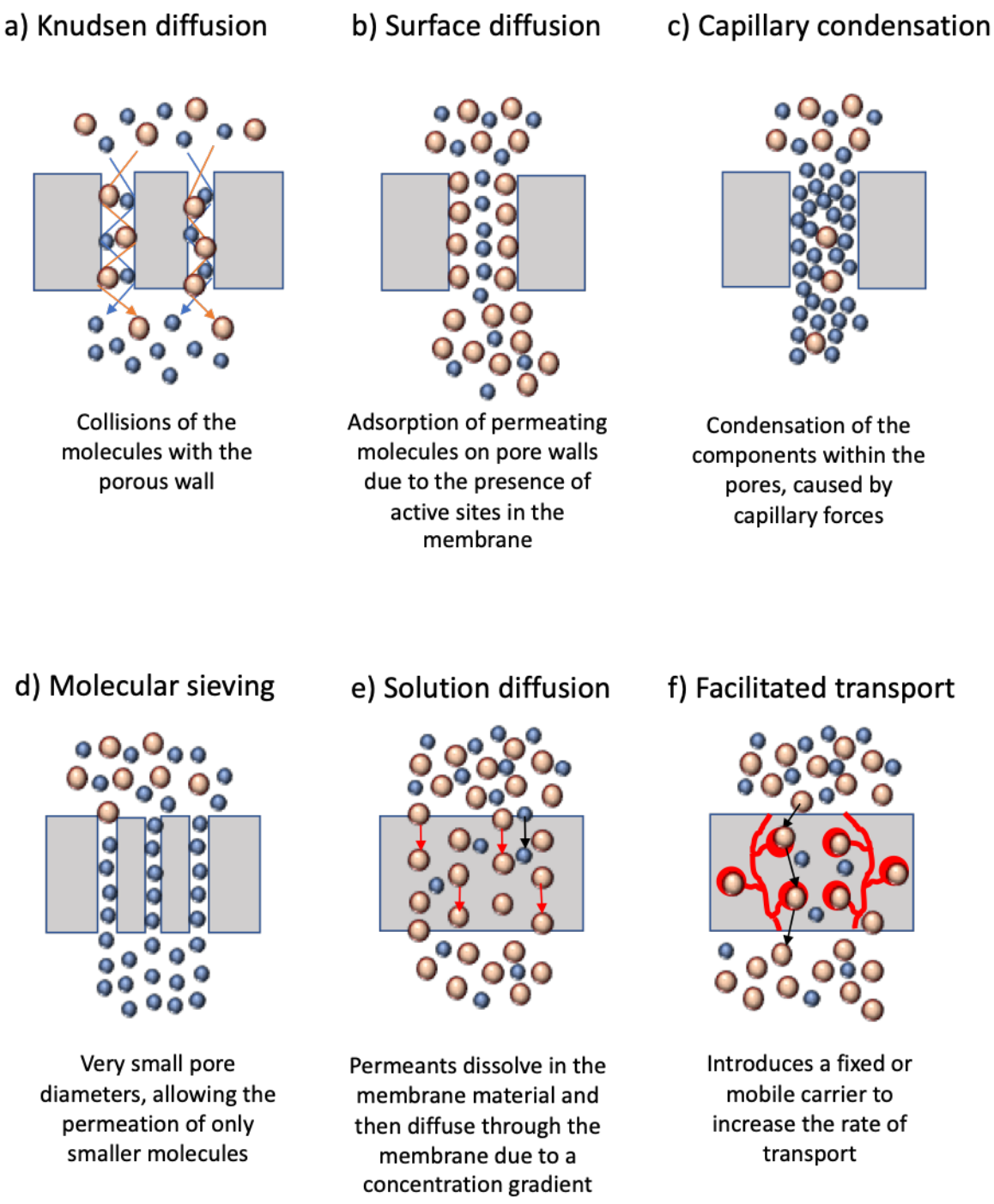

Figure 1.3: Gas permeation mechanisms through porous (a,b,c,d and f) and dense (e and f) membranes.

1.2.3 Membrane performance evaluation

Key membrane performance measures include flux, permeability, permeance and selectivity. Membrane flux (J) is defined as the volume, or number of moles of permeant (i) that are transported through the membrane per unit area per unit time, referred to as volumetric and molar flux, respectively. Permeability (*P*) is the intrinsic property of both the membrane material *i.e.* ceramic, metal, polymer, and its structure *i.e.* porous, dense, and is defined as the membrane flux, normalised for the membrane

thickness (L) and membrane partial pressure driving force ($P_f - P_p$). Permeance ($\mathcal{P}$) is defined as the flux, normalised only for the driving force ($P_f - P_p$) and selectivity (α) is the ratio of permeability (*P*) of the permeating gas (i) over a non-permeating gas (j) of the feed side.

$$P = \frac{J_i L}{P_f - P_p} \quad \text{(Eq. 1.1)}$$

$$\mathcal{P} = \frac{J_i}{P_f - P_p} \quad \text{(Eq. 1.2)}$$

$$\alpha = \frac{P_i}{P_j} \quad \text{(Eq. 1.3)}$$

Permeability (*P*) can be expanded into diffusivity (D) and solubility (S) coefficients of the permeant gas (i) through a membrane where the permeation mechanism relies on solution-diffusion, *i.e.* polymeric membranes.

$$P = S_i D_i \quad \text{(Eq. 1.4)}$$

Flux, permeance and permeability can evaluate membrane performance at a given temperature. Flux, or permeance, and the ability of the membrane to separate mixtures of practical interest are key measures of membrane performance. High flux and permeance depend on the development of thin membranes from materials that have high permeabilities. As a result, membranes that show high fluxes, permeances and permeabilities require smaller surface areas for a given volume of gas, and consequently, lower capital costs during their manufacturing process. However, the membrane's ability to separate a desired permeant with high permeability and selectivity at the same time, resulting in high purity products, is another main criteria for a membrane to be considered effective for separation [40]. Other important considerations for a membrane to be used efficiently in a gas separation process include membrane cost, packing density, stability and separation factor. For example, an ideal membrane would be defect-free and fabricated by relatively cheap materials that provide large surface-to-volume ratios for separation. If these membranes can be easily scaled-up into membrane modules this would further allow the processing of high volumes of gas in an efficient way. The membrane materials would also need to show thermal and chemical stability in the process environment and the ability to separate the desired gas with a high separation factor. This would reduce the need for membrane replacement and reduce the number of membrane modules in the process [41].

1.2.4 Transport through gas separation membranes

Overall, for the permeation of a gas from the feed to the permeate side of the membrane to be realised, there are at least five steps required. Initially, the molecules of a gas (i) on the feed side of the membrane (high partial pressure side for gas (i)) are transported to the membrane surface due to the applied partial pressure difference (step 1). Once they have reached the surface of the membrane, their sorption into the membrane surface occurs (step 2). The penetrant molecules (i) are then transported through the membrane (in the form of gas molecules, charged chemical species, or both, depending on the sorption process) (step 3) and upon reaching the surface of the permeate side of the membrane are released on the permeate side of the membrane (step 4). Finally, the molecules of gas (i) are transported by gaseous mass transfer to the permeate-side stream of the membrane (low partial pressure side for gas (i), step 5) and are removed along with the removal of the permeate stream [42–44]. The transport mechanism (steps 2 – 4) differs depending on the type of membrane used. Regardless of the type of membrane however, permeation steps 2 – 4 are the ones that largely impact the rate of transport through the membrane as sorption (step 2), bulk diffusion (step 3) and permeant release (step 4) provide greater resistances compared to mass transfer of the gas molecules in the gaseous phase (for membrane processes that have been engineered correctly). Bulk diffusion refers to mass transfer inside the membrane. Sorption and release processes on the membrane surface may occur by a single mechanism or by different combinations of mechanisms. The sorption and release mechanisms include physical sorption mechanisms, referred to as physisorption and chemical sorption mechanisms, referred to as chemisorption. Surface-exchange reactions refer to the chemical reactions that occur on the membrane surface between the gas species and the membrane material.

1.2.5 Membrane limitations in gas separation

Membrane operation where pressure difference is the driving force for separation can be considered in two main regions: the pressure-controlled region and the mass-transfer controlled region (Figure 1.4). In the pressure-controlled region, the increase of transmembrane pressure leads to an increase in flux as the concentration of desired component (i) on the membrane surface increases. However, if the concentration of component (i) on the membrane surface reaches the solubility value of the membrane for this component, further increase in transmembrane pressure will not result in flux increase as the membrane operation has entered the mass-transfer controlled region

[45]. To overcome mass transfer limitations of the membrane process and push the boundaries of the pressure-controlled region, higher flow rates, higher temperatures and/or lower concentrations of component (i) close to the membrane surface have been applied in membrane operation. Lower concentrations of component (i) close to membrane help avoid the effect of concentration polarisation, *i.e.* the accumulation of rejected molecules on the membrane surface. The use of a sweep gas or vacuum, has also proven to reduce concentration polarisation of the permeating component (i) on the permeate side of the membrane and consequentially increase driving force [46].

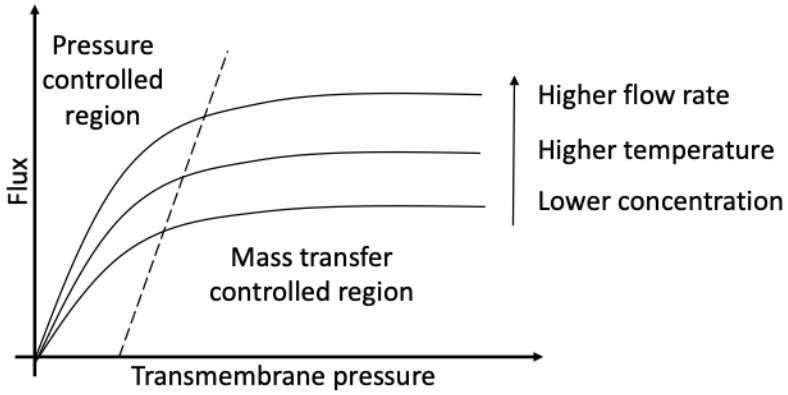

Figure 1.4*:* **Effect of operating parameters on membrane flux.** Pressure-controlled region and mass-transfer controlled region in membranes operating under transmembrane pressure differences. Image adapted from reference [45].

Membrane thickness and surface-exchange reactions have also been found to limit membrane performance depending on the membrane's operating temperature. In general, membranes with larger effective surface areas provide larger surface areas for surface-exchange reactions, resulting in higher transport rates through the membrane. Bulk diffusion however dominates the transport rate through the membrane when the membrane is relatively thick. Surface diffusion and bulk diffusion, whether that is Knudsen diffusion (flux $\propto T^{-1/2}$) [47] or solution diffusion, are weakly temperature activated processes compared to surface-exchange reactions, where the reaction rate increases with temperature based on the Arrhenius equation (flux $\propto \exp T^{-1/2}$) [48]. In membrane processes, apparent activation energy is calculated as the total of the activation energy corresponding to the permeation process (steps 2 – 4), since the activation energies of each step cannot be individually determined. At the temperature range where bulk diffusion is the rate-limiting step for the transport of the desired component (i) through the membrane, membrane flux is proportional to membrane thickness. An increase in thickness leads to a decrease in flux and *vice versa* [49]. Often, this is not the case however, as surface-exchange reactions

contribute to the rate-limiting step. As the membrane thickness decreases (for most membranes below 400 – 500 μm [50]), the contribution of surface exchange in the transport mechanism increases, finally reaching the point where surface exchange becomes the dominating rate-limiting step for the membrane. In a membrane process that is not controlled by mass-transfer limitation in the gas phase; when the increase in flux is reciprocal of the membrane thickness, surface exchange can be considered to control the permeation of the desired component (i) through the membrane [51,52]. Mass-transfer limitations in the gas phase can occur when the permeation rates of the membrane are higher than the mass transfer rate in the gas phase. The thickness at which a further decrease in thickness will not result in increased fluxes through the membrane is the membrane's critical thickness (L_c). The L_c depends on membrane properties, such as material and permeability, as well as operating conditions, such as temperature and feed and permeate-side flow rates [53].

Membrane operation in surface-exchange rate-limited region is usually more desirable as surface-exchange reactions are strongly activated by temperature compared to bulk diffusion [48]. Efforts to decrease membrane thickness so that membrane operation lies in the surface-exchange limited region have resulted in the development of asymmetric structures. Asymmetric structures possess two or more layers with different pore sizes in contrast to symmetric structures which only possess a single porous layer of uniform pore size or a single dense layer. The top layer (<5 μm thick) in asymmetric structures is usually dense or has a very small pore size, and acts as the selective layer for gas separation, whereas the rest of the layers are highly porous. The use of an asymmetric membrane allows the decrease of separation layer thickness in the order of microns and nanometres offering low mass transfer resistance in the bulk phase of the membrane [41,54–56]. This is not possible with symmetric structures as thickness is often a limiting factor for the mechanical strength of the membrane. Hence, in symmetric structures, the entire membrane thickness determines the membrane flux as opposed to asymmetric structure where flux is determined by the thickness of the selective layer. In addition to decreasing membrane thickness, research has also focused on membrane surface modification in order to enhance surface exchange between the gaseous phase and the membrane [51,57–60].

1.3 Membranes for carbon dioxide separation

For membranes targeted for carbon dioxide separation to be effective and economically feasible compared to conventional CCS technologies, their permeabilities must be between 1,000 to 10,000 Barrer (10^{-13} – 10^{-12} mol m^{-1} s^{-1} Pa^{-1} in SI, 1 barrer= 3.35 $\times$ 10^{-15} mol m^{-1} s^{-1} Pa^{-1}) and their carbon dioxide to nitrogen selectivity between 50-100 [61–63]. The integration of membranes in an industrial process (both generally and carbon dioxide separation specific), requires for the membrane to be chemically and mechanically stable and compatible with the process operating conditions. The membranes must also exhibit significant stability during long-term operation, amenability to fabrication and packaging and in some cases the ability to withstand high operating pressures [64]. Based on the material used for their synthesis, membranes for carbon dioxide separation in literature can be classified into two main categories: organic and inorganic.

1.3.1 Organic membranes for carbon dioxide separation

The majority of research on membranes for carbon dioxide separation has been focused on organic (polymeric) membranes as polymers can be easily processed, have a low production cost and can thus be applied in commercial large-scale applications. However, polymeric membranes cannot withstand high temperatures (generally> 100 °C) and suffer from plasticisation when exposed to a high carbon dioxide partial pressure (pCO_2) stream. This causes their efficiency to decrease with time due to chemical degradation and thermal instability, thus limiting their application as gas separation technologies [65–67]. Moreover, for polymeric membranes, permeability and selectivity have a trade-off relationship, with a highly permeable membrane showing low selectivity, and *vice versa.* This trade-off relationship is attributed to introducing a free-pore volume in the polymer membrane aiming to achieve higher permeability due to lower resistances. However, introducing this free-pore volume sacrifices membrane selectivity. The permeability and selectivity data of a large number of polymeric membranes determined a limit in the permeability *versus* selectivity relationship, characterised as the Robeson upper bound (Figure 1.5) [68,69]. Overcoming the upper bound for polymeric membranes, has been the focus of many studies that ultimately pushed the limit of the upper bound to higher permeability and selectivity values for polymeric membranes. Membranes that have overcome the Robeson upper bound have employed a combination of inorganic and

polymeric phases resulting in the creation of mixed matrix membranes (MMMs) [70], metal-organic framework membranes (MOFs) [71], or have aimed to facilitate transport through the membrane by introducing a fixed or mobile carrier in the membrane matrix that will react with the gas of interest (facilitated-transport mechanism in section 1.2.2) (Figure 1.5) [72]. Polymeric membranes with carbonate-based liquids as the mobile carrier and a polymer as the support, also known as supported liquid membranes (SLMs), have shown very high carbon dioxide permeabilities and a carbon dioxide to nitrogen selectivity above the Robeson upper bound. This is attributed to the creation of supported-liquid membranes where the liquid infiltrates the porous matrix creating the equivalent of a dense membrane for this system. By filling the free-volume in the membrane with a selective liquid, non-selective permeation through the free-volume, no longer occurs. The separation through the membrane is a result of the carbon dioxide selectivity of the liquid [40,73,74].

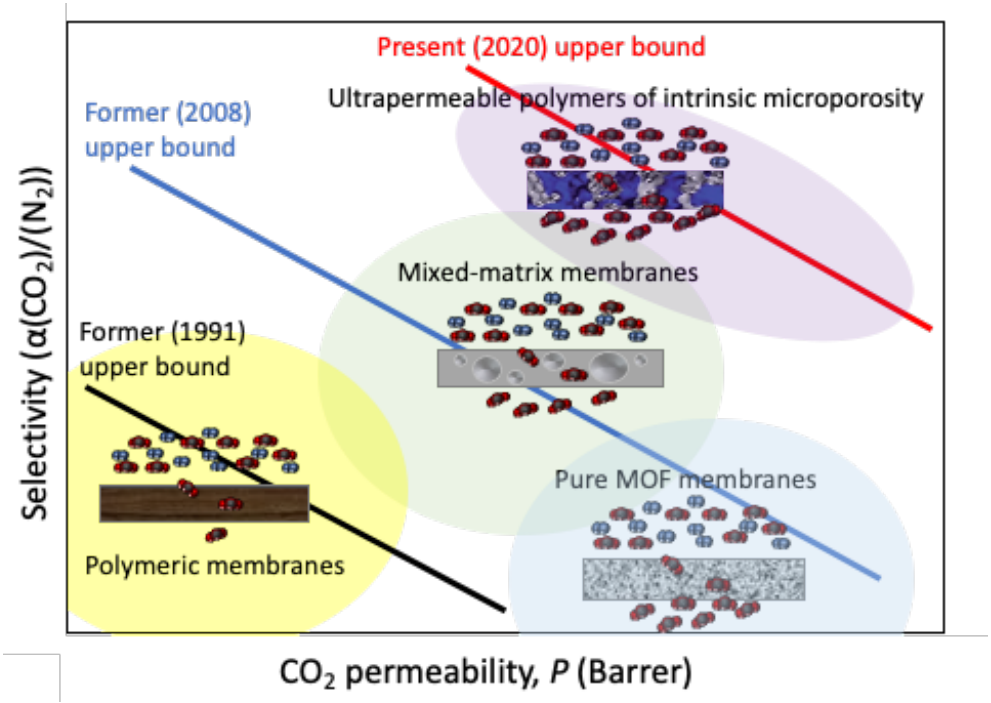

Figure 1.5: Robeson plot for carbon dioxide to nitrogen selectivity versus carbon dioxide permeability for polymeric, mixed-matrix and MOF membranes [62,68]. Image adapted from reference [70].

1.3.2 Inorganic membranes for carbon dioxide separation

Despite the progress in the field of polymeric membranes they cannot be used directly for carbon dioxide separation from flue gas at temperatures above 100 °C or in the WGS reaction (between 185 and 500 °C). Above 100 °C the majority of organic membranes soften (linear-chain polymers) or decompose (cross-linked chain

polymers) leading to loss of selectivity and mechanical strength [75,76]. Inorganic, mainly ceramic membranes however provide both thermal and chemical stability when exposed to harsh media, *i.e.* temperatures above 500 °C and organic solvents, and are able to perform gas separation directly out of the flue stream along with long-term durability. Inorganic membranes can be made from ceramics, silica, carbon, zeolites, metal oxides and metals [77] and even though the materials for their fabrication are generally more expensive than the ones used for polymeric membranes, their cost can be justified by their ability to operate in conditions where the use of polymeric membranes would not be feasible. An important aspect of the ability of inorganic membranes to operate at higher temperatures is that they can remove the need for gas cooling before carbon dioxide separation, which is an expensive process, and can be used in high temperature reaction environments directly, for e.g. separation enhanced reaction. Inorganic membranes can be classified into non-porous and porous membranes based on their micro-structure.

Non-porous or dense inorganic membranes are made of dense polycrystalline ceramics or metals and only allow the diffusion of certain gas species by a solution-diffusion mechanism or charged ions (facilitated transport) through the bulk of the membrane. The deposition of thin dense metal films on porous metals or ceramics can also produce dense inorganic membranes with asymmetric structures [78]. However, dense inorganic membranes are not specific to carbon dioxide separation as carbon dioxide is not soluble in the membrane materials used (e.g. palladium and solid oxide electrolytes such as modified zirconia and perovskites) [79]. Even though these membranes cannot be used for carbon dioxide separation, they can be used for hydrogen separation from carbon dioxide/hydrogen mixtures (products of the WGS reaction). Palladium and its alloys have been the dominant materials used for membranes specific to hydrogen separation as they provide high solubility of atomic hydrogen (resulting from the dissociation of molecular hydrogen on the gas-solid interface) through them [80]. The concentrated carbon dioxide stream can be then captured directly or it can be further purified from the remaining hydrogen in the stream in a carbon dioxide separation process [35,81].

Since dense inorganic membranes are not selective for carbon dioxide separation, most research for inorganic membranes for carbon dioxide separation has been focused on porous inorganic membranes. For the development of porous inorganic membranes, a thin microporous layer made of silicon carbide, carbon, glass, titania or

zeolite, is cast on a porous substrate, such as zeolite, zirconia, α- and γ-alumina and porous stainless steel [82,83]. The use of an asymmetric structure with a porous substrate provides mechanical strength for these membranes and offers low mass transfer resistance in the larger pores of the support. The main transport mechanisms through porous inorganic membranes depends on pore diameter, membrane active sites, component condensation and molecule/surface interactions and can be classified as Knudsen diffusion, surface diffusion, capillary condensation and molecular sieving, respectively, as mentioned in section 1.2.2 [35]. The majority of research for carbon dioxide separation from nitrogen at temperatures below 400 °C has been conducted using microporous membranes (pore size <2 nm), such as zeolites, silica and carbon membranes, and has taken advantage of surface diffusion by adsorption and the difference in kinetic diameter between the carbon dioxide and nitrogen molecules. At low temperatures (50 – 150 °C, *i.e.* membrane operational temperature for post-combustion capture), carbon dioxide transport through microporous membranes is controlled by the adsorption of carbon dioxide molecules onto the membrane material, instead of Knudsen diffusion. With the increase of temperature (>150 °C), the adsorption forces decrease and separation is controlled by the difference in kinetic diameter between the carbon dioxide and nitrogen molecules, as predicted by Knudsen diffusion [84].

Carbon molecular sieve (CMS) membranes are fabricated by the pyrolysis of a thin polymer film on a porous substrate and have so far shown moderate performance for the separation of carbon dioxide and nitrogen. The transport mechanism for CMS membranes can either rely on molecular sieving or selective surface adsorption followed by surface diffusion; depending on the type and pore size of the membrane [85]. Carbon dioxide permeability for CMS in literature is between 10^{-15} – 10^{-14} mol m^{-1} s^{-1} Pa^{-1} and shows a carbon dioxide to nitrogen selectivity between 10 and 20 for the majority of the CMS (Figure 1.6a). This falls short of what is required for the CCS permeability (10^{-13} – 10^{-12} mol m^{-1} s^{-1} Pa^{-1}) and selectivity target (50 – 100) mentioned at the start of this section [84].

Microporous silica membranes achieve carbon dioxide separation over nitrogen through surface diffusion and molecular sieving due to the small membrane pores (3-4Å, or 0.3 – 0.4 nm). These membranes are fabricated by sol-gel and chemical vapor deposition methods (CVD) and show better thermal, chemical and structural stability under oxidizing and reducing environments compared to carbon membranes.

However, some studies have shown that silica membranes fabricated by sol-gel method cannot withstand higher temperatures, especially in the presence of steam. For carbon dioxide separation from nitrogen, multi-layer microporous silica xerogel membranes, fabricated by sol-gel method has shown a carbon dioxide permeability between 10^{-14} – 10^{-13} mol m^{-1} s^{-1} Pa^{-1} and a carbon dioxide to nitrogen selectivity of 60 at 25 °C. Ultrathin microporous silica films, fabricated by sol-gel method on smooth mesoporous support surface have also shown a carbon dioxide permeability between 10^{-13} – 10^{-12} mol m^{-1} s^{-1} Pa^{-1} and a carbon dioxide selectivity over nitrogen of 20 [86–88]. The majority of the microporous silica membranes in literature show a better carbon dioxide permeability than carbon membranes, but lower selectivity values (Figure 1.6b) [84].

Zeolites are crystalline aluminosilicates exhibiting uniform pore structure and a pore diameter of 0.3 to 1 nm (3 – 10 Å). Most zeolite membranes can separate carbon dioxide from nitrogen, hydrogen and methane at low temperature due to stronger carbon dioxide heat of adsorption on zeolites compared to the other gases [6,89]. Carbon dioxide over nitrogen selectivity in a zeolite membrane in particular is attributed to the smaller effective kinetic diameter of carbon dioxide compared to nitrogen, inside a porous solid (0.33 nm for carbon dioxide and 0.36 nm for nitrogen) [90]. Y-type zeolites specifically, have shown a carbon dioxide permeability in the range of 10^{-13} – 10^{-12} mol m^{-1} s^{-1} Pa^{-1} and a carbon dioxide to nitrogen selectivity greater than 100, at 140 °C [91]. Other zeolites, such as zeolite 4A (pore size ~4Å or 0.4 nm), separate carbon dioxide *via* molecular sieving under the condition that the pore size of the membrane is close enough so that the packing of the pores does not allow the bulk diffusion of gas molecules through the membrane, ultimately compromising its selectivity [92]. The majority of the zeolite membranes show a carbon dioxide permeability between 10^{-13} – 10^{-11} mol m^{-1} s^{-1} Pa^{-1} and a carbon dioxide to nitrogen selectivity between 2-100 at 100 °C (Figure 1.6c), with permeability decreasing to the permeability predicted by Knudsen diffusion, as the temperature increases to 200 °C [84].

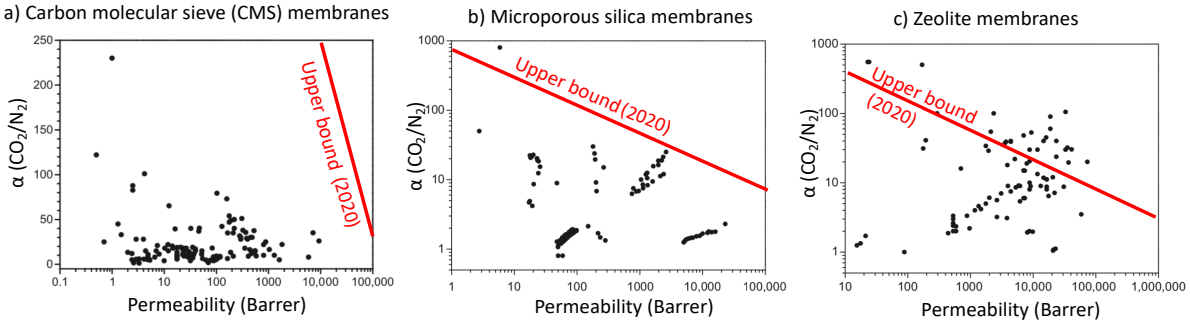

Figure 1.6: Robeson plots for carbon dioxide to nitrogen selectivity versus carbon dioxide permeability for inorganic: a) carbon molecular sieve (CMS), b) microporous silica and c) zeolite membranes. Image adapted from reference [62,84].

Even though microporous inorganic membranes offer better chemical and thermal stability than polymeric membranes, the use of inorganic membranes for carbon dioxide separation as a single-phase membrane is not efficient. Their carbon dioxide permeability and selectivity decrease considerably at temperatures above 500 °C, and the permeability *versus* selectivity trade-off relationship is still governing their performance. To overcome the limitations in permeability and selectivity with microporous inorganic membranes, nonconventional microporous inorganic membranes and methods to enhance permeability and selectivity have been developed, *e.g.* surface modification. The nonconventional microporous inorganic membranes were prepared by the deposition of a perovskite-type ceramic ABO_3 material, such as $BaTiO_3$, on a porous ceramic support. This type of material allows the physisorption of carbon dioxide at low temperatures, and the chemisorption of carbon dioxide at higher temperatures (>200 °C). Despite their permeability increasing with temperature, ~10^{-6} mol m^{-1} s^{-1} Pa^{-1}, the carbon dioxide over nitrogen selectivity of this type of membrane is quite low (<2), attributed to pinholes in the membrane matrix, rendering ABO_3 materials not suitable for carbon dioxide separation [93].

Ideally, a membrane system where a liquid phase would be dispersed inside an inorganic support to create a 'pseudo-dense' membrane would decrease the chance of membrane defects and increase membrane selectivity. The use of a solid and liquid phase would also minimise the thermal expansivity mismatch between membrane materials.

1.4 Dual-phase membranes for carbon dioxide separation

Dual-phase molten-salt membranes provide an alternative to the use of polymeric and inorganic membranes for carbon dioxide separation as they can separate carbon dioxide between 400 and 1000 °C [8,94,95]. The preparation of dual-phase molten-salt membranes relies on the incorporation of a liquid phase (molten carbonate for carbon dioxide separation) inside the porous network of a solid inorganic support, mainly ceramic (Figure 1.7). The physical and chemical properties of both support and molten phase contribute to the permeation mechanism and can be carefully selected to target the specifics of the membrane application, *i.e.* oxidising or non-oxidising stream, explained in detail in chapter 2, section 2.1.1. The physical properties of a membrane support include its porosity, tortuosity, thickness, wettability/acidity, whereas the chemical properties of the support include its ionic and/or electronic conductivity. The physical properties of the molten-salt phase, such as density, melting point, thermal expansion coefficient, physical solubility, wettability and spreading on the ceramic phase, can narrow down the support selection due to material compatibility. Finally, the chemical properties of the molten-salt phase determine the chemical solubility and speciation of molecules inside the melt [94,96,97]. For brevity, dual-phase ceramic molten-salt membranes are referred to as dual-phase membranes throughout this work.

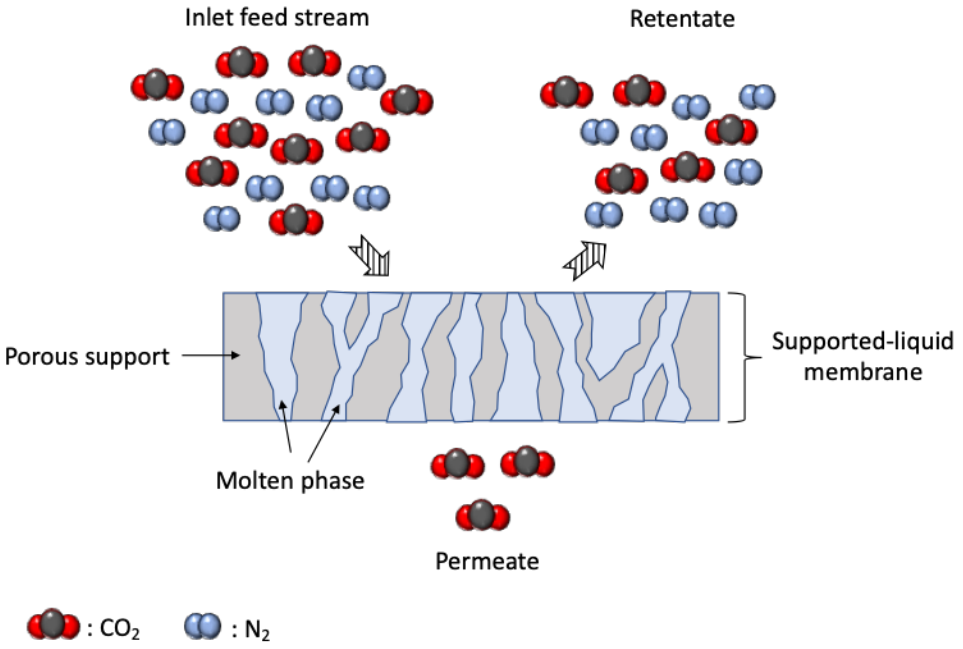

Figure 1.7: Schematic representation of a dual-phase membrane for carbon dioxide from nitrogen separation.

In general, dual-phase membranes have shown a carbon dioxide permeability between 10^{-12} – 10^{-11} mol m^{-1} s^{-1} Pa^{-1}, which is towards the higher end of the permeability requirements for carbon dioxide separation membranes mentioned at the start of section 1.3. But, most importantly dual-phase membranes have a carbon dioxide over nitrogen selectivity>1000, as shown in Figure 1.8, which is significantly better than any other membrane for carbon dioxide separation mentioned above. This high selectivity is attributed to the fact that nitrogen does not ionise, thus can only pass through the membrane by solution diffusion; exhibiting one order of magnitude lower physical solubility values and 50 times lower chemical solubility values compared to carbon dioxide [98]. When carbon dioxide dissolves into molten carbonate however, all the chemical species produced contribute towards its chemical solubility, resulting in facilitated transport with mobile carriers through the membrane. Physical solubility refers to the absorption of carbon dioxide as a molecule in the membrane material. Chemical solubility is what has been found to mainly contribute towards the high selectivity values for dual-phase membranes as the chemical solubility of carbon dioxide is expected to be ~50 times more important than its physical solubility in the melt [99]. Physical and chemical solubility of carbon dioxide in the melt will be referred to in more detail in chapter 2 section 2.3.4.

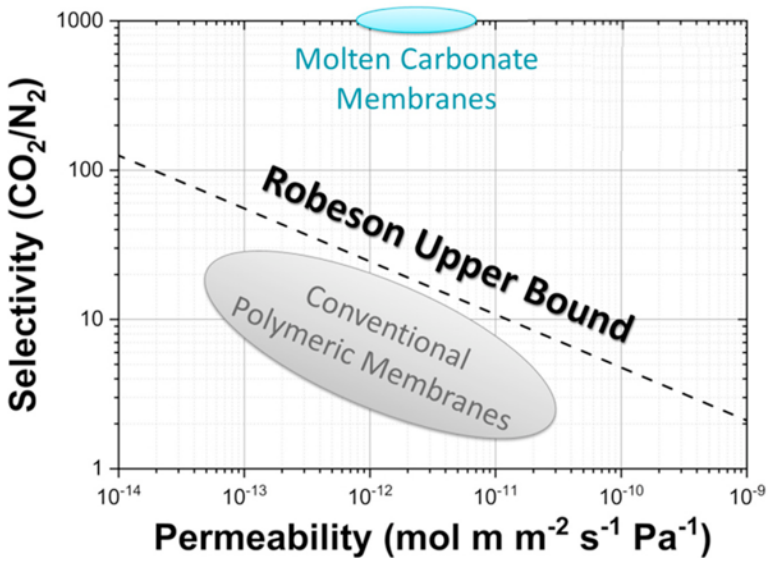

Figure 1.8: Robeson plots for carbon dioxide to nitrogen selectivity versus carbon dioxide permeability for dual-phase membranes. Image adapted from reference [100].

1.4.1 Commercialisation and scale-up of dual-phase ceramic molten-salt membranes for carbon dioxide separation

Dual-phase ceramic molten-salt membranes are still limited to proof-of-concept and lab-scale operation [8]. However, the experimental research done so far shows encouraging evidence for the potential application of these membranes in pre- (IGCC) and post-combustion (natural gas combined cycle (NGCC)) capture processes [101,102]. Experimental results for dual-phase membranes at lab-scale will be further analysed in chapter 2. In order for dual-phase membranes to achieve their separation potential, the membrane must be appropriately integrated in the process and show competitive performance with the already existing separating technologies in terms of energy efficiency and carbon dioxide capture rate. The integration of dual-phase membranes in NGCC and IGCC processes was investigated by Anantharanman *et al.* while using a wide range of capture conditions, *e.g.* feed pressure, operating temperature and temperature prior to expansion of the retentate, and was conducted by an Aspen Hysys and a Matlab-based model simulation [46]. This simulation is based on experimental and modelled carbon dioxide flux data of lab-scale dual-phase membranes and is the best analysis of full-scale use of dual-phase membranes available so far.

In the NGCC process investigated, the flue gas (exhaust stream) leaves the gas turbine at a temperature between 550 and 650 °C, at a pressure of 1 atm, with a low carbon dioxide partial pressure. Even though the operating temperature for dual-phase membranes is compatible with the temperature of the process, the pressure of the exhaust stream is atmospheric; hence it needs to be compressed (5 – 7.5 atm) in order to create the required driving force for separation. The presence of steam as a sweep gas (at a pressure of 1 atm) on the permeate side of the membrane is also used to develop a sufficient driving force across the membrane. In the aforementioned simulation, the dual-phase membranes were integrated in the process by either requiring the expansion of the retentate prior to utilisation (a process requiring less steam, but more work from the expander) as shown in Figure 1.9a, or by utilising the retentate prior to expansion (a process requiring more steam, but less work from the expander) as shown in Figure 1.9b. Overall, even though dual-phase membranes are thermally and chemically stable to be integrated in the NGCC process, the process evaluation conducted by Hysys and Matlab simulations, suggested that their use in the NGCC process would increase the energy penalty compared to post-combustion MEA

capture used so far. More specifically, in both cases, the integrated dual-phase membranes resulted in a net power that was at least 20 MW lower than the power output in NGCC with post-combustion MEA capture and with an energy penalty that was 2.5 – 3.5 % pts higher than post-combustion MEA capture. The increase in energy penalty can be explained by the compression requirements of the feed and sweep stream mentioned above [46].

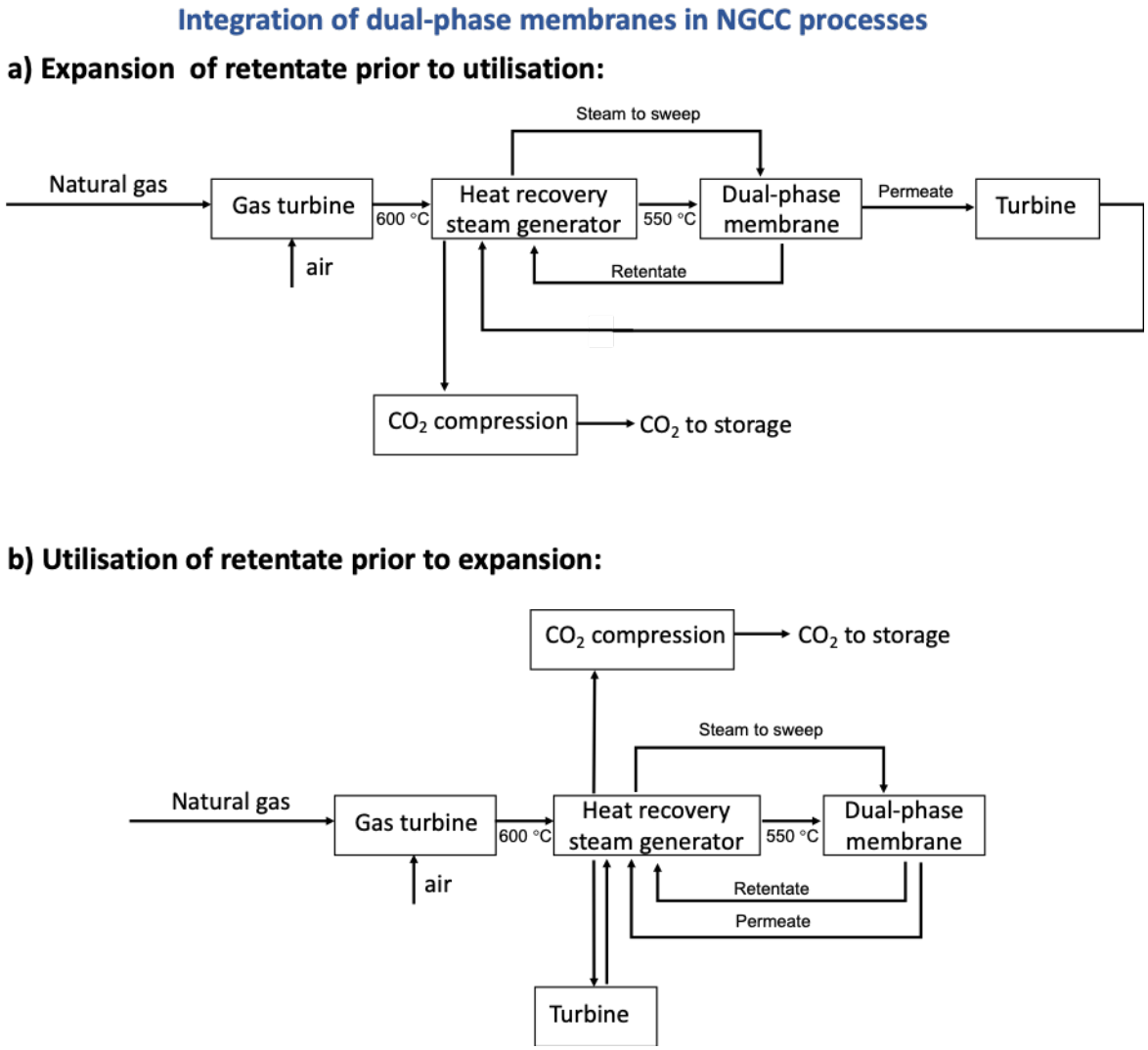

Figure 1.9: Integration of dual-phase membranes in the NGCC process: a) with the expansion of the retentate occurring prior to utilisation, and b) the expansion of retentate occurring after its utilisation. Image adapted from reference [46].

In the IGCC process however, the use of dual-phase membranes outperformed the conventional Selexol technology used in a Shell-type gasifier for pre-combustion, which selectively removes hydrogen sulphide and carbon dioxide in a two-step process. Carbon dioxide capture in the pre-combustion IGCC process required the capture of carbon dioxide from a mixture of hydrogen, carbon dioxide, carbon monoxide, nitrogen and hydrogen sulphide at a high pressure of 35 – 40 bar

(~35 – 40 atm). Several cases of the integration of dual-phase membranes were explored based on the conditions at which the feed stream was supplied to the membrane. In the first case, the carbon monoxide in the syngas coming from the gasifier is converted into carbon dioxide with the addition of steam over a two-stage shift process: a high temperature shift (HTS, at 520 °C) followed by a low temperature shift (LTS, at 180 °C). HTS provides a fast conversion of carbon monoxide to carbon dioxide due to better reaction kinetics at high temperature resulting in a significant conversion of 68.25%. The LTS process that follows increases the overall conversion of the reaction to 83.34% [103]. The resulting stream of the LTS process contains hydrogen, carbon dioxide (28.1 vol%) and water along with some unconverted carbon monoxide and is fed to the dual-phase membranes at 500 °C (Figure 1.10a). In the second case, water is removed from the stream exiting the LTS, resulting in a carbon dioxide concentration of 37.9 vol% in the feed stream going into the dual-phase membrane (Figure 1.10a, Case II). Additional cases investigated in this study considered the employment of a two-stage dual-phase membrane process (Figure 1.10b). In those cases, the stream exiting the high temperature shift (HTS) reactor at 520 °C, with a carbon dioxide concentration of 23 vol%, was directly fed in the first dual-phase membrane module. After the stream has been fed to the first dual-phase membrane module and carbon dioxide has been separated, the equilibrium in the first membrane's retentate stream (now used as the feed stream of the second dual-phase membrane) is shifted. A second HTS can be used in this case, as carbon dioxide removal from the resulting stream of the first HTS process (the retentate stream of the first dual-phase membrane) will lead to higher carbon monoxide to carbon dioxide conversion achieved in the second HTS process. The resulting stream of the second HTS, is then fed into the second dual-phase membrane module for carbon dioxide separation. In all investigated cases above, due to the high partial pressure created for carbon dioxide separation the use of a sweep stream on the permeate side of the membrane is not required. The overall efficiency of the dual-phase membranes, as evaluated by Aspen Hysys and Matlab-based simulation for dual-phase membranes, has proven to be better than the use of the Selexol process, showing an improvement in the energy penalty between 0.8 and 2.15% pts, and a net power production between 10-20 MWe higher for the dual-phase membranes (all investigated cases) [46].

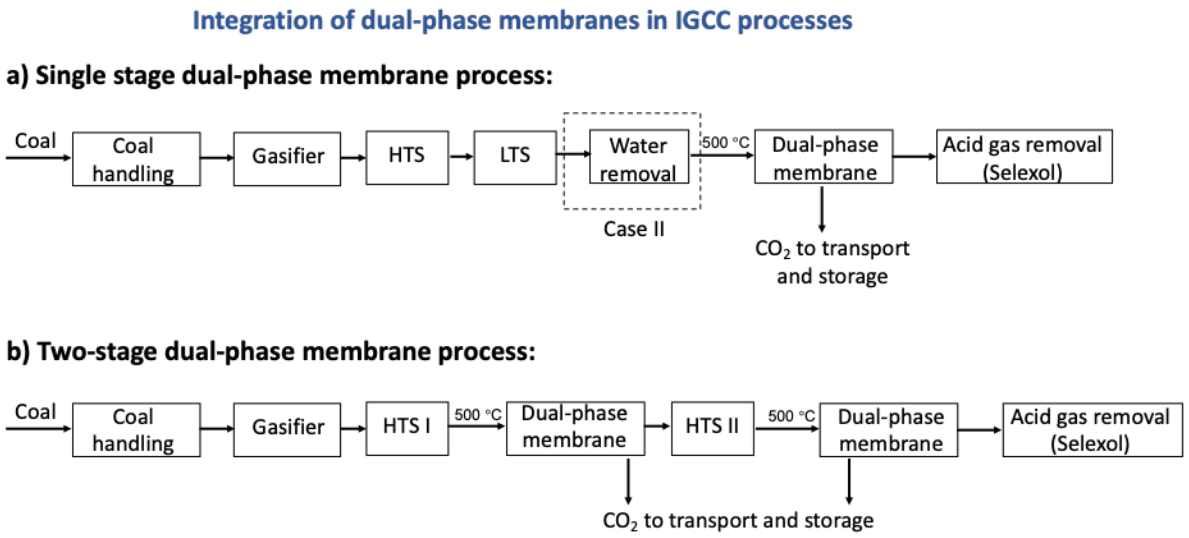

Figure 1.10: Integration of dual-phase membranes in the IGCC process: a) as a single stage membrane process, and b) two-stage dual-phase membrane process. Image adapted from reference [46].

The highest potential for dual-phase membranes could be achieved with the integration of the IGCC process as a two-stage separation unit. However, the area requirements for the use of a two-stage dual-phase membrane process (>105,000 m^2) are higher than the requirements for the use of a single-stage dual-phase membrane process (<45,000 m^2). Another parameter to be taken into consideration for the commercialisation of dual-phase membranes is the effect of flue gas impurities, such as fly ash and mercury, and sulphur dioxide and hydrogen sulphide poisoning, on membrane performance [104,105]. Dual-phase membranes must either show good functionality at high temperature with the presence of these contaminants in their inlet stream, or the contaminants must be removed. To remove the contaminants, the exhaust stream has to be cooled down and an acid gas removal (AGR) process needs to be used. Following AGR, the exhaust stream needs to be compressed at lower temperature (30 °C) and re-heated, to minimise compression work at higher temperature. The compression of the stream is necessary for creating the required driving force for separation prior to the stream being fed to the dual-phase membranes [94]. This leads to an increase of the energy requirements for this process. Further laboratory research targeted on optimising dual-phase membrane properties and achieving high transmembrane fluxes for low active membrane areas could facilitate their application in a wider scale.

1.4.2 Scale-up challenges for dual-phase ceramic molten-salt membranes

Based on the aforementioned integration of dual-phase ceramic molten-salt membranes in a high-temperature IGCC process (section 1.4.1), a number of manufacturing and scale-up challenges have derived. So far, the majority of research focuses on the infiltration of disk-shaped (pellet) porous supports at a laboratory scale either after or during the sintering of the ceramic phase. Although the use of these membranes has contributed towards the understanding of permeation mechanisms and materials selection, their production process does not favour scalability when accounting for their small active surface area. Dual-phase membranes with a tubular symmetric or asymmetric geometry offer a larger active surface area, but the infiltration method has not yet shown evidence of reproducibility [106,107]. The development of a reproducible process for the infiltration of asymmetric tubular ceramic supports (larger surface areas than symmetric) depends on the controlled infiltration of the molten salts inside the desired layer of the ceramic support, which could potentially reduce molten salt creep, *i.e.* molten salt leaving the support. In symmetric membranes, the molten carbonate is infiltrated in the entire membrane thickness, which has the same uniform pore size. In asymmetric membranes, the molten carbonate can be infiltrated in one of the separation layers, decreasing the membrane thickness required for separation [108]. Further challenges for the scale-up of dual-phase membranes include their long-term stability and performance under process conditions. For membranes to be applied in NGCC processes, they must be able to withstand pressures around 5 to 7.5 atm (0.5 to 0.75 MPa), as such pressures are required in order to create a sufficient driving force for carbon dioxide separation. In IGCC processes, the pressure of the carbon dioxide containing gas stream from which carbon dioxide is separated is between 35 and 40 atm (3.5 and 4 MPa, as mentioned in section 1.4.1) [46]. Membrane sealing, solid-liquid compatibility and the membrane's mechanical strength also need to exhibit stability under high pressure and process operating conditions. High temperature sealing has been a challenge for the application of membranes in a larger scale under high pressures as it often fails under long-term operation, causing the failure of the membrane itself. Failure of the membrane sealing can occur due to low thermal cycling capacity of the sealant and the excessive radial pressure applied at the compression points between sealant and membrane [109]. Therefore, membrane systems that reduce the sealing area *per* membrane area, have a lower risk of failure. Since a large surface of flat-sheet

membranes requires to be sealed on the support or frame (in the case of plate-and-frame configuration), compared to the surface area required to be sealed in the case of tubular membranes, membrane sealing inhibits the operation of pellet membranes at a larger scale. Furthermore, the reactor design must be tolerant to these conditions and to the corrosive nature of molten carbonate [94].

1.5 Research aims

The main aim of this work is to address issues with the application of dual-phase ceramic molten-salt membranes for carbon dioxide separation, specifically related to their manufacturing, scalability and long-term stability. To do that, the membrane development process must be carefully designed, and the membrane materials must be carefully selected. The geometry of the membrane must meet the conditions of modularity, high surface-to-volume ratio and potential for scale-up while using materials that are chemically and thermally robust and can be easily fabricated. Finally, the developed dual-phase ceramic molten-salt membrane must exhibit a carbon dioxide permeance and selectivity that is competitive to conventional CCS technologies and show potential for long-term durability.

To accomplish the main aim, this work focuses on:

a) exploiting the use of scalable supports and tackling issues with support damage during operation
b) understanding how the distribution of molten carbonate within the supports impacts the permeation and separation performance of the membrane, and
c) utilising the mobility of molten salts to selectively infiltrate specific layers within supports and to self-heal potential membrane damage.

These are the broad aims of this research, with more specific objectives given further on, after conducting a more detailed literature review on dual-phase ceramic molten-salt membranes (chapter 2, section 2.5).

Chapter 2

Literature review

2.1 Dual-phase molten-salt membranes in operation

In this section, the transport mechanism of carbon dioxide through dual-phase molten-salt membranes with different support properties will be analysed. The aim of this analysis is to identify material properties that will allow the development of a dual-phase membrane with enhanced permeation properties and simple fabrication methods. As mentioned earlier, in order for a dual-phase molten-salt membrane to be efficient in carbon dioxide separation, it must show permeabilities between 10^{-13} – 10^{-12} mol m^{-1} s^{-1} Pa^{-1} (or higher), accompanied by high carbon dioxide to nitrogen selectivity (>50).

2.1.1 Permeation mechanisms for dual-phase molten-salt membranes

The transport mechanism through dual-phase molten-salt membranes can be explained by the theory of ambipolar permeation of carbonate ions and electron and/or oxide ions through the membrane and relies on the chemical properties of the support and the physical and chemical properties of the molten salt. Support and molten salt properties can contribute to carbon dioxide separation reactions when the molten salt is molten carbonate. So far, in the development of dual-phase membranes, nominally electrically insulating supports, oxygen-ion-conducting supports, electron-conducting supports and mixed ion-electron conducting supports have been investigated. Nominally electrically insulating supports do not allow the transport of electrons and/or oxide ions through their matrix. In this case the carbon dioxide is expected to permeate through the molten phase only, with the surface-exchange reactions being limited to gas-liquid phase interactions (physical and/or chemical) (Figure 2.1a) [110]. The transport is enabled by a facilitated transport mechanism, where carbon dioxide in the gas phase reacts with species in the carbonate melt to form carbonate-based charged species (further discussed in section 2.3.4), depicted as carbonate ions in Figure 2.1 for simplicity. The compensating counter-current permeating species is not shown in Figure 2.1. If the support is oxygen-ion conducting the co- or counter-permeation of oxide ions inside the support results in carbon dioxide reacting with the oxide ions to form carbonate ions that permeate through the melt ($CO_2 + O^{2-} = CO_3^{2-}$) (Figure 2.1b) [111]. If the support is electron-conducting, oxygen in the gas phase reacts with carbon

dioxide in the gas phase and electrons to form carbonate ions that permeate through the melt and release carbon dioxide on the permeate side of the membrane ($CO_2 + 1/2\ O_2 + 2e^- = CO_3^{2-}$) [111]. Mixed ionic and electronic conductors (MIECs) have both an oxide ion and an electron conductivity [110,112]. With the addition of steam on the feed or permeate side of the dual-phase molten-salt membrane hydroxide ions have also been found to diffuse through the melt counter-currently with carbonate ions (Figure 2.1) [113]. In all cases, when carbon dioxide reacts with the oxide ions or electrons of the membrane support and dissolves in the melt, the gas surface-exchange reaction is considered to occur at the triple-phase boundary (TPB) between the support, molten salt and gaseous carbon dioxide [112]. At the same time, chemisorption and physisorption of carbon dioxide in the membrane can also occur through the surface of the melt, for all the cases described above. This will be further discussed in section 2.3.4.

a) Nominally electrically-insulating support

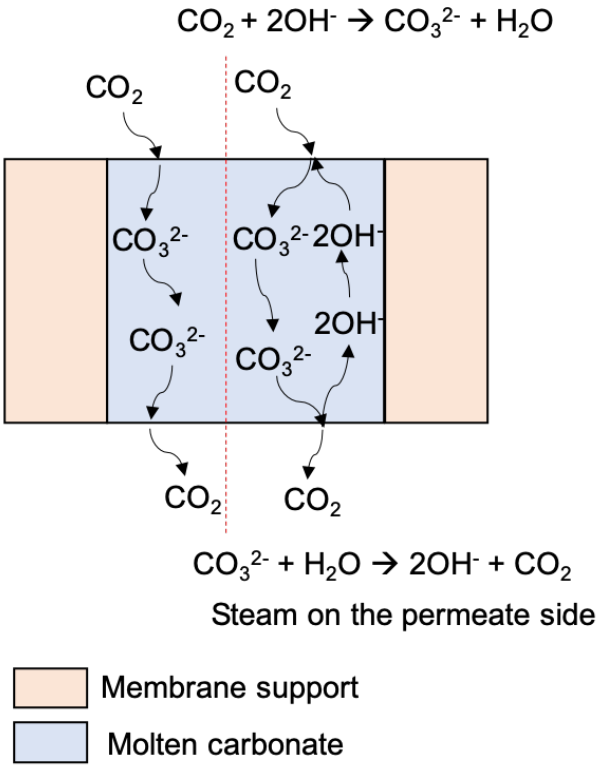

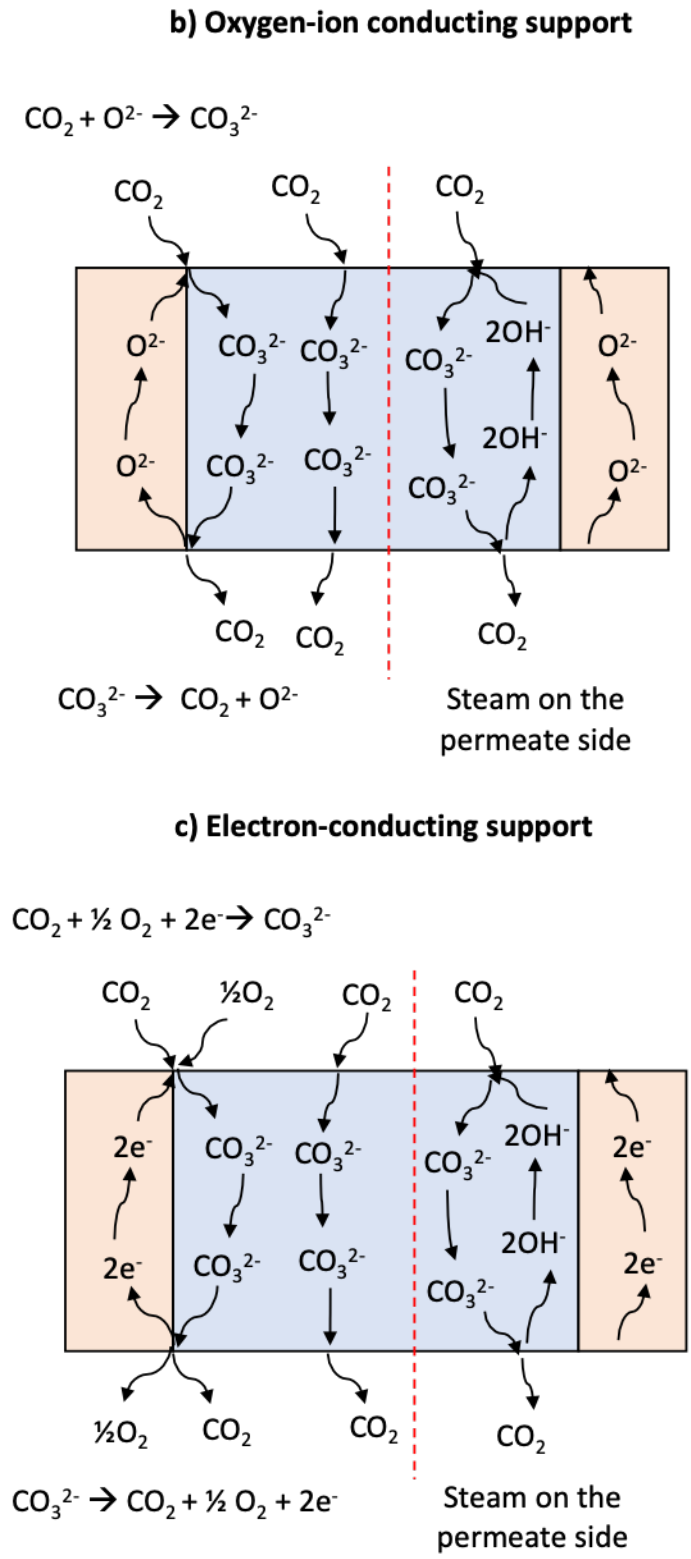

Figure 2.1: Permeation mechanism for different support properties without (left-hand side) and with (right-hand side) the presence of steam in the permeate side: a) nominally electrically-insulating support, b) oxygen-ion-conducting support, and c) electron-conducting support.

2.1.2 Flux equations for dual-phase molten-salt membranes

Flux equations for dual-phase molten-salt membranes were derived based on the driving force for separation and the transport properties of the support and the molten-salt phase. The flux of charged ions in the support and molten carbonate phase creates currents within the membrane that have a sum equal to zero when there is no external circuit applied on the membrane.

In order to express the transport of carbonate ions in the molten carbonate phase a multi-component force balance (considering the molten-phase as a concentrated salt) was used by Wade *et al.* [114]. This is possible by relating the conductance of carbonate ions through the molten carbonate phase to the conductance of ions through an electrolyte [115]. In steady-state and under a uniform concentration of carbonate ions in the melt (chemical potential of carbonate, $\nabla\mu_{CO_3^{2-}}=0$), carbonate flux in the molten carbonate phase can be written as:

$$J_{CO_3^{2-}} = -\left(\frac{\varepsilon}{\tau}\right)_c \frac{Z_{CO_3^{2-}} C_{CO_3^{2-}} D_{CO_3^{2-}} \mathcal{F}}{RT} \nabla\Phi_{CO_3^{2-}} \qquad \text{(Eq. 2.1)}$$

where ε is the porosity, τ is the tortuosity, $Z_{CO_3^{2-}}$ is the charge of carbonate (-2), $C_{CO_3^{2-}}$ is the concentration of carbonate in the melt (mol cm^{-3}), $\mathcal{F}$ is the Faraday constant (9.649×10^4 C mol^{-1}), R is the ideal gas constant (J mol^{-1} K^{-1}), T is the operating temperature of the dual-phase membrane (K) and $\Phi_{CO_3^{2-}}$ is the electrical potential in molten carbonate (volts). The solid support phase is indicated by using (s) whereas the molten carbonate phase is represented by (c).

Tortuosity (τ) of a porous membrane can be calculated by defining the ratio of the shortest distance between two points of a pore (L_g) over the length of the straight line between the same two points of a pore (L_s) [116].

$$\tau = \frac{L_g}{L_s} \qquad \text{(Eq. 2.2)}$$

Practically, it can be measured using high magnification imaging, *e.g.* SEM or X-ray tomography, or by using a combination of gas diffusion data and porosity data. Tortuosity can be calculated by SEM imaging for example by graphically defining the shortest distance a gas molecule has to travel inside a single pore to permeate from the feed to the permeate side of the membrane (L_g) and by defining the membrane thickness (L_s). Using the gas-diffusion and porosity data, the tortuosity over porosity ratio can be calculated by the following equation [117]:

$$\frac{\tau}{\varepsilon} = \frac{A_s D_{12}}{VL\alpha} \qquad \text{(Eq. 2.3)}$$

where A_s is the cross sectional area of the membrane (cm^2), D_{12} is the molecular diffusivity of helium in nitrogen ($cm^2\ s^{-1}$), V is the chamber volume (cm^3), L is the membrane thickness (cm) and α is the slope of the differential equation for diffusion *versus* time (linear plot). Tortuosity is then calculated by τ=ε(τ/ε), knowing the sample porosity.

For dual-phase membranes with an oxygen-ion conducting solid oxide support for example (Figure 2.2), carbon dioxide in the gas phase ($CO_{2(g)}$) reacts with an oxide ion in the solid oxide phase (O^{2-}) to form carbonate (CO_3^{2-}) and an oxygen vacancy ($V_{\ddot{O}}$) inside the solid oxide (SO) matrix ($CO_{2(g)}+O^{2-}= CO_3^{2-}+V_{\ddot{O}}$).

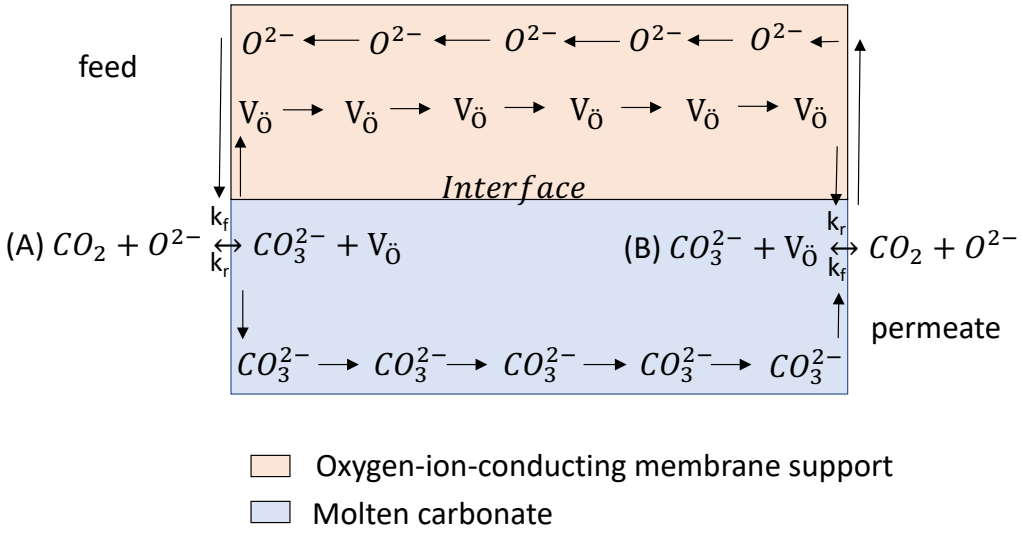

Figure 2.2: Permeation mechanism for a dual-phase membrane with an oxygen-ion-conducting support and molten carbonate as the molten phase, showing the surface reaction (A) on the feed side of the membrane, where carbon dioxide reacts with an oxide ion to form carbonate, and the surface reaction (B) where the reverse reaction occurs.

Assuming pseudo-steady state conditions at the membrane surface, the sum of the chemical potentials of the reactants is equal to the sum of the chemical potentials of the products (surface equilibrium), while taking into consideration the free energy contribution of the charged species. Therefore, the following equation applies at surface equilibrium at the feed side of the membrane, as is depicted by reaction A in Figure 2.2. The term $Z_i\,\mathcal{F}\nabla\Phi_i$ represents the free energy of the charged species:

$$\mu_{CO_2} + \mu_{O^{2-}} = \mu_{V_{\ddot{O}}} + Z_{V_{\ddot{O}}}\mathcal{F}\nabla\Phi_{SO} + \mu_{CO_3^{2-}} + Z_{CO_3^{2-}}\,\mathcal{F}\nabla\Phi_{CO_3^{2-}} \qquad \text{(Eq. 2.4)}$$

By assuming ideal gas conditions, the chemical potential of carbon dioxide can be expressed as:

$$\mu_{CO_2} = \mu^{o}_{CO_2} + RT\ln\frac{P_{CO_2}}{P^{o}} \quad \text{(Eq. 2.5)}$$

where μ^o and P^o are the chemical potential and pressure at standard state, respectively, whereas P_{CO2} is the partial pressure of carbon dioxide. Similarly, the chemical potential of the charged species (acting as charge carriers) $\mu_{V_{\ddot{O}}}$ can be expressed as $\mu_{V_{\ddot{O}}}{}^{o}$+RTln($C_{V_{\ddot{O}}}/C^o$), where $C_{V_{\ddot{O}}}$ is the concentration of oxygen vacancies in the oxygen-ion-conducting support.

Surface reaction (A) on the feed side of the membrane is considered an elementary reaction (Figure 2.2). Hence the correlation between the P_{CO2} and $C_{V_{\ddot{O}}}$ can be described by Eq. 2.6, as the law of mass action is applicable.

$$k_f P_{CO_2,feed} = k_r C_{V_{\ddot{O}},feed} \quad \text{(Eq. 2.6)}$$

whereas for surface reaction (B) (Figure 2.2), on the permeate side of the membrane, Eq. 2.7 applies:

$$k_r C_{V_{\ddot{O}},permeate} = k_f P_{CO_2,permeate} \quad \text{(Eq. 2.7)}$$

where k_f and k_r are the forward and reverse reaction rate constants, respectively, for surface reaction (A) and surface reaction (B) (Figure 2.2).

The relationship between $C_{V_{\ddot{O}}}$ and P_{CO2} ratios can then be derived from Eq. 2.6 and Eq. 2.7 [111]:

$$\frac{C_{V_{\ddot{O}},feed}}{C_{V_{\ddot{O}},permeate}} = \frac{P_{CO_2,feed}}{P_{CO_2,permeate}} \quad \text{(Eq. 2.8)}$$

The chemical potentials and concentrations of the molten carbonate and the oxide ions are considered to be constant. Eq. 2.4 can then be solved for $\nabla\Phi_{CO_3^{2-}}$, replacing the chemical potential terms for carbon dioxide (Eq. 2.5) and oxygen vacancies ($\mu_{V_{\ddot{O}}}{}^{o}$+RTln($C_{V_{\ddot{O}}}/C^o$)) and replacing Eq. 2.8 in the chemical potential terms [111,114].

The resulting carbonate flux ($J_{CO_3^{2-}}$) for dual-phase membranes with an oxygen-ion-conducting support is equal to the carbon dioxide flux (J_{CO2}) based on the stoichiometry of the surface reactions ($CO_{2(g)}+O^{2-} = CO_3^{2-}+V_{\ddot{O}}$) [111], and can be written as:

$$J_{CO_2} = \frac{\alpha RT}{4\mathcal{F}^2 L}\ln\left(\frac{P_{CO_2,feed}}{P_{CO_2,permeate}}\right) \quad \text{(Eq. 2.9)}$$

where α is the permeance coefficient of total conductance of the dual-phase membrane defined as:

$$\alpha = \frac{\left(\frac{\varepsilon}{\tau}\right)_c \sigma_{CO_3^{2-}} - \left(\frac{\varepsilon}{\tau}\right)_s \sigma_{O^{2-}}}{\left(\frac{\varepsilon}{\tau}\right)_c \sigma_{CO_3^{2-}} + \left(\frac{\varepsilon}{\tau}\right)_s \sigma_{O^{2-}}} \quad \text{(Eq. 2.10)}$$

and L is the membrane thickness (m), $\sigma_{O^{2-}}$ is the oxide ion conductivity of the support (Ω^{-1} m^{-1}), $\sigma_{CO_3^{2-}}$ is the carbonate-ion conductivity of the molten phase (Ω^{-1} m^{-1}) $P_{CO2,permeate}$, $P_{O2,permeate}$ and $P_{CO2,feed}$, $P_{CO2,feed}$ are the pCO_2 and pO_2 in the permeate and feed side of the membrane, respectively. The natural logarithm of carbon dioxide partial pressure difference is the only driving force in the system.

For dual-phase membranes with an electron-conducting support the flux (J_{CO2}) equation for carbon dioxide takes into consideration the partial-pressure driving force for oxygen and carbon dioxide, the effective electronic conductivity of the support (σ_{e^-} in Ω^{-1} m^{-1}) and the carbonate-ion conductivity of the molten phase ($\sigma_{CO_3^{2-}}$ in Ω^{-1} m^{-1}), as described in the work of Rui *et al.* by Eq. 2.11 [111]:

$$J_{CO_2} = \frac{\alpha RT}{4\mathcal{F}^2 L}\left[\ln\left(\frac{P_{CO_2,feed}}{P_{CO_2,permeate}}\right) + \frac{1}{2}\ln\left(\frac{P_{O_2,feed}}{P_{O_2,permeate}}\right)\right] \quad \text{(Eq. 2.11)}$$

The oxide ion conductivity ($\sigma_{O^{2-}}$) in the permeance coefficient α in the case of an oxygen-ion-conducting support (Eq. 2.10) is now replaced by the electronic conductivity (σ_{e^-}) of an electron-conducting support.

In the case of mixed ion-electron conducting supports (MIEC), the flux (J_{CO2}) equation for carbon dioxide in the presence of oxygen in the feed side of the membrane is expressed based on the electron and oxide ion conductivity of the support (Eq. 2.12).

$$J_{CO_2} = \frac{\alpha RT}{4\mathcal{F}^2 L}\left[(\sigma_{e^{2-}} + \sigma_{O^{2-}})\ln\left(\frac{P_{CO_2,feed}}{P_{CO_2,permeate}}\right) + \frac{\sigma_{e^{2-}}}{2}\ln\left(\frac{P_{O_2,feed}}{P_{O_2,permeate}}\right)\right] \quad \text{(Eq. 2.12)}$$

where the permeance coefficient of total conductance, α, is given by (Eq. 2.11):

$$\alpha = \frac{\left(\frac{\varepsilon}{\tau}\right)_c \sigma_{CO_3^{2-}} - \left(\frac{\varepsilon}{\tau}\right)_s (\sigma_{e^{2-}} + \sigma_{O^{2-}})}{\left(\frac{\varepsilon}{\tau}\right)_c \sigma_{CO_3^{2-}} + \left(\frac{\varepsilon}{\tau}\right)_s (\sigma_{e^{2-}} + \sigma_{O^{2-}})} \quad \text{(Eq. 2.13)}$$

If oxygen is not present in the system, the term $\ln(P_{O2,feed}/ P_{O2,permeate})$ in (Eq. 2.12) does not contribute to carbon dioxide flux and is equal to zero.

As can be seen in Figure 2.2, surface exchange reactions on the feed and permeate side of the dual-phase membrane and bulk diffusion are the steps that largely impact the rate of transport as they provide greater resistances than mass transfer of gas molecules in the gaseous phase (for membrane processes that have been engineered correctly). Between bulk diffusion and surface exchange reactions, bulk diffusion has

been found to control carbon dioxide separation through dual-phase membranes when the membrane thickness is above the critical thickness (L_c). When carbon dioxide permeation through the dual-phase molten-salt membranes is controlled by bulk diffusion the flux is inversely proportional to the membrane thickness and is dependent on properties of membrane micro-structure, *i.e.* porosity and tortuosity, as well as the oxide ion and/or electron conductivity of the support and the carbonate-ion conductivity in the molten phase. Based on the flux equations, a simple way to improve carbon dioxide flux in the bulk-diffusion-limited region of a membrane would be to decrease membrane thickness. In dual-phase molten-salt membranes however, membrane thickness is often inaccurately assumed as the equivalent of the permeation distance/pathlength of the permeating species through the membrane. The pathlength of carbonate ions in the molten phase, for example, needs to take into consideration the tortuosity of the membrane to be accurately determined. The decrease in pathlength, often achieved by decreasing membrane tortuosity, is what will ultimately increase carbon dioxide flux. Another way to improve flux based on the above flux equations, is to increase pCO_2 and/or pO_2 in the feed side of the membrane. When the membrane thickness is decreased below its critical thickness surface exchange becomes the rate-limiting step for permeation. In that case, carbon dioxide flux is controlled by carbon dioxide uptake and release on the feed and permeate side of the membrane, respectively, following a power-law dependence on pCO_2 and/or pO_2, depending on support chemical properties [113]. A practical way to increase carbon dioxide flux in membranes operating in a surface-exchange-limited region is to increase the membrane's operating temperature. Temperature activation will accelerate the feed and permeate side surface exchange reaction rate, which has been found to follow the Arrhenius equation [48]. Studies to determine which surface exchange reaction is rate-limiting on flux have also shown that the permeate-side surface exchange reaction is more rate limiting on flux than the reverse feed-side surface exchange reaction. This is believed to be due to the large pCO_2 on the feed side of the membrane compared to the permeate side pCO_2. Large pCO_2 in the feed side, causes concentration polarisation and carbon dioxide molecules on the surface can also block or occupy vacancy sites for carbonate [118,119]. Higher feed stream flow rates would reduce the concentration polarisation phenomenon on the feed side of the membrane, while freeing possible blocked or occupied areas on the membrane surface. Another way to increase carbon dioxide flux in surface-exchange-limited membranes would be to increase the available surface for carbon dioxide desorption

which would lead to a larger chemical potential gradient between the feed and permeate-side surface, increasing the driving force for the flux of carbonate ions through the membrane's bulk.

2.1.3 Permeation through dual-phase molten-salt membranes with an electron-conducting support

The first dual-phase molten-salt membrane reported in literature used a stainless-steel support infiltrated with the ternary molten carbonate eutectic (Li_2CO_3: Na_2CO_3: K_2CO_3= 43.5: 31:5: 25 mole ratio) and showed a carbon dioxide permeance value of 5×10^{-9} mol s^{-1} m^{-2} Pa^{-1} at 650 °C (permeability 7.9×10^{-12} mol s^{-1} m^{-1} Pa^{-1}) [120] and a carbon dioxide to nitrogen selectivity only around 3.5, which is particularly low for a dual-phase membrane. Both permeance and selectivity were improved by a factor of four at 650 °C with the presence of oxygen in the feed side of the membrane (carbon dioxide:oxygen in a 2:1 mixture) as carbon dioxide reacts with oxygen and electrons to form carbonate (CO_2 + 1/2 O_2 +2e^- = CO_3^{2-}) which will diffuse through the melt, increasing membrane permeability. The increase in membrane performance with the presence of oxygen, largely confines the operation of these membranes in separations with oxidising streams such as post-combustion decarbonisation. In addition to the low selectivity of this membrane, the metal electron-conducting support was found to oxidise to form $LiFeO_2$ at temperatures above 650 °C, decreasing membrane permeance significantly with further increase in temperature (3×10^{-9} mol s^{-1} m^{-2} Pa^{-1} at 750 °C) [120]. To overcome the oxidation problems described above, silver (Ag) was used as the porous support for the metal-molten salt membranes with a binary molten-salt eutectic (Li_2CO_3: K_2CO_3= 62:38 molar ratio) melt. Even with the use of silver, however, carbon dioxide permeance showed a decrease above 650 °C which was attributed to silver grain growth with the increase in temperature [121]. For better chemical compatibility between the two phases of the metal-molten salt dual-phase membranes, Zhang *et al.* and Tong *et al.* modified the surface of the porous silver supports by atomic layer deposition (ALD) [122,123]. The porous silver supports were coated with a ~20 nm nanolayer of alumina (~0.83 mm total membrane thickness) [122] and ~25 nm nanolayer of zirconia (ZrO_2) [123]. The development of metal-molten-salt membranes with a zirconia or alumina ALD layer on the porous silver support prevented silver sintering at higher temperatures and the membrane did not show a performance decrease above 650 °C. However, the modification of the molten-salt

phase itself was not ruled out in these experiments. Electrochemically dealloying of the silver matrix has also been investigated for the surface modification of dual-phase metal-carbonate membranes in order to increase the triple-phase boundary (TPB) between the support, molten salt and gaseous carbon dioxide [124,125]. NiO has also been used instead of silver as a support material [126]. The NiO-supported dual-phase membrane showed a stable performance at 850 °C with a high selectivity (>400) and a carbon dioxide permeance value of 6.1 x 10^{-7} mol s^{-1} m^{-2} Pa^{-1} (permeability 7.33 x 10^{-10} mol s^{-1} m^{-1} Pa^{-1}) at this temperature.

Based on the membrane systems described above, it is clear that the operation of electron-conducting dual-phase membranes depends on the presence of oxygen in the feed stream, which limits their application in streams such as post-combustion decarbonisation. Stainless-steel and silver-supported dual-phase membranes in particular, showed a decrease in permeation performance at temperatures above 650 °C due to interfacial reactions between the stainless-steel and the molten carbonate and due to silver sintering, respectively. In the case of silver, the increase in fabrication steps to prevent degradation by sintering also poses limitations in the wider application of these membranes in carbon dioxide separation. Moreover, even though the use of membranes in CCS can show cost advantages compared to current technologies (such as amine stripping using MEA); stainless steel (~80 $/kg) and silver (~800$/kg) are expensive membrane support materials compared to ceramics, e.g. YSZ (10-20 $/kg) or Al_2O_3 (~5 $/kg). This poses significant limitations in the scale-up of silver and stainless steel-based membranes, as their implementation in pre-combustion capture processes for example can require membrane surface areas up to 45,000 m^2 in order to achieve the same net power output as already existing CCS [46]. From reviewing dual-phase membranes with an electron-conducting support it is clear that the selection of support material is important, in order to ensure molten salt and support material compatibility, along with high permeation performance for these membranes.

Permeation of carbon dioxide through a dual-phase molten-salt membrane (ternary eutectic mixture) with a primarily electron-conducting support has also been achieved against its own chemical potential, characterised as ‘uphill’ permeation, by Papaioannou *et al.* [127]. A mixed ionic and electronic conducting support, $La_{0.6}Sr_{0.4}Co_{0.8}Fe_{0.2}O_{2-\delta}$ (LSCF), was used as an electron-conducting support for these membranes instead of stainless steel, or other electron-conducting supports, that

oxidise at high temperatures in the presence of oxygen (pO_2=0.2 atm). LSCF shows a rather low oxygen-ion conductivity (0.091 S cm^{-1}) compared to its electron conductivity (1217 S cm^{-1}) at 600 °C, and therefore functions as an electron-conducting material. Based on the carbonate forming reaction on the feed side of the LSCF-supported dual-phase membrane: $CO_2 + 1/2O_2 + 2e^- \rightarrow CO_3^{2-}$, carbon dioxide and oxygen can both be transported through the LSCF-supported dual-phase membrane. High oxygen partial pressure on the feed side (pO_2= 0.2 atm), along with a low partial pressure of carbon dioxide (pCO_2= 0.01 atm), led to 'uphill' permeation of carbon dioxide coupled with 'downhill' permeation of oxygen as the excess of oxygen in the feed side shifts the equilibrium of the carbonate forming reaction towards the production of carbonate. Since the support acts as an electron-conducting material, oxygen chemical potential difference is what drives the carbonate forming reaction and therefore, the 'uphill' permeation of carbon dioxide through the membrane. The 'uphill' permeation of carbon dioxide allows membrane operation with low carbon dioxide concentrations in the feed stream without the need for compression. The membrane (1 mm thickness) reached a carbon dioxide permeability of 1.5×10^{-12} mol m^{-1} s^{-1} Pa^{-1} (permeance 1.5×10^{-9} mol m^{-2} s^{-1} Pa^{-1}) at 600 °C, which is comparable with the permeability of MIEC-supported dual-phase membranes with a pCO_2= 0.5 atm and without the use of oxygen in their feed side [127]. The addition of oxygen on the feed side of the membrane was also found to improve the long-term stability (>60 h) of LSCF-supported dual-phase membranes with a ternary eutectic mixture as the molten phase, at temperatures between 800 and 900 °C [128]. X-ray powder diffraction (XRD) results (110 h of operation) suggested the decomposition of the LSCF ceramic phase when only carbon dioxide and nitrogen were used in the feed side, as carbon dioxide reacts with the ceramic support to form a strontium carbonate layer prohibiting the reaction of carbon dioxide with oxide ions at the membrane surface. Oxygen in the feed side of the membrane (pO_2= 0.25 atm, pCO_2= 0.5 atm in balance nitrogen) improved membrane stability as it prevented the reaction of LSCF with the molten-salt phase. The resulting carbon dioxide permeance in the presence of oxygen was two orders of magnitude higher compared to carbon dioxide permeance when oxygen was not present in the system [128].

2.1.4 Permeation through dual-phase molten-salt membranes with an oxygen-ion-conducting support

After the development of the first metal-molten salt dual-phase membranes, oxygen-ion-conducting ceramic supports, showing high thermal stability without grain growth up to 1000 °C, were used for the development of dual-phase membranes [129]. The oxygen-ion conductivity of the ceramic supports also allows the transport of oxide ions in the solid phase and does not require the presence of oxygen in the feed side of the membrane for the surface-exchange reaction to occur ($CO_2 + O^{2-} = CO_3^{2-}$). Hence, dual-phase membranes with an oxygen-ion-conducting support are preferentially used in processes where a reducing stream is present, such as pre-combustion decarbonisation. The diffusion of carbonate ions in the molten-salt phase is considered to be a weakly thermally activated process, whereas the surface-exchange reactions are strongly activated by temperature [130]. Thus, the increase in temperature is expected to result in the increase in transport rate in the absence of flux-limiting interfacial reactions between the support and the molten phase. This has been observed for dual-phase ceramic molten-salt membranes with an oxygen-ion-conducting support with the ternary eutectic mixture as the molten salt [130,131]. The most commonly used oxygen-ion-conducting support materials for the development of dual-phase membrane so far have a fluorite structure, such as yttria-stabilised zirconia (YSZ) [131,132] $Bi_{1.5}Y_{0.3}Sm_{0.2}O_{3-\delta}$ (BYS) [133], $Ce_{0.8}Sm_{0.2}O_{1.9}$ (SDC) [97,134–136] and $Ce_{0.9}Gd_{0.1}O_{1.95}$ (CGO) [131] with oxide ion conductivities (O^{2-}) of 0.004, 0.08, 0.005 and 0.005 S cm^{-1} at 600 °C, respectively [137]. However, membrane performance, as discussed in the introduction, also depends on membrane thickness, micro-structure (intra and inter-connectivity of the pores) and the wettability and stability of the molten phase within the ceramic support. If the membrane system is poorly characterised, the effect of membrane thickness and micro-structure on membrane performance is not clearly defined, leading to difficulties in comparisons between different membranes. Dual-phase ceramic molten-salt membranes with an oxygen-ion-conducting support in the literature have shown permeabilities starting from 10^{-13} [131–133] and reaching 10^{-10} mol m^{-1} s^{-1} Pa^{-1} [130] even at 600 °C. The membranes with the highest permeabilities possessed high inter- and intra-connectivity in their 3D porous network, reducing the pathlength for carbon dioxide diffusion inside the membrane [130]. An equimolar mixture of carbon dioxide and nitrogen as the feed-side inlet, and an inert gas as the sweep gas for the permeate-side inlet, unless stated otherwise.

In general, dual-phase membranes with oxygen-ion-conducting ceramic supports do not require the use of oxidising streams for separation to occur and show good stability with the increase in temperature. Carbon dioxide permeance for dual-phase membranes with oxygen-ion-conducting ceramic supports does not decrease above 650 °C, unlike dual-phase membranes with electron-conducting supports. However, for YSZ-lithium carbonate dual-phase membranes specifically, lithium carbonate has been found to react with zirconium oxide and result in the formation of lithium zirconate, at temperatures above 650 °C or low carbon dioxide pressures ($Li_2CO_3+ZrO_2 = Li_2ZrO_3+CO_2$). The formation of lithium zirconate decreases carbon dioxide uptake in the lithium carbonate melt and causes membranes developed from YSZ-lithium carbonate to fail [131]. With the presence of sodium and potassium carbonate in the molten carbonate mixture however, the formation of lithium zirconate was not observed, and additional studies have shown that the presence of sodium and/or potassium carbonate in the system, provide a higher carbon dioxide uptake than in the case of lithium carbonate alone [138,139]. When CGO was used as the oxygen-ion-conducting support material for the development of dual-phase membranes, the support did not appear to chemically react with the molten carbonate phase [131] and no studies have been conducted for interfacial reactions between BYS or SDC and molten carbonate. Overall, oxygen-ion-conducting ceramic supports have shown promising results when used as the supports for dual-phase ceramic molten-salt membranes.

2.1.5 Permeation through dual-phase molten-salt membranes with a mixed ionic- and electronic-conducting support

MIEC supports have also been used as the support of dual-phase membranes due to their high electronic and ionic conductivity at high temperature [111,140] and high chemical stability under simulated syngas and carbon dioxide conditions [128,141]. MIEC-supported dual-phase membranes were originally proposed as a support for dual-phase membranes aiming to eliminate the need for oxygen; a requirement for carbon dioxide permeation in the case of metal-supported dual-phase membranes [142]. Even though MIEC-supported dual-phase membrane can be used without oxygen in the feed side, carbon dioxide permeation has been found to improve by two orders of magnitude with the presence of oxygen in the feed-side inlet of the membrane [111,128,143]. The complexity of the mechanism for carbon dioxide transport through dual-phase membranes with an MIEC support requires careful selection of membrane

material, *i.e.* oxygen-ion and electron conductivity, thickness, micro-structure, and operating conditions, with or without the presence of oxygen. The majority of the studies on dual-phase membranes with an MIEC support have used a porous $La_{0.6}Sr_{0.4}Co_{0.8}Fe_{0.2}O_{2-\delta}$ (LSCF) support infiltrated with the ternary eutectic mixture in either a pellet or a hollow-fibre geometry [111,127,142,144]. LSCF has been used as a membrane support material as it has a high electron conductivity (1217 S cm^{-1}) and oxygen-ion conductivity (0.091 S cm^{-1}) at 600 °C [140]. The permeation through dual-phase membranes with an LSCF support has mostly been investigated without the use of oxygen in the feed side of the membrane but with an equimolar mixture of carbon dioxide and nitrogen instead; reaching carbon dioxide permeabilities of 10^{-11} mol m^{-1} s^{-1} Pa^{-1} at 900 °C with a carbon dioxide to nitrogen separation factor above 225 [142].

Overall, careful selection of support and molten-salt combination is important for the development of dual-phase membranes with MIEC supports as interfacial reactions can limit membrane performance when oxygen is not present in the feed-side inlet. In addition, the permeation mechanism for these membranes has not been extensively studied in the presence of oxygen, suggesting the mechanism might be more complex than originally described (Figure 2.1b and Figure 2.1c). Since molten-carbonate distribution and mobility inside the ceramic supports is one of the main objectives of this study, MIEC supports were not chosen as supports for membrane preparation in this work, to avoid limitations attributed to the complexity of the permeation mechanism.

2.1.6 Permeation through dual-phase molten-salt membranes with a nominally electrically insulating support

In dual-phase ceramic molten-salt membranes with a nominally electrically insulating support, such as aluminium oxide (Al_2O_3), carbon dioxide is expected to permeate through the molten phase alone as the support does not show oxide ion and/or electron conductivity. The transport mechanism through an Al_2O_3-molten nitrate membrane reported by Zhang *et al.* suggested nitrogen dioxide (NO_2) is likely to be transported through the molten nitrate *via* a solution-diffusion (physical solubility) and facilitated transport (chemical solubility) *via* mobile carriers in the melt mechanism [110]. Similarly, carbon dioxide transport through a dual-phase ceramic molten-salt membrane could occur through the melt by solution-diffusion mechanism attributed to the physical solubility of carbon dioxide in the melt, and by facilitated transport due to

reactions between carbon dioxide and charged species acting as mobile carriers in the melt. Based on counter-permeation mechanisms reported for hydroxide ions in the melt in the presence of steam [113], it is safe to assume that the permeation mechanism through dual-phase membranes with nominally electrically insulating supports is not as simple as originally described in section 2.1.1.

Al_2O_3 has previously been used in dual-phase ceramic and metal molten-salt membranes (chapter 2, section 2.1.3) as a method to modify the surface of the dual-phase membrane (ALD, surface layer deposition). The molten phase is highly wetting on Al_2O_3 resulting in good retention of the molten carbonate phase in the porous Al_2O_3 phase [145–147]. However, the use of a nominally electrically-insulating support (Al_2O_3) as the ceramic support of a dual-phase ceramic molten-salt membrane is not common and has only been reported by Wade *et al.* [131]. In their work, Al_2O_3-supported dual-phase membrane with a ternary eutectic carbonate mixture did not result in carbon dioxide permeability and selectivity as high as the dual-phase membranes with an oxygen-ion-conducting support, *e.g.* YSZ and CGO. Even at 900 °C the permeability of the Al_2O_3-supported dual-phase membrane (200 – 400 μm thickness) did not exceed values of 8×10^{-13} mol m^{-1} s^{-1} Pa^{-1} (Figure 2.3). The poor performance of the Al_2O_3-supported dual-phase membranes in this work was attributed to the absence of oxide ion conductivity in the solid oxide phase [131,148–150]. Indeed, the low permeation values above 700 °C for Al_2O_3-molten membranes compared to YSZ and CGO-molten salt membranes (Figure 2.3) implied that the TPB reaction of $CO_2 + O^{2-} = CO_3^{2-}$ in membranes with an oxygen-ion-conducting support is the reaction that mostly contributes towards the permeation mechanism with the increase in operating temperature. The carbon dioxide permeability of Al_2O_3-supported dual-phase membrane however is competitive with the permeability of YSZ and CGO-supported dual-phase membranes between 500 – 650 °C. This suggest that at these temperatures, chemical and physical solubility in the melt are determining carbon dioxide permeation through the membrane, rather than TPB reactions. However, Anderson *et al.* suggested that carbon dioxide transport through a dual-phase membrane was mostly conducted through the molten phase of the dual-phase membranes since the oxide ion conductivity of the MIEC solid phase used is much smaller in the absence of oxygen (0.17 S cm^{-1} at 900 °C) than the conductivity of the carbonate ions in the molten carbonate phase (2.6 S cm^{-1} at 900 °C calculated by reference [151]) [142]. This would mean that chemical and physical solubility in the

melt should contribute the most towards carbon dioxide permeation even at higher operating temperatures (>700 °C). The contradictory evidence from the work of Wade *et al.* and Anderson *et al.* suggests that further work needs to be done, to establish the transport mechanism and the membrane parameters, such as micro-structure, tortuosity and surface and/or TPB reactions, that limit carbon dioxide permeability and flux/permeance through dual-phase ceramic molten-salt membranes with a nominally electrically insulating support. Interfacial reactions between Al_2O_3 and molten carbonate, have not been identified as the reason for the membrane's low permeation values. Lithium aluminate, from the reaction of Al_2O_3 with lithium carbonate [152], has only been found to improve the wettability of the solid Al_2O_3 surface by molten carbonate [145].

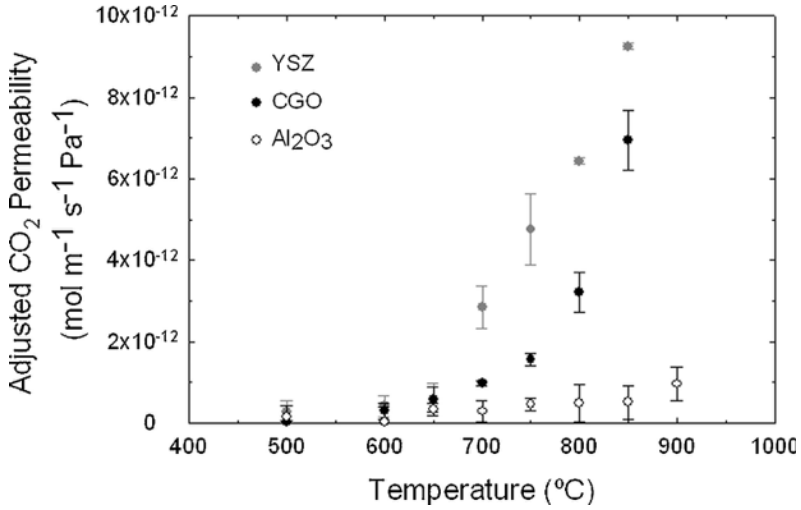

Figure 2.3: Comparison of permeabilities of dual-phase ceramic molten-salt membranes with oxygen-ion-conducting (YSZ, CGO) and nominally electrically-insulating (Al_2O_3) supports at temperatures between 500 and 900 °C. Image adapted from reference [131].

2.2 Physical support properties

As mentioned above, supports with pellet, tubular and hollow fibre geometry, both single-channel and multi-channel, have all been used for the development of dual-phase molten-salt membranes (Figure 2.4). The advantages and disadvantages of each geometry must be taken into consideration for the development of a dual-phase membrane with improved characteristics, such as reduced thickness, high porosity, low tortuosity, high scalability, high mechanical strength and an increased TPB area.

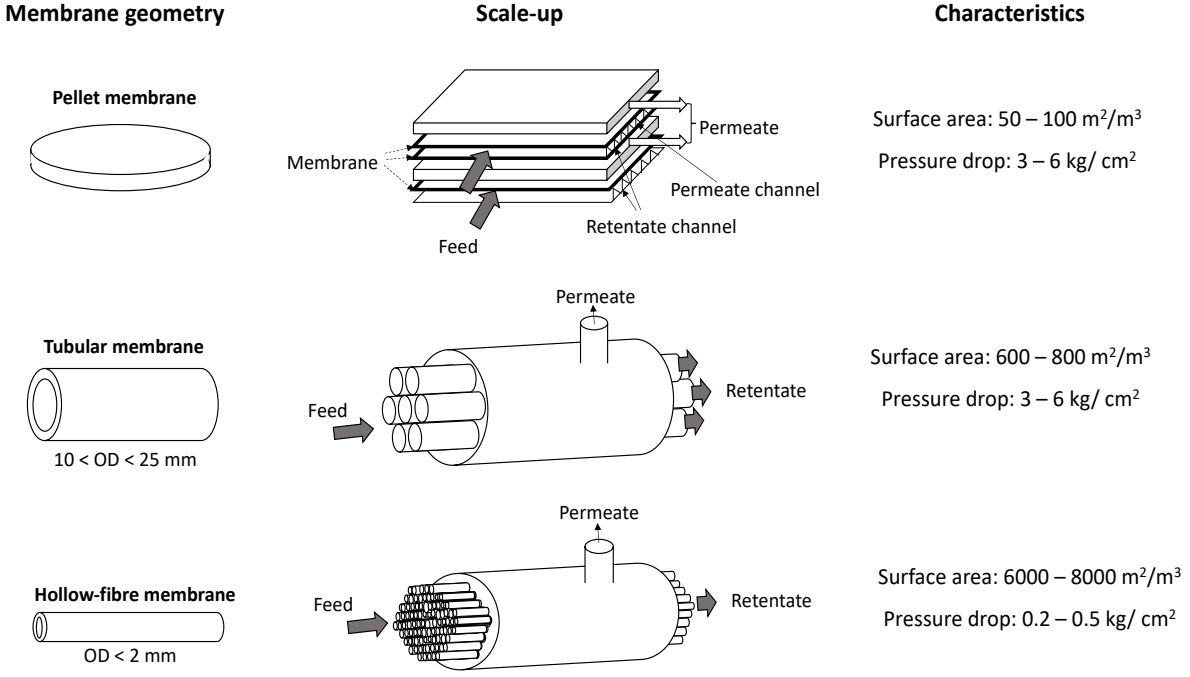

Figure 2.4: Comparison between three most common membrane support geometries used in dual-phase membrane development: pellet, tubular and hollow-fibre. Figure adapted from reference [153].

2.2.1 Dual-phase molten-salt membranes with a pellet geometry

Pellet supports with a planar geometry used in dual-phase membranes are mainly fabricated by isostatic powder compression and tape-casting [131,154]. These techniques however result in randomly created porosity inside the pellet supports limiting diffusion through the molten phase and their tortuosity cannot be represented accurately, even by the developed mathematical models [155]. The need for supports with a hierarchical structure and a defined micro-structure has led to the development of techniques that allow the tailoring of support properties. Pellet supports with a hierarchical structure can be fabricated by freeze-casting and phase-inversion techniques but have not been yet used in literature as the supports for dual-phase membranes [156,157]. Freeze-casted supports promote the creation of vertical aligned porosity by the creation of solvent crystals that reject the ceramic particles between

those crystals [156]. Phase-inversion supports show two phases, one thick layer with large finger-like pores created by the exchange of the organic solvent component of the ceramic suspension with water during the phase-inversion process, and a thin layer without large pores but with a micro-porous network [157]. Instead of using hierarchical pellet structures, efforts have been directed towards improving the wettability of the pellet surface (by dip-coating and ALD), and confining the molten salt in a thin layer inside porous pellet supports fabricated by isostatic compression [133,145–147]. In general, membranes with a pellet geometry are easy and cheap to fabricate. Pellet membranes can be scaled up as flat-sheet membranes in a plate-and-frame configuration where flat-sheet membranes are stacked on top of each other [158]. However, their use in a dual-phase membrane is mainly extended in lab-scale operation as they don't offer high surface-to-volume ratio, hence high scalability, compared to tubular and hollow-fibre geometries (Figure 2.4). High temperature sealing has also been a challenge for these membranes as it often fails under long-term operation. Since a large surface of pellet membranes requires to be sealed on the support or frame (in the case of plate-and-frame configuration), compared to the surface area required to be sealed in the case of tubular and hollow-fibre geometries, membrane sealing inhibits the operation of pellet membranes in larger scales. Limitations also occur in the preparation of thin ceramic membranes with a pellet geometry. With the decrease in support thickness, in the case of ceramic supports, their mechanical strength decreases requiring the increase in sintering temperature to restore their mechanical strength [159]. The increase in sintering temperature however results in a decrease in the support's porosity, which in turn affects the distribution of the molten phase inside the ceramic support [159]. This has been proven in the work of Zhang *et al.* where four SDC-supported dual-phase membranes with 0.3, 0.4, 0.45 and 0.5 volume fractions of the molten carbonate phase inside the SDC porous support, which shows a highly interconnected 3D network, were developed. Micro-structure, *i.e.* volume fraction of each phase, porosity and tortuosity, in oxygen-ion-conducting dual-phase membranes has also been considered as a factor that affects permeability and permeance of the membrane as poorly intra- and interconnected phases have been found to hinder oxide ion transport [111]. This also has implications in other support geometries, such as tubular and hollow fibre supports.

It is clear that pellets with a good inter- and intra-connectivity of the porous network reduce pellet tortuosity and provide faster transport for carbonate diffusion within the

molten phase. A lack of connectivity results in dead-end porosity inside the support which in extreme cases (highly tortuous networks) does not allow the diffusion of carbonate in the permeate side. In metal and ceramic supports with a pellet geometry the molten carbonate phase is, in most of the cases, confined inside the entire network of the porous supports. The pore size of the resulting support and its porosity depend on the pore size of the pore-former and its distribution and loading inside the network of the support material as well as the temperature of the heat treatment following support fabrication. In metal supports with a pellet geometry, a well-connected and uniform micro-structure has been achieved by chemical or electrochemical dealloying of an alloy from a metal by etching with an aqueous acid [124,125]. The electrochemical dealloying of a 50 at% Ag and 50 at% Zn sample has produced an Ag metal support with sub-micron porosity, 0.2 – 1 μm, resulting in good retention of the molten carbonate (500 h stable membrane operation) and increased triple-phase boundary (TPB) [125]. Sacrificial pore formers such as carbon black and microcrystalline methylcellulose have also been used to form porous networks in silver supports leading to the creation of pore structures with small pore sizes after firing (>650 °C), ~10 μm when carbon black is used and between 15 – 20 μm when microcrystalline methylcellulose is used [147,160,161].

In ceramic supports with a pellet geometry, porosity has also been formed with the use of sacrificial materials during the pellet fabrication process. The sacrificial materials are mixed along with the ceramic powders and are then removed by reduction, chemical etching or by increasing the temperature. The content of the sacrificial material and the sintering temperature define the support's porosity, pore size and pore size distribution, as well as mechanical strength [162,163]. As discussed earlier, an example of a high inter- and intra-connected 3D porous network was fabricated inside an SDC porous support using NiO as the sacrificial phase in a modified Pechini method. The NiO was reduced in a hydrogen atmosphere at 800 °C (after sintering in air at 1400 °C) and NiO was converted to Ni which was then leached out by chemical etching [130]. The resulting support (50% porosity, SDC50) benefited from a highly interconnected three-dimensional (3D) network, allowing fast ion transport inside the membrane bulk resulting in carbon dioxide permeability as high as 2×10^{-10} mol m^{-1} s^{-1} Pa^{-1} at 700 °C despite the membrane thickness being relatively high (1.2 mm), compared to other thin oxygen-ion-conducting molten-salt membranes (**Error! Reference source not found.**) [130]. When the porosity of the SDC-molten salt membrane with a 3D network

decreases to 30% (SDC30), leading to a decrease in the volume fraction of the molten phase, the permeability of the dual-phase membrane also decreased, as shown in **Error! Reference source not found.**.

In some cases, however, asymmetric structures are used in order to reduce the thickness of the separation layer. The molten carbonate is confined into a thin separation layer with a smaller pore size towards the surface of the porous ceramic support instead of the entire porous network of the support. To achieve that, macro-porous BYS disks of 470 μm average pore radius were dip-coated in a YSZ suspension and heat treated at 750 °C in air for 6h, resulting in a 10 μm YSZ layer with an average pore radius of 50 μm at the surface of the BYS support. The molten phase was then confined in the 10 μm YSZ layer, as it only wets the YSZ phase of the support [132]. Similarly, the molten phase was confined in a 50 μm layer inside an Al_2O_3 modified 1.85 mm thick BYS support, as molten salts only wet the Al_2O_3 phase [133]. Even though flux and permeance for the thin membranes was higher compared to thicker 200 – 400 μm membranes, they showed lower carbon dioxide permeability values (**Error! Reference source not found.**). This was attributed to the effect of the surface-exchange reaction on the permeation mechanism, resulting in an increase in flux (and permeance) that was not proportional to the predicted flux value for that thickness; assuming that bulk diffusion was the dominant rate-limiting step for permeation [132].

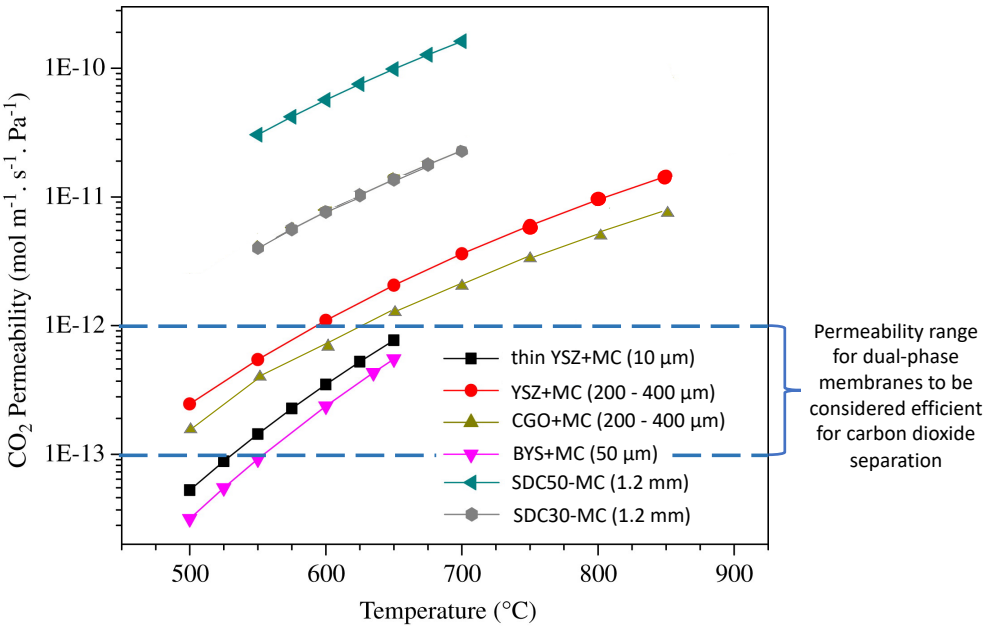

Figure 2.5: Comparison of carbon dioxide flux with the increase in temperature for dual-phase membranes with an oxygen-ion-conducting support. Image adapted from reference [132].

High carbon dioxide permeability of asymmetric dual-phase membranes (as can be seen in Figure 2.5), combined with the high selectivity of dual-phase membranes (>1000 [94,100,132]) increase the potential for the application of these membranes in CCS. However, dual-phase membranes have not yet been used in larger scale processes. In order for the upscale of dual-phase membranes to be successful, the membranes must show stability under flue gas conditions which contains gas contaminants*, i.e.* sulphur dioxide, hydrogen sulphide, and impurities, *i.e.* fly ash and mercury. Also, further testing needs to be done to ensure the homogeneity of molten salt distribution inside the membrane at a larger scale, *i.e.* the preparation of gas-tight membranes, and the long-term stability of the dual-phase membranes under operation conditions. Long-term operation under high operating pressure can cause molten salt creep which requires the membranes to be replaced often or additional molten carbonate to be re-introduced into the membrane system. Membrane replacement or additional amounts of molten carbonate would increase the original predicted cost of the dual-phase membrane systems. The membrane production cost plays an important role for the upscale implementation of dual-phase membranes as ceramic supports are more costly than polymeric. The cost for a polymeric Polaris membrane that is commercially used for carbon dioxide separation from syngas is \$39/ton CO_2, whereas typical costs for CCS technologies, such as amine scrubbing are between \$40-100/ton CO_2 [164]. For dual-phase ceramic molten-salt membranes to become commercially available, their cost should be ~\$40/ton CO_2.

2.2.2 Dual-phase molten-salt membranes with a tubular geometry

Supports with a tubular geometry have also been used in the development of dual-phase membranes as they offer higher surface area to volume ratios than pellet membranes and can be compacted in modules (Figure 2.4) [153]. Tubular membranes can be scaled-up in a shell-and-tube configuration of single or multi-channel tubes. In comparison to pellet membranes, tubular membranes do not face the challenge of high temperature sealing, as they can be sealed outside the high temperature zone of the configuration and sealing is also easier than in the case of pellet membranes due to the smaller surface that requires to be sealed. Tubular SDC (inner layer)/SDC-BYS (outer layer) support with an outer diameter (OD) of 7 mm and 1.5 mm wall thickness, fabricated by centrifugal casting, have already been used as the supports in dual-phase membranes [97]. The infiltration occurred on the inner 150 μm SDC layer due to the difference in wettability of the carbonate mixture between the SDC and BYS

layers and not due to a difference in porosity and pore size between the two layers, as could be envisaged for asymmetric structures [97]. Tubular symmetric SDC and asymmetric SDC (inner layer)/SDC-BYS (outer layer) supports with an OD of 10 mm and a wall thickness of 1 and 1.5 mm fabricated by centrifugal casting have also been used as supports for dual-phase membranes [107]. Even though tubular supports show benefits compared to supports of pellet geometry, regarding their use in future large-scale processes, their surface-to-volume ratio is not as high as in the case of hollow-fibre supports. Moreover, the thickness of the tubular support's walls cannot be easily manipulated requiring two centrifugal castings for the preparation of an asymmetric tubular support [107].

2.2.3 Dual-phase molten-salt membranes with a hollow-fibre geometry

Hollow fibres are micro-tubular structures (outer diameter (OD)~2mm) that have been widely used as membranes in gas and liquid applications such as reverse osmosis, water treatment, desalination, gas purification units and as contactors and compressed air dryers [165–168]. Hollow fibres can be used in scale-up applications based on their ability to increase the efficiency of the system proportionally to the number of fibres used in a bundle. Due to the complexity of their fabrication and high-cost production methods inorganic hollow-fibre membranes have not been as widely developed as organic hollow-fibre membranes compared to polymeric hollow-fibre membranes [169]. However, the chemical and thermal stability offered by inorganic hollow fibre membranes, along with their high volume-to-surface ratio has increased the amount of research aiming to produce inorganic hollow fibre membranes with low production costs and simple fabrication methods. As mentioned in section 1.4.1, surface area requirements for the implementation of dual-phase membranes in IGCC processes can exceed 105,000 m^2 for a two-stage membrane process and is just under 45,000 m^2 for a single-stage dual-phase membrane process. However, when steam is used as a sweep gas the membrane surface area required is decreased to 1/3 of the previously required surface areas for single and two-stage membrane processes [46]. To achieve a surface area of 15,000 m^2 for example 750,000 hollow fibres of ~1.6 m length and ~2 mm external diameter are required (~10^6 hollow fibres in a module) [170]. Challenges for the upscale of dual-phase hollow-fibre membranes in a module include membrane sealing, support strength to withstand operating pressure and homogeneous distribution of carbonate for the entire length of the hollow-fibre supports [41].

Inorganic hollow-fibre membranes are attractive as they can be applied for the filtration of corrosive fluids, high temperature reactions [171,172], as membranes for oxygen separation from air [173,174], solid oxide fuel cells [175,176] and as membrane supports in dual-phase ceramic molten-salt membranes for carbon dioxide separation [106,177]. So far, the methods used for the preparation of inorganic hollow fibre membranes include dry spinning of an inorganic material and binder system, wet spinning of an inorganic material containing solution and/or sols and pyrolysis of a polymer; all of which are classed as multistep fabrication methods [178,179]. In order to fabricate symmetric (Figure 2.6:a and b) and asymmetric (Figure 2.6:c,d,e and f) ceramic hollow-fibre supports that can be commercialised with a low production cost, a single-step viscous-fingering induced phase-inversion technique, initially used for the spinning of organic hollow-fibres, was successfully applied for the fabrication of ceramic hollow fibre supports [180–182]. This will be discussed in detail in chapter 3, section 3.1. Overall, the cost of a membrane module depends on module design and membrane application. However, the cost of hollow fibre membranes is on average significantly lower than the cost of tubular and flat-sheet membranes. More specifically, the cost of ceramic hollow fibre membranes fabricated by simple fabrication methods, such as a single-step viscous-fingering induced phase-inversion technique, is between 5 and 20 US$/$m^2$ whereas the production cost of ceramic membranes with a tubular geometry or a flat-sheet geometry (pellet geometry) is between 50 and 200 US$/$m^2$ [35].

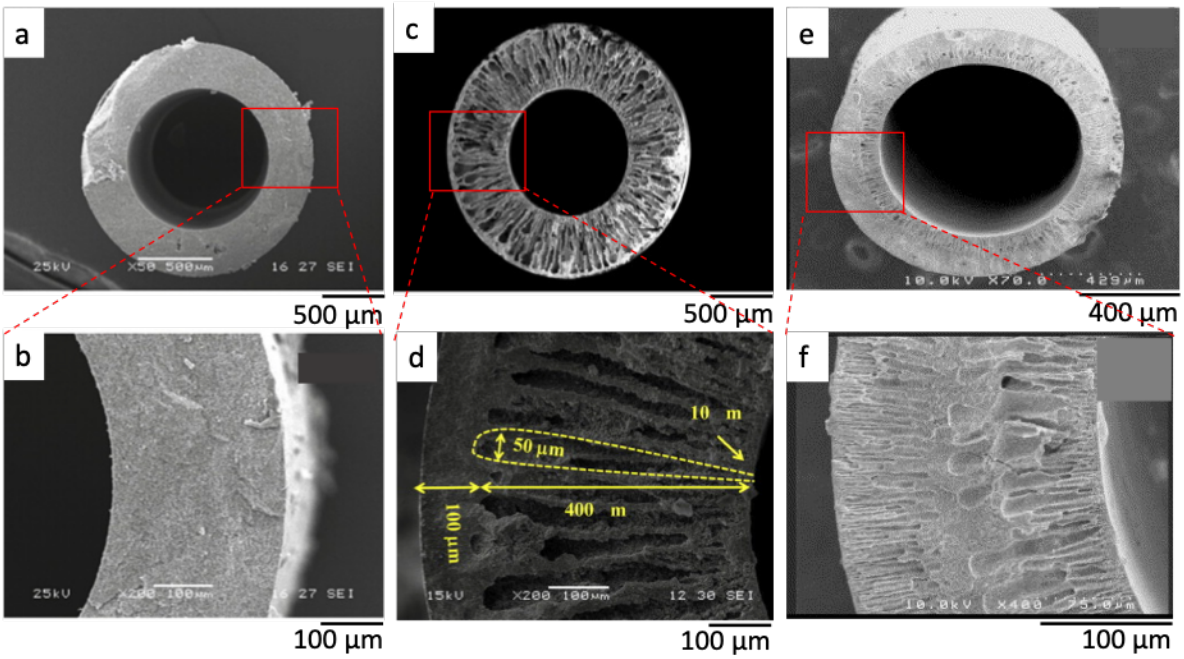

Figure 2.6: Symmetric (a, b) and asymmetric (c,d,e,f) ceramic hollow fibre supports. Image adapted from references [183] for images a,b,c and d, and from [184] for images e and f.

Porous ceramic hollow-fibre supports of an asymmetric structure have already been used as asymmetric catalytic hollow fibre reactors for methane steam reforming, as supports in micro-tubular solid oxide fuel cells and as supports for dual-phase ceramic molten-salt membranes [106,141,144,185]. Compared to LSCF-supported dual-phase pellet membranes, LSCF-molten salt hollow-fibre membranes, showed an improvement in carbon dioxide flux even below the critical thickness (L_c) for LSCF-supported dual-phase pellet membranes. This could be attributed to the micro-structure of the hollow-fibre support due its fabrication method, allowing a micro-structured porous network with a lower dead-end porosity and shorter permeation pathlengths than the randomly powder pressed pellets [159]. An $SrFe_{0.8}Nb_{0.2}O_{3-\delta}$ (SFN) multi-channel hollow fibre support with a controlled micro-structure was also used as the MIEC support for the development of dual-phase ceramic molten-salt membranes. The support possessed four channels with a thickness of ~220 µm and carbon dioxide permeability reached 5×10^{-12} mol m^{-1} s^{-1} Pa^{-1} (permeance 2.3×10^{-8} mol m^{-2} s^{-1} Pa^{-1}) at 700 °C [141]. Even though dual-phase ceramic molten-salt membranes have shown a high carbon dioxide over nitrogen selectivity (>1000 [94,100,132]) and high carbon dioxide permeability, they have not yet been applied in a larger scale. Despite the fact that dual-phase membranes with a hollow fibre geometry are highly scalable, their wider-scale application still needs to address

challenges regarding the reproducibility of molten carbonate infiltration inside the ceramic supports [106,141,144], possible molten salt creep, high pressure tolerance of hollow fibre supports [186], separation performance under flue gas conditions [104,105] and long-term stability of membrane and sealing under high pressure [94]. Addressing the above issues, will bring dual-phase membranes, and particularly DPHFMs, closer to industrial application. However, significant research still needs to be carried out.

2.3 Molten-carbonate properties

The most common molten carbonate mixture used for dual-phase membranes is the ternary eutectic mixture of Li_2CO_3, Na_2CO_3 and K_2CO_3 at a molar ratio of 43.5, 31.5 and 25 respectively. Thus, the properties of this melt need to be taken into consideration for good material compatibility, long-term stability as well as potential self-healing of created cracks on dual-phase membranes, which will ensure the long-term operation of these membranes. Here self-healing may well be possible if the wetting of the molten salt on the ceramic support is high, so that spreading of molten salt into newly formed cracks becomes a realistic route to self-healing. As mentioned in sections 2.1.3 and 2.1.4, other carbonate melts have been used for the preparation of dual-phase membranes, such as Li_2CO_3 and the binary Li_2CO_3: K_2CO_3= 62:38 molar ratio melt. However, the presence of sodium and potassium carbonate in the melt results in better stability between melt and support, minimizing interfacial reactions [138,139]. Hence, section 2.3 focuses on the properties of the ternary eutectic carbonate mixture which will be further used in membrane preparation in this thesis.

2.3.1 Operational temperature and thermal stability

The melting points of the individual pure Li_2CO_3, Na_2CO_3 and K_2CO_3 are 723, 858 and 898 °C, respectively. However, when Li_2CO_3, Na_2CO_3 and K_2CO_3 are mixed in the ternary eutectic mole ratio the melting point of the mixture decreases to 397 °C [187]. Thermal stability of the molten ternary eutectic mixture is necessary to ensure membrane operation at high temperatures will not affect membrane stability and separation performance. The decomposition of Li_2CO_3 (Li_2CO_3 = Li_2O + CO_2(g)) and K_2CO_3 (K_2CO_3 = K_2O + CO_2(g)) has been found to generate carbon dioxide and contribute to the weight loss of the carbonate mixture [188]. Indicatively, in an atmosphere of inert argon gas, the carbonate melt begins to decompose above 658°C, with a total weight loss of 0.05% up to 794 °C, reaching a weight loss of 18.7% at 944.3 °C. The full decomposition of the melt under these conditions occurs at 1010 °C as measured by simultaneous thermal analysis (STA) [189]. The melt however remains stable up to 1000 °C under a pure carbon dioxide atmosphere rendering the increase in carbon dioxide partial pressure as an effective way to decrease the decomposition rate of the melt [190]. The melt can remain stable even in the presence of low carbon dioxide partial pressures due to the Coulombic interactions in molten carbonate, which

provide low vapour pressures for the melt, requiring a small amount of carbon dioxide partial pressure to reach equilibrium [99,191].

2.3.2 Melt density and viscosity with the increase in temperature

The viscosity (η) of the molten ternary eutectic mixture decreases with the increase in temperature. At 600 °C the viscosity of the molten carbonate is 10 mPa s^{-1}, the same order of magnitude as the viscosity of water at 20 °C (1 mPa s^{-1}) [94]. This was calculated based on the empirical equation for viscosity (Eq. 2.14) determined by An *et al.* [192]:

$$\eta = 0.065 \exp(\frac{4431.3}{T}) \quad \text{(Eq. 2.14)}$$

where η is the viscosity in mPa s^{-1} and T is the operating temperature in K [192]. The low viscosity of the ternary molten carbonate eutectic allows its infiltration in various porous structures with submicron pore sizes.

The density (ρ) of the ternary molten carbonate eutectic decreases with the increase in temperature and can be calculated by the empirical equation (Eq. 2.15) [193],

$$\rho = \alpha + \beta T \quad \text{(Eq. 2.15)}$$

where T(K) is the operating temperature of the melt, and α (2389) and β (-0.4447) are constants calculated from the experimental data of density measurements for the ternary eutectic mixture [151]. In dual-phase ceramic molten-salt membranes, the density of the ternary eutectic mixture is required in order to determine the amount of carbonate required for the infiltration of the porous ceramic support, especially because of the volume expansion of the molten carbonate phase at temperatures above its melting point. Experimentally determined density values of the molten ternary eutectic mixture in literature are shown for a range of temperatures in Table 2.1 along with the calculated volume increase (%) of carbonates when molten, compared to their volume at 25 °C [151]. The volume of carbonates at 25 °C was calculated assuming 0.1 g of carbonate which is often the case in infiltration of pellets with 2 cm diameter and 1 mm thickness.

Table 2.1: Density values (ρ, g cm^{-3}) of the ternary eutectic mixture of carbonates at 25, 400, 500, 600, 700 and 800 °C and the percentage of volume increase (%) of the melt at these temperatures.

T (°C)	ρ (g cm^{-3})	Volume increase (%)
25	2.36	0
400	2.09	12
500	2.05	15
600	2.01	17
700	1.96	20
800	1.92	23

2.3.3 Surface tension and wettability of molten carbonate on the ceramic supports

The surface tension of the ternary eutectic mixture is a property of the melt that affects its retention on the solid support surface and has been found to decrease with the increase in temperature [194]. When the difference between the surface tension of the support and the molten carbonate is high, the gas-molten salt contact area increases, resulting in high wetting of the support by the melt and near zero contact angle values [94]. In general, surface tensions between the three phases (gas, solid, liquid) can be calculated by the Young-Dupre equation which relates the contact angle and the forces acting on a liquid drop in mechanical equilibrium on a solid surface [195]:

$$\gamma_s - \gamma_{sl} = \gamma_l \cos\theta \qquad \text{(Eq. 2.16)}$$

where γ_l is the surface tension between the liquid-gas interface (J m^{-2}), γ_s is the surface tension between the solid-gas interface (J m^{-2}), γ_{sl} is the surface tension between the solid-liquid interface (J m^{-2}), and θ is the contact angle. The liquid-gas surface tension of the ternary eutectic mixture 400 °C is approximately 227 mJ m^{-2}, whereas at 700 °C the surface tension of the melt decreases to 215 mJ m^{-2}, calculated based on the work of Kojima *et al.* [151]. The surface tension of ceramic supports for dual-phase membranes however, such as YSZ and Al_2O_3, reaches values above 1,500 mJ m^{-2} at 650 °C. The one order of magnitude difference between the surface tensions of support and melt suggests that the molten phase is highly wetting on the solid ceramic supports and facilitates infiltration of the melt inside the support's porous network. The high wetting of the molten salt on the ceramic surface, increases its spreading on the ceramic and leads to a reduction of the surface energy of the prepared membrane,

which facilitates the absorption of carbon dioxide. Lu *et al.* proved that carbonates highly wet Al_2O_3 and YSZ supports by monitoring the weight gain of the supports over time during their infiltration with molten carbonate. Porous Al_2O_3 supports were fully infiltrated after 20 s, porous YSZ supports were fully infiltrated after 30 s, whereas porous BYS support did not show weight gain even after 20 minutes, suggesting carbonates do not wet BYS supports [132]. YSZ, Al_2O_3 and a SDC layers have been used to increase the wetting of the carbonates on BYS and SDC-BYS ceramic supports (for the SDC layer), improving surface wettability and molten-salt retention inside the support's porous network [97,132,133].

During infiltration, the molten salt fills the micro-porosity of the supports due to the produced capillary pressure:

$$P_c = -\gamma_l \cos\theta \frac{1}{r} \quad \text{(Eq. 2.17)}$$

where γ_l is the carbonate surface tension in the liquid-gas interface, θ is the contact angle of molten carbonate on the solid surface of the support, and r is the pore radius. In order for the carbonates to be retained in the porous network, there are limitations on the feed (P_f) and permeate (P_p) pressure that can be applied on the membrane, assuming a straight pore. These limitations can be estimated by the Laplace equation:

$$P_f - P_p = \frac{2\gamma_l \cos\theta}{r} \quad \text{(Eq. 2.18)}$$

When the wetting of the carbonate on the solid support phase is high, with contact angles close to zero, the pressure differences the molten carbonate can withstand are higher than when the molten phase does not wet the support's surface well. Good wetting of the molten phase and consideration of pressure differences are important in order to avoid molten carbonate creep [94].

Finally, the ability of the molten phase to spread, determines the ability of the melt to redistribute inside the matrix of the ceramic support. The condition for spreading, requires the spreading coefficient at equilibrium to be less than zero for partial wetting, and equal to zero for complete wetting [196]. The spreading coefficient is calculated based on Eq. 2.19 [197]:

$$S = \gamma_s - (\gamma_{sl} + \gamma_l) \quad \text{(Eq. 2.19)}$$

The spreading coefficient for the ternary eutectic carbonate mixture on Al_2O_3 will be calculated in chapter 5, section 5.3.3, after determining the surface tensions between the interfaces in the system.

The wetting nature of carbonate on Al_2O_3, YSZ and SDC supports, opens a new scientific path for the use of molten salts as a self-healing medium in the dual-phase membrane matrix. Depending on the nature and dimensions of the crack, the molten salts could spread and self-heal the created crack by filling it. Self-healing in ceramic materials plays an important role in their long-term stability and operation, especially since ceramic supports are brittle and sensitive to flaws due to thermal shock, or the creation of micro-cracks that result in failure of the material [198]. For the application of dual-phase membranes in industrial processes it will be crucial to tackle such problems without replacing the membrane or disturbing the process. This could be provided by developing self-healing dual-phase membranes. Self-healing mechanisms and their potential application in a dual-phase membrane system are discussed in chapter 5, section 5.1.

2.3.4 Solubility of carbon dioxide in molten carbonate and speciation in the melt

The solubility of carbon dioxide in the molten carbonate eutectic can be both physical and/or chemical. The concentration of carbon dioxide (c_{CO_2}) physically dissolved in molten carbonate can be calculated based on Henry's law as it is related to carbon dioxide's partial pressure (P_{CO_2}):

$$c_{CO_2} = k_H P_{CO_2} \quad \text{(Eq. 2.20)}$$

Henry's constant (k_H) for carbon dioxide in the ternary molten carbonate eutectic is 3.6×10^{-3} mol dm^{-1} atm^{-1} at 700 °C [199]. However, the solubility data for carbon dioxide in the ternary molten carbonate eutectic are scarce, highly inconsistent and do not take into consideration the chemical solubility of carbon dioxide in the melt. Claes *et al.* measured the chemical solubility of carbon dioxide and dicarbonate ions, formed by the auto-dissociation reaction of carbonates ($2CO_3^{2-} = C_2O_5^{2-} + O^{2-}$) by a titration technique, concluding that the contribution of chemical solubility of carbon dioxide in the melt is approximately 50 times more important than its physical solubility. Chemical solubility results in speciation in the melt, as the dissolution of carbon dioxide produces oxygen, carbon and carbonate-based ions that have been found to be stable in the melt at 700 °C [200]. Carper *et al.* did an extensive computational density functional theory (DFT) study at high temperature (700 °C) in order to identify the species that can theoretically be stable in the molten carbonate phase [200]. The molecular structures in the melt were considered to include O^{2-}, O_2^-, O_2^{2-}, CO_3^{2-}, CO_4^{2-}, CO_4^-, CO_4^{4-}, CO_5^{2-}, $C_2O_6^{2-}$ as well as carbonate-based and oxygen-based charged species and neutral molecular species of the alkali metals. Hence, it has been proposed that

carbon dioxide can react with oxides or carbonate in the melt to form carbonate ($CO_2 + O^{2-} = CO_3^{2-}$) or pyrocarbonate ion ($CO_2 + CO_3^{2-} = C_2O_5^{2-}$), respectively [94,200,201].

2.4 Objectives of this work

The specific objectives of this project, aiming to provide insight in scalability of dual-phase membranes and their durability under long-term operation, include the following:

- Development of a model dual-phase membrane system that allows the control of molten-carbonate thickness, membrane tortuosity and surface-exchange area for carbon dioxide permeation (chapter 4).
- Identification of the parameters that affect carbon dioxide flux through the use of model dual-phase membranes where the support does not participate in the permeation mechanism, *i.e.* nominally electrically insulating support (chapter 4).
- Development of dual-phase membranes with a hollow-fibre geometry which provide the potential for scale-up, while taking into consideration the parameters that affect carbon dioxide flux, identified above. To do so, the following steps are necessary (chapter 3):
    - Identification of hollow-fibre properties that will affect the infiltration of the molten phase inside the hollow-fibre supports.
    - Development of a carbonate coating method that will allow the controlled distribution of carbonates inside the hollow fibre supports.
- Understanding how the controlled distribution of carbonates inside the hollow fibre supports affects carbon dioxide flux through dual-phase hollow-fibre membranes (DPHFMs) (chapter 4).
- Investigation of the effect of support contribution in carbon dioxide flux in the case of DPHFMs with a controlled distribution of carbonates (chapter 4).
- Address the common failure issues of dual-phase ceramic molten-salt membranes by exploiting the wettability of molten salts on the ceramic supports and their ability to self-heal cracks (chapter 5). To do that:
    - The development of a crack simulation mechanism needs to be developed,
    - followed by evidence of restoration of the membrane performance to its previous state of operation.

Chapter 3

Controlled distribution of molten carbonate inside ceramic hollow-fibre supports

The challenge in this chapter was to prepare DPHFMs where the distribution of the molten salt component inside the hollow-fibre support was controlled. As a result, the development of well-characterised DPHFMs with an increased surface area for carbon dioxide sorption or desorption was achieved, in contrast to DPHFMs developed in current literature.

The following chapter includes results also presented in the manuscript *'Controlling molten carbonate distribution in dual-phase molten salt-ceramic membranes for improved carbon dioxide flux'*, currently under review in the Journal of Membrane Science.

Figures 3.8, 3.12, 3.13 and 3.14 have been used in a similar form in the aforementioned manuscript and were remade for the purpose of this chapter.

3.1 Introduction

Large-scale applications for membranes require the processing of large volumes of gas, and in turn defect-free large surface areas [202,203]. For this reason, tubular and hollow-fibre geometries, both benefiting from high surface-to-volume ratios, are amongst the most suitable support geometries with potential for scale-up. Hollow-fibre supports fabricated by phase-inversion further benefit from a single-step fabrication method, a lower production cost (5-20 US$/m^2) and higher packing-density compared to tubular membranes (production cost between 50 and 200 US$/m^2, packing density: 7000 m^2 m^{-3}, compared to <800 m^2 m^{-3} for traditional tubular packed and plate contractors) [204–208]. For inorganic hollow-fibre membranes, the asymmetric micro-structure is characterised by two distinct porosity domains: a) a plethora of micro-channels, resembling finger-like voids, and b) a packed-pore network, located in-between the micro-channels and towards the outer (shell) (Figure 3.1a) and/or inner surface (lumen) (Figure 3.1b) of the hollow-fibre supports. The part of the packed-pore network that is not penetrated by micro-channels, *i.e.* the layer of packed-pore network starting from the tip of the micro-channels and extending towards the outer or the inner surface of the hollow-fibre supports, is characterised as sponge-like layer (Figure 3.1a and Figure 3.1b). The asymmetric structure provides a higher lumen surface-to-volume ratio and lower mass transfer resistances for the separation of the desired species through the bulk phase of the hollow-fibre support compared to the equivalent symmetric structure [209]. The fabrication of inorganic, asymmetric hollow-fibre supports by phase-inversion will be analysed in this chapter. First, the spinning of a ceramic suspension, followed by a viscous-fingering induced-phase inversion process which defines the morphology of the hollow-fibre precursors occurs. The hollow-fibre precursors are then sintered at high temperatures to form the hollow-fibre supports.

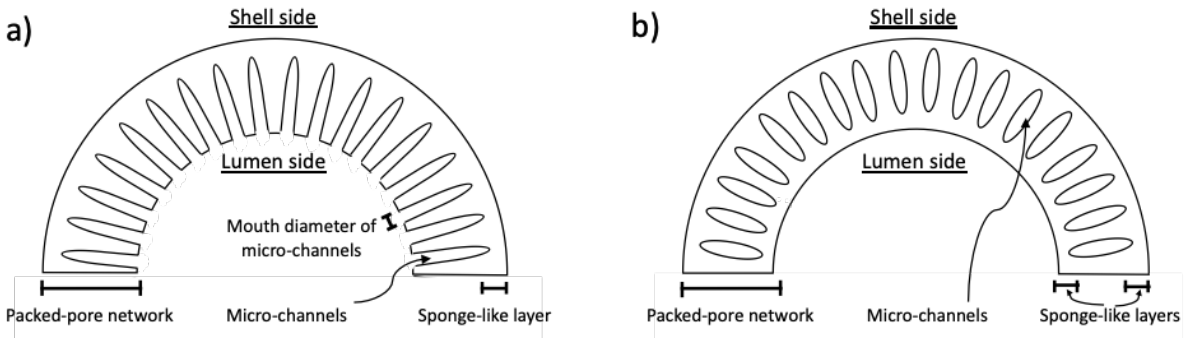

Figure 3.1: Asymmetric hollow-fibre supports with one (a) or two (b) sponge-like layers in their packed-pore network.

To prepare the ceramic suspension for spinning, a ceramic powder, a solvent, a polymer binder and additives such as pore formers and dispersant agents are mixed together. The ceramic powder is initially added in a polymer solution followed by the additives and finally the solvent. In order to prepare a homogeneous ceramic suspension, and consequently decrease the defect formation during the spinning process, the selected solvent has to completely dissolute the polymer binder and the additives inside the ceramic suspension. The addition of a dispersant as an additive in the ceramic suspension aims to increase the homogeneity of the suspension as it reduces the agglomeration of the ceramic powder. The homogeneity, viscosity and packing density of the particles (referring to the density of the particles in the ceramic powder, rather than the bulk density of the ceramic material) in the ceramic suspension prepared for spinning are the parameters that determine the defect formation during the spinning process, the realisation of the viscous fingering process and the porosity, pore size and pore size distribution of the final hollow-fibre supports, respectively [180]. After mixing, the ceramic particles in the suspension are coated by the polymer binder and immobilised. The formation of the hollow-fibre precursors takes place due to the precipitation of the polymer binder when the ceramic suspension (more viscous fluid) comes in contact with the non-solvent (less viscous fluid used as an external coagulant) during the spinning process.

During the viscous-fingering induced-phase inversion process the ceramic suspension is co-extruded along with an inert bore fluid (internal coagulant) through a tube-in-orifice spinneret into a coagulation bath of the non-solvent (external coagulant) as shown in Figure 3.2. The hydrodynamic pressure at which the bore fluid is extruded results in the formation of the hollow/lumen structure inside the hollow fibre. The bore fluid used for the spinning process is an inert liquid mixture that does not participate in the phenomenon of hydrodynamically viscous fingering. As the ceramic suspension is extruded in the external coagulant bath, the non-solvent diffuses through the higher viscosity area of the ceramic suspension and forms micro-channels when it reaches the less viscous area of the suspension. Finger-like voids are formed due to the phenomenon of hydrodynamically viscous fingering which occurs at the interface between a less viscous fluid; the non-solvent, and a more viscous fluid; the ceramic suspension [210]. During the hydrodynamically viscous fingering phenomenon, the more viscous fluid is displaced by a less viscous fluid due to viscosity differences between the two phases [211]. The spinning parameter which affects the direction of

the micro-channel formation from the inner or from the outer surface is the air gap. The air gap is the vertical distance between the extrusion point from the tube-in-orifice spinneret (ceramic suspension and bore fluid exit) until the coagulation bath of the external coagulant when the ceramic suspension comes in contact with air (Figure 3.2).

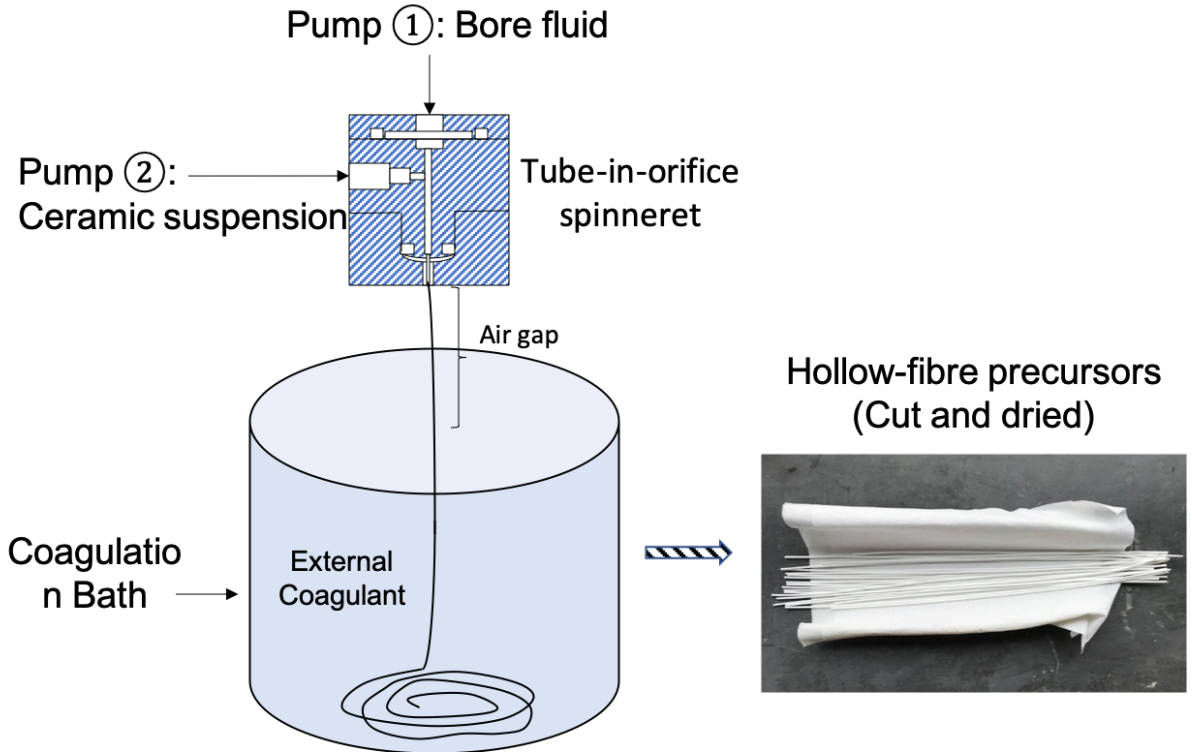

Figure 3.2: Schematic representation of the fabrication process of ceramic hollow-fibre supports by phase-inversion.

The effect of air gap in the formation of micro-channels on the preparation of Al_2O_3 hollow-fibre supports (58.7 wt% Al_2O_3 in the ceramic suspension, NMP/H_2O mixture as the bore fluid and H_2O as the external coagulant) was studied in more detail by Kingsbury *et al.* who found that by increasing the air gap, the formation of micro-channels on the outer surface decreases, until they are completely eliminated from the outer surface of the hollow fibres [210]. At the same time, the length of the micro-channels in the inner surface of the hollow fibre increases with the increase in the air gap. For a 0 cm air gap, the non-solvent penetrates the ceramic suspension from both inner and outer surface, creating a structure with a sponge-like layer in the middle and equal micro-channel lengths on both sides of the hollow-fibre support, referred to as sandwich-like structure (Figure 3.3a). A 2 cm air gap, decreased the length of the micro-channels on the outer surface (Figure 3.3b), which were completely eliminated when the air gap was increased to 15 cm (Figure 3.3c). However, the increase in the air gap, led to the decrease of the sponge-like layer. The thickness of the sponge-like

layer is also affected by the composition and flow rate of the internal coagulant. High flow rates for the internal coagulant lead to thinner sponge-like layers whereas low flow rates lead to dense sponge-like layers as the driving-force is too low for diffusion of the internal coagulant through the suspension to occur [210].

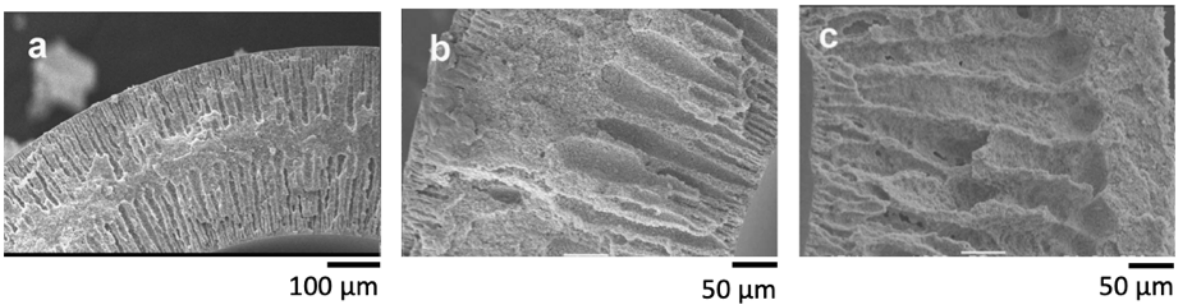

Figure 3.3: Cross-sectional SEM images of Al_2O_3 hollow-fibre precursors (a-c) fabricated by viscous-fingering induced-phase inversion process with a 0 cm air gap (a), a 2 cm air gap (b) and a 15 cm air gap (c). Figure adapted from reference [210].

The sintering of the hollow-fibre precursors aims to increase their mechanical strength and define their micro-structure. Shrinkage occurs in all directions during sintering, resulting in the decrease of hollow-fibre length, inner and outer diameter. As the sintering temperature increases, the pore size, volumetric and surface porosity of the hollow-fibre supports as well as the total length and the number of micro-channels was found to decrease [180,212]. Sintering of hollow-fibre precursors into hollow-fibre supports can be divided into three stages: initial heating, pyrolysis and final sintering. During the pre-sintering stage, water trapped in the micro-structure of the hollow-fibre precursors evaporates above 100 °C. Following the initial heating, the removal of the polymer binder and dispersant takes place during the pyrolysis stage. For the final, solid state sintering of the ceramic material the temperature must be increased to at least half of the material's melting point (Tamman temperature), in order to achieve the required degree of atomic diffusion [213]. Grain growth and coalescence bind the ceramic particles together due to surface diffusion between particles and form the ceramic hollow-fibre supports. To avoid deformation, rapid and uncontrolled expansion of the pores and distortion, the heating rate until the pyrolysis stage needs to be slow (~2 °C min^{-1}). As a general indicator, shrinkage accompanied by limited grain growth and surface diffusion is observed at lower temperatures (up to the pyrolysis stage), whereas grain growth and surface diffusion are taking place at higher temperatures (above the pyrolysis stage). The porosity and the micro-channels of the hollow fibres can be completely eliminated with the increase in the sintering temperature as can be seen in Figure 3.4, where the same fibre was sintered at both 1450 and 1600 °C [210].

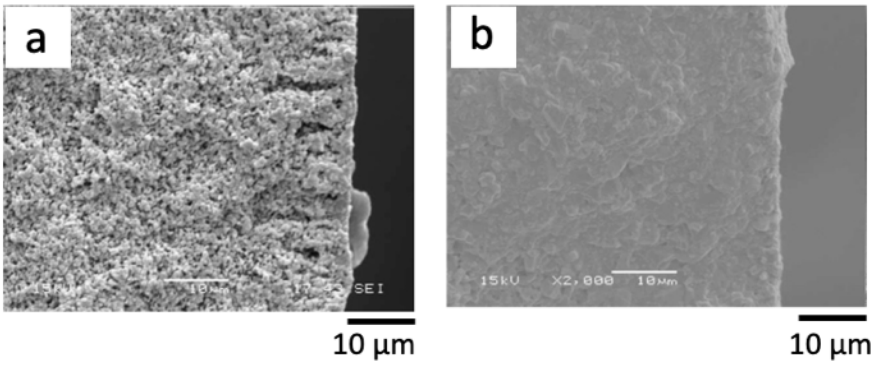

Figure 3.4: Asymmetric Al_2O_3 hollow-fibre precursors sintered at 1450 (a) and 1600 °C (b) fabricated by viscous-fingering induced-phase inversion process with a 15 cm air gap (c). Figure adapted from reference [210].

In general, inorganic hollow-fibre membranes are characterised by low mechanical strength compared to inorganic tubular and pellet geometries made of the same material and sintered at the same temperature, due to their thin support walls (~0.5 mm compared to ~1.5 mm for tubular and ~1 mm for pellet geometries) [107,131,154,180–182]. However, it has been found that asymmetric hollow-fibre membranes with a small average pore size in their sponge-like layer show good mechanical strength, as thin layers with wide pores are mechanically unstable and prone to cracking [209]. The sponge-like layer provides the bulk of the mechanical strength and achieving an increased relative ratio of sponge-like layer region to micro-channels region has been found to increase the fibre's mechanical strength [214]. The effect of sintering temperature on mechanical strength has been extensively studied on asymmetric porous Al_2O_3 hollow fibres, indicating a sharp increase in the hollow-fibre's mechanical strength above 1500 °C, while sacrificing its permeability with the increase in temperature [184,215]. So far, the highest mechanical strength for Al_2O_3 hollow-fibre supports (58 MPa and 116 MPa when sintered at 1342 and 1455 °C, respectively) has been obtained for hollow fibres with an asymmetric structure and ~30 µm sponge-like layer on their outer surface [184,210,216]. However, the trade-off relationship between the mechanical strength of the hollow fibre supports and their equivalent available porosity; which is important for the incorporation of molten carbonate during the preparation of DPHFMs, has not yet been studied.

Hollow-fibre supports with wide (5-20 µm) and long conically shaped micro-channels (more than 90% of the cross-sectional thickness) and a single thin sponge-like layer at their outer surface have been predominantly used in dual-phase ceramic molten-salt membrane preparation. This is due to their thin sponge-like layer, that can lead to membranes with a reduced molten carbonate thickness (different from the overall

support thickness) if the carbonate is restricted in this region [106,144]. The morphology of those hollow-fibre supports is attributed to the use of a solvent-based internal coagulant which prevents the precipitation and the increase in local viscosity at the inner surface of the extruded ceramic suspension. Hence, the micro-channels are formed from the precipitation of the polymer on the outer surface of the extruded ceramic suspension and grow towards the inner surface, until they have penetrated through and formed a sponge-like layer on the outer surface of the hollow-fibre precursors. The external coagulant for the preparation of these fibres was deionised water and a 0 cm air gap was used [216]. The use of this specific structure reduces mass transfer resistances across its cross-sectional area and facilitates separation by providing a thin separation layer [207,217–219]. This structure has been favoured for the preparation of dual-phase membranes over the sandwich-like structure (micro-channels on both surfaces of the hollow-fibre supports as can be seen in Figure 3.3a) and other structures where the micro-channels have a smaller diameter and cover smaller lengths inside the cross-sectional area of the hollow-fibre supports.

Even though asymmetric hollow-fibre supports offer high and tailorable surface areas on their lumen-side surface, along with low mass transfer resistances across their cross-sectional area, this has not yet been exploited when used as the supports for DPHFMs due to the non-selective infiltration method used for their preparation. So far, the infiltration of the hollow-fibre supports has been conducted by immersing the supports in a molten carbonate bath, infiltrating molten carbonate *via* capillary forces into both micro-channels and packed-pore network (Figure 3.5) [106,141,144]. By infiltrating the micro-channels and the packed-pore network, the molten carbonate thickness for these membranes is subsequently equivalent to the thickness of the support. Restricting the molten carbonate in the sponge-like layer of the asymmetric hollow-fibre supports would significantly decrease membrane thickness and increase flux [49].

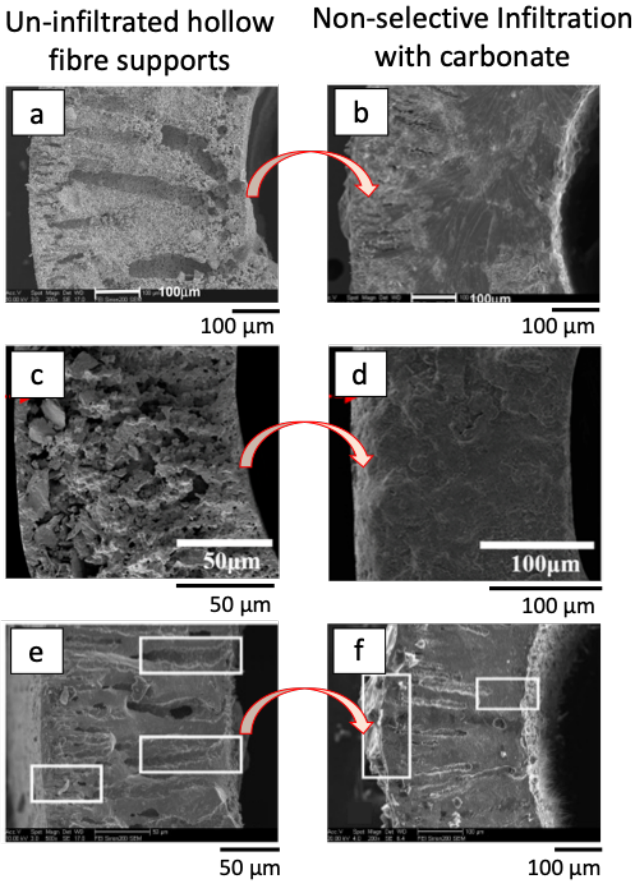

Figure 3.5: Non-selective infiltration of hollow fibre supports in literature. SEM images a, c and e show the inorganic hollow-fibre supports without carbonate, with both micro-channels and packed-pore network visible. SEM images b, d and f show hollow-fibre supports a, b and c, respectively, after their non-selective infiltration with carbonate, *i.e.* both micro-channels and packed-pore network are infiltrated with carbonate. Image adapted from references [106,141,144].

For the preparation of DPHFMs with high fluxes, it is necessary to prepare membranes with decreased molten carbonate thickness and/or high surface areas for carbon dioxide surface exchange [41]. To do that, the infiltration process of the molten phase inside the support needs to allow control over the distribution of carbonate inside the hollow fibre support. The prepared DPHFMs must also be robust and highly reproducible. The supports selected for this study are Al_2O_3 and 3% YSZ. As mentioned in sections 2.1.4 and 2.1.6, oxygen-ion-conducting ceramic supports, such as YSZ, and nominally electrically insulating supports, such as Al_2O_3, have shown promising results for the development of dual-phase ceramic molten-salt membranes [131,132] and benefit from a low production cost [204–208]. YSZ-supported DPHFMs infiltrated *via* a non-selective infiltration method have previously been investigated in literature, showing high temperature stability, high selectivity and a carbon dioxide flux which reaches 0.22 ml min^{-1} cm^{-2} at 950 °C [106]. Therefore, the effect of carbonate distribution on flux can be compared between the controlled infiltrated YSZ-supported

DPHFMs in this study and the uncontrolled infiltrated YSZ-supported DPHFMs in literature. The focus of this chapter, however, is the development of a methodology for the controlled distribution of carbonate inside the hollow fibre supports, so further flux comparisons will be presented in chapter 4.

In this chapter, the hollow-fibre supports were thoroughly characterised in order to select the support that would produce DPHFMs with the best trade-off relationship between the support's three-point (3P) bending strength and available porosity for the infiltration of the molten carbonate. Careful support characterisation also enabled control over the distribution of carbonate inside the hollow fibre supports. After identifying the amount of carbonate needed to infiltrate the packed-pore network of the hollow-fibre supports alone, it was possible to develop a novel two-step coating and infiltration method, allowing the infiltration of carbonate from the outer towards the lumen surface of the supports. This infiltration method aims to leave the micro-channels un-infiltrated by carbonate and subsequently decrease the molten carbonate thickness inside the hollow-fibre supports, ultimately decreasing the overall membrane thickness. Since the sponge-like layer of the packed-pore network structure has a smaller average pore size than the rest of the packed-pore network, the molten phase is expected to be retained in the sponge-like layer due to higher capillarity. The hollow-fibre supports were infiltrated with carbonate loadings aiming to fill 25, 50, 75 and 100 vol% of the packed-pore network porosity and create a thin carbonate layer inside the sponge-like layer of the hollow-fibre packed-pore network. The infiltrated supports were subsequently tested for gas-tightness at room temperature and at higher operating temperature (>400 °C) to identify the carbonate loading that would produce consistently selective dual-phase membranes during operation.

3.2 Experimental

3.2.1 Chemicals and materials

For the fabrication of the Al_2O_3 hollow fibre precursors a ceramic suspension consisting of α-Al_2O_3 powder (Alfa-Aesar, <1 μm, 2-4 m^2 g^{-1}, 99.9%), dimethyl sulfoxide (DMSO, VWR), Arlacel P135 (Uniqema) and polyethersulfone (PESf, Ameco Performance) as the ceramic material, solvent, dispersant and polymer binder, respectively, was prepared. 15 wt% 1,4 dioxane in n-hexane (HPLC grade, VWR) was also used as the bore fluid for the spinning process. For the fabrication of the YSZ hollow fibre precursors a ceramic suspension consisting 3% YSZ powder (zirpro, 0.2-0.3 μm, 7-15 m^2 g^{-1}, 99.99%), n-methyl-2-pyrrolidone (NMP, VWR, prolabo chemicals), Arlacel P135 and poly(methyl methacrylate) (PMMA, VWR) was prepared. Ethanol (Absolute, Analytical reagent grade, Fisher) and NMP were used as the bore fluid for the spinning process of the YSZ hollow fibres.

Lithium carbonate (Alfa Aesar, Li_2CO_3, ACS, 99% min), potassium carbonate (Alfa Aesar, K_2CO_3, ACS, 99% min) and sodium carbonate monohydrate (Alfa Aesar, Na_2CO_3, ACS, 99.5% MIN Granular $Na_2CO_3{\cdot}H_2O$) were used for the preparation of the carbonate eutectic mixture. Ethanol was used for the preparation of a carbonate suspension and isopropyl alcohol (anhydrous, 99.5%, Sigma-Aldrich) was used to clean the hollow fibres prior to carbonate infiltration. The hollow fibres were sealed into the supports using epoxy resin (Araldite® Rapid). White glaze (Scarva, G261/W) was used for partly glazing the hollow fibre supports. Leak detection was conducted with the use of a leak detection fluid (Snoop ® Liquid Leak Detector, Swagelok ®). All the gases used were purchased from BOC and were of high purity gas mixtures grade.

3.2.2 Preparation of hollow fibre supports

Asymmetric Al_2O_3 hollow fibres with a micro-structured porous network were prepared by a viscous-fingering induced-phase inversion followed by a high temperature sintering technique [210,214,216,220]. [1] The ceramic suspension used for their

[1] The entirety of the hollow fibre supports used in this work were provided and fabricated by professor Kang Li's group at Imperial college. Dr Bo Wang and Dr Tao Li of Imperial college provided both the Al_2O_3 and the 3% YSZ hollow-fibre support precursors used in this research project.

preparation consisted of α-Al_2O_3 powder, DMSO as the solvent, Arlacel P135 as the dispersant and PESf as the polymer binder. The suspension was ball milled for 24 h (Planetary Ball Mill PM 100, Retsch) with 30 zirconia balls (Inframat advanced materials, grinding media spherical, 10.0 mm, D) at 350 rpm and then transferred inside a vacuum chamber (10L, manufactured) to remove air bubbles. A vacuum pump (Welch, Model 2027) attached to the vacuum chamber was used for the degassing of the ceramic suspension (5 h). After degassing, the suspension was transferred into 200 ml stainless-steel syringes and extruded through a tube-in-orifice spinneret (3 mm OD, 1.2 mm inner diameter (ID)) at a rate of 7 ml min^{-1} into a coagulation bath of deionised (DI) water with no air gap (0 cm) (Figure 3.2). A solvent mixture of 15 wt% 1,4 dioxane in n-hexane was used as the bore fluid, also extruded at a rate of 7 ml min^{-1}. The formed precursors were extruded as a continuous string of fibre in loops at the bottom of the coagulation bath. After removing the precursor loops from the coagulation bath, they were cut into 30 mm pieces and submerged in a tank of DI water for a minimum of 12 h to ensure the full removal of excess solvent. The formed precursors were then gently washed with DI water, both on the lumen and outer surface, and were straightened by placing them on a clean flat surface between 1 mm thick rulers. The precursors were left to dry at room temperature for 48 h and when then sintered in a tubular furnace (Carbolite®, STF 15/610) at 1200, 1250, 1300 and 1350 ºC in air [171,221].

Following the same viscous-fingering induced-phase inversion technique, 3% YSZ hollow fibres were also fabricated as the supports for dual-phase ceramic molten-salt membranes. The ceramic suspension for the fabrication of 3% YSZ fibres consisted of 3% YSZ powder, NMP as the solvent, Arlacel P135 as the dispersant and PMMA as the polymer binder. The bore fluid used during the spinning of the YSZ hollow fibre precursors was a mixture of ethanol and NMP in a 2:1 weight ratio and both the ceramic suspension and the bore fluid were extruded with a flow rate of 8 ml min^{-1}. The same process as for the Al_2O_3 hollow-fibre precursors was followed for the removal of excess solvent, the straightening, and the drying of the 3% YSZ precursors. The precursors were then sintered in a tubular furnace (Carbolite®, STF 15/610) at 1200, 1250, 1300 and 1350 ºC in air [222–224]. The composition of the ceramic suspensions used for the fabrication of the Al_2O_3, 3% YSZ hollow fibres is shown in Table 3.1 and the sintering profiles used for the fabricated fibres are shown in Figure 3.6. The temperature was initially increased to 600 ºC, followed by a 2 h dwelling

period, for the Al_2O_3 hollow fibres, in order to remove the residual liquid introduced during the fabrication process. For the YSZ hollow fibres the temperature was initially increase to 400 ºC, followed by a 2 h dwelling period, and then increased to 600 ºC, also followed by a 2 h dwelling period, to assist in the elimination of additives, such as organic binders and dispersant, which were included at a higher weight ratio in the YSZ ceramic suspension. Finally, the temperature was increased to 1200 ºC (or higher) by 5 ºC min^{-1} to allow grain growth, and subsequently a more rigid and dense body for the hollow-fibre supports, *via* high temperature sintering [225].

Table 3.1: wt% composition of the ceramic suspension for the fabrication of Al_2O_3, 3% YSZ hollow fibre precursors.

(wt%)	Al_2O_3 suspension	3 % YSZ suspension
Ceramic powder	62.7	54.8
Polymer binder	6.3 (PESf)	10.27 (PMMA)
Solvent	30.6 (DMSO)	34.25 (NMP)
Dispersant	0.4 (Arcarel P135)	0.68 (Arcarel P135)

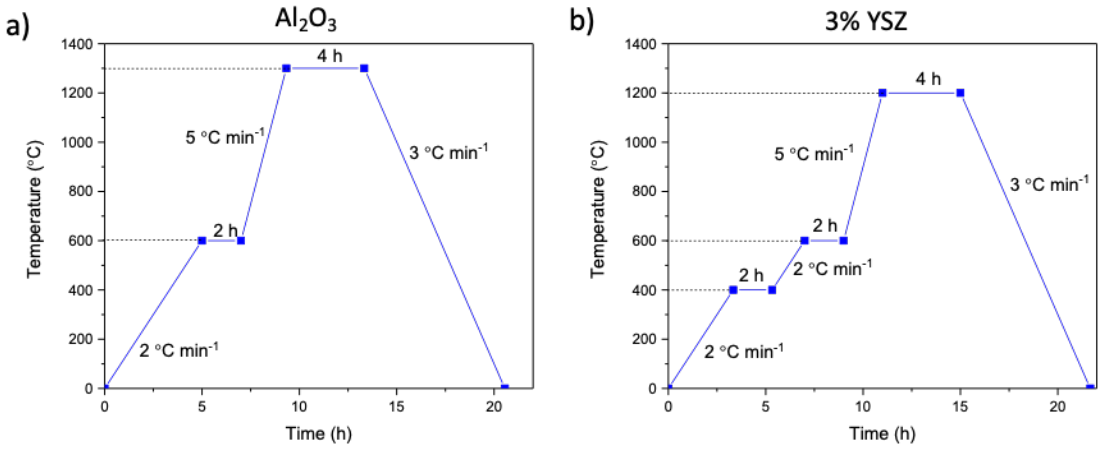

Figure 3.6: Sintering profiles for Al_2O_3 and 3% YSZ hollow fibres.

3.2.3 Preparation of carbonate eutectic mixture

To prepare the carbonate at solid state Li_2CO_3, Na_2CO_3, and K_2CO_3 were placed in individual crucibles and dried in a furnace (Carbolite®, STF 15/610) at 400 ºC for 24 h. The dehydrated carbonate were then mixed in a eutectic mole ratio (Li_2CO_3:Na_2CO_3:K_2CO_3=43.5:31.5:25) and the mixture was dispersed in ethanol to a resulting concentraion of 0.1 g l^{-1} [99]. To reduce the particle size and narrow the particle size distribution, the suspension was placed in a ball miller (Pascal Engineering Inc., Parvalux elecric motor) for 48 h with a speed of 30 rpm using 15 zirconia balls (Inframat advanced materials, grinding media spherical, 10.0 mm, D). The particle size

and particle size distribution of the carbonate mixture was measured at specific time intervals during the milling and after 48 h using dynamic light scattering with non-invasive backscatter optics (Zetasizer Nano ZS).

3.2.4 Development of dual-phase ceramic hollow fibre membranes

Dual-phase hollow fibre membranes (DPHFMs) were prepared by a novel two-step coating method resulting in the controlled infiltration of the carbonate into the packed-pore network of the hollow fibre supports. After glazing the fibres with a commercial ceramic sealant (Scarva, G261/W) (diluted in DI water) on both sides to create a gas-tight layer, the fibres were coated with a solid carbonate mixture by a vacuum-assisted method (step 1), followed by the infiltration of the carbonate into the support, by heat treatment (step 2).

Glazing of ceramic hollow fibres

Ceramic hollow fibres were glazed on both sides with a commercial ceramic sealant (Scarva, G261/W) in order to allow 4 cm as the active membrane length in the middle, matching the isothermal zone of the furnace used for the permeation experiments. The desired 4 cm active membrane length of the hollow fibre was wrapped in PTFE tape and the remaining uncovered surface of the fibre was dip-coated in the glazing solution. The tips of the fibres were also dip-coated in the glazing solution in order to create a dead-end configuration (Figure 3.7), and the dip-coated fibres were left to dry for 1 h to allow the evaporation of the DI water. The dip-coated fibres were then inserted inside a tubular furnace at 900 °C, for 15 min, where the firing of the ceramic glaze led to the creation of a gas-tight layer around the ceramic fibres. The gas-tightness of the glazed part was confirmed by pressure-drop method (chapter 3, section 3.2.5) and did not contribute to the permeation mechanism.

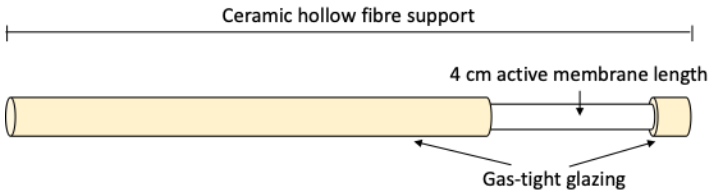

Figure 3.7: A glazed hollow fibre support with a dead-end configuration and an active 4 cm membrane length.

Coating of hollow fibres with a solid carbonate layer

In order to calculate the amount of solid carbonate required to fill the desired porosity of the support, the volume of mercury intruding in the support's porosity during the mercury intrusion porosimetry (MIP) tests was converted to mass of carbonate

required for infiltration. The density used for the above calculations was the density of the eutectic carbonate mixture at room temperature, ρ= 2.36 g cm^{-3}. In order to investigate the effect of carbonate loading inside the ceramic hollow-fibre supports 25, 50, 75 and 100 vol% of the packed-pore network was filled with carbonate. The 0.1 g l^{-1} eutectic carbonate suspension prepared by milling in section 3.2.3 was diluted further to a concentration of 0.025 g l^{-1} to cover more of the supports surface. The fibres were attached to a flexible plastic tube and connected to a solvent trap and an in line vacuum pump (Welch, Model 2027) and were then immersed in the 0.025 g l^{-1} carbonate suspension (Figure 3.8). By applying a vaccum on the open-end of the fibres, ethanol was retained in the solvent trap and a cabonate layer was formed on the outer surface of the hollow fibre. By controlling the volume of the suspension used for coating it was possible to control the vol% loading of carbonate inside the ceramic hollow-fibre supports. The carbonate suspension was stirred throughout the coating process, using a magnetic stirrer (1000 rpm), aiming to achieve a homogeneous carbonate layer on the outer surface of the hollow fibres. The carbonate coating layer was compacted under vacuum for 10 min after the coated fibre was removed from the suspension. The residual solvent was evaporated at 50 ºC in a fan dry oven for 5 h.

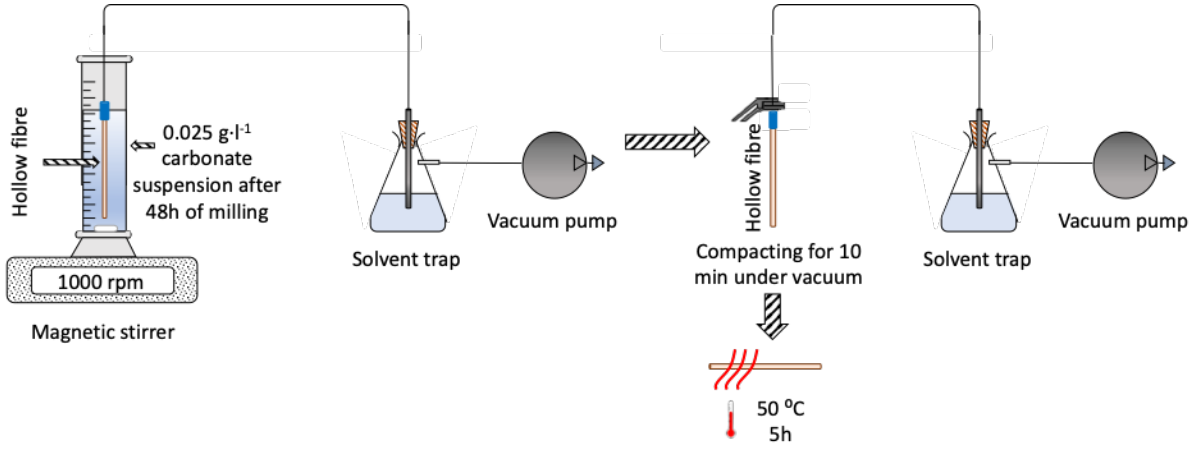

Figure 3.8: Carbonate coating of hollow fibre supports. Schematic representation of the experimental procedure for coating of hollow fibres with carbonate by a vacuum-assisted method.

Infiltration of molten salts

After coating, the samples underwent a heat-treatment for the infiltration of the molten phase inside their packed-pore network. The samples were heated to 600 ºC, at a heating rate of 1 ºC min^{-1}. During this step, the carbonate melted at approximately 400 ºC and infiltrated the hollow fibre supports due to capillary forces. The samples were then cooled down to room temperature at 1 ºC min^{-1} and the infiltrated fibres were immediately stored in a fan dry oven at 50 ºC since the carbonate mixture is highly

hygroscopic. The carbonate loading inside the hollow fibres was determined by comparing the weights of the hollow fibres before and after the coating and infiltration steps. After the infiltration process the samples were used for gas-tightness measurements at room temperature.

3.2.5 Gas-tightness testing of infiltrated ceramic hollow-fibre supports at room temperature

The gas-tightness of the hollow-fibre supports infiltrated with 25, 50, 75 and 100 vol% carbonate in their packed-pore network was evaluated by nitrogen permeation measurements at room temperature, either by flow rate or pressure drop methods (Figure 3.9). The preparation of gas-tight membranes at room temperature is important to ensure that the membranes will be defect-free and permselective at high temperatures (>400 °C). The specific volume of the eutectic carbonate mixture increases upon melting, so gas-tight membranes at room temperature are expected to produce gas-tight membranes at the membrane's operational temperature.

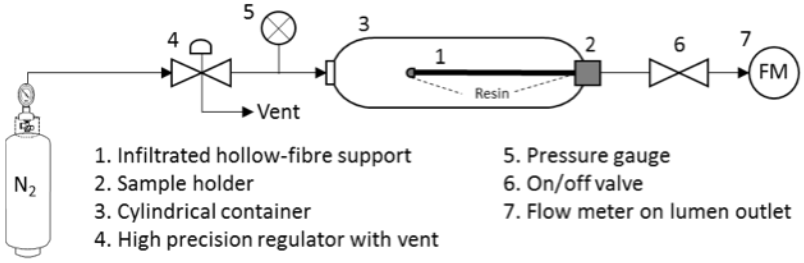

Figure 3.9: Gas-tightness testing of membranes. Schematic representation of the experimental apparatus designed for nitrogen permeation measurements on infiltrated hollow-fibre supports at room temperature. When the infiltrated Al_2O_3 hollow fibres are porous, the flow rate method is performed with applied pressures from 14 and 138 kPa. When the permeability of the infiltrated Al_2O_3 hollow fibres was below the detection limit, the pressure drop method was performed at P_{shell} = 138 kPa.

In gas permeation measurements by flow rate method the infiltrated supports were subjected to nitrogen permeation tests, by increasing the pressure of the cylindrical container in increments on the shell side of the hollow fibre (14-138 kPa). The flow rate of permeating nitrogen gas was monitored on the lumen-side outlet of the hollow-fibre supports allowing the calculation of nitrogen flux through the infiltrated supports. The flow rate method was applied when the samples were still porous at room temperature. When the permeability of the infiltrated supports was beyond the detection level of the flow rate method (<0.5 ml min^{-1}) the pressure drop method was used. Gas permeation measurements by pressure drop at room temperature allow to determine the gas-tightness of the membrane, *i.e.* permeance below 1×10^{-10} mol m^{-2} s^{-1} Pa^{-1}, by

monitoring the pressure change of the cylindrical container over a 18 h period. The pressure inside the cylindrical container was initially set to 138 kPa and in order to monitor the pressure change of the cylindrical container, the lumen outlet flow of the infiltrated support was blocked by switching valve 6 (Figure 3.9) to the off position. By trapping the gas inside the cylindrical container, the pressure change was monitored through pressure gauge 5 and the nitrogen gas could only escape through the vent of the high precision regulator. The nitrogen permeance, $\mathcal{P}$ (mol m^{-2} s^{-1} Pa^{-1}) of the infiltrated supports was then calculated based on the cylindrical container pressure change with time using the equation below [226]:

$$\mathcal{P} = \frac{V}{RTA_s t} \ln\left(\frac{P_0 - P_a}{P_t - P_a}\right) \quad \text{(Eq. 3.1)}$$

where V is the volume of the cylindrical container (m^3); R is the gas constant (8.314 J mol^{-1} K^{-1}); T is the measured temperature (K); P_0 and P_t are the initial and final measured pressures in the test cylinder (Pa); P_α is the atmospheric pressure (Pa) and t is the measurement time (s). A_s (m^2) is the outer lateral membrane surface area $2\pi R_0 L$ (m^2), where R_0 is the outer radius of the hollow fibre (m) and L is the active length of the infiltrated hollow fibre supports (m).

For both methods, the infiltrated supports (1) were sealed on one end with epoxy resin (2), while the other end was also glued onto stainless-steel holders. All the samples were dried for 24 hours at 50 °C before subjected to gas-tightness tests. A single sample was placed into a cylindrical container (3) (125 ml) and connected to the inlet and outlet streams, as shown in Figure 3.9. Nitrogen gas was introduced to the system directly from the gas cylinder and nitrogen gas flow was controlled by a high precision regulator with vent (4). In both methods, the permeation set-ups were initially pressurised at 138 psi and a leak detection fluid was used to ensure there were no leaks. The pressure of the shell side was monitored with a pressure gauge (5) and the on/off valve (6) at the lumen outlet of the infiltrated hollow-fibre support was used to block the lumen flow during the pressure-drop method. The permeating nitrogen flow through the infiltrated hollow-fibre support during the flow-rate method, was measured from pressures of 14 to 138 kPa using an electronic flow meter (GFM Pro Flowmeter, Thermo Scientific).

3.2.6 High temperature testing of infiltrated ceramic hollow-fibre supports

The gas-tightness of Al_2O_3 hollow-fibre supports coated with 50, 75 and 100 vol% of carbonate were also tested at high temperature (>400 °C) as the volume expansion of

the carbonate when melted [151] can produce membranes that are gas-tight at higher temperature even if they are not gas-tight at room temperature. The carbonate coated and glazed Al_2O_3 hollow fibres were glued on a stainless-steel fitting with epoxy resin. To prepare the permeation apparatus, the stainless-steel fitting was connected onto a stainless-steel tube (3/8' OD, Swagelok) and was inserted in the centre of the isothermal zone of the horizontal tubular furnace (Eurotherm 2416, Vecstar) as shown in Figure 3.10. The part of the fibre glued with epoxy resin was kept out of the heating zone of the furnace. The system was pressurised (138 kPa) with argon and tested for leaks with a leak detection fluid, before introducing the feed-side inlet. In the absence of leaks, the feed gas was introduced on the shell side of the Al_2O_3 hollow fibre and the temperature was increased to 500 °C. The flow rate of the feed gas was controlled by an individual mass flow controller (Bronkhorst, EL-FlOW® Select) attached to a collective reader (Bronkhorst, HIGH-TECH®). The temperature at the centre of the membrane was monitored by a type-K thermocouple located on the outside of the permeation apparatus. The composition of the permeate-side outlet was analysed by a gas chromatographer (Varian 3900) with a shin carbon column (RESTEK, packed column, ST100/120) and the permeate nitrogen flow was monitored using an electronic flow meter (GFM Pro Flowmeter, Thermo Scientific).

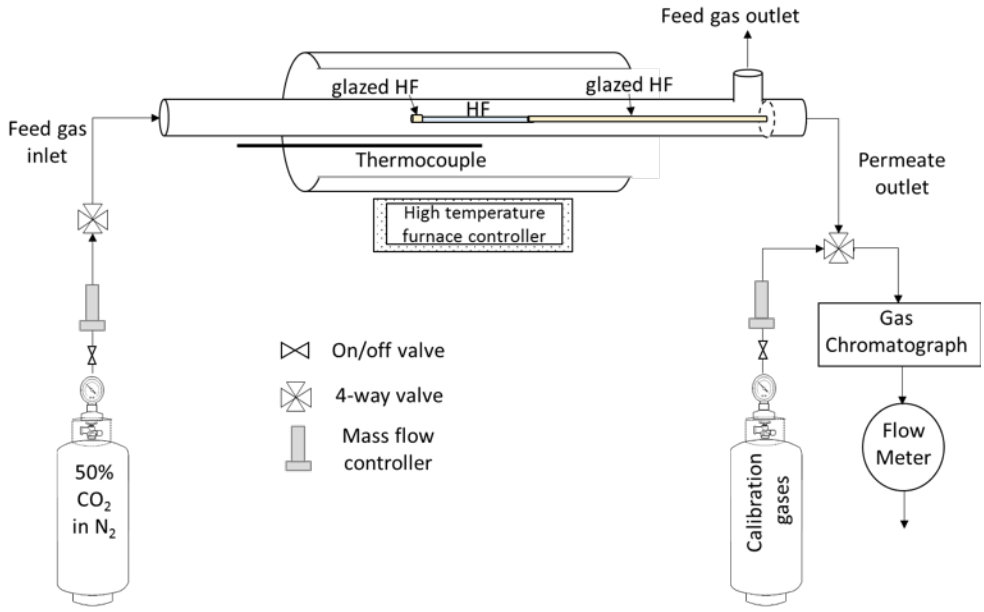

Figure 3.10: Permeation apparatus for high-temperature testing of Al_2O_3 hollow-fibre membranes.

Volumetric flux, J_{CO_2} (ml min^{-1} cm^{-2}) is calculated based on (Eq. 3.2):

$$J_{CO_2} = \frac{\varphi_{CO_2}\dot{V}}{A_S} \qquad \text{(Eq. 3.2)}$$

where φ_{CO_2} is the volume fraction of carbon dioxide in the permeate-side outlet, $\dot{V}$ is the volumetric flow rate on the permeate side (ml min^{-1}), and A_s is the portion of the surface area of the membrane contributing to permeation (cm^2). This means that the surface area has been corrected for the surface porosity of the membrane and will be referred to as effective surface area from this point on.

As mentioned in section 1.4, dual-phase ceramic molten-salt membranes operating at high temperature (>400 °C) can provide a high selectivity for carbon dioxide over nitrogen permeation, with the highest reported carbon dioxide over nitrogen selectivity value reaching up to ~1000 [100]. This practically means that for a membrane to be considered selective, the carbon dioxide flux measured through the membrane needs to be higher than the nitrogen flux. And for a membrane to be considered well-sealed at high temperature, the nitrogen flux through the membrane needs to be around the detection limit of the analytical equipment. For the gas chromatographer used in this study, the limit for the nitrogen volume fraction that can be detected is ~25 ppm, which corresponds to a nitrogen flux of ~ 0.0007 ml min^{-1} cm^{-2} and a nitrogen permeance of 1 x 10^{-10} mol m^{-2} s^{-1} Pa^{-1} for DPHFMs with a surface area A_s of ~1.8 cm^2 (r=0.12 cm, l = 4 cm, accounting for an external surface porosity of 56%). Therefore, the threshold permeance value for considering a dual-phase ceramic molten-salt membrane a well-sealed selective membrane needs to be lower than or close to 1 x 10^{-10} mol m^{-2} s^{-1} Pa^{-1}.

3.2.7 Characterisation

SEM imaging

The micro-structure of the prepared DPHFMs was analysed by scanning electron spectroscopy (SEM) instruments (Hitachi, TM3030 and Tescan, Vega3). Samples were coated with gold in a vacuum chamber for 20 min at 10 mA (Polaron SEM Coating Unit). Energy-dispersive X-ray spectroscopy (EDX; Bruker Flash 6130) analysis was used, in connection to SEM, to identify the distribution of carbonate within the Al_2O_3 hollow-fibre supports.

SEM imaging, in connection to ImageJ analysis software, was also used to determine the surface porosity of the hollow-fibre supports. The SEM images were analysed using the adjust threshold function of the ImageJ software which returns a surface porosity value based on the colour contrast of the porous regions detected on the SEM

image. Each surface porosity value in this work is the result of the porosity value as calculated by an average of 20 measurements, allowing for an error of +/-5%.

MIP analysis

The porosity and pore size distribution of the hollow-fibre supports was calculated by mercury intrusion porosimetry (MIP, Pascal 440, Porosimeter) analysis over a pressure range of 0.01 to 1,000 MPa (indicating a pore size cut-off of ~5 nm) and with a set stabilisation time of 10 s.[2] MIP analysis is based on the non-wetting properties of mercury and, as a result, the mercury will only penetrate the pores within the support when applying external pressure [227]. Pressure versus intrusion data generates volume and size distribution based on the Washburn equation:

$$P = -\frac{2\gamma \cos \theta}{r} \quad \text{(Eq. 3.3)}$$

where P is the applied pressure (atm), γ is the surface tension of mercury (J m^{-2}), θ is the contact angle between pore wall and mercury and r represents the pore radius (μm). The volume of mercury intruding the support's porosity increases with the increase in pressure, with the larger pores, *i.e.* micro-channels, being filled at lower pressures and the smaller pores, *i.e.* packed-pore network, being filled at larger pressures. The cut-off point, where mercury starts intruding the packed-pore network, is found by associating the applied pressure with the pore size diameter from the MIP results. After identifying the average diameter of the micro-channels, the intruded volume corresponding to this diameter (cut-off point) is subtracted from the intruded volume at the highest applied pressure, to give the packed-pore network volume *per* gram of fibre.

3P bending strength

Evaluation of the mechanical strength of the hollow fibres was performed by diametrical compression tests using a 3P bending tester (Instron 5543) with a load of 10 kN.[3] The 3P bending strength was calculated based on Eq. 3.4 [184,228,229]:

$$\sigma_F = \frac{8FlD_o}{\pi(D_o^4 - D_i^4)} \quad \text{(Eq. 3.4)}$$

where F is the force measured (N) when the fracture of the hollow fibres occurs and l, D_o and D_i are the length of the hollow fibre (m), the outer, and the inner diameters of the hollow fibres (m), respectively.

[2] MIP measurements were conducted by Dr Oliver B. Camus at Bath University.
[3] The 3P bending tests were performed by Dr Tao Li at Imperial College London.

3.3 Results and discussion

3.3.1 Morphology of micro-structured hollow-fibre supports

Al_2O_3 and 3% YSZ ceramic hollow-fibre supports prepared by viscous-fingering induced phase-inversion technique and sintered at temperatures between 1200 and 1350 °C were analysed by SEM. By manipulating the fabrication parameters, the prepared Al_2O_3 hollow-fibre supports benefit from a thick sponge-like layer; 50 +/- 10 µm, attributed to a 0 cm air gap between the tip of the tube-in-orifice spinneret and the coagulation bath of DI water. Compared to other asymmetric Al_2O_3 hollow-fibre supports in literature with a similar morphology (*i.e.* a plethora of micro-channels and a single sponge-like layer towards the outer surface of the support) that have been prepared using a 0 cm air gap and tap water in the coagulation bath [216,230], the Al_2O_3 hollow-fibre supports in this study possess a thicker sponge-like layer (50 µm instead of ~25 µm sponge-like layer for the Al_2O_3 hollow-fibre supports in literature [216,230]). The porous surface of the packed-pore network inside the Al_2O_3 hollow fibre supports was found to cover less than 20% (+/- 5%) of its cross-sectional area (Figure 3.11:Al_2O_3a). From Figure 3.11:Al_2O_3c, it was also calculated that ~38,200 micro-channels *per* cm^2 are present on the support's lumen side. The number of micro-channels *per* cm^2 in the lumen side of the Al_2O_3 hollow fibre supports in this study is higher than the number of micro-channels *per* cm^2 of Al_2O_3 hollow fibre supports in literature (~38,200 micro-channels *per* cm^2 for the Al_2O_3 hollow-fibre supports in this study, compared to ~8,600 micro-channels *per* cm^2 for the aforementioned Al_2O_3 supports in literature [216]).

The morphology of the hollow fibre supports used in this study, *i.e.* sponge-like layer thickness and number of micro-channels, is attributed to the use of a solvent-based internal coagulant which causes micro-channel growth only from the outer surface of the extruded ceramic suspension towards the inner surface [216]. The number and length of micro-channels (consequently the thickness of the sponge-like layer) depends on the content of the solvent in the internal coagulant; in this case 85 wt% n-hexane in 1,4 dioxane for the Al_2O_3 hollow fibres and 66 wt% NMP in ethanol for the 3% YSZ hollow fibres. Hollow fibre precursors formed with high solvent content in the bore fluid mixture, usually >70 wt%, show an increased number of micro-channels with a large mouth diameter that penetrate deep into the cross section of the hollow fibre precursors. If the solvent is NMP however, an increase of the solvent content in the

internal coagulant fluid above 70 wt% results in the disappearance of the sponge-like layer, allowing the micro-channels to penetrate all the way through the cross section of the hollow fibre precursors [231]. For YSZ membranes with a similar geometry in literature, the solvent-based internal coagulant used was a mixture of 10 wt% water, 20 wt% ethanol in NMP. The higher content of NMP in this mixture decreased the sponge-like layer thickness and the number of micro-channels in these supports compared to the sponge-like layer thickness and number of micro-channels in supports prepared in this work [106]. In Al_2O_3 hollow fibres with a similar geometry in literature, DMSO is used as the solvent. DMSO is highly miscible with the non-solvent (water), allowing solvent and non-solvent exchange at the inner surface, and therefore decreasing the possible achieved thickness of the sponge-like layer. In this work, the use of an 'inert'-based solvent, such as n-hexane, does not contribute to the solvent and non-solvent exchange at the inner surface of the hollow fibre precursors, resulting in hollow fibre supports with increased sponge-like layer thickness [216].

The higher number of micro-channels *per* cm^2 results in increased available surface area on the lumen side of the Al_2O_3 hollow fibre supports which has been found to increase flux. 3% YSZ hollow-fibre supports could only be compared with 8% YSZ hollow-fibre supports of the same morphology that have been prepared in literature under similar conditions (0 cm air gap, tap water in the coagulation bath) [232]. 8% YSZ hollow-fibre supports in literature have a thinner sponge-like layer (3 – 5 µm) than the 3% YSZ hollow-fibre supports in this study (10 +/- 5 µm) and show a similar number of micro-channels *per* cm^2 on their lumen surface [232]. The number of micro-channels present on the 3% YSZ support's lumen side is ~10,400 micro-channels *per* cm^2 as calculated by Figure 3.11:3%YSZc. For the 3% YSZ hollow fibres for the 3% YSZ hollow-fibre supports, the packed-pore network covered less than 25% (+/- 5%) of the support's cross-sectional area (Figure 3.11:3%YSZa). The thicker sponge-like layer of the supports in this study is expected to produce DPHFMs with a higher mechanical strength than the already existing DPHFMs in literature [214].

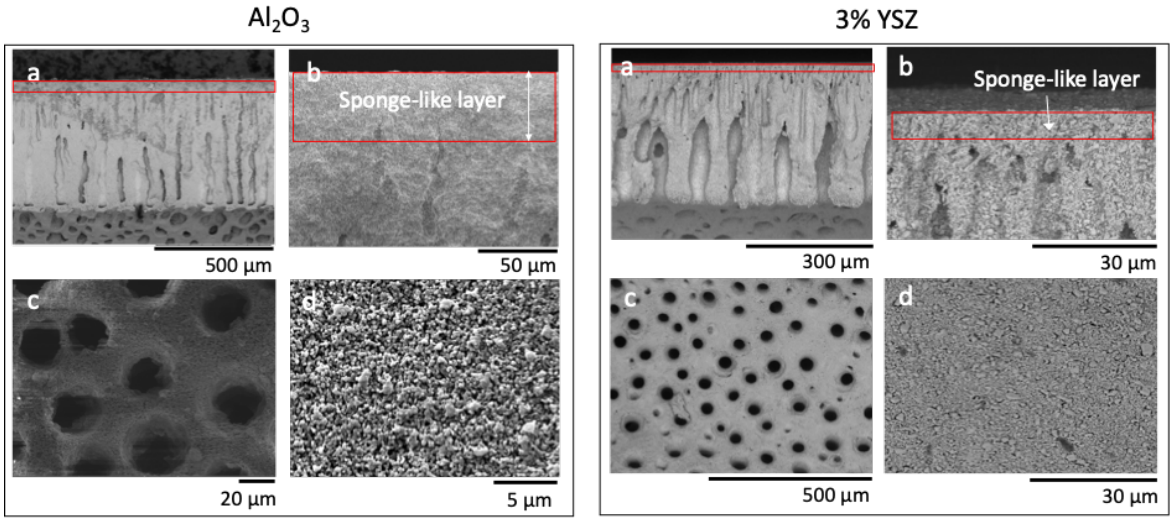

Figure 3.11: Asymmetric micro-structured ceramic hollow-fibre supports: SEM images of Al_2O_3 and 3% YSZ hollow fibres showing their a) cross-section, b) sponge-like layer, c) inner/lumen surface, d) outer porous surface.

3.3.2 Properties of micro-structured hollow-fibre supports

In order to control the incorporation of carbonate in the hollow-fibre supports and prepare DPHFMs with a decreased molten carbonate thickness compared to previously developed DPHFMs, it was essential to confine the carbonate in the sponge-like layer of the packed-pore network; leaving the micro-channels unblocked. To do that, the pore volume associated with the porosity domains of the hollow fibre supports must be determined. The hollow-fibre precursors were initially sintered at 1200, 1250, 1300 and 1350 °C to determine the support with the most desirable properties for the incorporation of the molten carbonate. As the sintering temperature was increased, both the volumetric (calculated by MIP tests) and surface porosity (estimated by SEM images analysed with ImageJ of the surface as describe in section 3.2.7) of the Al_2O_3 and 3% YSZ hollow-fibre supports decreased while the 3P bending strength of the hollow-fibre supports increased (Figure 3.12:a, b and c). More specifically, the 3P bending strength of the Al_2O_3 and 3% YSZ supports increased by a factor of three from 1200 to 1350 °C in both cases, while the overall porosity decreased by 25% and 40%, respectively (Figure 3.12a). In general, the loss of porosity is higher in the sections of the packed-pore network with lower average pore size, *i.e.* the sponge-like layer [180,233], which is not desirable for the purpose of confining the molten salts to a thin layer in the sponge-like layer of the hollow-fibre supports. However, hollow-fibre supports that benefit from high mechanical strength are desirable in DPHFMs due to the fragile nature of ceramic supports [110,131,234].

Therefore, a trade-off relationship between the 3P bending strength and the porosity of the hollow fibre supports needs to be established.

Amongst the Al_2O_3 hollow fibre supports sintered at 1200, 1250, 1300 and 1350 °C, the ones sintered at 1200 and 1250 °C possessed the highest overall porosity yet showed the lowest 3P bending mechanical strength. Despite the Al_2O_3 hollow fibre supports sintered at 1350 °C showing the highest 3P bending strength, the 12% loss in porosity for that support, compared to the support sintered at 1300 °C, is not ideal for the incorporation of the molten salt phase. Since Al_2O_3 is a nominally electrically insulating material, carbon dioxide permeation will occur through the molten phase, hence it is desirable for the surface and volumetric porosity of the supports to be as high as possible, without compromising its 3P bending strength. For DPHFMs to be applied in an IGCC or NGCC process for example, the hollow fibre supports should possess a minimum mechanical strength of 10 MPa, based on the process pressure requirements [235]. In reality, the mechanical strength of the hollow fibre supports should be higher than 10 MPa, to withstand stresses generated from membrane sealing and handling [235]. Amongst the sintered Al_2O_3 hollow fibre supports, the ones sintered at 1300 °C offer the best trade-off relationship between high 3P bending strength and high porosity. Establishing the best trade-off relationship between 3P bending strength and porosity for the hollow fibre supports, helps increase the robustness and the permeation performance of the DPHFMs that can be developed using these supports. Sacrificing 3P bending strength over a higher porosity within the micro-structured hollow-fibre supports also allows for better inter-connectivity between the pores and ultimately better inter-connectivity for the transport pathways of charged species in the molten carbonate [130,171]. Al_2O_3 hollow fibres sintered at 1300 °C, with an overall porosity of 58% and a 3P bending strength of 70 MPa were used exclusively in all further experiments. In general, Al_2O_3 hollow-fibre supports in literature with a similar porous asymmetric structure and ~30 μm thick sponge-like layer have shown a lower 3P bending strength, between 41 and 58 MPa, when sintered between 1300 and 1342 °C [171,216] compared to the Al_2O_3 hollow-fibre supports fabricated in this study. Typical values of 3P bending strength for Al_2O_3 hollow-fibres with different porous asymmetric structures in literature are between 100 and 150 MPa [184,236] when sintered at 1500 and 1550 °C, with the 3P bending strength reaching 350 MPa for dense Al_2O_3 hollow-fibre supports when the sintering temperature is increased to 1600 °C [184].

For 3% YSZ hollow fibres, it was experimentally determined that the supports sintered at temperatures 1250 °C and above, with an outer porosity below 15%, do not allow the coating of the hollow-fibre supports with a carbonate layer, as they are too dense for ethanol in the carbonate suspension to pass from the shell to the lumen side of hollow fibre supports when vacuum is applied on the lumen side (process described in section 3.2.4, Figure 3.8). Moreover, 3% YSZ hollow fibres sintered at 1250 °C and above possess low outer surface porosity (<15%, analysed by ImageJ software) and a large grain distribution on their outer surface, which decrease the TPBs available for surface exchange between the gaseous and liquid phase carbon dioxide (Figure 3.12c: 3% YSZ sintered at 1250, 1300 and 1350 °C). These factors combined limit the rate of permeation to undesirable levels, hence this preparation method is not suitable [124]. 3% YSZ supports sintered at 1200 °C, showed an overall porosity of ~45% with a small grain distribution on their outer surface (as analysed by ImageJ software, Appendix A) and a 3P bending strength of 97 MPa, providing the best trade-off relationship between 3P bending strength and porosity amongst the 3% YSZ sintered supports. Hence, 3% were further used for the development of 3% YSZ-supported DPHFMs.

Based on the trade-off relationships between the 3P bending strength and the porosity for the Al_2O_3 and 3% YSZ hollow fibre supports, an overall porosity of ~60% and a 3P bending strength of 70 MPa and above should be considered for the development of future DPHFMs.

After choosing the desired sintering temperature, MIP tests were used to determine the pore size distribution and pore volume of the hollow fibre supports. The pore size diameter of the micro-channels for all the supports is represented by the wider peak from 2 to 30 μm (Figure 3.12d), and the packed-pore network (including the sponge-like layer) is represented by the sharper peak ranging from 0.05 to 0.4 μm, which are similar to previous studies on asymmetric hollow-fibre supports [216]. The pore volume associated with the packed-pore network alone, was determined based on the results showing the cumulative intrusion of mercury inside the hollow-fibre supports with the increase in pressure (Figure 3.12e), following the procedure described in section 3.2.7 for the MIP analysis. Determining the porous volume corresponding to the packed-pore network alone, allows control over the amount of carbonate that is used for infiltration. For the Al_2O_3 hollow fibre supports sintered at 1300 °C the pore volume associated with the volume of the micro-channels is 0.12 ml *per* gram of fibre (pressure

0 – 6,000 MPa), whereas the pore volume associated with the volume of the packed-pore network is 0.2 ml *per* gram of fibre (pressure 6,000 – 14,000 MPa). For the 3% YSZ fibres sintered at 1200 °C, the pore volume associated with the micro-channels is 0.08 ml *per* gram of fibre (pressure 0 – 7,000 MPa), whereas the pore volume associated with the packed-pore network is 0.1 ml *per* gram of fibre (pressure 7,000 – 14,000 MPa). The volume of the packed-pore network occupies 62 and 55% of the overall porous volume of the Al_2O_3 and 3% YSZ hollow fibre supports, respectively. Hence, aiming to infiltrate the sponge-like layer of the packed-pore network reduces significantly the amount of carbonate required for infiltration, compared to infiltrating the entire porous volume of the hollow fibre supports, which has previously been done in literature [106,141,144].

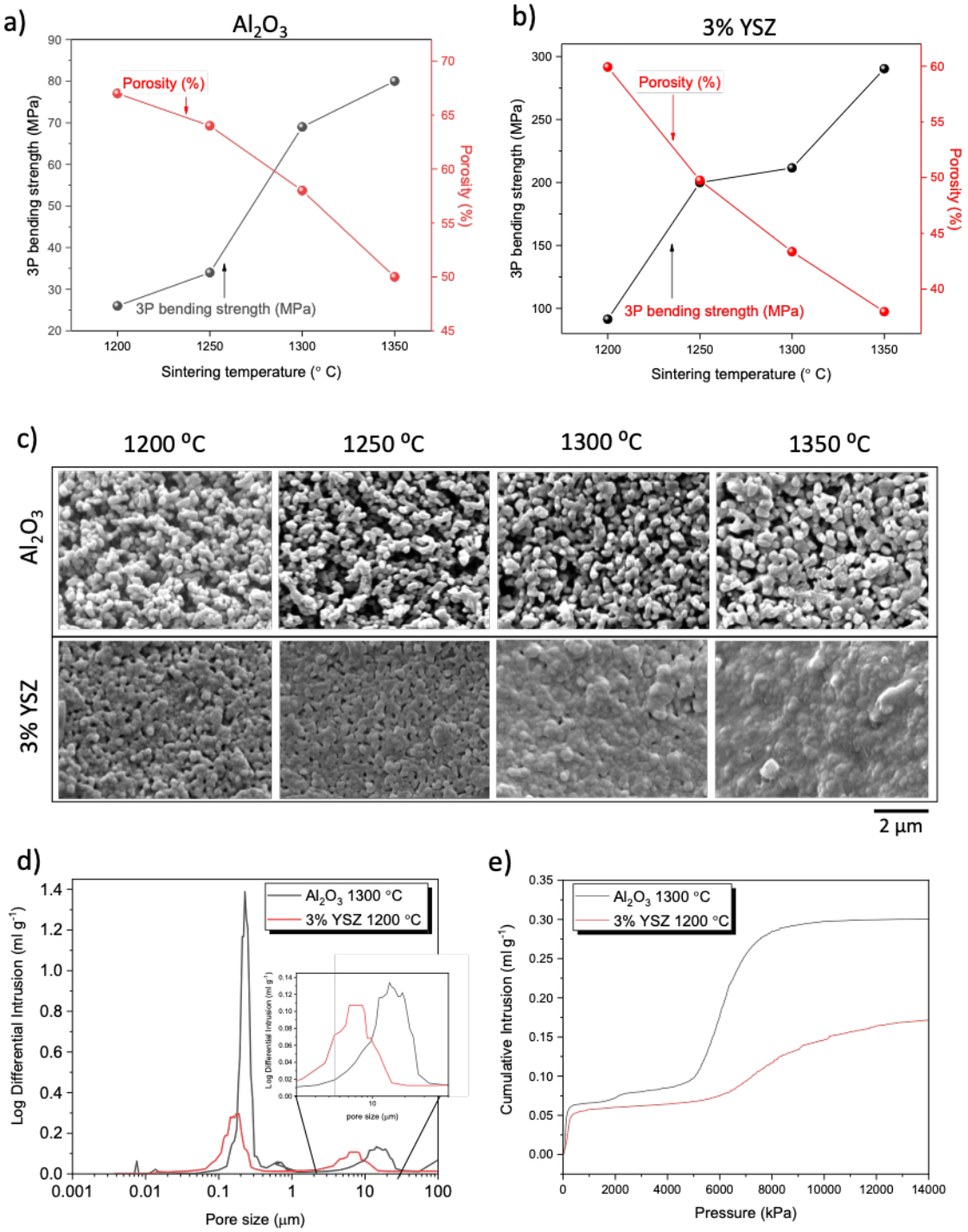

Figure 3.12: Mechanical strength and porosity of Al_2O_3 and 3% YSZ hollow fibres. 3P bending strength (MPa) *versus* total porosity (%) of a) Al_2O_3 and 3% YSZ hollow fibres sintered at 1200, 1250, 1300 and 1350 °C. c) Outer surface porosity of Al_2O_3 (1st row) and 3% YSZ (2nd row) hollow-fibre supports sintered at 1200, 1250, 1300 and 1350 °C. d) Pore size distribution of Al_2O_3 and 3% YSZ hollow-fibre supports sintered at 1300 and 1200 °C, respectively. e) Cumulative intrusion volume over temperature for Al_2O_3 and 3% YSZ hollow fibre supports sintered at 1300 and 1200 °C, respectively.

So far, YSZ-supported dual-phase phase ceramic molten-salt membranes in literature use 8-mol% yttria doped zirconia (8% YSZ) for the preparation of the hollow-fibre supports as it shows a ~50% higher oxygen-ion conductivity than the 3-mol% yttria

doped zirconia (3% YSZ) [237]. However, the oxygen-ion conductivity of 8% YSZ at 600 °C (0.004 S cm^{-1}) is quite lower than the conductivity of the molten phase at 600 °C (1.2 S cm^{-1}, calculated from reference [151]). Therefore, solubility of carbon dioxide in the melt is expected to contribute the largest to carbon dioxide permeation through YSZ-supported dual-phase membranes. 8% YSZ hollow fibre supports were initially prepared for this study and the hollow fibre precursors were sintered at 1200, 1250, 1300 and 1350 °C (SEM images can be found in Appendix A). However, the outer porosity of the 8% YSZ hollow fibres sintered at 1200 °C was ~14% which is quite low compared to the outer porosity of the 3% YSZ hollow fibres sintered at the same temperature, which reaches an outer porosity value of 45% (Appendix A). As mentioned above, outer porosity values below 15% do not allow the coating of the hollow-fibre supports with a carbonate layer, as the supports are too dense for ethanol in the carbonate suspension to pass from the shell to the lumen side of hollow fibre supports (determined experimentally, process described in section 3.2.4, Figure 3.8). Therefore, 8% YSZ supports were not chosen for the development of DPHFMs as they don't fit the purpose for the preparation of DPHFMs with controlled distribution of carbonate inside the hollow fibre supports, which is the aim of this study.

3.3.3 Effect of carbonate infiltration on support micro-structure

To infiltrate the carbonate in the sponge-like layer of the selected hollow-fibre supports, the supports were initially coated with a carbonate layer by a vacuum-assisted method. The carbonate formed a layer on the support's outer surface, as the average pore size of the hollow-fibre surface (0.05 to 0.4 μm) was smaller than the average particle size of the carbonate suspension (~0.8 μm, after 48 h of ball milling, Appendix A) (Figure 3.13a and b). The ternary eutectic carbonate mixture was infiltrated in the hollow-fibre supports by heat treatment and due to capillary forces and the good wettability of the melt on the Al_2O_3 surface [132,145]. The sponge-like layer provides a smaller average pore size than the micro-channels, thus higher capillarity for the molten phase, which is expected to be confined in a thin layer towards the outer surface of the hollow fibre without infiltrating the micro-channels, which remained clearly visible (Figure 3.13c and d). This is a diversion from current literature where the need for DPHFMs with a thin separation layer has been discussed, but has not yet been developed [106].

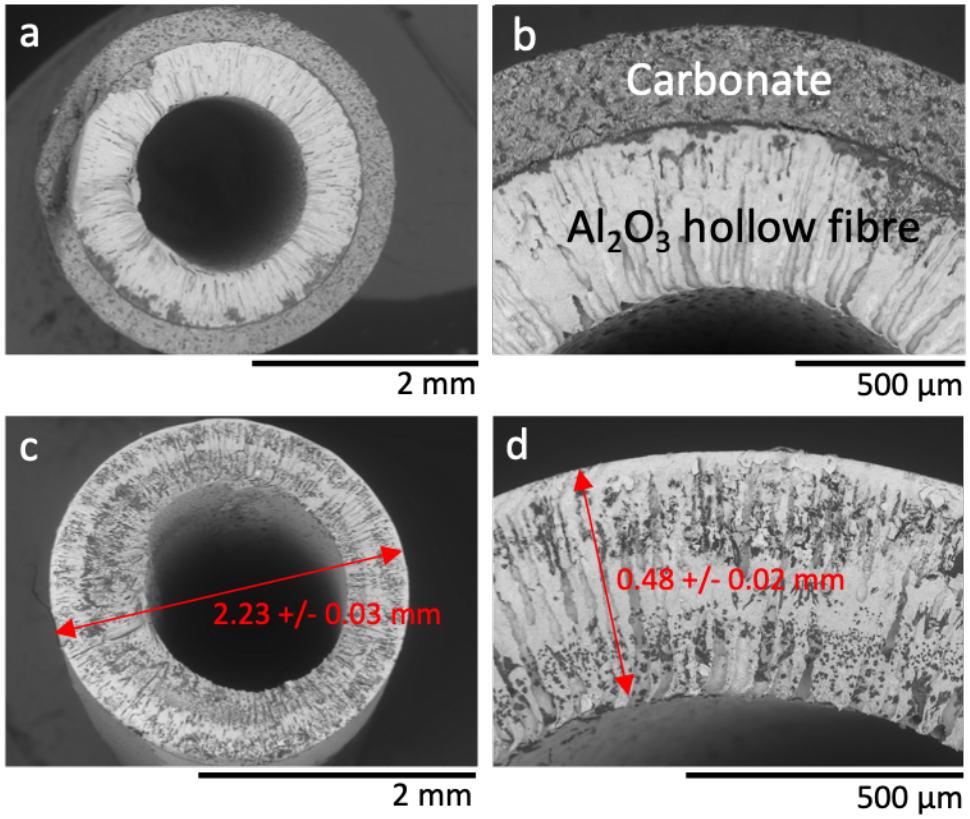

Figure 3.13: Coating and controlled infiltration of Al_2O_3 hollow fibres sintered at 1300 °C. a) and, b) SEM images of an Al_2O_3 hollow fibre coated with a carbonate layer at room temperature by a vacuum-assisted method and, c) and, d) infiltrated with carbonate after heat treatment at 600 °C, due to capillary forces.

As mentioned above, since the pore size of the sponge-like layer is smaller than the rest of the packed-pore network, infiltrating a percentage of the packed-pore network could result in a gas-tight layer inside the support's sponge-like layer without requiring the infiltration of the entire packed-pore network. To do that, the packed-pore network volume (calculated in section 3.3.2 from Figure 3.12e) was converted to the equivalent mass of carbonate using the density of the eutectic mixture of carbonate at room temperature, (ρ= 2.36 g cm^{-3}, $\rho(LiNaK)_2CO_3$= 33.4$\rho(Na_2CO_3)$ + 32.1$\rho(Li_2CO_3)$ + 34.5$\rho(K_2CO_3)$). The grams of carbonate per grams of hollow-fibre required for the infiltration of the packed-pore network were then calculated (Appendix A). Different carbonate loadings, aiming to infiltrate 25, 50, 75 and 100 vol% of the packed-pore network were used in Al_2O_3 hollow-fibre supports. The 25, 50, 75 and 100 vol% carbonate coated Al_2O_3 hollow fibres supports can be seen in (Figure 3.14a). The coating process was conducted with (red line) and without (black line) the use of a magnetic stirrer, in order to produce hollow fibre supports with a homogeneous carbonate layer. Figure 3.14b shows that both methods - with and without the magnetic stirrer – fit well to their linear regression lines, with R^2 values of 0.97 and 0.94 for fibres

coated with and without the use of a magnetic stirrer respectively. The R^2 values and mean absolute errors of both models indicate that the use of a magnetic stirrer produces a more linear relationship between the carbonate loading and the carbonate thickness, since the statistics indicate a better goodness of fit. The use of a magnetic stirrer was further adopted for all fibre coatings in this work. The linear relationship between the thickness of carbonate layer and carbonate loading also confirmed that the novel two-step coating and infiltration method allows control over the carbonate layer thickness by controlling carbonate loading, which would not have been possible using the immersion technique previously used in literature [106,141,144]

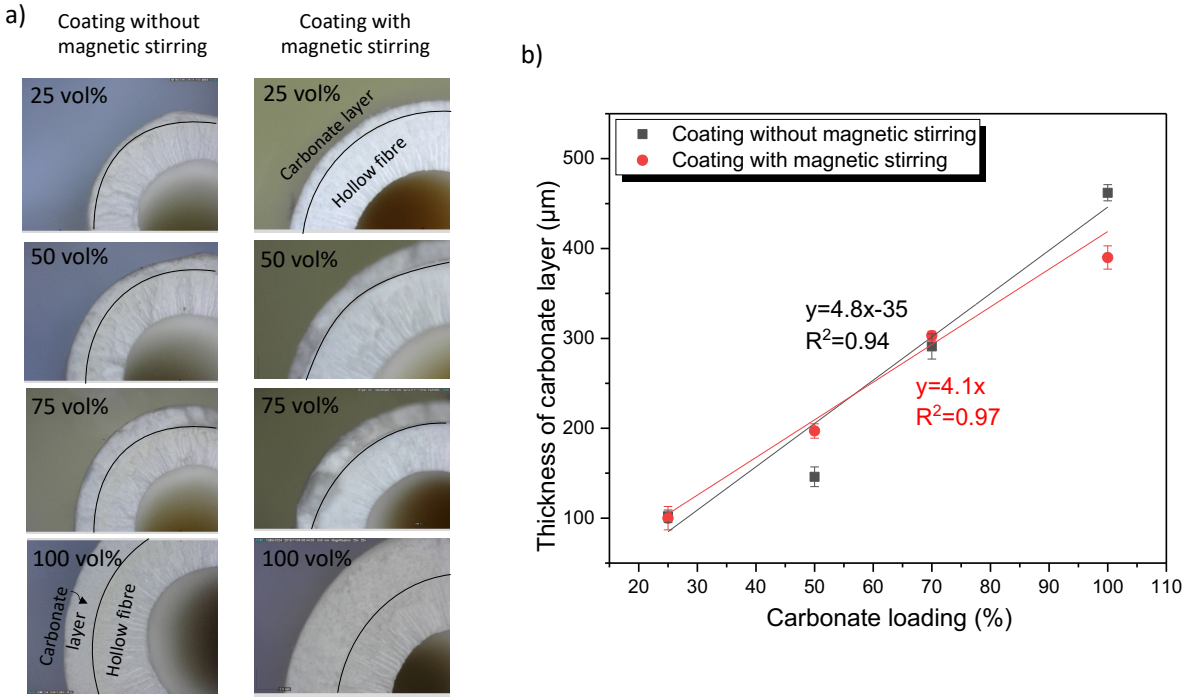

Figure 3.14: Coating of hollow-fibre supports by a vacuum-assisted method. a) Digital images of carbonate 25, 50, 75 and 100 vol% coated Al_2O_3 hollow fibre supports without (I) and with (II) the use of a magnetic stirrer. b) Thickness of carbonate layer on Al_2O_3 hollow fibre supports versus the aimed carbonate loading (%) with and without the use of a magnetic stirrer.

The cross-sectional SEM and EDX images of 25, 50, 75 and 100 vol% carbonate infiltrated Al_2O_3 supports showed a homogeneous distribution of carbonate throughout the support's packed-pore network, at room temperature, while the micro-channels remained un-infiltrated for all investigated loadings (Figure 3.15a). ImageJ analysis of the SEM images also showed that the porosity increased from the top (outer surface, small pore size) towards the bottom (lumen surface, larger pore sizes) of the supports' cross section creating a porosity gradient inside the hollow-fibre support. The 100 vol% infiltrated support was the only one that showed a dense sponge-like layer, as can be seen in Figure 3.15b (100 vol%, first row) and as was analysed by SEM imaging using the ImageJ software. However, ternary eutectic carbonate mixture has infiltrated the

entire cross-section of the support's packed-pore network, and was not confined, as expected, in the sponge-like layer alone. This is still a significant diversion from literature where the carbonate has infiltrated in both porosity domains of the hollow fibre supports. Carbonate coating *via* a vacuum-assisted method can also be considered for the infiltration of hollow fibre supports in a wider scale, as it is performed at room temperature, it shows good reproducibility and it provides a simple and effective method for the development of DPHFMs while using less carbonate volume *per* gram of fibre than the immersion method, performed at temperature above 400 °C in literature [106,141,144].

The cross-sectional SEM and EDX images of infiltrated 3% YSZ supports also showed a homogeneous distribution of carbonate throughout the support's packed-pore network without infiltrating the micro-channels, and can be found in Appendix A.

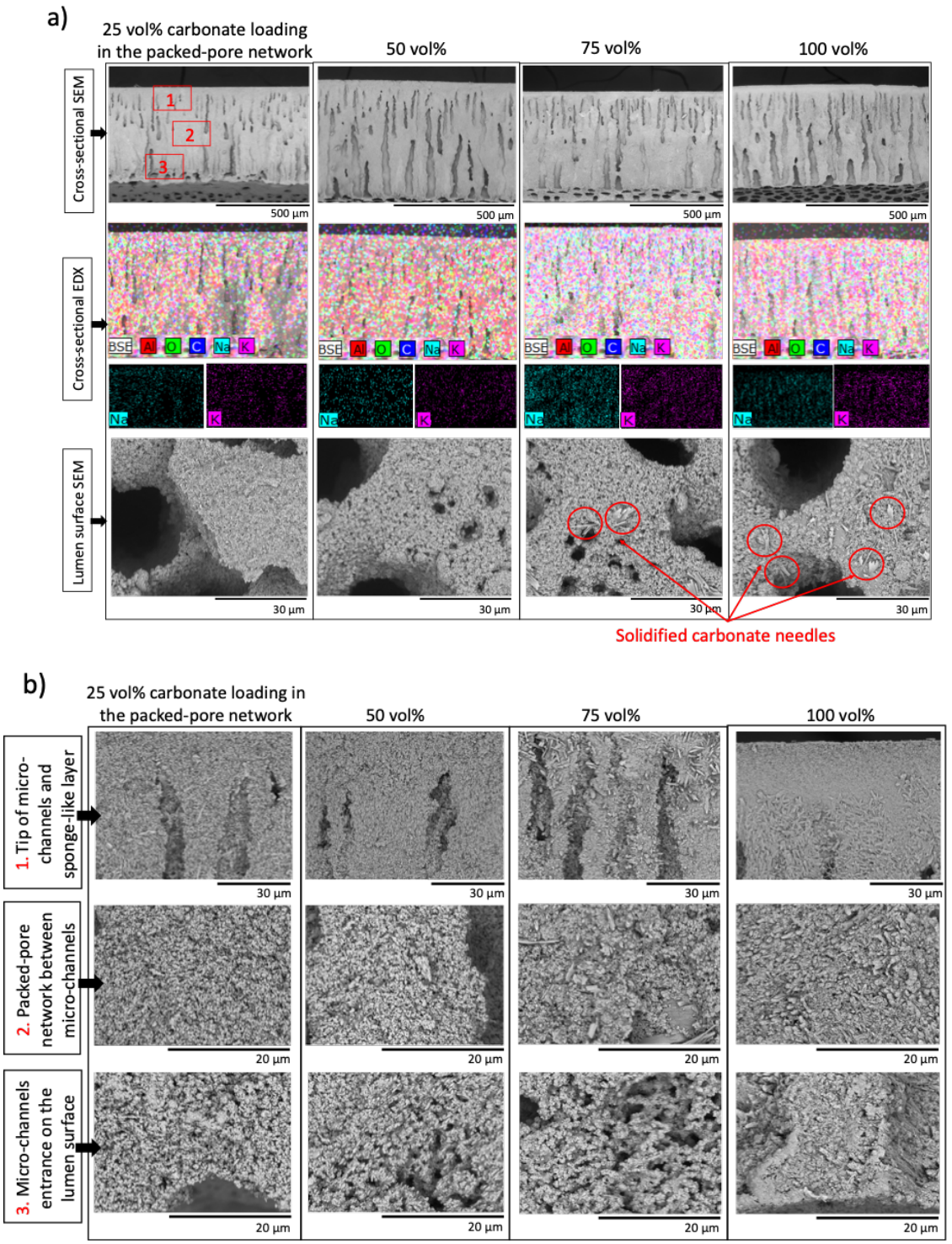

Figure 3.15: SEM and EDX analysis of the cross-sectional and lumen surface areas of 25, 50, 75 and 100 vol% infiltrated Al_2O_3 hollow-fibre supports. a) Cross-sectional SEM and EDX, and SEM images of the lumen surface area of the 25, 50, 75 and 100 vol % Al_2O_3 hollow fibres. b) Analysis of different regions across the 25, 50, 75 and 100 vol% infiltrated Al_2O_3 hollow-fibre cross-section. SEM images of the tip of micro-channels and the sponge-like layer of the infiltrated Al_2O_3 hollow-fibre supports, the packed-pore network between the micro-channels, and the micro-channels entrance on the lumen side of the hollow fibres; showing the concentration gradient of the carbonate inside the support.

To verify the amount of carbonate that infiltrated the support, the weight of the infiltrated fibres was compared to the original hollow fibre support weight, without any

carbonate. It was found, that the carbonate loading infiltrated in the Al_2O_3 hollow-fibre supports was 80 ± 7 vol% (error calculated from 5 samples), which is less than the targeted 100 vol% carbonate loading (calculations in Appendix A). This can be attributed to manual fibre handling during the coating process, as well as saturation of carbonate in the sponge-like layer, where the average pore size distribution is smaller than the rest of the packed-pore network, thus the capillary forces are higher (Eq. 2.17, chapter 2, section 2.3.3). The saturation of carbonate in the sponge-like layer can cause the excess of carbonate to melt and flow down on the shell side of the support, as they are not withheld by capillary forces in the pores. However, with the increase in temperature, the volume of the molten phase has been found to increase (chapter 2, section 2.3.2), resulting in an increase of 15 % at an operating temperature of 500 °C compared to the volume of carbonate at room temperature [238]. Taking into account the volume increase of the melt, the molten carbonate mixture is expected to infiltrate the remaining porosity of the packed-pore network, resulting in a carbonate loading of 92 ± 8 % at 500 °C. Hence, even with the increase in temperature, the molten carbonate is not expected to infiltrate the micro-channels, but to fill the remaining packed-pore network that was left un-infiltrated instead, due to the higher capillary forces developed in the packed-pore network.

3.3.4 Gas-tightness of infiltrated supports

The gas-tightness of the Al_2O_3 hollow fibre supports infiltrated with 25, 50, 75 and 100 vol% and 3% YSZ infiltrated with 50, 75 and 100 vol% of carbonate in their packed-pore network was evaluated by nitrogen permeation tests at room temperature, where the carbonate mixture was in solid state, over an applied pressure range of 14 to 138 kPa (transmembrane pressure range: 0 to 244 kPa) (Figure 3.16). This method has been previously used to evaluate the gas-tightness of dense MIEC hollow-fibre supports for oxygen and air separation [226,239] and is used here to determine whether a dense, defect free layer of carbonate has been created inside the packed-pore network of the hollow-fibre supports. Standard practice in the literature is to practice gas-tightness tests at room temperature. Preparing infiltrated hollow-fibre supports that are gas-tight at room temperature will guarantee the supports will be gas-tight and permselective at higher temperatures (>400 °C), during membrane operation. Moreover, subjecting the infiltrated supports at a transmembrane pressure difference explores their use in application where carbon dioxide separation needs to be performed under a feed pressure that is above atmospheric, *i.e.* above 101 kPa [46].

Infiltrated supports that remain gas-tight even with the increase in transmembrane pressure, show potential as DPHFMs in applications where the feed side pressure is above atmospheric, *i.e.* NGCC and IGCC processes [46].

As a reference point, the nitrogen permeation flux of infiltrated supports was compared against the nitrogen flux of the un-infiltrated Al_2O_3 and 3% YSZ supports. The nitrogen flux of un-infiltrated supports was at least an order of magnitude higher compared to the 25, 50, 75 and 100 vol% infiltrated supports (Al_2O_3: 135 ml min^{-1} cm^{-2} at 14 kPa and 1,758 ml min^{-1} cm^{-2} at 138 kPa, Figure 3.16a, 3% YSZ: 200 ml min^{-1} cm^{-2} at 14 kPa and 5,000 ml min^{-1} cm^{-2} at 138 kPa, Figure 3.16b) and followed a linear nitrogen flux increase with the increase in transmembrane pressure. Nitrogen permeation flux through the infiltrated supports decreased with the increase in carbonate loading as a result of the decrease in free porous space inside the supports. A linear relationship is also observed between nitrogen flux and applied pressure differences for 25, 50, 75 vol% infiltrated supports. Even though nitrogen permeation flux of the infiltrated supports was considerably lower than the un-infiltrated ones, only the 100 vol% infiltrated supports gave a stable (Al_2O_3: 0.08 ml min^{-1} cm^{-2}, 3% YSZ: 0.2 ml min^{-1} cm^{-2}) nitrogen flux which was at the detection limit of the equipment, at all applied pressure differences (Figure 3.16a). The 100 vol% infiltrated supports were further tested by pressure drop method over a 18 h period at room temperature and their permeance value was compared against the literature value of 1×10^{-10} mol m^{-2} s^{-1} Pa^{-1}, below which a membrane may considered to be gas-tight [226]. The Al_2O_3 and 3% YSZ supports infiltrated with 100 vol% carbonate in their packed-pore network gave a permeance value of 1.5×10^{-9} and 3.75×10^{-9} mol m^{-2} s^{-1} Pa^{-1}, respectively, when subjected to the pressure drop method. This indicates that only membranes with 100 vol% of carbonate infiltrated in their packed-pore network approached the condition for gas-tightness at room temperature.

In general, the consistency at which the nitrogen flux decreases with the increase in carbonate loading implies that the distribution of carbonates inside the hollow fibre supports is homogeneous. The linear relationship between nitrogen flux and applied pressure differences is also a good indication of defect-free infiltrated hollow-fibre supports that possess good reproducibility [226,239–241].

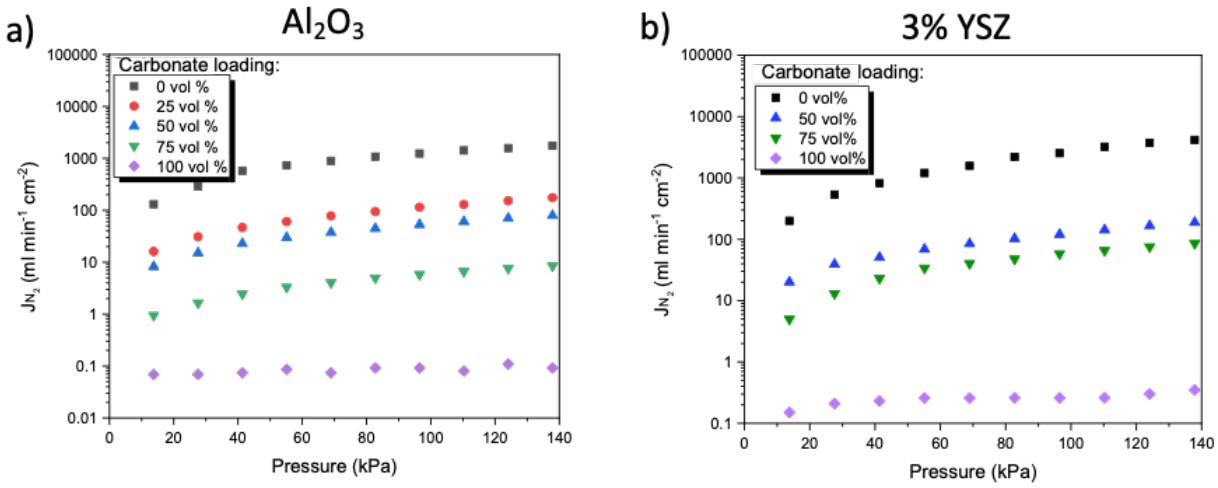

Figure 3.16: Gas-tightness testing of DPHFMs. Nitrogen permeation measurements by flow rate method at room temperature with applied pressure differences across the infiltrated supports between 14 and 138 kPa for a non-infiltrated Al_2O_3 hollow-fibre support (0 vol %) and supports with 25, 50, 75 and 100 vol % of carbonate in their packed-pore network.

The gas-tightness of coated Al_2O_3 supports was also investigated at higher temperatures as the volume increase of the molten carbonate is expected to result in 'pseudo-dense', gas-tight membranes. Glazed Al_2O_3-infiltrated supports with 50, 75 and 100 vol% carbonate in their packed-pore network were sealed on a stainless-steel permeation apparatus and subjected to nitrogen permeation measurements over a temperature range of 500 °C (Figure 3.17). The carbonate, coated by a vacuum-assisted method on the Al_2O_3 supports, formed a porous layer on the support's shell-side surface allowing the nitrogen to permeate through the membrane reaching a nitrogen flux of 1,000 ml min^{-1} cm^{-2} for the 50 vol% coated supports and 700 ml min^{-1} cm^{-2} for both 75 and 100 vol% coated supports. The carbonate melted at 407 °C, where a decrease in nitrogen flux was observed (Figure 3.17). However, the infiltration of the carbonate was not instantaneous but was achieved over a 30 °C temperature range. All infiltrated supports showed a low nitrogen flux as measured by gas chromatography, and the permeance values for the 50, 75 and 100 vol% infiltrated supports at 500 °C were 9.64×10^{-10}, 3.34×10^{-10} and 1.14×10^{-11} mol m^{-2} s^{-1} Pa^{-1}, respectively. Only the 100 vol% infiltrated supports were gas-tight (permeance $< 1 \times 10^{-10}$ mol m^{-2} s^{-1} Pa^{-1}) at higher temperature, agreeing with what was suggested by the gas-tightness tests at room temperature. It was concluded, that the evaluation of the gas-tightness of carbonate infiltrated hollow-fibre supports at room temperature alone is not sufficient to establish whether the carbonate loadings used will provide a gas-tight membrane at high temperature operating at atmospheric pressure. Gas-tightness tests at high temperature are necessary to determine whether the DPHFMs

will be gas-tight towards nitrogen at operating conditions. Al_2O_3 and 3% YSZ supports used for the preparation of DPHFMs, were all infiltrated with 100 vol% of carbonate in their packed-pore network for further experiments.

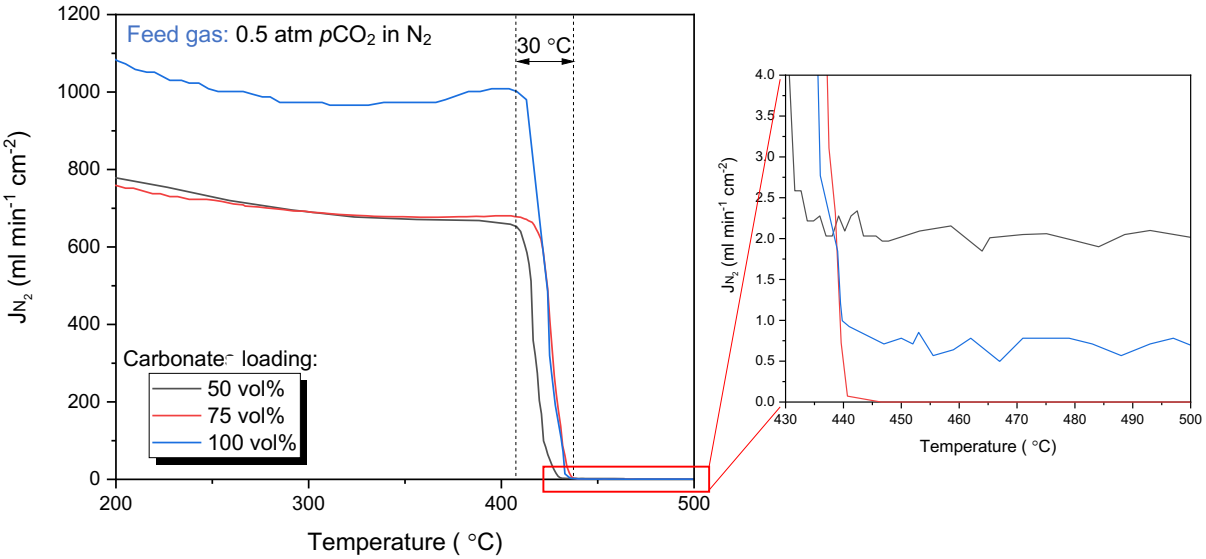

Figure 3.17: Melting point of carbonate in Al_2O_3-supported DPHFMs. Carbonate melting range for Al_2O_3-supported DPHFMs infiltrated with 50, 75 and 100 vol% of carbonate in their packed-pore network.

Overall, the confinement of the molten carbonate in a thin separation layer inside the sponge-like layer of the hollow-fibre supports, as described in the introduction of this chapter, was unsuccessful (Figure 3.18c). However, the careful characterisation of the hollow-fibre supports, and the controlled infiltration method developed in this work allowed the incorporation of the molten carbonate in the packed-pore network of the hollow-fibre supports alone which is still a significant diversion from literature (Figure 3.18d). This has not been previously achieved through the infiltration methods available in literature where both micro-channels and packed-pore network were infiltrated with carbonate (Figure 3.18b) [106,141,144]. Even though the DPHFMs in literature have an asymmetric structure with open micro-channels on their lumen side (Figure 3.18a), due to their non-selective infiltration method (as shown in Figure 3.18b), the lumen side surface after infiltration is assumed to be the projected surface of the internal surface of a cylinder. In this work, by confining the molten carbonate in the packed-pore network, the lumen side surface area of the DPHFM was increased to that sum of the projected surface areas of the micro-channels and the areas between them (Figure 3.18d). The effect of the increase in the lumen side surface area on carbon dioxide flux and permeance will be further investigated and quantified in chapter 4. Even though the challenge of preparing controlled DPHFMs was overcome at a laboratory scale, the infiltration process that results in controlled

DPHFMs also needs to be applicable at a wider scale. Dry spraying of the carbonate mixture on the membrane's outer surface at room temperature (solid carbonate mixture) is one of the methods that could be used for upscaling the controlled infiltration method. This way, the amount of carbonate required could be controlled and the membrane development process would not involve the melting of the carbonate mixture, which can cause significant corrosion issues when in contact with the walls of the membrane reactors.

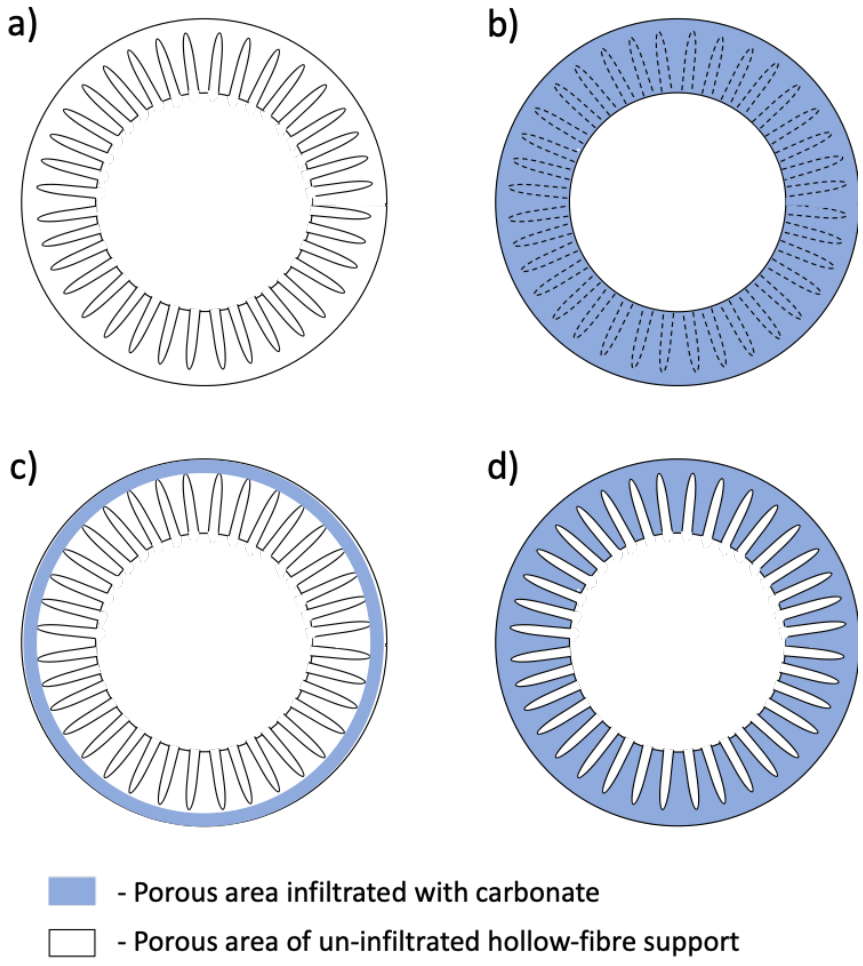

Figure 3.18: Schematic representation of un-infiltrated and infiltrated asymmetric hollow-fibre supports: a) an un-infiltrated asymmetric hollow-fibre support structure used in this study (without any carbonate), b) a non-selectively infiltrated with carbonate asymmetric hollow-fibre support as used in literature [106,141,144] (packed-pore network and micro-channels infiltrated with carbonate), c) restricting carbonate infiltration in the sponge-like layer of the hollow-fibre supports, d) infiltrating the entire packed-pore network, leading to an increase in the available lumen surface area (micro-channels not infiltrated).

3.4 Conclusions

Careful characterisation of hollow fibre supports allowed the control of molten carbonate distribution inside DPHFMs. The trade-off relationship between the mechanical strength and porosity of the hollow-fibre supports sintered at a range of temperatures (1200, 1250, 1300 and 1350 °C) helped identify hollow-fibre supports with potential/future use in the preparation of DPHFMs. Al_2O_3 and 3% YSZ hollow fibres sintered at 1300 °C and 1200 °C, respectively, were considered to be the best candidates for the incorporation of molten carbonate showing a porosity of 58 % and 59 % and a 3P bending strength of 72 and 95 MPa, respectively. Aiming to only fill the sponge-like layer of the Al_2O_3 and 3% YSZ supports (smaller pore size than the rest of the sponge-like layer), a new, vacuum-assisted coating method was developed, allowing the infiltration to occur from the outer towards the inner (lumen) side of the hollow-fibre supports, while controlling the amount of carbonate incorporated inside the supports. This was a diversion from the non-selective infiltration methods used so far in literature, where nor the amount nor the distribution of carbonate inside the hollow-fibre supports is possible to be controlled [106,141,144]. The porosity of the sponge-like layer, unlike the porosity of the packed-pore network, could not be individually quantified from MIP results, hence 25, 50, 75 and 100 vol% carbonate loadings were used to infiltrate the equivalent packed-pore network porosity; aiming to identify the loading that would result in the confinement of the carbonate in a thin layer towards the outer surface of the packed-pore network (sponge-like layer). However, the carbonate infiltrated the entire packed-pore network of the hollow-fibre support, without infiltrating the micro-channels (observed by SEM-EDX), for all investigated loadings. The gas-tightness of both Al_2O_3 and 3% YSZ infiltrated supports was tested by nitrogen permeation tests and pressure drop tests at room temperature which showed that only the supports loaded with 100 vol% of carbonate in their packed-pore network gave low enough nitrogen permeance values (1.5×10^{-9} and 3.75×10^{-9} mol m^{-2} s^{-1} Pa^{-1}, respectively) close to that of a gas-tight membrane (10^{-10} mol m^{-2} s^{-1} Pa^{-1}). At temperatures above the melting point of the carbonate mixture, Al_2O_3 supports infiltrated with 100 vol% did result in gas-tight membranes, thus 100 vol% carbonate loading was used for all membranes prepared in next chapters of this work. Even though carbonate were not successfully confined in the sponge-like layer, the available surface area on the lumen side of the DPHFMs was

successfully increased, by infiltrating the carbonate in the packed-pore network of the hollow-fibre supports.

Chapter 4

Dual-phase ceramic molten-salt membranes with improved properties for carbon dioxide separation

The aim of this chapter is to increase carbon dioxide flux achieved through DPHFMs. To do that, parameters that limit carbon dioxide flux were initially identified using a model membrane system, which allows precise control over molten-carbonate thickness, tortuosity and surface area. The parameters that were found to increase carbon dioxide flux in a model membrane system were then applied in a DPFHM system.

The following chapter includes results also presented in the manuscript *'Controlling molten carbonate distribution in dual-phase molten salt-ceramic membranes for improved carbon dioxide flux'*, currently under review in the Journal of Membrane Science.

Figures 4.2, 4.3, 4.4, 4.5 and 4.6 have been used in a similar form in the aforementioned manuscript and were remade for the purpose of this chapter.

4.1 Introduction

Selectivity and permeability are key parameters for gas permeation of carbon dioxide through dual-phase membranes. The selectivity of dual-phase membranes can be further improved by fabricating thin layers or separation, and therefore decreasing the risk of interfacial gaps between support and molten carbonate phase as well as reducing the chance of selectivity-destroying defects in the membrane's thickness. The permeability of dual-phase membranes can be further improved by increasing the specific surface area for carbon dioxide sorption (step 2 for carbon dioxide permeation through a membrane, described in chapter 1, section 1.2.4) and desorption at the feed and/or permeate side of the membranes (step 4, chapter 1, section 1.2.4) [142,242].To date, the molten carbonate phase has been supported in a pellet [131,142], hollow fibre [106,141,144], and tubular geometry [97,107] with hollow fibre and tubular geometries providing high surface area to volume ratio and potential for scale-up operation. Confining the molten carbonate phase inside a thin ceramic layer of an asymmetric pellet structure led to high carbon dioxide flux at 650 °C, reaching 0.52 ml min^{-1} cm^{-2} [132]. The molten carbonate phase was confined in a thin 10 μm layer of oxygen-ion-conducting 8% yttria-stabilised zirconia (YSZ), which was deposited on a ~1500 μm macroporous $Bi_{1.5}Y_{0.3}Sm_{0.2}O_{3-\delta}$ (BYS) support as the molten carbonate only wet the YSZ phase [132]. The reported flux for the thin-YSZ dual-phase membranes was ~10 times higher than carbon dioxide flux for 200 – 400 μm thick symmetric oxygen-ion-conducting YSZ-supported dual-phase membranes at 650 °C [131]. The flux for the thin-YSZ dual-phase membranes described above was also ~10 times higher than carbon dioxide fluxes reported for dual-phase membranes at 700 °C where the molten carbonate was infiltrated inside a 375 μm thick MIEC $La_{0.6}Sr_{0.4}Co_{0.8}Fe_{0.2}O_{3-\delta}$ (LSCF) symmetric ceramic support [142]. This implies that thickness and structure can have a greater effect on flux than conductivity, offered by the chemical nature of the ceramic support, as LSCF has a higher oxygen-ion conductivity than YSZ at the same operating temperature [137,140]. Even with the increase in operating temperature, the carbon dioxide flux through thicker membranes (LSCF and YSZ-supported membranes mentioned above), at temperatures as high as 900 °C, still did not match the carbon dioxide flux of the thin-YSZ dual-phase membrane at 650 °C.

The effects of thickness and micro-structure were also investigated with symmetric and asymmetric dual-phase membranes and an oxygen-ion-conducting samarium doped

ceria ($Ce_{0.8}Sm_{0.2}O_{1.9}$, SDC) support. The use of an asymmetric structure led to higher carbon dioxide flux compared to when a symmetric structure was used as the support of the dual-phase membranes. A thin asymmetric dual-phase membrane was produced by infiltrating a 150 μm thin layer of SDC deposited on a microporous 60% SDC-40% BYS pellet support (total support thickness not reported) [134] and was compared to a symmetric SDC-supported dual-phase membrane where the molten carbonate thickness (equivalent to membrane thickness) was 1500 μm [130]. The reported flux for the thin asymmetric SDC-supported dual-phase membrane was ~5.6 times higher than the symmetric, thick SDC-supported dual-phase membrane at 600 °C. Similarly, for a tubular geometry, the use of an asymmetric structure resulted in higher flux than the use of symmetric supports, as in the asymmetric structure the molten carbonate was confined in a thin separation layer (120 μm) of porous SDC supported on BYS [107].

Decreasing molten carbonate thickness inside the ceramic supports, has been found to increase the achieved carbon dioxide flux through dual-phase membranes. However, with the decrease in thickness below the critical thickness (L_c), surface exchange replaces bulk diffusion as the rate-limiting step in the membrane separation process and further decrease in thickness below the L_c does not result in increased flux. Studies on MIEC LSCF-supported dual-phase membranes showed that the critical thickness for this type of dual-phase membranes was 750 μm. Below this thickness, flux for LSCF-supported dual-phase membranes is limited by the available active surface area for carbon dioxide sorption and desorption provided by the ceramic support (where active surface area is defined as the part of the surface area that contributes to permeation) [142]. Any improvement in flux for membranes with a molten carbonate thickness below the critical thickness can be attributed to the effect of surface-exchange reactions on carbon dioxide permeation through those membranes, in the investigated temperature range [243]. The active surface area of the dual-phase membranes in literature, however, is often poorly defined and leads to the inaccurate calculation of carbon dioxide flux. In this work, a model crucible membrane, with a defined permeate-side surface area for carbon dioxide permeation was developed. The model crucible membrane was fabricated by a nominally electrically insulating support material, *i.e.* Al_2O_3, isolating carbon dioxide permeation to the molten carbonate phase alone. The use of a model crucible as the support, allowed the precise control of the molten-carbonate thickness and active permeate-side surface

area for carbon dioxide exchange, while providing low-tortuosity permeation path lengths, as shown in Figure 4.1. At the same time, it was possible to determine the operating temperature region and critical membrane thickness (L_c) where surface-exchange reactions on the permeate-side of the membrane were rate-limiting on its operation. This has not previously been achieved with an Al_2O_3-supported dual-phase membrane.

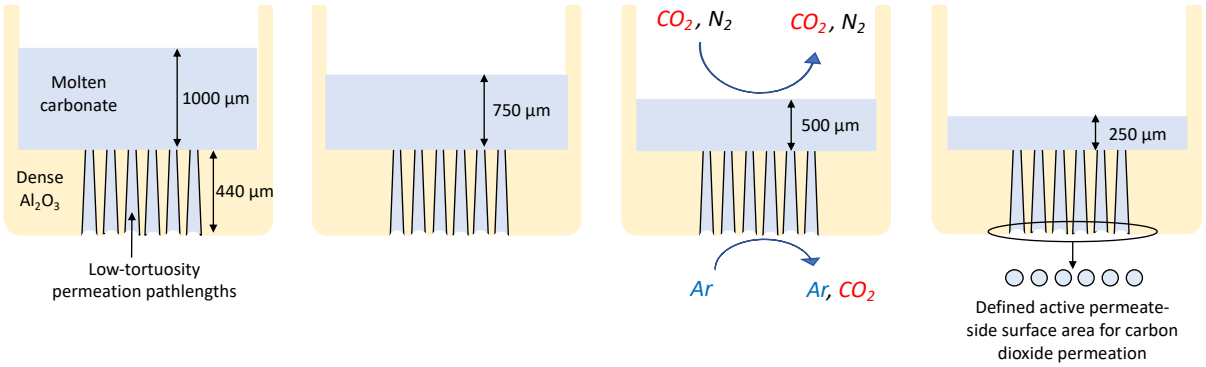

Figure 4.1: Schematic cross-section of the model crucible supports used in this work, providing low-tortuosity permeation pathlengths and control over molten carbonate thickness: 1000, 750, 500 and 250 µm molten carbonate thickness on top of the 440 µm drilled channels.

Hollow fibre supports (Figure 4.2) were further used as supports in dual-phase membranes, as they are highly scalable, hence the most desirable geometry for dual-phase membrane development [204–206,208,244].

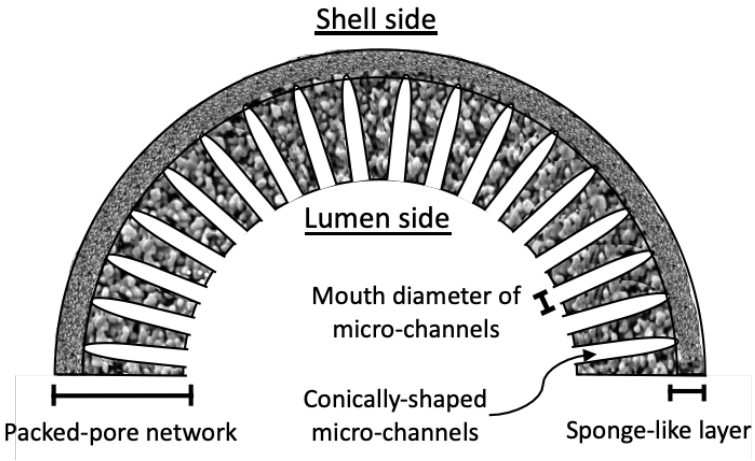

Figure 4.2: Schematic cross section of a hollow fibre support, showing its characteristic porosity domains.

As mentioned extensively in chapter 3, section 3.1, the molten carbonate phase has previously been infiltrated non-selectively, into both porosity domains of asymmetric hollow-fibre supports, *i.e.* micro-channels and packed-pore network (Figure 4.3a). The surface area available for carbon dioxide surface exchange in this case, is that of the

internal surface area of a cylinder, depicted as A_1 in Figure 4.3a. It is known, that decreasing the available active surface area for carbon dioxide exchange limits the achievable carbon dioxide flux with this geometry in the surface-exchange-limited region [106,141,144]. Therefore, preparing DPHFMs with increased surface area for carbon dioxide surface exchange would improve their performance in the surface-exchange-limited region. The impact of DPHFMs preparation on carbon dioxide flux was also highlighted by Zuo *et. al* [106]. In their work, Zuo *et. al*, suggested that the confinement of the molten carbonate inside the sponge-like layer of the hollow-fibre support, without the carbonate blocking the micro-channels, would improve carbon dioxide flux.

In chapter 3 of this work, a process to confine the molten carbonate phase in the packed-pore network alone, aiming to increase the lumen-side surface area for carbon dioxide surface exchange, was developed. In this case, the surface area for carbon dioxide exchange is increased to that of the sum of the projected surface areas of the micro-channels and the area between them (corrected for porosity in membranes with an electrically insulating support), depicted as A_2 in Figure 4.3b.

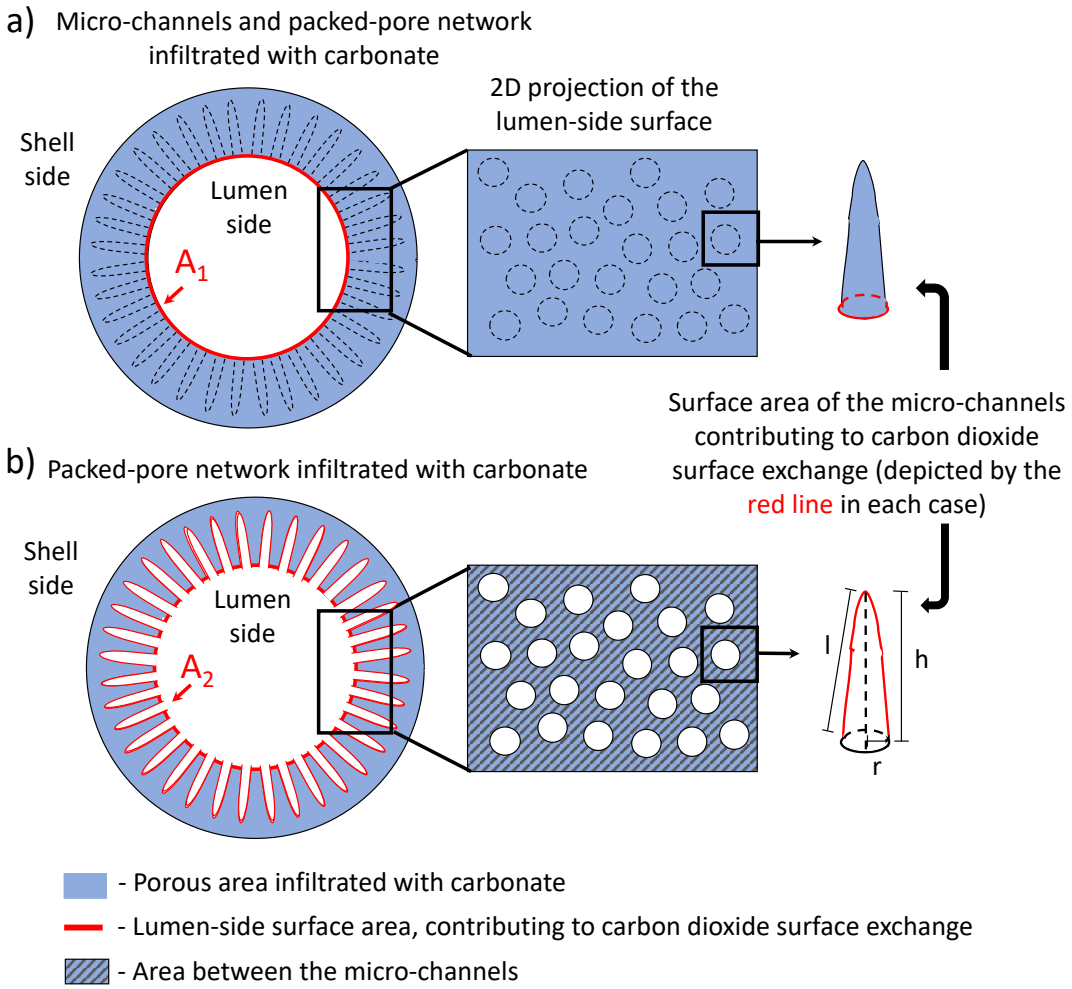

Figure 4.3: Schematic representation of hollow fibre supports where a) both micro-channels and packed-pore network are infiltrated with carbonate: surface A_1 and b) where only the packed-pore network is infiltrated with carbonate: surface A_2. The surface area that contributes to carbon dioxide surface exchange is depicted using red lines.

The increase in surface area for carbon dioxide exchange due to the confinement of the molten carbonate in the packed-pore network can also be expressed mathematically by the following surface equations.

A_1 in Figure 4.3a is given by Eq. 4.1:

$$A_1 = 2\pi rl \qquad \text{(Eq. 4.1)}$$

where l is the length of the DPHFM.

Whereas, A_2 in Figure 4.3b can be calculated using Eq. 4.2:

$$A_2 = A_1 + (\text{No of micro} - \text{channnels})(A_{cone}) - (\text{No of micro} - \text{channels})(A_{circle}) \qquad \text{(Eq. 4.2)}$$

where A_{cone} is the sum of the curved surface area and the area of the cone's base:

$$A_{cone} = \pi r^2 + \pi rl \qquad \text{(Eq. 4.3)}$$

l is equal to $\sqrt{h^2 + r^2}$ and the surface area of a circle is equal to πr^2. Replacing l and the surface area of a circle in Eq. 4.3, results in Eq. 4.4:

$$A_2 = A_1 + (No\ of\ micro - channnels)(\pi r(\sqrt{h^2 + r^2})) \quad \text{(Eq. 4.4)}$$

Which mathematically confirms that $A_2 > A_1$.

Therefore, the well-characterised hollow-fibre supports prepared in chapter 3, with a controlled distribution of carbonate in their packed-pore network, were further used for membrane development. The controlled distribution DPHFMs provide an increased surface area for carbon dioxide surface-exchange compared to conventionally prepared DPHFMs in literature, as confirmed by equations 4.1 and 4.4. The performance of the DPHFMs developed using the well-characterised hollow-fibre supports with a controlled distribution of carbonate in their packed-pore network, was compared against DPHFMs developed using hollow-fibre supports where both packed-pore network and micro-channels were filled with carbonate (uncontrolled distribution). Since Al_2O_3-supported DPHFMs have not yet been developed in literature, the novel vacuum-assisted coating method, resulting in controlled infiltration of carbonate in the hollow-fibre supports, was also applied on 3% YSZ hollow-fibre supports. This allowed the comparison between carbon dioxide flux values for YSZ-supported DPHFMs with an uncontrolled distribution in literature and YSZ-supported DPHFMs with a controlled distribution of carbonate, developed in this work. The controlled DPHFMs were also used to chart the potential of DPHFMs over a range of different partial pressure differences.

4.2 Experimental

4.2.1 Chemicals and materials

For the fabrication of the micro-structured Al_2O_3 phase-inversed pellets, a ceramic suspension consisting of α-Al_2O_3 powder, DMSO, Arlacel P135 and PESf as the ceramic material, solvent, dispersant and polymer binder, respectively, was prepared. Silver paste (Fuel Cell Materials, Silver, AG-1) was used as the high temperature sealant to seal the model crucible and pellet membranes on the aluminium tube, and vacuum grease (Fomblin Vacuum Grease) was used at the base of the aluminium tube that was inserted inside the stainless-steel base of the permeation apparatus. For the membranes with a hollow-fibre geometry, the stainless-steel needle used for the permeate-side gas inlet was sealed on the aluminium tube with the use of epoxy resin (Araldite ®, Rapid).

4.2.2 Preparation of model Al_2O_3-crucible supports

For the preparation of model Al_2O_3-crucible membrane supports, dense Al_2O_3 cylindrical crucibles (14 mm H, 25.5 mm OD, 22 mm ID) (Almath) were used, with a base thickness of 440 μm. The low-tortuosity permeation pathlengths were created by laser-drilling the crucibles from the outside surface to the inside, in a circular area (11 mm diameter) at the centre of the base. The laser drilling was realised by Laser Micromachining Limited. The geometrical properties of the Al_2O_3 crucibles were determined by digital microscopy.

4.2.3 Preparation of eutectic carbonate mixture

Dried carbonate (chapter 3, section 3.2.3) were mixed in a eutectic mole ratio (Li_2CO_3: Na_2CO_3: K_2CO_3= 43.5: 31.5: 25) and were then mixed for 30 min (MU-K-Mixer_60Hz, FLUXANA) inside a container with five zirconia balls. The mixture was immediately stored inside a drying oven at 50 °C. The preparation of the carbonate mixture used for the Al_2O_3 hollow-fibre supports followed the same process as described in chapter 3, section 3.2.3.

4.2.4 Infiltration of eutectic carbonate mixture into the selected supports

For crucible supports the carbonate mixture was pressed into a pellet form (Specac, Atlas, T25) under a 200 MPa load for 5 min and was then placed inside the crucible supports. For the DPHFMs the partially glazed fibres were coated with a solid

carbonate layer on their outer surface by a vacuum-assisted method described in detail in chapter 3, section 3.2.4.

4.2.5 Carbon dioxide permeation measurements through dual-phase ceramic molten-salt membranes

The permeation performace of the model dual-phase crucible membranes, micro-structured phase-inversed dual-phase pellet membranes and DPHFMs was evaluated using the experimental apparatus illustrated in Figure 4.4. The prepared membrane was inserted into a custom made reactor with a stainless-steel base and a quartz shell, similar to the one used by Patricio *et al.* [245]. The permeation apparatus was then placed and centered inside a tubular furnace (Carbolite®, EVA/EVC) so that the membrane studied each time was within the isothermal zone of the furnace. The feed and sweep gases were confined in two different permeation chambers, separated by applying vacuum grease at the base of the permeation apparatus which remained outside the heating zone of the furnace. The flow of the feed and sweep gases were controlled by individual mass flow controllers (Bronkhorst, EL-FlOW® Select) attached to a collective reader (Bronkhorst, HIGH-TECH®) and were set at 50 ml min^{-1} for both gases. The inlet gases were connected to the feed and sweep-gas inlet of the permeation apparatus with plastic tubing (PFA, Swagelok). In order to check for leaks the system was purged with argon (50 ml min^{-1}) for 10 min and a leak detection fluid was used on the system's connections. The total gas flow rate of each inlet and outlet stream was monitored with an electronic flow meter (GFM Pro). The permeation performance of the membranes was evaluated at each temperature, P=1 atm, after 1 h of stabilisation time, ensuring the flux deviation was below 3%. The system was heated by 1 °C min^{-1} to allow the vacuum grease to soften and set and prevent uncontrolled thermal expansion of the molten carbonate within the ceramic supports. The temperature of the vertical furnace (Carbolite®, EVA/EVC) was controlled by a temperature controller (Eurotherm 3216) and monitored by a type-K thermocouple located in close proximity to the surface of the membrane in each case. The melting of the ternary eutectic carbonate mixture typically occurred between 400 and 430 ºC under a pCO_2 = 0.5 atm in nitrogen on both sides of the membrane.

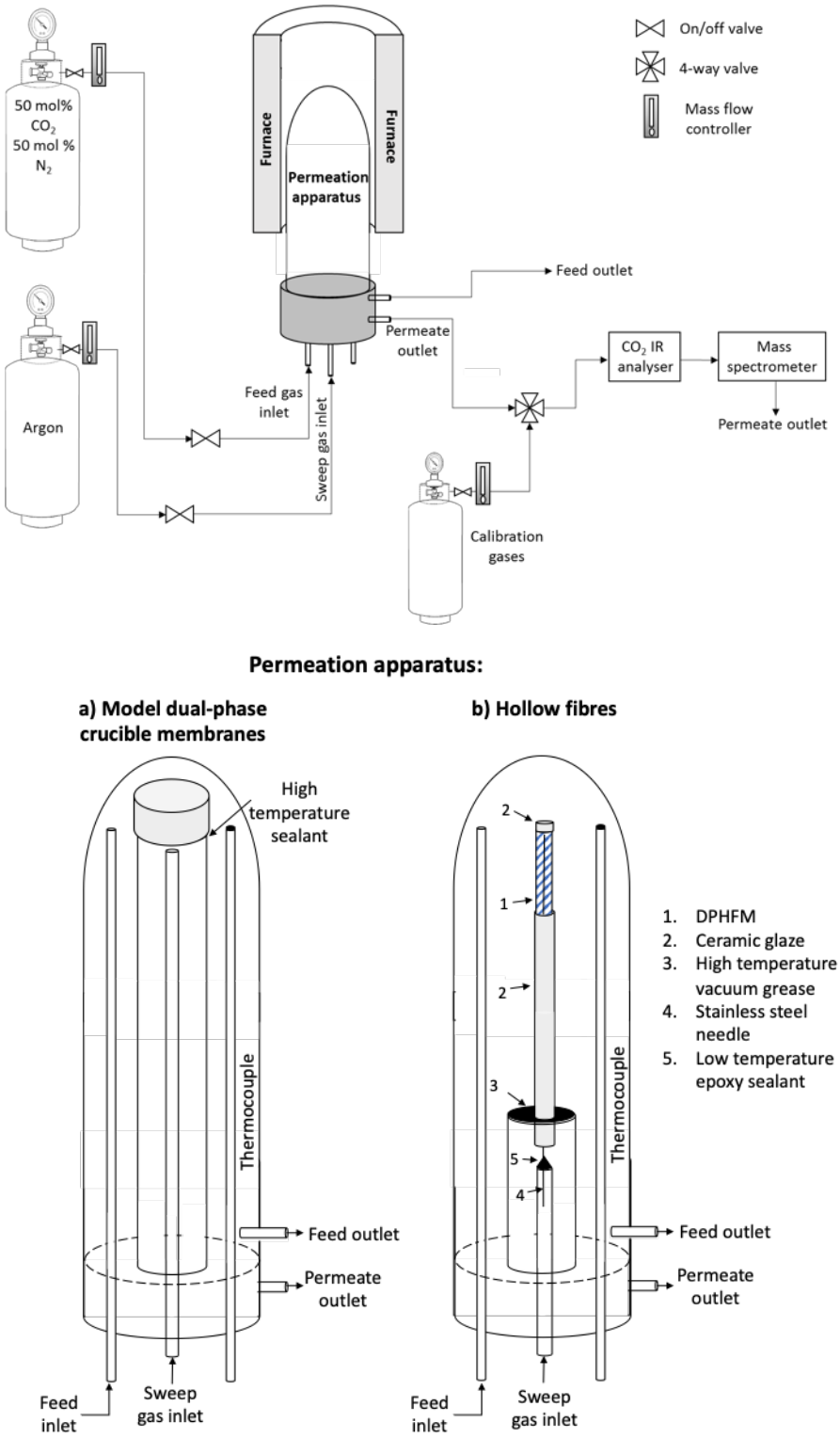

Figure 4.4: Experimental set-up for dual-phase ceramic molten-salt membranes for carbon dioxide separation. Feed and permeate gases are connected to the feed and permeate-side inlets of a custom-made permeation apparatus that houses the dual-phase membrane. The permeation apparatus is centered in the isothermal zone of a furnace and the permeate-side outlets are analysed by an in-series infrared analyser and a mass spectrometer. Depending on the membrane geometry, *i.e.* crucible or hollow fibre, the sealing of the membrane is explained by schematics a and b, respectively.

The set-up for each permeation apparatus was different depending on the geometry of the membrane used:

Model dual-phase crucible membranes

The model dual-phase crucible membranes (Figure 4.4a) were mounted on top of a hollow alumina tube (1.2 cm OD) using silver paste and were left to dry in a drying oven at 100 °C for a minimum of 12 h before they were inserted in the permeation apparatus. Pressed pellets consisting of varied mass of the ternary eutectic carbonate mixture were placed inside the crucible in separate experiments, to produce membranes with a well-defined molten-carbonate thickness. In order to calculate the carbonate amount needed for each carbonate layer, the volume of the desired layer was converted to the equivalent carbonate amount by using the value of the molten salt density at 500 °C. A 15% increase in volume of carbonate at 500 °C, as calculated in chapter 2, section 2.3.2, was also taken into consideration [238]. The density of the molten salts at 500 °C was 2.073 $g.cm^{-3}$ hence, the carbonate amount needed for membranes with 250, 500, 750 and 1000 μm molten-carbonate layer were 0.2, 0.4, 0.6 and 0.8 g respectively [238]. The partial pressure of carbon dioxide (pCO_2) in the feed gas was 0.5 atm in nitrogen (50 ml min^{-1}) and argon was used as the sweep gas (50 ml min^{-1}), with the base of the crucible as the permeate side and the reservoir of molten carbonate in the crucible as the feed side. The permeation performance of the model dual-phase crucible membranes was evaluated between 500 and 800 °C and the composition of the permeate gas was analysed in-line first by an infrared analyser (Rosemount X-STREAM X2GP, Emerson) and then by a quadrupole mass spectrometer (Hiden, QGA).

Dual-phase hollow-fibre membranes

The permeation performance of the DPHFMs for carbon dioxide separation at high temperature was evaluated using the permeation apparatus illustrated in Figure 4.4b. After preparation, the DPHFMs (1) were inserted in the permeation apparatus where a high temperature vacuum-grease sealant allowed the creation of two permeation chambers (3). The sweep gas was introduced into the permeation apparatus *via* a stainless-steel capillary tube (4) (STN, 19G) that was glued onto a thin ceramic tube (OD, ID) with a low temperature epoxy sealant (5). Both cold sealants remained outside the isothermal zone of the furnace. The composition of the permeate side gas was analysed in-line first by an infrared radiation (IR) analyser (Vaisala CARBOCAP® Carbon Dioxide Probe GMP343) and then by a quadrupole mass spectrometer (ESS, GeneSys). The permeation performance of the DPHFMs was evaluated between 600 and 800°C, P=1 atm, in various pCO_2. The pCO_2 used in the feed side was

0.1, 0.5 and 0.9 atm in nitrogen, whereas the pCO_2 used in the permeate side were 0, 0.0004 and 0.01 atm in argon.

The mass spectrometer and IR analysers used to analyse the composition of the permeate gas deriving from each membrane, were calibrated by a three-point concentration method for both carbon dioxide and nitrogen before each experiment. The concentrations used for calibration for both gases were proportional to the expected intensity of the two gases on the permeate side of the membrane, *i.e.* within a 0-0.001 atm partial pressure range.

The volumetric flux, J_{CO2} (ml min^{-1} cm^{-2}) and molar permeance $\mathcal{P}$ (mol m^{-2} s^{-1} Pa^{-1}) of carbon dioxide were calculated based on equations 4.1 and 4.2, respectively, as described in chapter 1, section 1.2.3:

$$J_{CO_2} = \frac{x_{CO_2}\,\dot{V}}{A_S} \qquad \text{(Eq. 4.5)}$$

$$\mathcal{P} = \frac{x_{CO_2}\,\dot{V}}{A_S\,(P_f - P_p)} \qquad \text{(Eq. 4.6)}$$

where x_{CO_2} is the mole fraction of carbon dioxide in the permeate-side outlet, $\dot{V}$ is permeate volumetric flow rate (ml min^{-1}), A_s is the active surface area of the membrane (cm^2) and (P_f – P_p) is the membrane partial pressure driving force expressed as the difference in pCO_2 between the feed-side and the permeate-side inlet (nominal P= 1 atm). Active surface area refers to an approximation of the molten salt-gas interface area used for dual-phase membranes with a nominally electrically insulating support. For dual-phase membranes with an oxygen-ion conducting support, active surface area refers to the entire surface area of the support. Detail is given in section 4.3.2.

4.2.6 Characterisation

SEM imaging

The micro-structure of the prepared membranes was analysed by scanning electron spectroscopy (SEM) and the distribution of carbonate within the ceramic supports was identified by EDX in connection to SEM.

3D cross-sectional X-ray micro-CT tomography

The controlled and un-controlled DPHFMs were also analysed by X-ray micro-computed tomography (X-ray micro-CT), using a Zeiss Xradia 520 Versa (Carl Zeiss X-ray Microscopy, Pleasanton, USA) at the Electrochemical Innovation Lab at

University College London (UCL) by Dr Josh Baily, Dr Paul Shearing, Proffesor Dan J L Brett [246]. The DPHFMs were analysed using a 4x magnification and a binning of 1. For the controlled DPHFM, the 4x magnification, along with a geometrical magnification, resulted in a voxel dimension of 1.27 µm, using 50 kV and 4 W for the X-ray beam voltage and power, respectively. A low-energy filter ('LE2') was used to remove the lower energy non-penetrating X-rays, resulting in beam hardening and consequentially, greater X-ray penetration in the solid phase of the controlled DPHFM. A total of 1,601 projections were acquired for the controlled DPHFM, at an exposure time of 45s each. Through the denser region of the controlled DPHFM, an average of 5,000 counts *per* pixel were collected, to ensure a sufficient noise to signal ratio. Similarly, for the uncontrolled DPHFM, the same magnefications, binning, voltage and power, gave a voxel dimension of 1.49 µm. A total of 1,501 projections were acquired for the uncontrolled DPHFM, at an exposure time of 11s each, with an average of 5,000 counts *per* pixel for the denser region. The low-energy filter that was chosen for the uncontrolled DPHFMs ('LE1'), attenuates the beam less than the 'LE2' filter used for the controlled DPHFMs, requiring less exposure time.

The acquired data were processed in Avizo (Avizo 2019.2, Thermo Fischer Scientific, Waltham, USA) at the Electrochemical Innovation Lab at UCL. Using Avizo, the area of the X-ray micro-CT images corresponding to the volume of air inside the hollow fibre supports, *i.e.* porosity and empty space in lumen, was represented by the colour black. The contrast within the solid phase of the hollow-fibre support was also maximised using the Avizo software. To confirm that the controlled or uncontrolled distribution of the carbonate phase inside the hollow-fibre supports was homogeneous across their length, 2-D ortho-slices were recorded at random positions along the length of the DPHFMs. 3-D volume renderings of the controlled and uncontrolled DPHFMs were also produced, after the selective removal of data, which resulted in better representation of the porous network inside the DPFHMs.

4.3 Results and discussion

4.3.1 Permeation performance of model dual-phase crucible membranes with a dense nominally electrically insulating support

The effect of molten carbonate thickness and temperature on carbon dioxide flux were investigated with the use of model dual-phase crucible membranes; a system where the molten carbonate thickness, tortuosity and active surface area for carbon dioxide exchange could be controlled (Figure 4.5a). Aiming to study the permeation of carbon dioxide through the molten phase only, an electrically insulating material, Al_2O_3, was used as the ceramic support. A total of 745 permeation pathlengths of a truncated cone shape with D= 160 μm and d= 75 μm (where D is the outer-surface diameter, and d is the inner-surface diameter) provided a low-tortuosity model membrane with a fixed feed-side and permeate-side active surface area (Figure 4.5a). Different quantities of carbonate were then added in the model crucibles to produce membranes with a 250, 500, 750 and 1000 μm molten carbonate thickness on top of the drilled channels (Figure 4.5a). The overall membrane thickness of the model dual-phase crucible membranes was 0.69, 1.13, 1.19 and 1.44 mm for the 250, 500, 750 and 1000 μm molten carbonate layers on top of the 440 μm long drilled channels, respectively. Hereafter, the model-crucible membranes will be referred to as 250, 500, 750 and 1000 μm, emphasising the controllable molten carbonate layer created by the respective carbonate loading used. The active feed-side surface area was considered as the molten carbonate surface area inside the model crucible covering the entire area of the model crucible support, equal to 3.8 cm^2 (2.2 cm ID). The active permeate-side surface was considered as the sum of the surface area of the truncated cone ends on the permeate side of the support, equal to 0.15 cm^2 (Figure 4.5a). The active permeate-side surface area was further used to calculate flux through model dual-phase crucible membranes as it is considered the main surface-exchange resistance that limits flux through various types of membranes, e.g. ion transport membranes for oxygen transport [118,119]. As mentioned in section 1.2.4, carbon dioxide permeation through a dual-phase membrane is governed by surface exchange reactions at the membrane surfaces, *i.e.* physical sorption and chemical reactions at the feed and permeate-side surface [119]. Even though the carbonate formation reaction on the feed side of the membrane (forward reaction Figure 2.2) and the carbonate release reaction on the permeate side of the membrane (reverse reaction Figure 2.2) are the forward and reverse of the same reaction, the gas atmosphere on the feed and

permeate side of the membrane is different. This reacts differently with the surface as the large pCO_2 in the feed stream drives the carbonate formation reaction and as a result the feed-side surface can become saturated with carbonate. In contrast, the permeate-side surface is exposed to a low pCO_2 allowing the release of carbon dioxide in the permeate-side stream whilst being the rate-limiting step for carbon dioxide flux through the membrane.

With the increase of operating temperature, carbon dioxide flux through model crucible membranes increased as can be shown in Figure 4.5b. Furthermore, carbon dioxide flux increased with the decrease in molten carbonate thickness, for all operating temperatures investigated (Figure 4.5b). The effect of molten carbonate thickness in flux is more apparent between 650 and 750 °C, where a clear increase in carbon dioxide flux can be observed with the decrease in molten carbonate thickness. Between 750 and 800 °C, the rate of increase in the carbon dioxide flux was significantly lower than the rate of increase observed when the temperature was increased from 700 to 750 °C. For the model crucible membrane with 1000 μm molten carbonate thickness, the flux was noticeably lower than the carbon dioxide flux of the 250, 500 and 750 μm at all investigated temperatures. The effect of temperature on carbon dioxide flux was further modelled through nonlinear regression using a sigmoidal function. The experimentally determined fluxes, for each molten carbonate thickness were fitted through the sigmoidal curve based on the following equation:

$$J_{CO_2} = \frac{J_{CO_2\_min} - J_{CO_2\_max}}{1 + e^{((T - T_{50})/\Delta T)}} + J_{CO_2\_max} \qquad \text{(Eq. 4.7)}$$

where J_{CO2_min} and J_{CO2_max} are the lowest and highest fluxes that can be achieved in the temperature range (450 – 1200 °C); based on the experimental flux data, T_{50} is the temperature at which the carbon dioxide flux would be 50% of the maximum flux, ΔT is a model coefficient describing the behaviour of the slope of the process, and T is the operating temperature variable. J_{CO2_min}, J_{CO2_max}, T_{50} and ΔT are all model parameters that were derived from fitting the model to the experimental flux data using a nonlinear solver for each molten carbonate thickness. The coefficient of determination (R^2) for the models confirmed that the sigmoidal curve fitted the data well, with an R^2 value higher than 0.97 for all the fitted curves. More specifically, the R^2 value was 0.995 for the 250 μm membrane, 0.974 for the 500 μm membrane, 0.996 for the 750 μm

membrane and 0.991 for the 1000 μm membrane. The lowest R^2 value of 0.974, for the 500 μm membrane, was attributed to the anomalous data point for this membrane at 800 °C. In order to correct for the anomalous data point at that temperature, the model parameters for the 250, 750 and 1000 μm membranes (identified above) were fitted against each molten carbonate thickness and the derived exponential and polynomial equations were then used to identify the corrected parameters for the 500 μm membrane. The interpolated corrected parameters for the 500 μm were then applied on Eq. 4.7 in order to force the highest achieved flux for the membrane at 1200 °C in-between the highest carbon dioxide flux for the 250 and 750 μm membranes.

The sigmoidal curve function governing the behaviour of carbon dioxide flux with the increase in temperature in the 450 – 1200 °C temperature range (Figure 4.5b) suggested that carbon dioxide flux through molten carbonate can be identified in two main temperature regions:

1. Low-temperature region (450 – 750 °C): increasing rate of flux increase with the increase in temperature; surface exchange on permeate-side surface is considered as the dominant rate-limiting step. Process is considered to be temperature activated.
2. High-temperature region (750 – 1200 °C): decreasing rate of flux increase with the increase in temperature compared to the low-temperature region. Bulk diffusion becomes the rate-limiting step, as diffusion is weakly activated by temperature.

The interpretation of the flux *versus* temperature model for model-crucible membranes, suggested the membranes were operating in a predominately surface-exchange limited regime during the high-temperature permeation experiments (500–750 °C). At 600 °C, carbon dioxide flux is not improved with the decrease in thickness below 750 μm. This observation comes in agreement with studies conducted on MIEC-supported dual-membranes by Anderson *et al.* [142], where a critical thickness of 750 μm was determined. In general, for the low-temperature region (450 – 600 °C), where surface exchange was considered as the rate-limiting step, the effect of thickness was not as evident on carbon dioxide flux compared to its effect in the high-temperature region (650 – 1200 °C). This behaviour can be observed more clearly in Figure 4.5c, where the experimental carbon dioxide flux has been normalised ($(J_{CO2}- J_{CO2\_0})/J_{CO2\_0}$) over the initial experimental carbon dioxide flux value at 500 °C.

The normalised flux over temperature, showed that the percentage increase in flux with the increase in temperature reached a maximum at 750 °C for all membranes, above which there was no increase observed in normalised flux for different molten carbonate thicknesses (Figure 4.5c).

Finally, Figure 4.5d, shows the two different activation energies (E_a) for the low-temperature (I) and high-temperature (II) region, reflecting the shift in the rate-limiting step in the separation process. The temperature transition step between the two E_a was considered to be between 700 and 750 °C. Above 750 °C bulk diffusion was considered as the rate-limiting step for the membrane process, which comes in agreement with the range for the bulk-diffusion-limited high-temperature region (750 – 1200 °C), identified through the sigmoidal curve function model (Figure 4.5b). The presence of two separate E_a has also been reported by Zhu *et al.* [247] and Li *et al.* [248] for oxygen permeation through MIEC membranes, with a transition temperature between 800 and 850 °C. For model dual-phase crucible membranes the E_a in the bulk diffusion limited region, is lower than the E_a in the surface-exchange-limited region for all molten carbonate thicknesses investigated, as can be seen in Table 4.1. The E_a in the bulk-diffusion region was calculated using the experimental data for carbon dioxide flux at 800 and 850 °C (filled symbols in Figure 4.5d (I)), and the carbon dioxide flux data derived from the flux *versus* temperature model described by Eq. 4.7 at 900 °C (open symbols in Figure 4.5d (II)). The higher E_a in the surface-exchange-limited region is indicative of the higher thermal activation nature of surface-exchange reactions compared to bulk diffusion, as was discussed in chapter 1, section 1.2.5. Overall, the E_a of model crucible dual-phase membranes in the bulk-diffusion (highest value 11 $\pm$ 3 kJ mol^{-1}) and in the surface-exchange-limited region (highest value 76 $\pm$ 5 kJ mol^{-1}), shown in Table 4.1, are lower than the E_a for dual-phase membranes in literature with oxygen-ion conducting and MIEC supports, reported to be between 70 and 113 kJ mol^{-1} [130,131,133,142]. The lower E_a of model crucible dual-phase membranes with nominally electrically insulating supports, is attributed to the separation taking place through the molten salt phase alone, as there is no reaction taking place between the nominally electrically insulating ceramic support, the molten carbonate and the carbon dioxide of the gaseous phase [123].

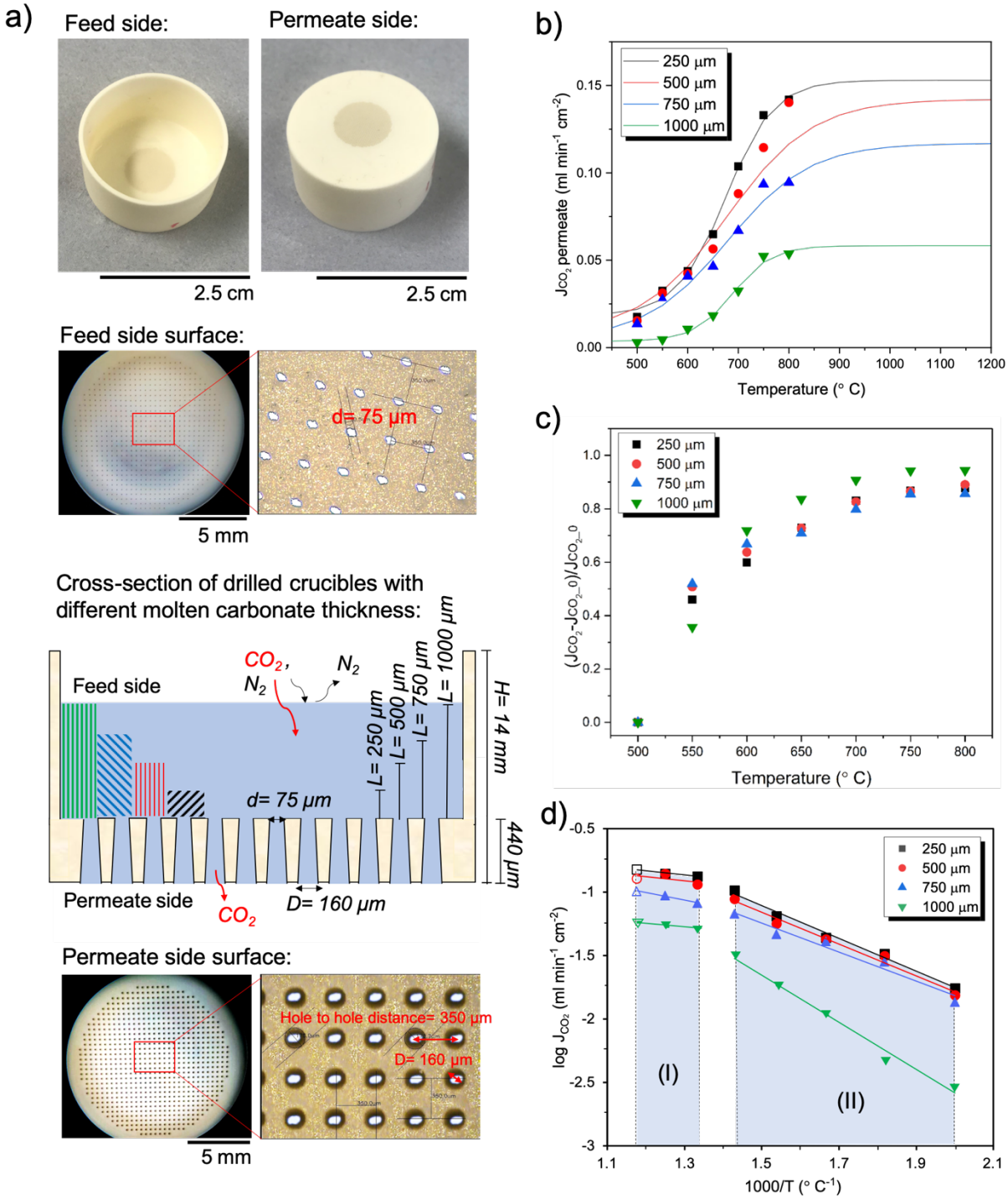

Figure 4.5. Impact of molten carbonate thickness on carbon dioxide flux in model dual-phase crucible membranes. a) Model dual-phase crucible membrane schematic and digital microscopy images showing the number and diameter of feed and permeate side pores and the various molten carbonate thicknesses, 250, 500, 750 and 1000 µm on top of the 440 µm drilled channels; b) effect of molten carbonate thickness on carbon dioxide flux in model dual-phase crucible membranes where the experimentally determined fluxes (graph data points) for membranes with a carbonate layer of 250, 500, 750 and 1000 µm were fitted through nonlinear regression to their respective sigmoidal curve, c) increase in the experimentally determined flux over the investigated temperature range (500-800 ºC), and d) Arrhenius plot for the bulk diffusion (I) and surface-exchange (II) limited temperature region.

Table 4.1: Activation energies (E_a) corresponding to the bulk-diffusion-limited region (I) and the surface-exchange-limited temperature region (II) for model dual-phase crucible membranes with a molten carbonate thickness of 250, 500, 750 and 1000 μm. The E_a values were calculated based on the slope values of Figure 4.5d following the Arrhenius equation [48].

Molten carbonate thickness (μm)	E_a for the bulk-diffusion-limited region (I) (kJ mol $^{-1}$)	E_a for the surface-exchange-limited region (II) (kJ mol $^{-1}$)
250	5 ± 1	53 ± 6
500	11 ± 3	51 ± 7
750	6 ± 1	46 ± 10
1000	6 ± 2	76 ± 5

Dual-phase crucible membranes have allowed precise control over molten carbonate thickness and available active area for carbon dioxide desorption, while offering low-tortuosity permeation path lengths. Low tortuosity path lengths have been proven to increase membrane flux, as the ratio of open-end pores on both sides of the membrane over dead-end pores (not permitting carbon dioxide permeation through the membrane thickness), as well as the intra- and interconnectivity of membrane pores, is increased [111]. Supports with a highly interconnected 3D porous network have been previously developed but the development of supports with straight pores, at the extend this was achieved with the crucible supports, has not previously been reported. Moreover, the performance of dual-phase crucible membranes with a nominally electrically insulating support indicates that increasing the available active area for carbon dioxide desorption while the membrane operates in a surface-exchange-limited region (500 – 750 °C), will result in higher carbon dioxide flux. However, the crucible supports do not allow the tailoring of the permeate-side surface area available for carbon dioxide desorption, due to the nature of the laser-drilling process. To investigate the effect of available surface area on flux, a membrane system which allows the upscale of dual-phase membranes; the controlled infiltrated DPHFMs developed in chapter 3, were used. The asymmetric structure of the hollow fibres supports allows control over carbonate distribution inside the supports and as a result, the tailoring of the lumen-side surface area that is available for carbon dioxide exchange. In previous studies, where the distribution of carbonate inside the hollow fibre supports was not controlled, the control of the lumen-side surface area was not possible, decreasing the possibly achieved lumen-side surface area available for carbon dioxide desorption. Hollow-fibre

supports were also chosen in this study for their upscale potential as they have a high area-to-volume ratio (7000 m^2 m^{-3}, compared to <100 m^2 m^{-3} for traditional packed and plate contractors), are easily bundled into modules, and provide low mass transfer resistances (100 – 1000 higher mass transfer rates compared to traditional packed and plate column contactors) [204–206,208,244].

4.3.2 Permeation performance of DPHFMs with a controlled distribution of carbonate

i. Al_2O_3-supported DPHFMs with a controlled distribution of carbonate

In order to test the impact of the preparation method for DPHFMs developed in chapter 3, Al_2O_3 hollow fibre supports with 100 vol% of carbonate in their packed-pore network and purposefully-hindered DPHFMs; where both the packed-pore network and the micro-channels were infiltrated with carbonate (*i.e.* replicating the preparation of DPHFMs previously published in literature), were tested for their performance in high-temperature carbon-dioxide separation. The membranes with 100 vol% of carbonate in their packed-pore network are refered to as DPHFMs with a controlled distribution of carbonate, and the purposefully-hindered DPHFMs are refered to as DPHFMs with an uncontrolled distribution of carbonate, hereafter. The distribution of molten carbonate inside the controlled DPHFM supports was determined *via* SEM image analysis (Figure 4.6b: sponge-like layer). The micro-channels in the case of controlled distribution DPHFMs remained devoid of carbonate as they were still clearly visible at room temperature. Of course, the carbonate is expected to migrate and spread when molten (>400 °C). However, due to the smaller pore size and higher capillary forces developed in the packed-pore network compared to the micro-channels, it is expected that the carbonate will remain confined in the packed-pore network. The molten carbonate distribution inside the uncontrolled DPHFMs was also determined *via* SEM image analysis and showed that the carbonate clearly infiltrated both the micro-channels and the packed-pore network at room temperature (Figure 4.6c: cross section). EDX mapping of 400 x 300 μm^2 cross-sections of the DPHFMs (both micro-channels and packed-pore network were included), showed Al and K in a ratio of 11 for controlled distribution DPHFMs, which was higher than the 0.95 ratio in the uncontrolled distribution DPHFMs (Figure 4.6b: EDX cross section and Figure 4.6c: EDX cross section). The low Al/K ratio for the controlled DPHFMs verified that the amount of carbonate used in the case of the controlled distribution DPHFMs was a lot less than in the case of the uncontrolled distribution DPHFMs, confirming that the

micro-channels were not infiltrated with carbonate. Moreover, in the case of controlled distribution DPHFMs, a higher concentration of Na (purple) and K (green) was observed in the sponge-like layer of the packed-pore network (Figure 4.6b: EDX cross section).

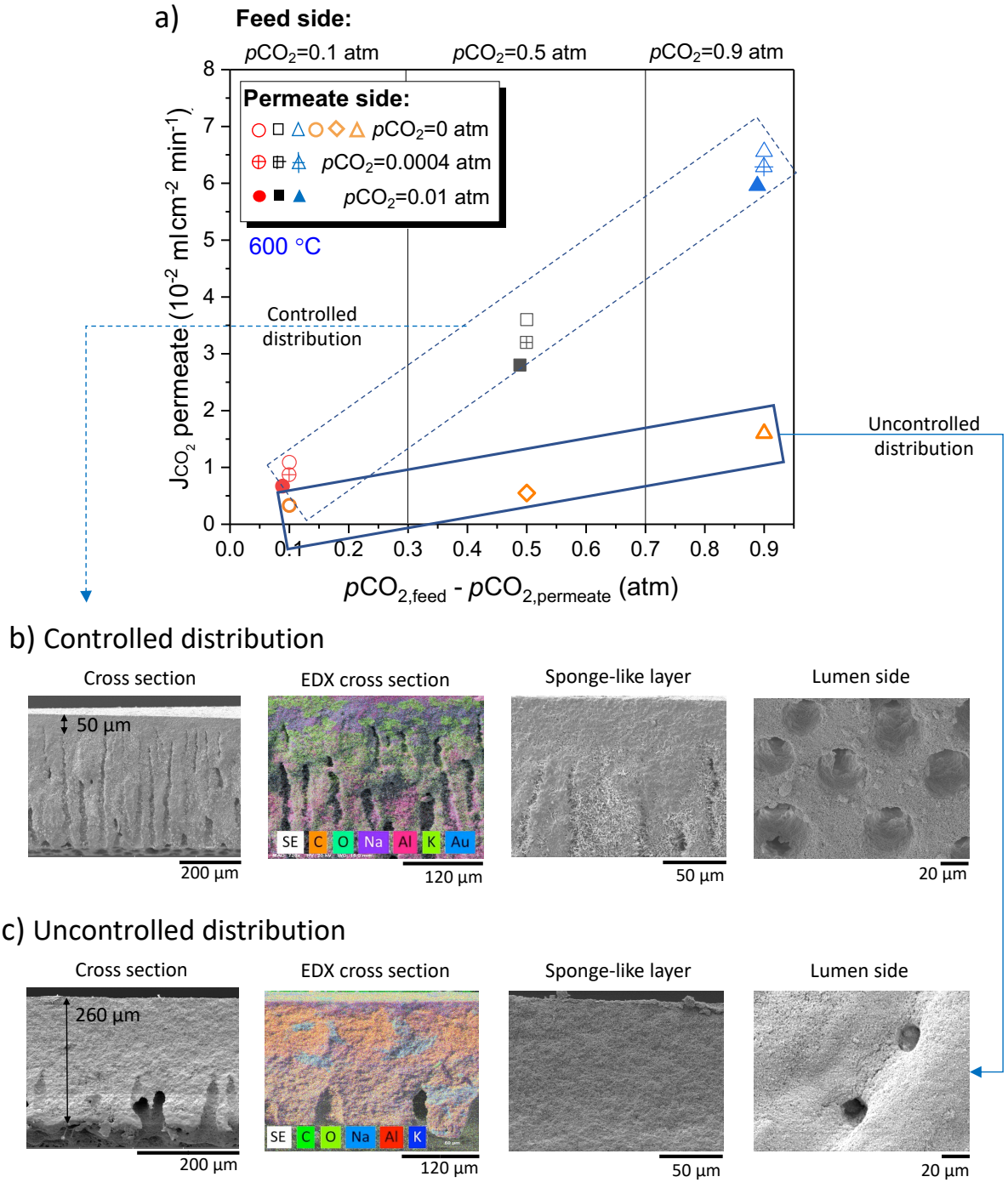

Figure 4.6: Effect of molten carbonate loading on carbon dioxide flux in Al_2O_3-supported DPHFMs. a) Effect of partial pressure difference on the carbon dioxide flux through Al_2O_3-supported DPHFMs at T= 600 °C. b) SEM images of a controlled distribution DPHFM where the minimum carbonate thickness is 50 µm. The points in the graph corresponding to controlled distribution DPHFMs are enclosed inside a blue dashed rectangle area and are depicted by the colours red, black and blue. c) SEM images of the uncontrolled distribution DPHFMs, where the carbonate thickness is 260 µm. The points in the graph corresponding to

uncontrolled distribution DPHFMs are enclosed inside a blue solid rectangle area and are depicted by the colour orange.

The carbon dioxide flux of controlled and uncontrolled DPHFMs, was investigated for a range of driving forces at 600 °C, by varying pCO_2 on the feed and permeate side of the DPHFMs. The operating temperature was chosen within the surface-exchange-limited region for Al_2O_3-supported dual-phase membranes, in order to investigate the impact of structural changes deriving from the prepartion method of the DPHFMs. Carbon dioxide flux at 600 °C for controlled and uncontrolled DPHFMs is shown in Figure 4.6a and was calculated based on the active surface area for carbon dioxide sorption, on the shell side of the membrane. This allowed the evaluation of the effect of the permeate-side surface area on carbon dioxide flux. The surface area for carbon dioxide sorption (shell side) for both membranes was considered to be the lateral surface area of a cylinder (r=0.12 cm, l = 4 cm), ~1.8 cm^2, accounting for an external surface porosity of 56%. The active surface area, *i.e.* part of the surface that contributes to permeation, was determined by analysing the shell-side surface of Al_2O_3 by ImageJ software (~10 samples). To understand the flux-driving force relationship, a pCO_2 of 0.1, 0.5 or 0.9 atm in nitrogen was applied on the feed side and a pCO_2 of either 0.0004, 0.01 or 0 atm in argon was applied on the permeate side of the membrane. Carbon dioxide flux increased linearly with the increase in pCO_2, both with the increase in feed-side pCO_2 while the permeate-side pCO_2 remained constant, and with the decrease in permeate-side pCO_2 while feed-side pCO_2 remained constant. The carbon dioxide flux of both Al_2O_3-supported DPHFMs prepared, increased linearly with the difference in pCO_2 between the feed and permeate side ($pCO_{2,feed} - pCO_{2,permeate}$) of the membrane, acting as the driving force for separation [38]. Based on mathematical models developed in the literature for dual-phase membranes with an oxygen-ion-conducting support, carbon dioxide flux was found to increase linearly with the natural logarithm of pCO_2 in the feed over the pCO_2 in the permeate side of the membrane ($\ln(pCO_{2,feed}/pCO_{2,permeate})$) instead [111,144,205,206].

By comparing the carbon dioxide flux for all driving forces investigated it was also found that the uncontrolled DPHFMs achieved a lower carbon dioxide flux than the controlled distribution DPHFMs. For the most commonly used driving force in the dual-phase membrane literature (feed-side inlet: pCO_2 = 0.5 atm in nitrogen, permeate-side inlet: pure argon), the carbon dioxide flux for the controlled distribution DPHFM (flux: 0.036

ml min^{-1} cm^{-2}, permeance: 1.65×10^{-9} mol m^{-2} s^{-1} Pa^{-1}) was 8 times higher than the uncontrolled distribution DPHFM (flux: 0.004 ml min^{-1} cm^{-2}, permeance: 1.83×10^{-10} mol m^{-2} s^{-1} Pa^{-1}). Even when the driving force applied on the uncontrolled DPHFM was increased to 0.9 atm, the carbon dioxide flux achieved was only comparable to the fluxes achieved by the controlled distribution DPHFMs when exposed to a driving force of 0.1 atm. In both controlled and uncontrolled distribution DPHFMs, the molten-carbonate thickness was below the determined critical thickness for model dual-phase crucible membranes with an Al_2O_3 support (750 μm), so no further increase in flux should be observed at 600 °C [142]. The noticeable improvement in carbon dioxide flux for the controlled DPHFMs, however, implies that the controlled preparation method has resulted in structural changes due to the un-infiltrated micro-channels; facilitating surface exchange on the permeate, lumen side, surface (permeation direction: shell to lumen).

In order to quantify the increase in permeate side surface area offered by the un-infiltrated micro-channels, the permeate-side surface areas available for carbon dioxide desorption were calculated using ImageJ analysis software for both controlled and uncontrolled DPHFMs. The results were also confirmed by X-ray micro-CT, as can be seen in Figure 4.7. The surface area for carbon dioxide desorption for the uncontrolled DPHFMs was considered as the inner lateral surface of a cylinder (Eq. 4.1, r = 0.08 cm, l = 4 cm), ~2.1 cm^2, as the micro-channels were considered to be fully infiltrated with carbonate (very few remaining compared to the open micro-channels in the controlled-infiltrated DPHFMs) creating the projection of a flat cylindrical surface (Figure 4.7). On the other hand, in order to estimate the surface area for carbon dioxide desorption in the controlled distribution DPHFMs, as shown in Figure 4.7a, the lumen-side surface area of the un-infiltrated micro-channels must also be considered. First, the average micro-channel mouth diameter and the average length of the micro-channels (Figure 4.6b: lumen side and Figure 4.6b: cross section, respectively), was estimated using ImageJ analysis software. This enabled calculation of the surface area of a single un-infiltrated micro-channel (1.22×10^{-4} cm^2, for r = 10 μm and l = 380 μm). It was also determined (Figure 4.6b: lumen side), that the number of micro-channels on the lumen side was ~38,000 per cm^2 resulting in a total micro-channel surface area for the 4 cm long hollow fibre, equal to 8.19 cm^2. The surface area of the micro-channels was then added to the inner lateral surface area of a cylinder (~2.1 cm^2) and the total surface area of the mouths of the micro-channels,

0.12 cm^2 (assuming surface area of a circle), was finally subtracted from the previous sum, as described in section 4.1 and Eq. 4.4. The total desorption area for the controlled DPHFMs was ~10 cm^2, an order of magnitude higher compared to the uncontrolled DPHFMs. Since only the desorption surface on the permeate-side of the controlled DPHFMs was increased through the infiltration method, the 8-fold improvement in flux was attributed to the structural change of the membrane surface available for desorption. The surface porosity was not accounted for in the calculation of the lumen-side surface area as there is a gradient in pore size diameter along the length of the micro-channels which makes the accurate calculation of surface porosity on the lumen side quite complex. Considering a minimum porosity value of 65% for the lumen surface (~10 samples), the resulting active area for desorption in the controlled DPHFMs is still ~5 times higher than the active surface area for desorption in the uncontrolled DPHFMs.

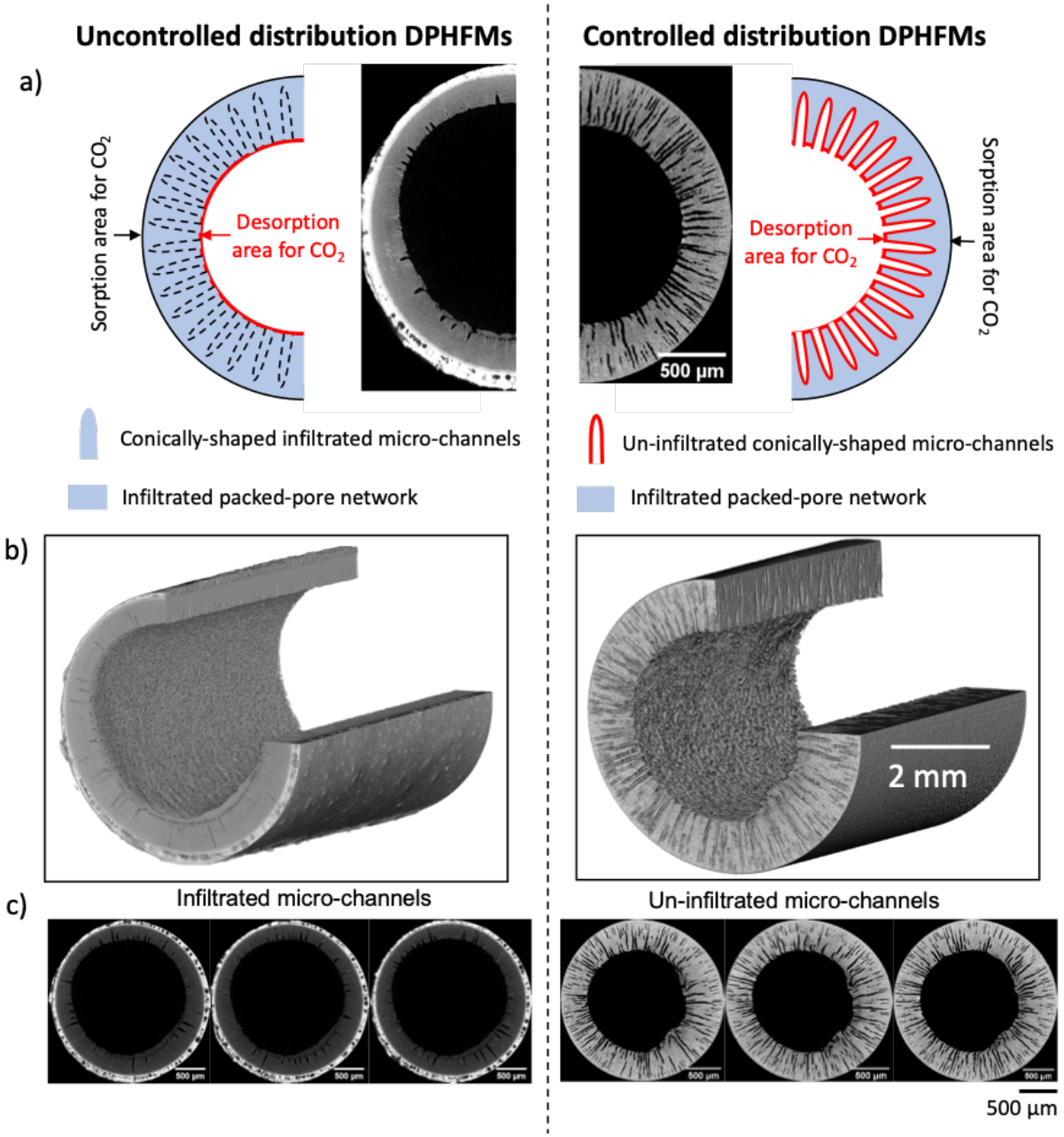

Figure 4.7: Available surface area for carbon dioxide sorption and desorption in uncontrolled and controlled distribution DPHFMs. a) X-ray micro-CT cross-section of uncontrolled and controlled distribution DPHFMs, b) 3D cross-sectional X-ray micro-CT of the two samples, and c) cross-sectional X-ray micro-CT images across the length of the 3D cross-sectional X-ray micro-CT of uncontrolled and controlled DPHFMs.

As Al_2O_3-supported DPHFMs with a controlled distribution of carbonate achieved a higher carbon dioxide flux than the uncontrolled distribution DPHFMs, controlled DPHFMs were further considered for determining the dominant surface resistance in carbon dioxide surface exchange. The open-micro-channel lumen-side surface, ~6.5 cm^2 (corrected for 65% porosity, following a conservative approach) was initially used as the surface area for carbon dioxide desorption (permeation direction from the shell to the lumen side), and the shell-side lateral surface area of the cylinder, ~1.8 cm^2 (corrected for 56% porosity) was used as the surface area for carbon dioxide

sorption (Figure 4.8: red symbols). To calculate experimental flux values, the active permeate-side surface area was used, depending on the direction of permeation. A pCO_2 of 0.5 atm in nitrogen was initially introduced on the shell side of the membrane, and pure argon (pCO_2 of 0 atm) was introduced on the lumen side. Carbon dioxide flux increased with the increase in temperature, following the sigmoidal curve model (R^2=0.997) derived from model dual-phase crucible membranes, in the examined temperature range (600 – 900 °C). By switching the permeate and feed-side gases, the open-micro-channel lumen-side surface was instead used as the surface area for carbon dioxide sorption (permeation direction from the lumen to the shell side), and the shell-side lateral surface area of the cylinder was used as the surface area for carbon dioxide desorption (Figure 4.8: blue symbols). As with the previous direction of permeation, the carbon dioxide flux followed a sigmoidal curve model (R^2=0.999) with the increase in temperature. At all investigated temperatures, the use of the lumen side surface (~6.5 cm^2) as the permeate-side surface for carbon dioxide desorption, resulted in ~4 times higher carbon dioxide flux, compared to when the shell-side surface (~1.8 cm^2) was used as the permeate side surface area for desorption. If the feed and permeate side areas had the same influence on flux, the resulting flux would be the same for every direction of permeation. Since the flux was higher when the direction of permeation was from the shell towards the lumen side surface of the DPHFMs, the permeate side surface was confirmed as the dominant surface resistance for carbon dioxide permeation.

When the lumen side surface was used as the surface area for carbon dioxide desorption (red symbols in Figure 4.8), carbon dioxide flux was found to be approximately the same at 600, 700 and 800 °C despite the increase in temperature. Similarly, for DPHFMs where the permeation direction is from the lumen towards the shell side surface (blue symbols in Figure 4.8) carbon dioxide flux does not increase with the increase in temperature from 600 to 700 °C. The flux versus temperature model for the dual-phase crucible membranes (investigated in section 4.3.1) has been found to follow a sigmoidal curve function where surface-exchange is the rate-limiting step between 450 and 750 °C and bulk-diffusion is the rate-limiting step between 750 and 1200 °C (Figure 4.5). However, in real membranes like DPHFMs the complexity of the porous network and the difficulty to define the effective permeation length, due to membrane tortuosity, results in difficulties in defining rate-determining-step regions. Even though the DPHFMs have an overall thickness of ~450 μm and a sponge-like

layer thickness of ~50 µm (both below the critical length identified for the dual-phase crucible membranes L_c =750 µm), the range of path lengths carbonate species have to travel to reach the permeate side of the membrane, *i.e.* the effective membrane thickness, is large, as some of the path lengths are quite long due to high membrane tortuosity. Long permeation pathways in high tortuous DPHFMs could result in bulk diffusion being the dominant permeation resistance for carbon dioxide permeation at lower temperatures, requiring higher temperatures (above 700 or 800 °C) to transition to the surface-exchange-limited region. Without being able to define the effective membrane thickness however, the effect of temperature on flux through DPHFMs cannot be accurately determined.

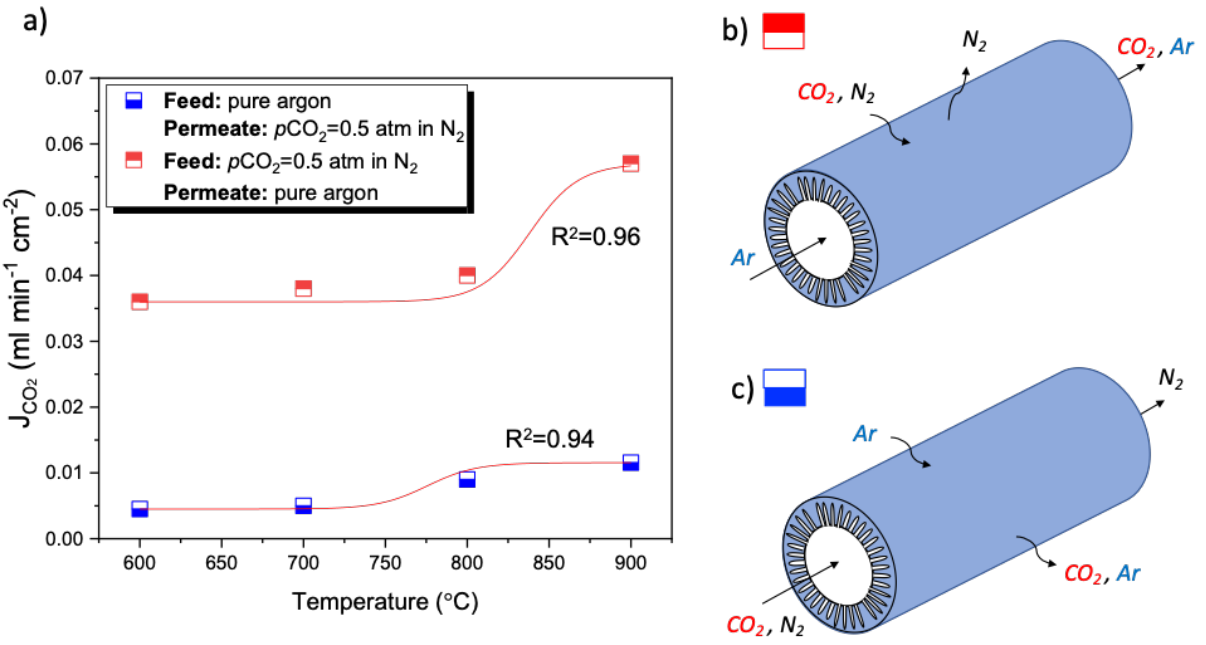

Figure 4.8: Impact of permeate side surface area for carbon dioxide sorption and desorption on carbon dioxide flux through a controlled DPHFM. The red symbols represent a DPHFM where the feed-side inlet of pCO_2=0.5 atm in nitrogen is supplied on the outer surface of the DPHFM and the pure argon sweep gas is supplied on the open-micro-channel lumen side of the DPHFM. The blue symbols represent a membrane where the feed and lumen-side inlet gases have been switched to argon on the shell side, and pCO_2=0.5 atm in nitrogen on the open-micro-channel lumen side of the DPHFM.

As was mentioned in chapter 2, section 2.1.6, the carbon flux of dual-phase ceramic molten-salt membranes using a nominally electrically insulating support is expected to be lower than the flux of dual-phase ceramic molten-salt membranes with an oxygen-ion and/or electron-conducting support. However, by controlling the distribution of carbonate inside the ceramic support, the prepared Al_2O_3-supported DPHFMs benefited from an increased active surface area for carbon dioxide desorption. This resulted in increased carbon dioxide flux, outperforming dual-phase membranes with

oxygen-ion-conducting supports. The carbon dioxide flux of the Al_2O_3-supported controlled distribution DPHFMs (0.036 ml min cm^{-2}) was higher than the reported flux for a YSZ-supported DPHFM (0.028 ml min cm^{-2}) at 600 °C in literature with a thickness of 500 μm [106]. The flux reported for the Al_2O_3-supported controlled distribution DPHFMs was also higher than the achieved flux of a disc shaped BYS-supported dual-phase membrane (0.025 ml min cm^{-2}) with a thickness of 50 μm (pore surface modified with γ-Al_2O_3), at 600 °C [133].

ii. 3% YSZ-supported DPHFMs with a controlled distribution of carbonate

The effect of carbonate distribution inside an asymmetric hollow-fibre support was also investigated using 3% YSZ; an oxygen-ion-conducting support, that contributes to the permeation mechanism [111]. To establish the relationship between carbon dioxide driving force and resulting membrane flux, the range of applied driving forces previously investigated for Al_2O_3-supported DPHFMs were also applied in 3% YSZ-supported controlled DPHFMs. The carbon dioxide flux achieved by 3% YSZ-supported DPHFMs with a controlled distribution of carbonate at 600 °C is shown in Figure 4.9. The permeate-side surface area for controlled 3% YSZ-supported DPHFMs was calculated based on the methodology used for the controlled Al_2O_3-supported DPHFMs. For the controlled 3% YSZ-supported DPHFMs, the available surface area for desorption is ~13 cm^2 which is 6.5 times higher than the surface area for carbon dioxide sorption (~2 cm^2, for r = 0.08 cm and l = 4 cm). In oxygen-ion-conducting supports, both support and carbonate participate in the permeation mechanism. It is therefore important to note that the entire permeate-side surface area is the active surface area for carbon dioxide desorption; without accounting for surface porosity and was used to calculate experimental flux. As predicted by the flux equation for carbon dioxide through an oxygen-ion-conducting dual-phase membrane (chapter 2, section 2.1.2, Eq. 2.9) the permeating carbon dioxide flux increased linearly with the increase in the natural logarithm of the feed to permeate ratio of pCO_2 ($\ln(pCO_{2,feed}/pCO_{2,permeate})$ (Figure 4.9) [111,144,205,206]. Carbon dioxide flux through controlled 3% YSZ-supported DPHFMs was higher than the flux of controlled Al_2O_3-supported DPHFMs for all driving forces investigated. More specifically, when a pCO_2=0.5 atm in nitrogen was used in the feed side and argon

was used in the permeate side, carbon dioxide flux for the 3% YSZ-supported DPHFMs was 2.5 times higher than the Al_2O_3-supported DPHFMs.

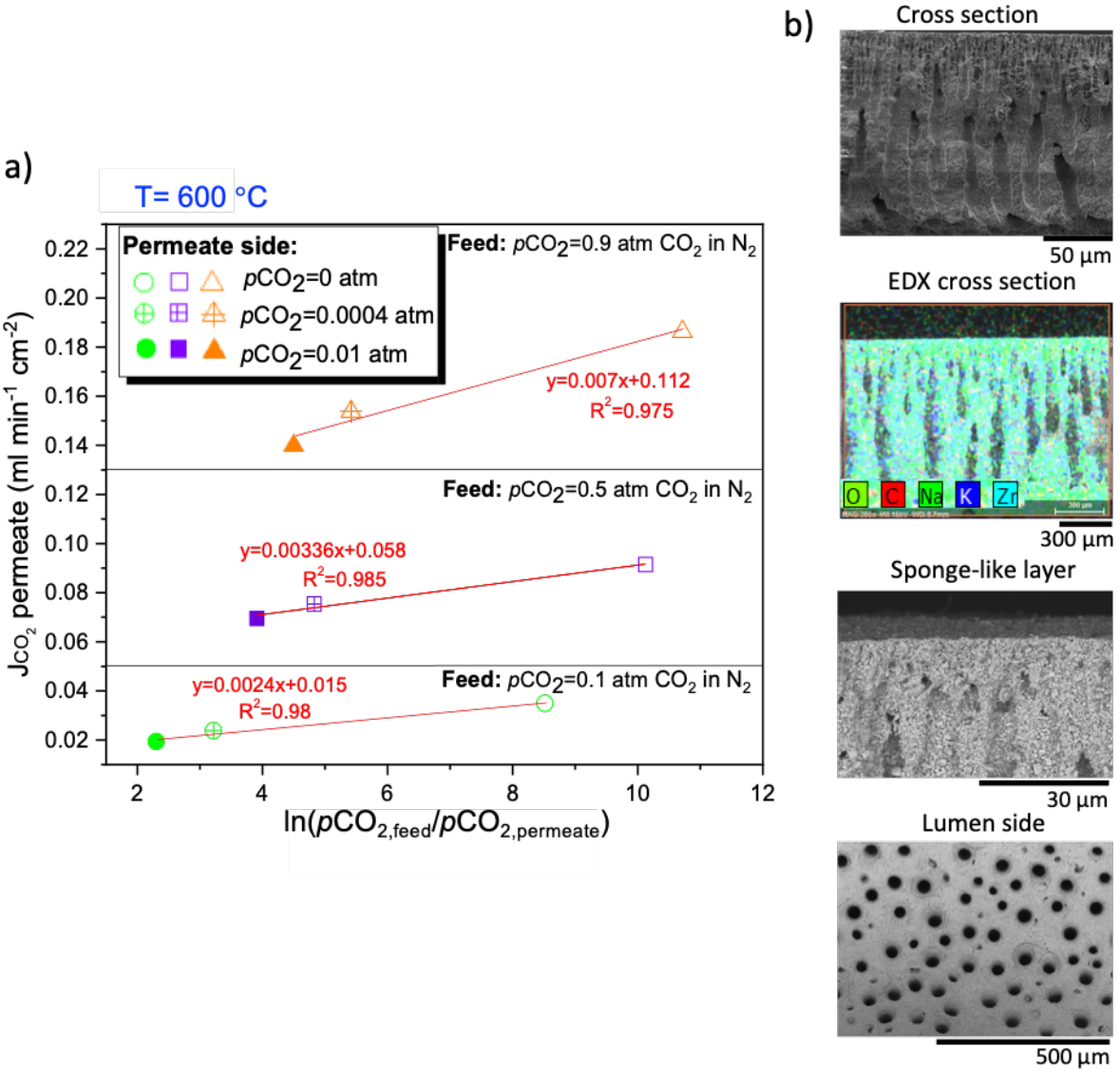

Figure 4.9: Impact of molten carbonate distribution on carbon dioxide flux in YSZ supported DPHFMs. a) Effect of the natural logarithm of the feed to permeate pCO_2 ratio on experimentally determined carbon dioxide flux through a controlled 3% YSZ-supported DPHFM at T= 600 °C. b) SEM images of a controlled 3% YSZ-supported DPHFM where the minimum carbonate thickness is 10 µm.

The controlled YSZ-supported DPHFMs in this work, were compared to DPHFMs in literature, using a pCO_2 of 0.5 atm in nitrogen on the feed side of the membrane and argon on the permeate side of the membrane. The flux through controlled 3% YSZ-supported DPHFMs (0.09 ml min^{-1} cm^{-2}) at 600 °C, is ~3.3 times higher than the flux of YSZ-supported DPHFMs in literature, where the distribution of carbonate inside the ceramic support was not controlled, and both packed-pore network and micro-channels were infiltrated with carbonate [106]. Even though the controlled YSZ-supported DPHFMs in this work had a higher active surface area for permeation

(oxygen-ion conductivity: 0.004 S cm^{-1} at 600 °C [249]) compared to MIEC-supported DPHFMs, the achieved carbon dioxide flux was comparable, but not higher than the flux of uncontrolled MIEC-supported DPHFMs in literature (oxygen-ion conductivity: 0.091 S cm^{-1} at 600 °C [140]). Uncontrolled LSCF-supported DPHFMs and multi-channel SFN-supported DPHFMs where the micro-channels were infiltrated with carbonate (resulting in a molten carbonate thickness of 300 and 220 μm, respectively) showed a carbon dioxide flux of 0.125 and 0.12 ml min^{-1} cm^{-2}, respectively, at 600 °C [141,144]. Overall, the increase in available active permeate-side surface area, was found to outperform the achieved carbon dioxide flux of DPHFMs with an oxygen-ion-conducting support and showed a comparable flux to DPHFMs with a MIEC support. This has not previously been achieved, as the flux of MIEC-supported DPHFMs with blocked micro-channels was at least 4 times higher than the flux of DPHFMs with an oxygen-ion-conducting support where the micro-channels were also blocked (overall molten carbonate thickness of 500 μm) [106,144]. Finally, the flux of controlled distribution 3% YSZ-supported DPHFMs was also found to be more than two times higher than the flux of controlled distribution Al_2O_3-supported DPHFMs developed in this work, confirming that the oxygen-ion-conductivity of the support contributes to carbon dioxide permeation through the membrane. However, when the flux of controlled distribution 3% YSZ-supported DPHFMs was compared to the flux of uncontrolled distribution Al_2O_3-supported DPHFMs developed in this work, the flux was found to be more than 20 times higher. This is another example of how controlled distribution of carbonate inside the hollow fibre supports leads to higher surface areas for carbon dioxide desorption and therefore competitive flux through dual-phase membranes with nominally electrically insulating and oxygen-ion-conducting supports. The comparisons made amongst the model crucible membranes and DPHFMs developed in this work and dual-phase membranes developed in literature, are summarised in Table 4.2.

Table 4.2: Comparison of carbon dioxide flux through dual-phase membranes in literature and dual-phase membranes developed in this work.

Ceramic phase	Geometry/ carbonate distribution	Thickness (μm)	Flux (ml min^{-1} cm^{-2}) at 600 °C
$Bi_{1.5}Y_{0.3}Sm_{0.2}O_{3-\delta}$ (BYS) [133]	Pellet (pore surface modified with γ-Al_2O_3)	~50	0.025
8% $Y_{0.16}Zr_{0.84}O_{2-\delta}$ (YSZ) [106]	Hollow fibre/ uncontrolled	500	0.028
$La_{0.6}Sr_{0.4}Co_{0.2}Fe_{0.8}O_{3-a}$ (LSCF) [144]	Hollow fibre/uncontrolled	300	0.125
$SrFe_{0.8}Nb_{0.2}O_{3-\delta}$ (SFN) [141]	Multi-channel hollow fibre/ uncontrolled	220	0.12
Al_2O_3 (this work)	Model crucible	250	0.048
Al_2O_3 (this work)	Hollow fibre/ controlled	min. ~50 max. ~480	0.036
Al_2O_3 (this work)	Hollow fibre/ uncontrolled	~260	0.004
3% YSZ (this work)	Hollow fibre/ controlled	min. ~10 max. ~200	0.09

4.4 Conclusions

Dual-phase molten-carbonate membranes, with a nominally electrically insulating support, were studied using two support geometries: model crucible membranes and realistically scalable hollow-fibre supports. In model crucible membranes, surface-exchange reactions were found to be rate-limiting on carbon dioxide flux for all investigated molten carbonate thicknesses (250, 500, 750 and 1000 μm) between 500 and 750 °C, as carbon dioxide flux showed an increasing rate of increase with the increase in temperature. Bulk-diffusion limitations occurred at operating temperatures above 750 °C as further increase in temperature did not result in a significant improvement in flux compared to the increase observed in the surface-exchange-limited region. Furthermore, in the surface-exchange-limited region, there was no further increase in flux by decreasing membrane thickness below 750 μm, consistent with a critical thickness (L_c) of 750 μm. Based on the flux-limiting parameters identified through the model crucible membranes, the increase of permeate-side active surface area in the surface-exchange-limited region was expected to result in improved carbon dioxide flux in DPHFMs. The controlled distribution of carbonate inside hollow fibre supports, resulted in DPHFMs with one order of magnitude higher surface area for carbon dioxide desorption (lumen side) compared to the uncontrolled distribution DPHFMs (micro-channels and packed-pore network filled with carbonate). Due to the increase in permeate-side surface area, controlled DPHFMs provided an 8-fold increase in carbon dioxide flux compared to uncontrolled DPHFMs, suggesting permeate-side surface area was the rate-limiting step for permeation at 600 °C. Indeed, at temperatures below 800 °C, when the lumen side of a controlled DPHFM was used as the permeate-side surface, the resulting carbon dioxide flux was 4 times higher than when the shell side of a controlled DPHFM was used as the permeate-side surface. Finally, controlled DPHFMs with an oxygen-ion-conducting support, showed ~3.3 higher fluxes than the equivalent oxygen-ion-conducting-supported DPHFMs in literature, where the micro-channels were blocked with carbonate.

Chapter 5

Self-healing of a dual-phase ceramic molten-salt membrane by exploiting the molten salt spreading inside the ceramic support

In this chapter, the potential of the molten carbonate phase to self-heal a crack on a ceramic-supported dual-phase membrane is investigated. The aim is to demonstrate that the molten carbonate phase can spread, redistribute, and self-heal created cracks in dual-phase ceramic molten-salt membranes, while providing a selective layer for carbon dioxide permeation.

The following chapter includes results also presented in the paper *'Autonomously self-healing molten-salt membrane for carbon dioxide permeation'* published in the Journal of Membrane Science (https://doi.org/10.1016/j.memsci.2020.117855).

Figures 5.1, 5.2, 5.4 and 5.4 are schematic representations of the equipment used for conducting the experimental work and are presented the same form in both the manuscript and the following chapter.

Figures 5.7, 5.8 and 5.9 have been used in a similar form in the aforementioned manuscript and were remade for the purpose of this chapter.

5.1 Introduction

Membrane failure can occur due to materials expansivity mismatch, stresses accumulated at sealing points, and simply by manual handling of membrane modules during maintenance. In order to lengthen membranes lifespan, the self-healing of membrane cracks generated during operation is desirable. Self-healing is defined as the ability of materials to heal when damage occurs and aims at the restoration of the material's structural integrity. As mentioned in chapter 2, section 2.3.3 self-healing membranes could be the answer to the susceptible nature of ceramic-supported membranes; and therefore dual-phase ceramic molten-salt membranes. However, little research has been done in this field, with scientific efforts mainly focusing on self-healing of polymeric materials since polymers and composites are being increasingly and widely used in structural applications in the aerospace, automobile, maritime, defense and construction industries. The research on self-healing ceramics is limited due to their high sintering temperature which results in their rigid nature and makes it difficult to tailor their properties for self-healing purposes. The application of self-healing for membranes is even more limited, with only a few self-healing membrane examples in literature (presented later in this section). Hence, the understanding of individual self-healing mechanisms on polymeric and ceramic materials could provide insights into how self-healing can be further applied to membranes; more specifically to dual-phase ceramic molten-salt membranes in this work. As a general instruction, for self-healing to be considered successful, the healed zone needs to restore the physical properties of the material to its before damage state. For membranes in particular, restoration of its physical properties is not enough. Self-healing must restore the membrane's functionality, *i.e.* permselectivity, at operational conditions to its before failure state, in order to be considered successful. Depending on whether self-healing occurs as an automatic response to damage or failure of the material or requires the presence of an external trigger mechanism to take place, it is classified as autonomous and non-autonomous self-healing, respectively [250]. Self-healing can be further classified as intrinsic and extrinsic depending on the materials that participate in the self-healing process, and will be analysed below [251].

For intrinsic self-healing, only the materials already existing in the system are involved in the self-healing process. Intrinsic self-healing in polymeric materials is enabled under specific conditions, often activated by temperature, *i.e.* non-autonomous self-healing; and can occur by either physical or chemical interactions. Intrinsic self-healing

by physical interactions occurs at temperatures equal to above the glass transition temperature [252], where surface rearrangement is followed by wetting, diffusion and finally randomization of the crack-interface molecules. Intrinsic self-healing by chemical interactions relies on the structural changes of atoms or molecules, such as chain scission and inverse reactions, *i.e.* recombination of broken molecules or thermally reversible cross-linking behaviour [253,254].

Non-autonomous intrinsic self-healing in ceramic materials is most likely to occur by thermal or chemical re-sintering of surface cracks, by relaxation of tensile residual stress at the indentation site or by oxidation [198]. Thermal self-healing by re-sintering triggers a diffusive crack-healing process that causes regression and generates regular arrays of cylindrical voids in the immediate crack-tip vicinity. Similarly, relaxation of tensile residual stress at the indentation site can be completely removed by heat treatment above 900 °C [255]. Lastly, self-healing by oxidation occurs *via* the oxidation of the inorganic components *i.e.* silicon-carbide or silicon nitride particles, dispersed within the cracked walls of the ceramic. The oxidation process fills the cracks of the ceramic matrix with oxide particles that grow and coalesce when exposed to air at 1100 ºC as oxidation progresses; ultimately forming a dense oxide layer consisting of ordered nano-sized particle arrays [256]. Oxidation is considered the most efficient process amongst the three as it does not rely on the slow process of thermal diffusion from the base material to the crack zone [257]. An example of healing of surface cracks by oxidation is the crack healing process of a cracked metallo-ceramic MAX phase material, in particular Ti_3AlC_2, undergoing oxidation [258]. The average width and length of the examined crack were 5 μm and 7 mm respectively and after a heat treatment for 2 h at 1100 ºC in air, the crack was fully filled by newly formed fine oxide particles. Formation of Al_2O_3 layers was observed adjacent to the surfaces of the crack and the surface of the sample, whereas a TiO_2 layer was formed at the surface of Al_2O_3, which was continuously forming and mixing with the TiO_2 particles. The final healed sample was covered by a coarse layer of TiO_2 and the crack gap was fully filled with the Al_2O_3 and TiO_2 particles [258]. The same behaviour has been observed on other MAX phase materials like Ti_3SiC_2 and Cr_2AlC, where the oxidation of the A-element has resulted in crack healing [259–263]. Intrinsic self-healing in ceramics by re-sintering, thermal treatment or by oxidation is a non-autonomous process as it requires an external trigger to occur.

Autonomous and intrinsic self-healing has predominantly been studied in cement to address the issue of cement micro and macro-cracking. The self-healing mechanisms are based on physical, chemical and mechanical processes, which can be swelling and hydration of cement pastes, precipitation of calcium carbonate crystals, and blockage of flow paths due to deposition of water impurities or movement of concrete fragments that detach during the cracking process [198].

Based on the mechanisms used for intrinsic self-healing on polymeric, ceramic materials and cement, self-healing on dual-phase ceramic molten-salt membranes could be applied by wetting and thermal re-sintering. However, thermal re-sintering for cracks on the ceramic support requires particularly high temperatures to occur (>1100 ºC), at which the molten salt has been found to decompose [189]. Wetting, followed by spreading of the molten phase in the ceramic support would be an efficient way to restore cracks, since the molten salt has shown high wetting on the ceramic phase. However, it has not yet been explored. The volume increase of the molten salt with the increase in temperature, as discussed in section 2.3.2, could also potentially result in restoration of cracks in dual-phase membranes, but that would require an increase in the operating temperature, which is not always energy efficient for the separation process.

Whereas intrinsic self-healing depends on the material itself, in extrinsic self-healing, additional pre-embedded materials acting as self-healing agents need to be involved in the self-healing process, as the material's matrix itself does not possess healing properties [251,264]. It is often the case that those pre-embedded agents do not contribute to the original system performance and interrupt active sites or pathways destined for the original function of the material. In polymeric materials, extrinsic self-healing is achieved by encapsulation followed by the embedment of a healing agent into the polymeric material [250]. Encapsulation by embedment has been achieved by loading the material with healant-loaded pipelines or microcapsules. The basis of the healant-loaded pipelines technique is to fill the brittle-walled vessels with polymerisable medium which should be fluid at the healing temperature. The healing agent for the healant-loaded microcapsules is being stored in fragile microcapsules instead. Upon formation of a crack, the capillary forces will force the healing agent towards the crack and as soon as the fragile capsule of the encapsulated agent is destroyed the healing agent will be released [265]. This allows the autonomous extrinsic self-healing of cracks in polymers, as there is no external trigger that causes the wall of the micro-

capsules or healant-loaded pipelines to rupture. Microencapsulation techniques can be divided depending on the presence of one or more healing agents, their location within the matrix and their physical properties [266].

Extrinsic self-healing for ceramic materials has mainly been achieved by adding whiskers, particles or platelets of a desired material inside the ceramic, which upon oxidation forms an oxide and fills/heals the created crack. As an example, SiC particles or whiskers [267–269] and TiC particles [270] have in separate cases been dispersed in Al_2O_3 in order to examine their self-healing properties upon oxidation. After a minimum of 1 h in air and at a minimum temperature of 1100 ºC, SiC and TiC oxidized to their respective oxides and filled the created crack by diffusion. The optimum amount of SiC or TiC required in Al_2O_3 to self-heal surface cracks was found to be between 15 – 30 vol% [271]. Self-healing of Al_2O_3 by crack-healing oxides has successfully resulted in the healing of surface cracks up to 100 µm in length and 50 µm in width [269].

Even though methods for extrinsic self-healing have been proven effective for the crack-healing in polymers and ceramics, they are energy demanding (high temperatures), time consuming and are mainly applicable to the repair of external and accessible damages instead of the internal and invisible micro-cracks [272]. Moreover, microencapsulation techniques for polymers are complex, requiring multiple fabrication steps, and in ceramics the addition of a secondary phase also increases fabrication steps and/or restricts fabrication parameters [266]. Rather than applying a method for extrinsic self-healing for repairing crack growth, numerous healing techniques aim to improve the intrinsic self-healing of the already existing materials in the system, avoiding extrinsic self-healing entirely. Extrinsic self-healing on dual-phase membranes would require the addition of a self-healing agent in the ceramic matrix or the melt. This could potentially lead to a decrease in overall membrane performance since the self-healing agent would not contribute to permeation and would block permeation pathways. Therefore, dual-phase ceramic molten-salt membranes with autonomous and intrinsic self-healing properties need to be developed [198].

Dual-phase membranes with a non-polymeric support that have showcased promising potential for self-healing in literature are ultra-thin solid-state Li-ion electrolyte membranes [55] and ceramic-supported ionic-liquid membranes for olefin-paraffin separation [273]. The Li-ion electrolyte membranes possess a self-healing network of reversible cross-linking polymers in their matrix that would fill the voids of the solid

electrolyte in case of cracking. However, the aforementioned membranes were neither tested for extrinsic self-healing of cracks, nor for their performance prior and post-cracking. It was only suggested that the dispersed polymer within the solidified matrix would interconnect the solid particles and restore the membrane's integrity in case of cracking [55]. In ceramic-supported ionic-liquid membranes for olefin-paraffin separation, self-healing was demonstrated by switching the feed gas between a propylene/propane mixture and pure nitrogen. When the gas on the feed side of the membrane was pure nitrogen (not desirable separation for olefin-paraffin separation membranes), the ionic liquid decomposed, resulting in the solidification of the salt to its corresponding solid salt. With the solidification of the salt, the volume it occupies in the membrane support decreased and the membrane became porous, allowing the non-selective permeation of nitrogen. When the gas was switched back to the propylene/propane mixture, the salt liquified and restored the selective permeation for this membrane, under operating conditions [273]. However, the self-healing behaviour of the olefin-paraffin separation membrane was not demonstrated during operation, or under the normal permeating conditions for this membrane. Even though self-healing could lengthen the lifespan of dual-phase membranes, research so far, has failed to demonstrate self-healing under normal operating conditions and in particular autonomous and/or intrinsic self-healing mechanisms.

In this chapter, it is shown how a dual-phase ceramic molten-salt membrane with a highly wetting carbon dioxide selective liquid [145] as the molten phase, with significant potential for high temperature carbon dioxide separation [94], can self-heal during operation. Self-healing was initially observed in a DPHFM during operation, after increasing the operating temperature and causing the carbonate volume to increase, showcasing an intrinsic and non-autonomous self-healing mechanism. DPHFMs however possess a complex structure that is not ideal for understanding the self-healing behaviour inside the ceramic support. To allow control over the formation of the leak-path and the simulation of crack-growth in the form of a membrane defect, Al_2O_3/sacrificial defect-inducing material pellet supports were developed. A porous Al_2O_3 support was used to allow the infiltration of carbonate inside its porous volume, which acts as the carbon dioxide selective phase. By exploiting two highly wetting carbon dioxide selective liquids: one with a melting point above and one with a melting point below the oxidation temperature of the sacrificial defect-inducing material, the self-healing behaviour of dual-phase membranes was demonstrated both as an

intrinsic non-autonomous and an intrinsic autonomous process, respectively. In order to demonstrate the self-healing process during operation, each dual-phase ceramic molten-salt membrane was tested against three conditions:

1) Proof of membrane permselectivity towards carbon dioxide separation;
2) Defect creation due to the oxidation of the sacrificial defect-inducing material;
3) Self-healing of the created defect due to the wettability and spreading of the molten-salt phase; regaining the membrane's previous permselectivity.

Defect creation was dependent on the sacrificial material used inside the ceramic support. When carbon fibre was used as the sacrificial defect-inducing material, its oxidation resulted in a controlled, throughout defect inside the membrane's matrix (Figure 5.1a). When spherical glassy carbon was used as the sacrificial defect-inducing material, its oxidation resulted in randomised porosity inside the membrane's matrix (Figure 5.1b). Overall, the intrinsic and autonomous self-healing of a dual-phase membrane was proved by molten carbonate contact angle measurements, carbonate spreading and carbon dioxide permeation experiments.

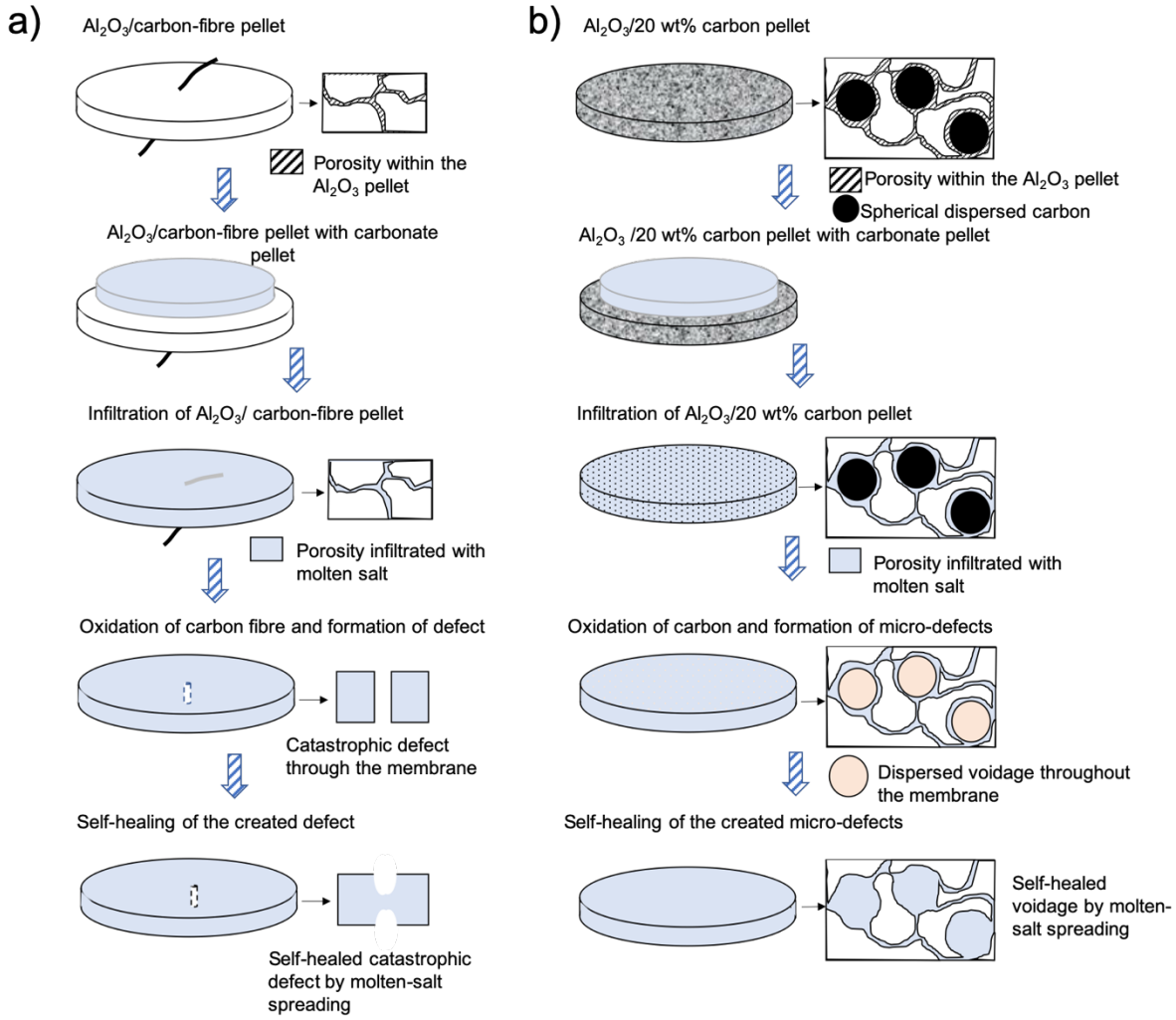

Figure 5.1: Proposed self-healing mechanism for dual-phase ceramic molten-salt membranes with an incorporated sacrificial defect-inducing material. a) carbon fibre as the sacrificial defect-inducing material, and b) glassy carbon as the sacrificial defect-inducing material.

5.2 Experimental

5.2.1 Chemicals and materials

α-Al_2O_3 powder, carbon fibre (Fibre glass ltd.) and glassy carbon spherical powder (0.4-12 μm, Alfa Aesar) were used for the fabrication of the Al_2O_3/sacrificial defect-inducing material pellets. Polyvinyl alcohol (PVA, 98%-98.8 mol% hydrolysis, Sigma-Aldrich) dissolved in deionized water was used for the incorporation of the carbon fibre inside the pellets. Lithium, potassium and sodium carbonate monohydrate were used for the preparation of the carbonate mixtures. Silver paste was used as the high temperature sealant for the membranes and vacuum grease was used as the low temperature sealant in the permeation apparatus.

5.2.2 Fabrication of Al_2O_3/ sacrificial defect-inducing material pellets

Al_2O_3/carbon fibre pellets: To prepare each of the Al_2O_3/carbon-fibre pellets, 1 g of α- Al_2O_3 powder was used. One drop of PVA that has been dissolved in deionized water at 7 wt%, was also used to facilitate the incorporation of the carbon fibre inside the Al_2O_3 pellet. The Al_2O_3/carbon fibre pellet was prepared by the uniaxial compaction of powders at a pressure of 425 MPa for 10 min, with the carbon fibre vertically incorporated inside the pellet (Figure 5.2).The pellets were then sintered at 1300 °C (Carbolite ®, STF 15/610) with a dwell time of 4 h using a heating and cooling rate of 5 °C min^{-1} under a nitrogen flowing atmosphere (200 ml min^{-1}); used to prevent the oxidation of the carbon fibre. The furnace was also purged with nitrogen for 1 h with a flow rate of 200 ml min^{-1} prior to the start of the sintering process, to ensure the air trapped in the furnace chamber had been removed.

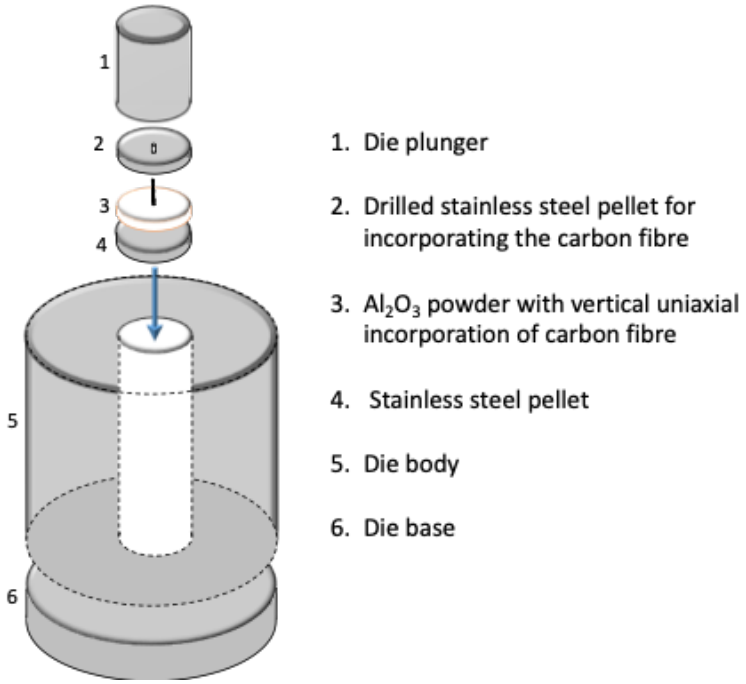

Figure 5.2: Isostatic compression of Al_2O_3/carbon fibre pellets. The Al_2O_3 powder and the carbon fibre are pressed into a pellet after being inserted in a pellet die where the top stainless-steel pellet has been drilled for the uniaxial incorporation of the carbon fibre.

Al_2O_3/dispersed glassy carbon pellets: To prepare the Al_2O_3/dispersed glassy carbon pellets, α-Al_2O_3 powder and glassy carbon spherical powder were mixed in a 4:1 weight ratio. The powders were compacted at a pressure of 220 MPa for 5 min. The pellets were then sintered at 1300 °C with a heating rate of 1 °C min^{-1}. To prevent glassy carbon oxidation while sintering, the pellets were sintered under a nitrogen flowing atmosphere (200 ml min^{-1}). The furnace was also purged with nitrogen (200 ml min^{-1}) for 1 h prior to the start of the sintering process.

5.2.3 Preparation of carbonate mixture and wettability measurements

To prepare the carbonate pellets used for the infiltration of the Al_2O_3/carbon-fibre and Al_2O_3/dispersed glassy carbon pellets, dehydrated Li_2CO_3, Na_2CO_3, and K_2CO_3 carbonate were mixed in a eutectic (Li_2CO_3 : Na_2CO_3 : K_2CO_3 = 43.5 : 31.5 : 25, m.p. 397 °C) or a Li_2CO_3 : Na_2CO_3 : K_2CO_3 = 20 : 60 : 20 mole ratio (m.p. 640 °C) and pressed by isostatic pressing [151,274]. The wettability of the Li_2CO_3 : Na_2CO_3 : K_2CO_3 = 20 : 60 : 20 mole ratio carbonate mixture on a dense Al_2O_3 pellet was tested in a controlled atmosphere furnace (Vecstar, VCTF) with a custom-made quartz window, allowing the observation of the contact angles of the two carbonate melts on Al_2O_3 at high temperature (Figure 5.3). A carbonate pellet was placed on top of the dense Al_2O_3 ceramic pellet (Multilab) and the two stacked pellets were then inserted in the middle of the heating zone of the controlled atmosphere furnace. A flow of 30 ml min^{-1} with a

pCO_2 of 0.5 atm in nitrogen was introduced to the system and the temperature of the furnace was increased by 1 °C min^{-1} using a Eurotherm 2416 temperature controller. The temperature was increased to 400 °C for the eutectic and to 670 °C for the Li_2CO_3 : Na_2CO_3 : K_2CO_3 = 20 : 60 : 20 mole ratio mixture. The measurements for the eutectic carbonate mixture were performed by Dr Georgios Triantafyllou.

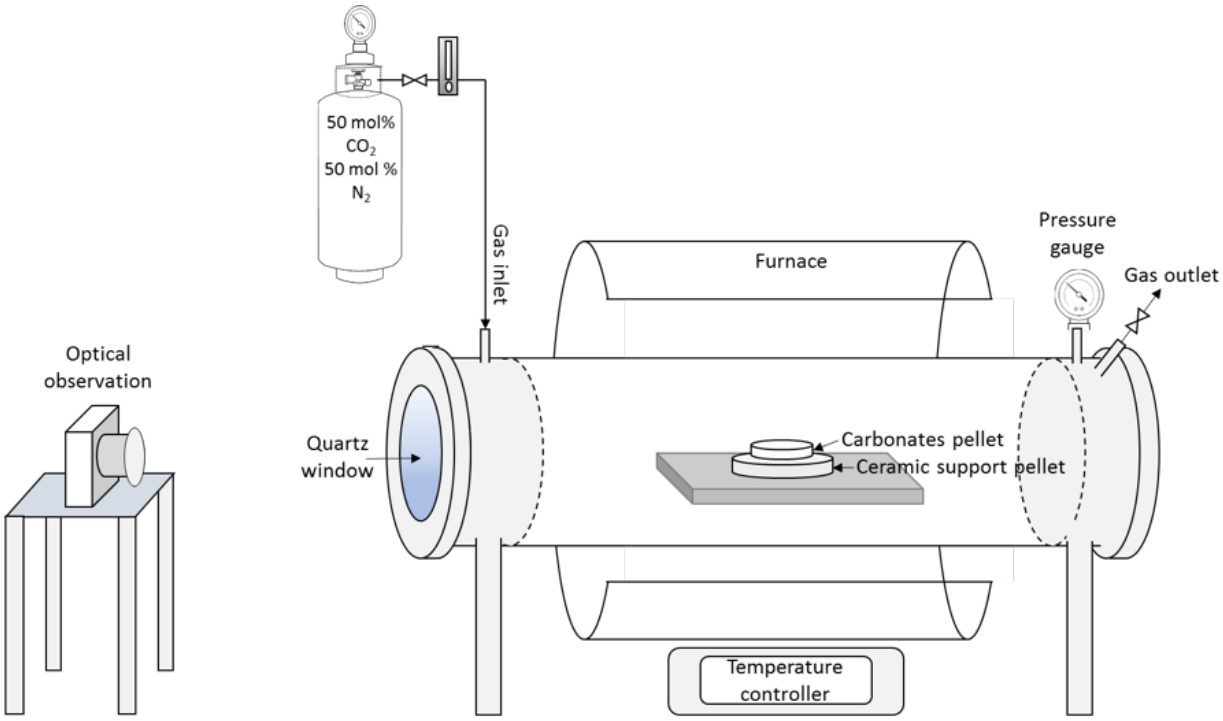

Figure 5.3: Controlled atmosphere furnace with a custom-made quartz window allowing the determination of carbonate contact angle on dense Al_2O_3 (ceramic support pellet).

5.2.4 Self-healing performance of dual-phase ceramic molten-salt membranes

The self-healing performance of the molten carbonate phase inside the investigated dual-phase membranes, was evaluated using the experimental apparatus illustrated in Figure 5.4. The permeation apparatus and the sealing process used was the same as in model crucible membranes (described in chapter 4, section 4.2.5). The melting of the carbonate eutectic mixture typically occurred between 400 and 430 °C and the melting of the Li_2CO_3 : Na_2CO_3 : K_2CO_3 = 20 : 60 : 20 mole ratio carbonate mixture typically occurred between 630 and 660 °C under a pCO_2 of 0.5 atm in nitrogen. The feed gases used contained a pCO_2 of 0.5 atm in nitrogen during the permselectivity test of the membranes and a pCO_2 of 0.001 atm, pO_2 of 0.196 atm and pN_2 of 0.794 atm during the oxidation process of the sacrificial defect inducing material. The sweep gases used were pure argon for the permselectivity test of the membrane and a pO_2 of 0.2 atm in argon during the oxidation process of the sacrificial defect inducing material. The composition of the permeate was analysed in-line by an infrared radiation

(IR) analyser (Vaisala CARBOCAP® Carbon Dioxide Probe GMP343) and a quadrupole mass spectrometer (ESS, GeneSys) following the same calibration and performance evaluation process described in chapter 4, section 4.2.5.

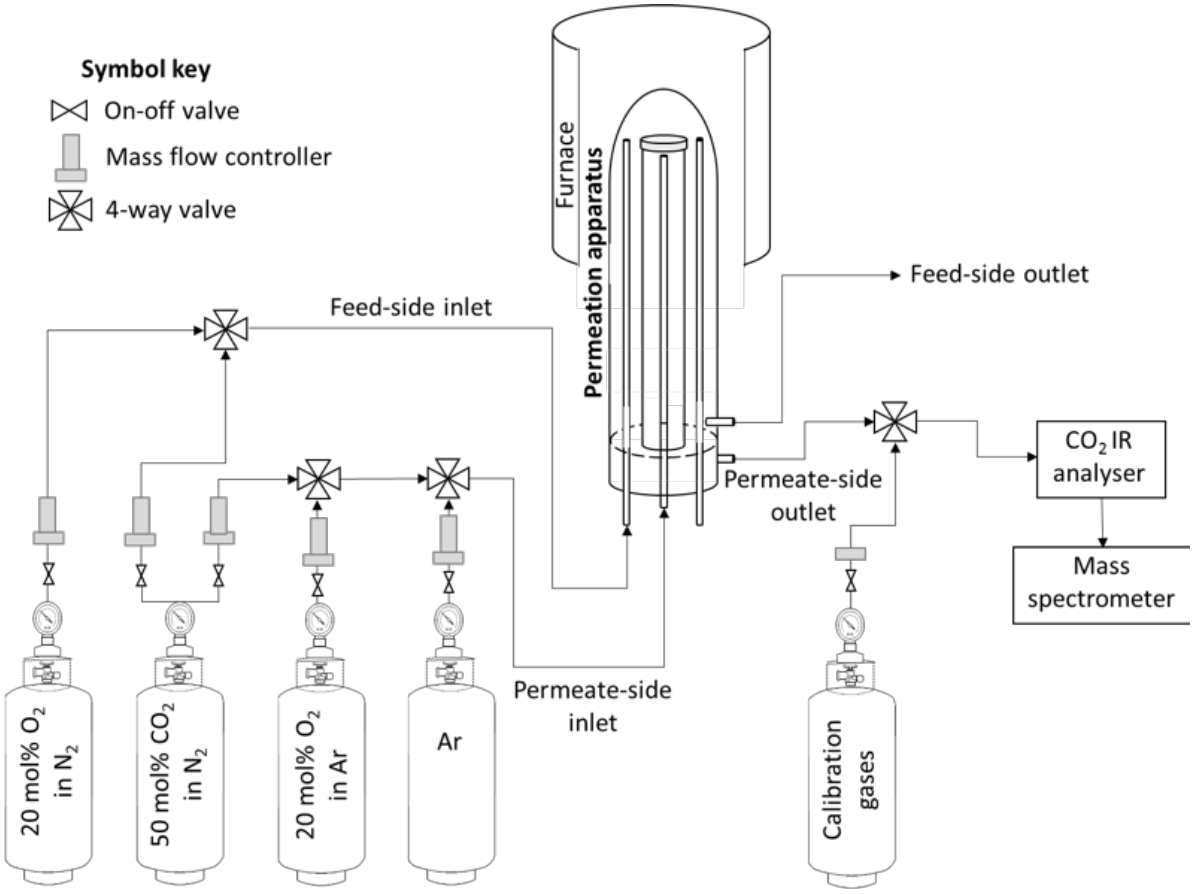

Figure 5.4: Experimental set-up for self-healing experiments. Feed and permeate-side inlet gases are connected to the feed and permeate side of a custom-made permeation apparatus that contains the self-healing membrane. The permeate-side outlets are analysed in series by an infrared analyser and a mass spectrometer.

The selectivity of the dual-phase membranes was evaluated prior and post-oxidation of the sacrificial defect-inducing material, based on Eq. 5.1. as mentioned in chapter 1, section 1.2.3:

$$\alpha = \frac{P_{CO_2}}{P_{N_2}} \qquad \text{(Eq. 5.1)}$$

where P_{CO2} and P_{N2} is the permeability of carbon dioxide and nitrogen, respectively, as calculated by Eq. 5.2:

$$P_{CO_2} = \frac{x_{CO_2}\,\dot{V}L}{A_S\,(P_f - P_p)} \qquad \text{(Eq. 5.2)}$$

where x_{CO2} is the mole fraction of carbon dioxide in the permeate-side outlet, $\dot{V}$ is permeate volumetric flow rate (ml min^{-1}), L is the membrane thickness (cm), A_s is the active surface area of the membrane (cm^2) and (P_f – P_p) is the membrane partial

pressure driving force expressed as the difference in pCO_2 between the feed-side and the permeate-side inlet (nominal P= 1 atm).

5.2.5 Characterisation

The micro-structure of the prepared Al_2O_3/sacrificial defect-inducing material pellets was analysed by scanning electron microroscopy (SEM) (Hitachi, TM3030 and Tescan, Vega3) prior and post-experimental procedure. Analysis of the porosity and pore size distribution of the pellet supports prior and post-oxidation of the sacrificial defect-inducing material was achieved by MIP. The mass loss percentage for mixtures of:

a) carbon fibre and Al_2O_3 powder,

b) carbon fibre, Al_2O_3 and ternary eutectic carbonate mixture powder,

c) 20 wt% glassy carbon and Al_2O_3 powder, and

d) 20 wt% glassy carbon, Al_2O_3 and ternary eutectic mixture of carbonate powder

were calculated by thermal gravimetric analysis (TGA, TGA Q500 V20.13 Build 39). The mass loss percentage was calculated at 600 °C using a gas mixture of pO_2= 0.2 atm in nitrogen (60 ml min^{-1}) for 24 h. To prevent oxidation of the sacrificial defect-inducing materials, the heating to 600 °C was carried out in an atmosphere of nitrogen at a rate of 5 °C min^{-1}.

5.3 Results and discussion

5.3.1 Intrinsic and non-autonomous self-healing in DPHFMs

The DPHFMs used in this work (chapter 4) had a high membrane failure to success ratio, identifying thermal expansivity mismatch between the high temperature sealant and the DPHFM, as the main cause of membrane failure. Defects on the membrane surface and uncontrolled volume expansion of carbonate inside the ceramic supports also resulted in membrane cracking. Figure 5.5 shows a 200 μm wide and 1.5 cm long crack on both feed and permeate side of a micro-structured membrane with a pellet geometry possessing a hollow fibre structure (fabrication method in Appendix C). The membranes were analysed *via* SEM imaging at room temperature, after high temperature operation. The crack appeared to progress from micro-channel to micro-channel on the permeate side of the membrane and was also present on the feed side of the membrane, suggesting a throughout membrane crack.

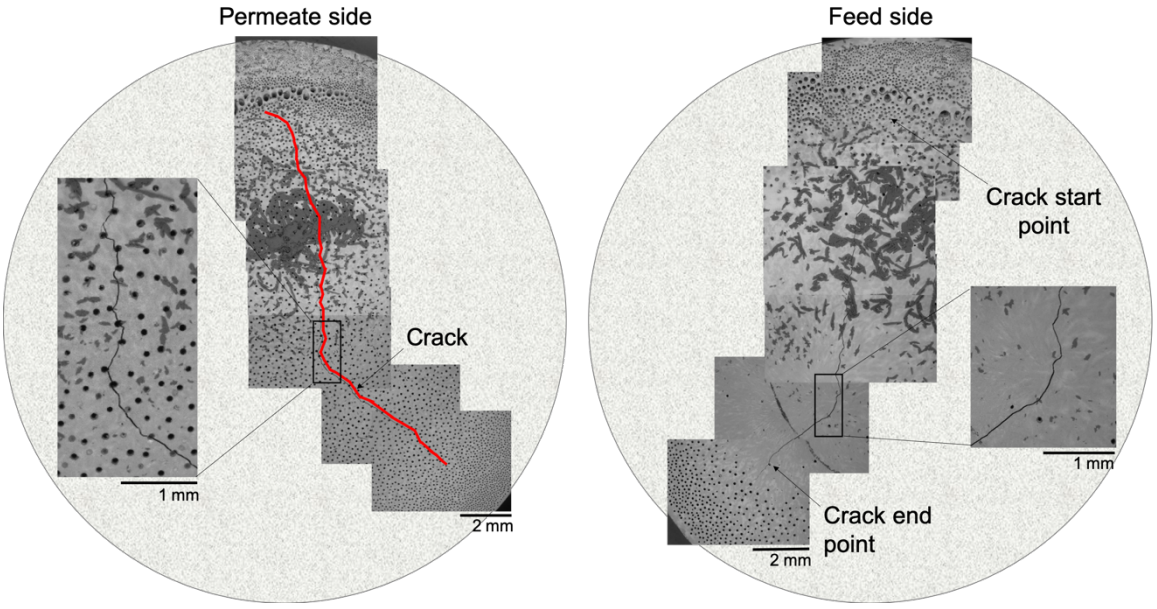

Figure 5.5: Throughout crack on a micro-structured pellet membrane with a hollow fibre structure. The red line follows the crack on the permeate-side surface of the pellet.

Membrane cracking was also observed and recorded during the operation of a controlled distribution DPHFM by monitoring the flux of the leak-detecting nitrogen gas on the permeate side of the DPHFM (Figure 5.6). The temperature was originally increased to 400 °C (1) where the carbonate mixture infiltrated the hollow fibre support and nitrogen flux consequently decreased, reaching 0.02 ml min^{-1} cm^{-2}. However, after dwelling at 500 °C for 3 h (2) the nitrogen flux increased to 5 ml min^{-1} cm^{-2}, indicating membrane failure (3). To investigate the effect of carbonate volume expansion at

higher temperatures, the operating temperature was increased to 600 (4) and then to 700 °C (5). Even though the nitrogen leak persevered at 600 °C (4), it decreased to 0.013 ml min^{-1} cm^{-2} at 700 °C, dropping below the detection limit of the instrument (0.001 ml min^{-1} cm^{-2}) over a 2 h operation at 700 °C (5). At 700 °C carbon dioxide flux through the DPHFM reached 0.02 ml min^{-1} cm^{-2}. The volume expansion of the molten carbonate with the increase in temperature (chapter 2, section 2.3.2, Table 2.1) showed that the carbonate phase can act as a self-healing material in a dual-phase ceramic molten-salt membrane [151,238]. After removing the membrane from the permeation apparatus, the crack origin was experimentally identified as a throughout membrane crack, using digital microscopy and by submerging the sealed membrane in deionised water while introducing pressurised air on its permeate side.

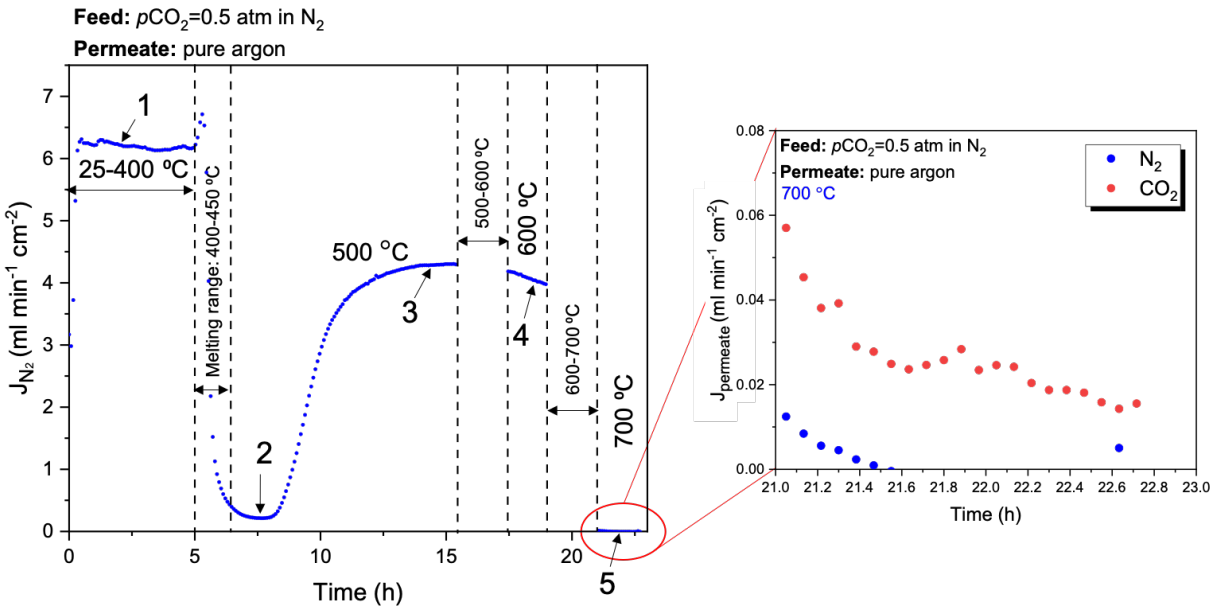

Figure 5.6: Self-healing of an Al_2O_3-supported controlled DPHFM due to the volume expansion of carbonate with the increase in temperature.

The carbonate volume expansion with the increase in temperature showed promising results for self-healing membrane cracks in DPHFMs. However, the self-healing mechanism cannot be easily studied in the hollow-fibre geometry as it is difficult to incorporate a sacrificial defect-inducing material during the fabrication of the hollow fibre supports. Therefore, it is difficult to produce a controlled crack, in the form of a defect, in a DPHFM. Moreover, the self-healing mechanism was non-autonomous, requiring temperature increase in order to occur. To explore the self-healing nature of carbonate inside a dual-phase ceramic molten-salt membrane, dual-phase membranes with a pellet geometry and an incorporated sacrificial defect-inducing material that was removed *via* oxidation were developed.

5.3.2 Al_2O_3/ sacrificial defect-inducing material pellets

Both geometries of the sacrificial defect-inducing materials were incorporated in the Al_2O_3 pellets by isostatic co-pressing, resulting in a randomly tortuous pore network for the pellet supports. The Al_2O_3/sacrificial defect-inducing material pellets had an overall diameter of 2 cm and a thickness of ~1.4 – 1.5 mm. The carbon fibre was incorporated in the pellet perpendicular to its feed-side surface and had a diameter of 350 µm (Figure 5.7a: SEM images a and b). Upon oxidation (pO_2= 0.2 atm in nitrogen gas mixture at 1300 °C), the carbon fibre was removed, leaving a single 350 µm void throughout the pellet (Figure 5.7a: SEM images c and d). The overall porosity of the Al_2O_3/carbon fibre pellet prior to sintering was 41% as calculated by MIP, shown in Figure 5.7b. The porous Al_2O_3 support had an average pore size diameter of 0.2 µm and a total mercury intruding volume of 0.18 ml *per* gram of pellet. It was not possible to measure the porosity created by the oxidation of the carbon fibre by MIP, as the pore diameter of the created void was above the upper limit of detection (<100 µm) for the MIP measurement. However, by subtracting the approximate volume the carbon fibre occupied inside the pellet, the overall pellet porosity remained approximately the same (~40.95%).

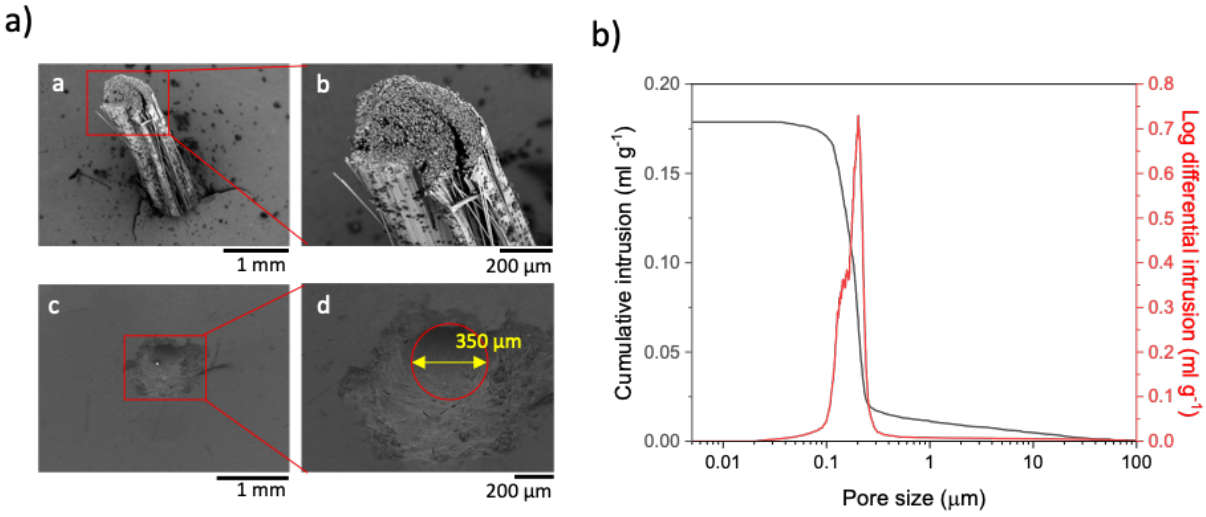

Figure 5.7: SEM images (a) and MIP results (b) for Al_2O_3/carbon fibre pellets. a) SEM images of an the Al_2O_3/carbon fibre pellet sintered in nitrogen at 1300 °C (a and b) and SEM images post-oxidation of the carbon fibre after sintering the pellet in a gas mixture of pO_2= 0.2 atm in nitrogen (c and d). b) MIP cumulative intrusion volume and pore size distribution for the Al_2O_3/carbon fibre pellet after sintering in a nitrogen at 1300 °C.

Al_2O_3 pellets with 20 wt% randomly-dispersed glassy carbon pellets also resulted in an overall pellet porosity of 40%, as measured by MIP shown in Figure 5.8a, allowing the consistent infiltration of the prepared pellets with the same quantity of carbonate. The

average pore size of the Al_2O_3/20 wt% glassy carbon pellet was 0.2 µm (maximum pore size 1 µm), with a total mercury intruding volume of 0.26 ml *per* gram of pellet. The glassy carbon can be identified inside the pellet's matrix as the spherical particles in Figure 5.8a with a diameter between 2 and 5 µm [275]. The oxidation of the glassy carbon resulted in spherical-like voids (Figure 5.8b) within the pellet, and the overall porosity of the pellet increased from 40 to 58% based on MIP results (Figure 5.8b). Between the MIP tests for the Al_2O_3/20 wt% glassy carbon pellet prior and post-oxidation, a clear increase in the mercury intruding the volume of pores with a diameter 0.2 and 10 µm was also observed verifying that the increase in porosity was attributed to glassy carbon oxidation. The total volume of mercury intruding the porous volume of the pellet was also increased from 0.25 to 0.4 ml *per* gram of pellet.

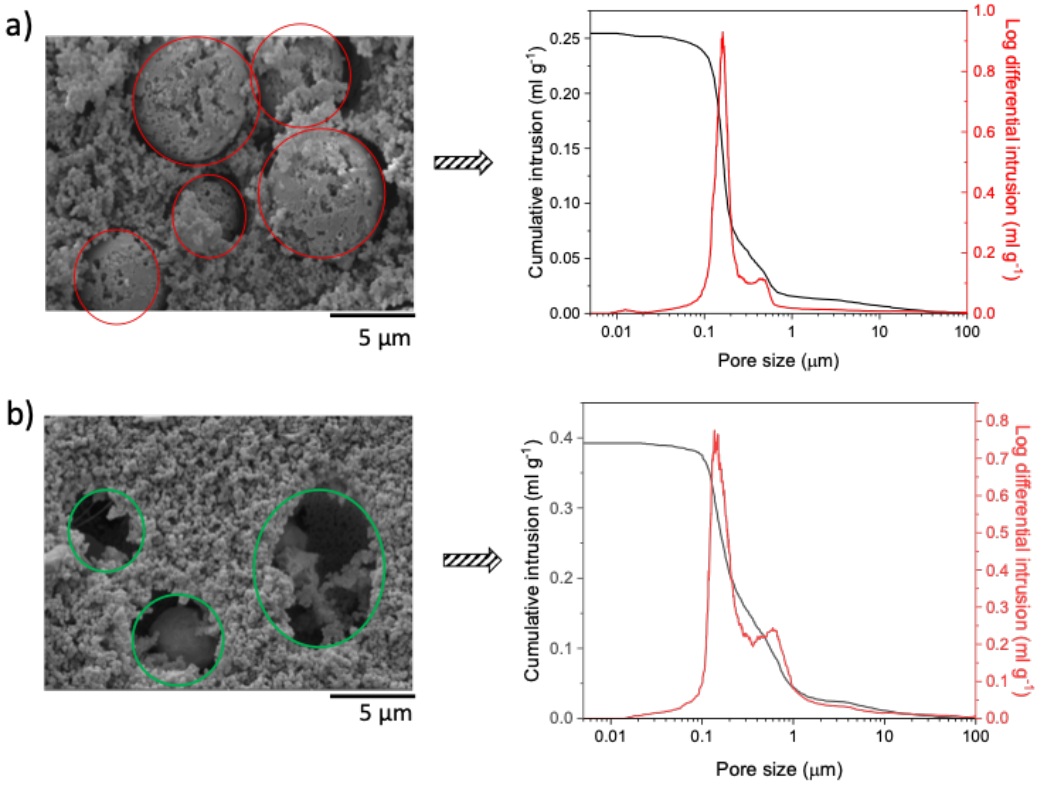

Figure 5.8: Al_2O_3/20 wt% glassy carbon pellets and MIP tests prior- and post-oxidation of the glassy carbon. a) SEM image of Al_2O_3/20 wt% glassy carbon pellet after sintering in a nitrogen flowing furnace at 1300 °C where spherical glassy carbon particles are dispersed within the pellet's matrix (indicated by the red circles), and MIP cumulative intrusion volume and pore size distribution results, and b) SEM image of the same pellet sintered at 1300 °C in a pO_2= 0.2 atm in nitrogen gas mixture, where the creation of spherical voids is caused by the oxidation of the glassy carbon (indicated by the green circles), confirmed by MIP cumulative intrusion volume and pore size distribution results.

Even though the sacrificial defect-inducing materials are easily removed from the Al_2O_3 support at temperatures equal and greater than 600 °C in the presence of oxygen, the presence of molten salt has been found to protect ceramic powders from oxidation

during high-temperature processing [145,276]. In this case, molten carbonate could prevent the oxidation of the sacrificial defect-inducing material. Therefore, it was necessary to determine the time required for the removal of the sacrificial defect-inducing materials in the presence of molten carbonate. TGA experiments conducted on samples containing 1) carbon fibre, Al_2O_3 and the ternary eutectic carbonate mixture (Figure 5.9a), and 2) 20 wt% glassy carbon powder mixed with Al_2O_3 and the ternary eutectic carbonate mixture (Figure 5.9b), were performed at 600 °C in a pO_2= 0.2 atm in nitrogen atmosphere. The presence of the 20:60:20 carbonate powder was not investigated as the m.p. of this melt (640 °C) is above the oxidation temperature used for the removal of the sacrificial defect-inducing material (600 °C). Instead, the above TGA samples were compared to their equivalent mixtures without the presence of carbonate. Hereafter, the Li_2CO_3: Na_2CO_3: K_2CO_3=20:60:20 mole ratio carbonate mixture used is referred to as the 20:60:20 carbonate mixture.

For the carbon fibre mixed with Al_2O_3 powders sample (without the presence of carbonate), the carbon fibre was oxidised after 18 h at 600 °C (Figure 5.9a). The average oxidation rate was 1.6×10^{-5} mol m^{-3} s^{-1}, thus a minimum of 9h was required for the oxidation of the carbon fibre inside an Al_2O_3/carbon fibre pellet (carbon fibre weigh ~0.034 g). With the addition of the ternary eutectic carbonate mixture powder to the Al_2O_3 powder and carbon fibre sample, the required oxidation rate for the carbon fibre decreased to 1.55×10^{-5} mol m^{-3} s^{-1} at 600 °C (~2 wt% loss was attributed to carbonate decomposition [190]). As a result, the oxidation time of the carbon fibre in the presence of the eutectic mixture of carbonate increased to 22.5 h. For the 20 wt% glassy carbon powders mixed with Al_2O_3 powders sample, the glassy carbon powder contained in the sample was oxidised after 0.3 h at 600 °C (Figure 5.9b). The oxidation rate was 11.4 mol m^{-3} s^{-1}, suggesting that the minimum time required to oxidize the glassy carbon inside an Al_2O_3/20 wt% glassy carbon pellet (~0.2 g) would be 3.5 h. When the ternary eutectic mixture of carbonate was added to the sample, the oxidation rate for glassy carbon decreased to 1.55 mol m^{-3} s^{-1}, requiring 15 h of oxidation at 600 °C (~2 wt% loss was attributed to carbonate decomposition [190]). Hence, for the Al_2O_3/20 wt% glassy carbon pellets used in the self-healing experiments, the required time for the oxidation of the glassy carbon was 23.5 h. Taking into consideration the oxidation time for each mixture, the oxidation of the self-healing process was set between 20 and 24 h (24h when the ternary eutectic mixture was used) to ensure the decomposition of the sacrificial defect-inducing material. The volume used to calculate

the concentration of the carbon fibre was based on the carbon fibre density, 1.7 g m^{-3}, whereas the volume of the glassy carbon powder was calculated based on its surface area (m^2 g^{-1}), calculated using the Brunauer – Emmett – Teller (BET) technique by Braun *et al.* [277].

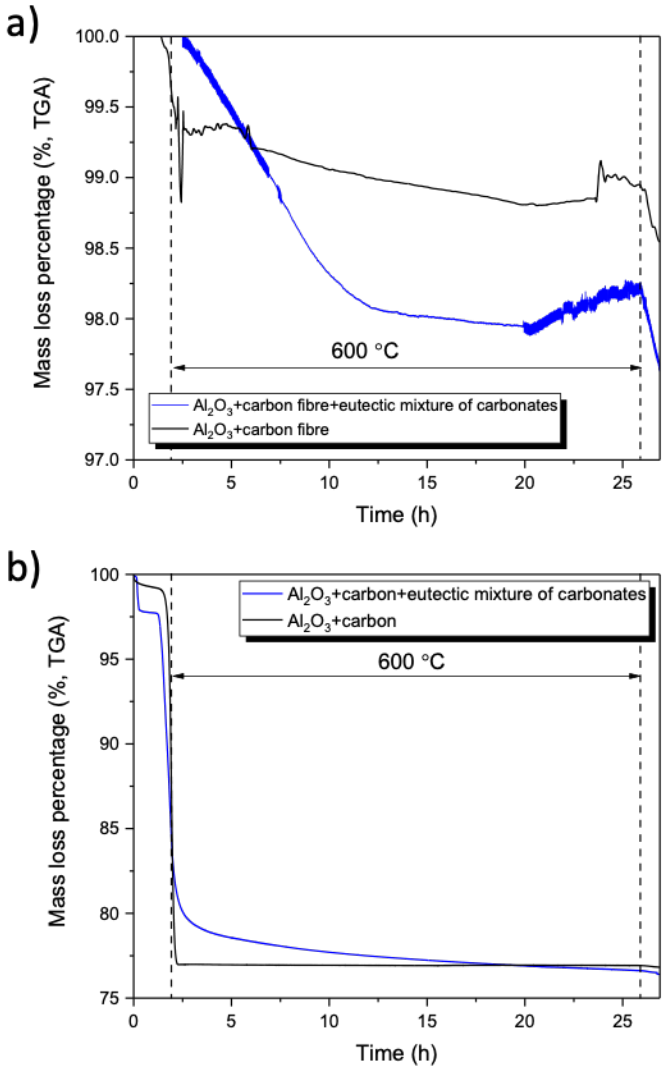

Figure 5.9: TGA measurements on a sample containing Al_2O_3 and sacrificial defect-inducing materials (black) and on a sample containing Al_2O_3, sacrificial defect-inducing materials and carbonate (blue). a) Mass loss percentage (%) over time (h) for a sample containing carbon fibre, Al_2O_3 and the ternary eutectic carbonate mixture (blue), and for a sample containing Al_2O_3 and carbon fibre (black). b) Mass loss percentage (%) over time (h) for a sample containing 20 wt% glassy carbon, Al_2O_3 and the ternary eutectic carbonate mixture (blue), and for a sample containing Al_2O_3 and 20 wt% glassy carbon (black).

5.3.3 Conditions for the molten carbonate phase to self-heal the created defect

In addition to ensuring the removal of the sacrificial defect-inducing material under oxidative conditions, the molten carbonate phase inside the ceramic support need to show sufficient wetting on the Al_2O_3 surface for self-healing to occur. The wetting of the ternary eutectic and the 20:60:20 mole ratio carbonate mixture on a dense Al_2O_3

pellet was optically observed and image recorded during the melting of the carbonate phase. By determining the contact angle (θ) between the carbonate melt and the dense Al_2O_3 support, it was possible to calculate the surface tension, spreading coefficient and maximum pore radius the carbonate can be withheld within the ceramic support, under the transmembrane operating pressure. As can be seen in Figure 5.10a, the melting of the 20:60:20 mole ratio carbonate mixture occurred at 630 °C and the final wetting angle of 1° (calculated by ImageJ as the average of 10 measurements, using the contact angle software) was achieved at 670 °C. For the ternary eutectic carbonate mixture, the melting occurred after dwelling at 400 °C for 20 min, and the contact angle between the liquid-solid interface was 3° (calculated by ImageJ as the average of 10 measurements, using the contact angle software) (Figure 5.10b). For θ<10°, the solid surface is considered to be highly wetted by the liquid phase [278].

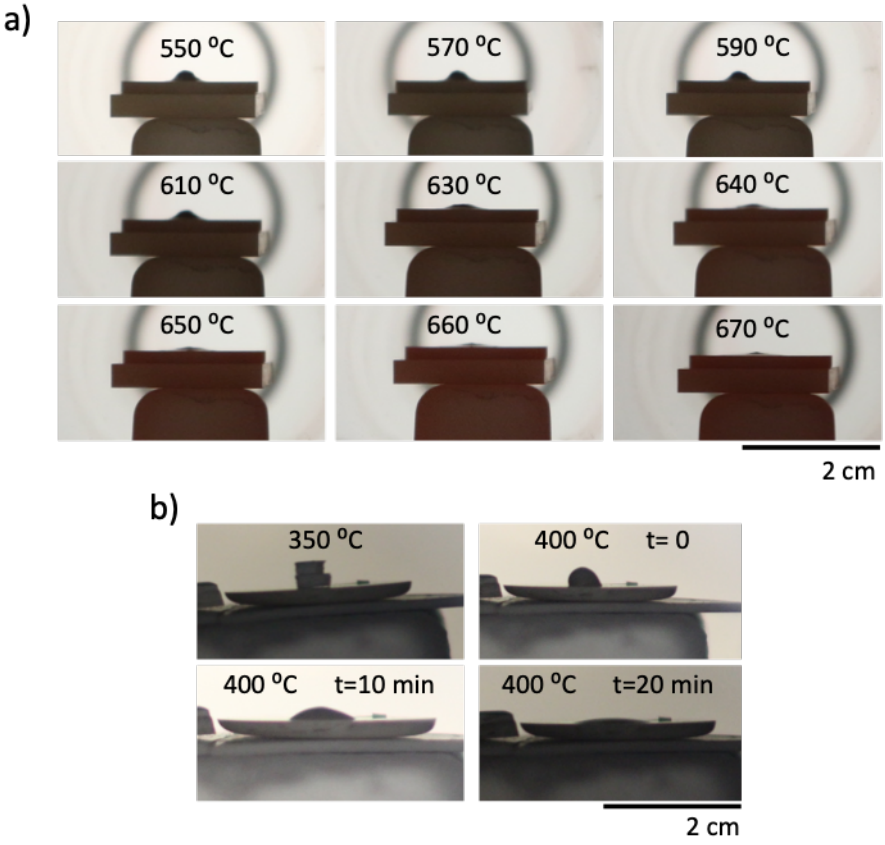

Figure 5.10: Wettability measurements of a Li_2CO_3 : Na_2CO_3 : K_2CO_3 = 20 : 60 : 20 mole ratio carbonate mixture and a ternary eutectic carbonate mixture on a dense Al_2O_3 pellet in a controlled atmosphere furnace with a custom-made quartz window. a) Measurements of the contact angle of the Li_2CO_3 : Na_2CO_3 : K_2CO_3 = 20 : 60 : 20 mole ratio carbonate mixture on a dense Al_2O_3 pellet at 550, 570, 590, 610, 630, 640, 650, 660, and 670 °C and b) measurements of the contact angle of the eutectic carbonate mixture on a dense Al_2O_3 pellet at 350 and 400 °C, at t=10, 20 and 30 min.

At 700 °C, the surface tension for the 20:60:20 carbonate melt is 209 mJ m^{-2} whereas for the eutectic carbonate melt the surface tension is slightly higher, reaching 215 mJ m^{-2} [151,193]. The solid-gas surface tension for Al_2O_3 is 1,790 mJ m^{-2} at 700 °C [279], which is one order of magnitude higher than the surface tension of the molten-carbonate mixtures. The difference between the surface tension of the Al_2O_3 and molten carbonate phases enhances the gas-melt contact area which in turn leads to high wetting, achieved by very low values of contact angles and spreading [94].

The spreading coefficient for the 20:60:20 mole ratio carbonate mixture and the eutectic carbonate mixture are -2.4×10^{-4} for both melts and were calculated based on Eq. 2.19 (chapter 2, section 2.3.3) [197]. The close to zero value for the spreading coefficient for both melts, indicates that the molten carbonate achieve a close to complete spreading on the Al_2O_3 surface at equilibrium conditions [196]. Spreading is important for self-healing, as carbonate needs to be mobile, redistribute and spread inside the matrix in order to fill created defects.

Even though the molten carbonate is highly wetting on the Al_2O_3 support, there are limitations in the width and length of defects they can self-heal. Therefore, it is essential to calculate the limit of pore diameter the molten salt can be held within at a given transmembrane pressure. Assuming the oxidation of the carbon fibre would result in the formation of a straight, throughout pore inside the membrane, it was possible to calculate the maximum pore radius that can hold the carbonate under the given operating transmembrane pressure using the Laplace equation. The Laplace equation (chapter 2, section 2.3.3, Eq. 2.18) was solved for the radius of the pore, r [94]:

$$r = \frac{2\sigma\cos\theta}{P_f - P_p} \qquad \text{(Eq. 5.3)}$$

where θ is the contact angle of the molten carbonate, σ is the surface tension (J m^{-2}) and P_f and P_p are the total pressure in the feed and permeate side, respectively. During the experiments, the pressure of both the feed and the permeate side inlet and outlets were set to 1 atm. However, instrumental systematic error and random error due to environmental conditions could result to an increase or decrease in the feed and permeate-side pressure by a maximum of 0.5% resulting to a P_f-P_p equal to 0.01 atm. Based on the previously calculated contact angle of each melt on the Al_2O_3 support, the maximum pore radius the molten carbonate can be withheld within was ~410 μm for both carbonate mixtures (Table 5.1). As mentioned in section 5.3.2, the oxidation of the carbon fibre will result in a throughout membrane defect with an

average diameter of 350 μm, which is below the maximum pore diameter limit that the carbonate can be withheld within.

Table 5.1: Maximum pore radius the two molten salt mixtures can be held within the Al_2O_3 supports at the operating transmembrane pressure.

Composition mol% Li_2CO_3 : Na_2CO_3 : K_2CO_3	γ_l (mJ m^{-2}) at 700 °C	Contact angle θ (°)	Max pore radius, r (μm)
20:60:20 (m.p. 640 °C)	209	1 ± 0.5	412
43.5:31.5:25 (eutectic, m.p. ~400 °C)	215	3 ± 1	411

5.3.4 Self-healing of dual-phase Al_2O_3/molten salts pellets by reproducing crack propagation

The permselectivity of the dual-phase membranes prior and post-oxidation of the sacrificial defect-inducing material was investigated using a carbon dioxide and nitrogen feed-gas mixture with equal partial pressures (pCO_2 = 0.5 atm, pN_2 = 0.5 atm) and pure argon as the permeate-side gas (*i.e.* sweep gas), as has been most commonly used in literature for dual-phase membranes. The driving force created due to the absence of carbon dioxide on the permeate side of the membrane allows the permeation of carbon dioxide from the carbon-dioxide rich to the carbon-dioxide lean side of the membrane. Dual-phase membranes in literature with molten carbonate as the liquid phase have been found to provide a carbon dioxide to nitrogen selectivity >1000 [94,100,132]. In this work, carbon dioxide to nitrogen selectivity was calculated prior and post-oxidation of the sacrificial defect-inducing material, to confirm the membrane regained its permselectivity after self-healing of the created defect. In well-sealed and leak-free membranes nitrogen permeation flux is low, close to the limit of the gas detection equipment (0.001 ml min^{-1} cm^{-2}). In this work, permselective membranes had a nitrogen permeation flux that often showed a drift around zero for over 10 h of operation, after subtracting the background contribution for nitrogen. Any detection of nitrogen in the permeate-side outlet that causes a loss of membrane selectivity (*i.e.* nitrogen above detection level) is an indication of a transmembrane leakage due to defect creation or carbonate melt solidification. Carbonate melt solidification results in a decrease in its specific volume, creating voidage in the support's pores, and non-selective carbon dioxide and nitrogen permeation pathways.

For self-healing to be considered successful, the membrane should demonstrate three main regions during its operation:

1) Initially the membrane needs to be permselective to carbon dioxide separation (Region I: light blue colour in Figure 5.11-5.14),

2) then show a clear transmembrane leakage upon the creation of a defect (Region II: white colour in Figure 5.11-5.14),

3) and finally regain its permselectivity towards carbon dioxide after self-healing has occurred (Region III: beige colour in Figure 5.11-5.14).

i. Non-autonomous self-healing in supported molten-salt membranes: carbon fibre as the sacrificial defect-inducing material

The ability of the molten carbonate mixture to self-heal a defect throughout the membrane's thickness created by the oxidation of the carbon fibre, or additional voidage in the membrane's matrix created by the oxidation of the glassy carbon, was originally investigated using the 20:60:20 mole ratio carbonate mixture. The use of this carbonate mixture, that has a melting point of 640 °C, allows the observation of the self-healing process in separate steps, as the melt is solidified during the oxidation of the sacrificial defect-inducing materials, which occurs at 600 °C. Therefore, the membrane is expected to leak due to carbonate solidification, and the already existing leak is expected to increase upon removal of the sacrificial defect-inducing materials during oxidation. Self-healing due to molten carbonate redistribution and spreading will only occur with the increase in operational temperature above the melting point of the carbonate mixture. This type of self-healing is considered intrinsic and non-autonomous as the increase in temperature is the trigger mechanism for self-healing to occur. When the carbon fibre is the sacrificial defect-inducing material in the membrane, a catastrophic throughout membrane defect of 350 μm diameter is expected to occur upon its oxidation. Based on Eq. 5.3 and Table 5.1, the width of this defect lies within the limits the carbonate can spread and self-heal.

Region I: Membrane permselectivity *prior* to defect creation

Initially, with the increase in temperature to 700 °C (feed-side inlet: pCO_2=0.5 atm in nitrogen, permeate-side inlet: pure argon) the membrane showed a carbon dioxide flux of 0.012 ml min^{-1} cm^{-2} with carbon dioxide to nitrogen selectivity >1000 after 12 h of operation (1) (Figure 5.11a: 0-12 h). At around 12 h, the operating temperature was

decreased to 600 °C (12-14 h), which is below the melting point of the 20:60:20 melt (m.p. ~ 640 °C). As expected, the membrane lost selectivity due to carbonate solidification (14-17 h), which resulted in non-selective permeation of both carbon dioxide and nitrogen, reaching fluxes of 7.3 ml min^{-1} cm^{-2} for both gases at 600 °C (2).

Region II: Defect creation

At ~18 h the feed and permeate-side gases were switched to oxygen containing gases on both sides of the membrane (3), allowing for the oxidation of the sacrificial defect-inducing material from both sides of the membrane (Figure 5.11a: 17-38 h). A small amount of carbon dioxide (pCO_2=0.001 atm) was also added on the feed side of the membrane to avoid any carbonate decomposition. During the first three hours of carbon-fibre oxidation (Figure 5.11a: 17-20 h) carbon dioxide flux increased, as carbon dioxide was released during oxidation. After the first three hours of oxidation, carbon dioxide flux reached steady state, followed by a nitrogen flux increase; suggesting the carbon fibre had been oxidised and an additional leak pathway for nitrogen had been created. It is important to note that during oxidation, the driving force for the carbon dioxide, pCO_2 = 0.01 atm, was significantly lower than the driving force for carbon dioxide during the permselectivity step (1), pCO_2 = 0.5 atm. Moreover, the driving force for nitrogen was significantly higher during oxidation (pN_2 = 0.796 atm) than the driving force for nitrogen during the permselectivity step (1) (pN_2 = 0.5 atm). Post-oxidation of the carbon fibre (38 h), the feed and permeate-side inlets were switched back to pCO_2 of 0.5 atm in nitrogen and pure argon, respectively, in order to compare the permselectivity of the membrane prior and post-oxidation of the carbon fibre (4). The creation of a throughout defect was confirmed at 600 ºC (Figure 5.11a: 38-46 h) where the leak caused by the oxidation of the carbon fibre increased the previously observed flux of carbon dioxide and nitrogen at 600 ºC (12-17 h), only attributed to the solidification of the molten phase, by 40%.

Region III: Self-healing of created defect

By increasing the temperature to 700 ºC, and re-melting the carbonate mixture, the membrane was finally tested against the self-healing properties of the melt. Carbon dioxide flux was restored to 0.01 ml min^{-1} cm^{-2}, as shown in Figure 5.11c, between 46 and 52.8 h, showing a minor decrease from the originally reported value of 0.012 ml min^{-1} cm^{-2} (Figure 5.11b), but ultimately the membrane regained its

permselectivity towards carbon dioxide, achieving its previous carbon dioxide to nitrogen selectivity>1000.

The removal of the sacrificial defect-inducing carbon fibre after the oxidation process, was also confirmed by SEM imaging of the self-healing membrane at room temperature; after removing the membrane from the permeation apparatus (Figure 5.11a). The resulting membrane after the oxidation of the carbon fibre, infiltrated with the 20:60:20 was cut in half and the cross-section of the membrane was sanded with a sanding paper in order to reveal the part where the carbon fibre was initially incorporated. As can be seen in Figure 5.11a the carbon fibre was fully oxidised in the presence of the 20:60:20 melt, creating a throughout membrane defect of approximately 350 μm diameter.

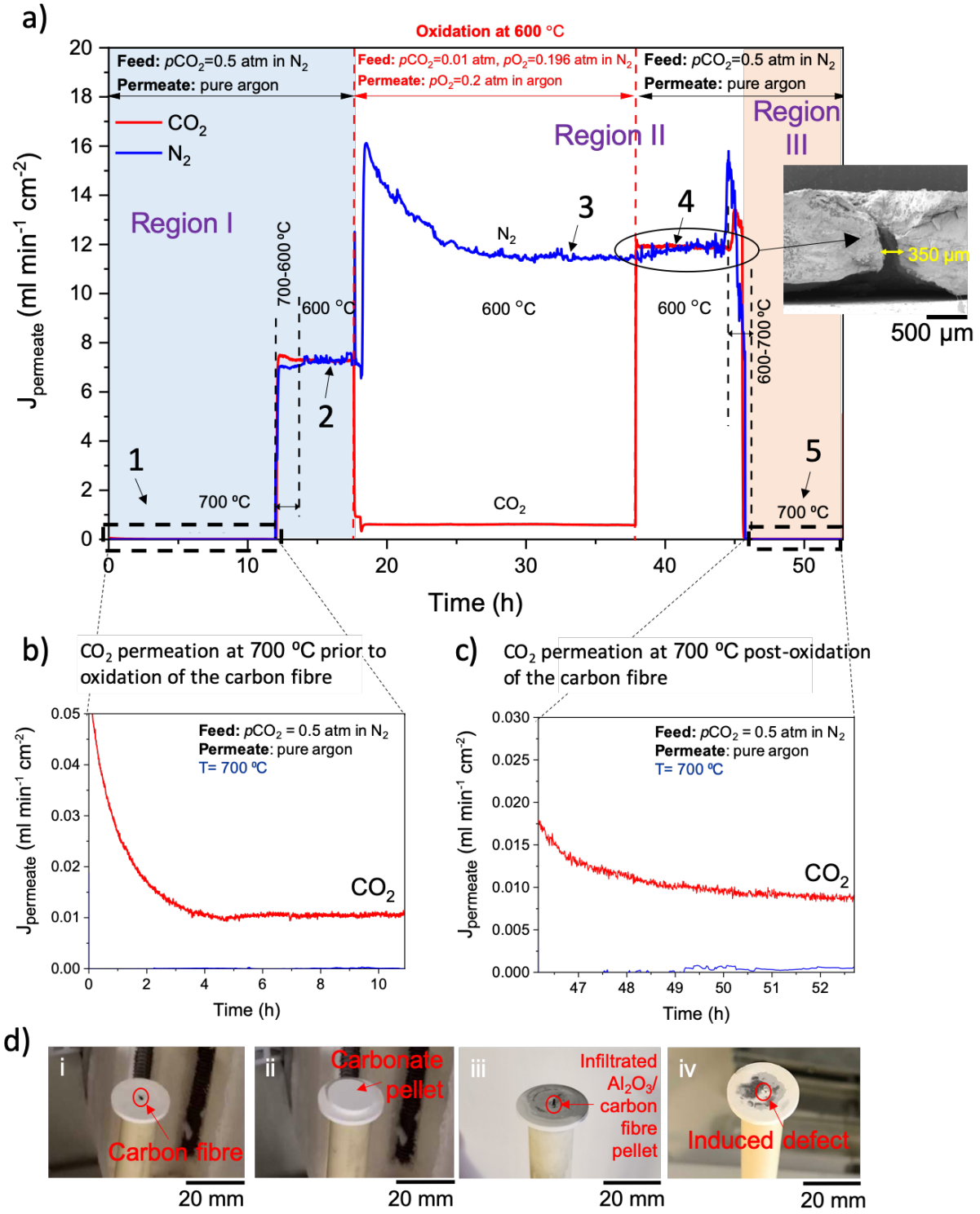

Figure 5.11: Non-autonomous intrinsic self-healing of an Al_2O_3/carbon fibre membrane infiltrated with the Li_2CO_3 : Na_2CO_3 : K_2CO_3 = 20 : 60 : 20 mole ratio carbonate mixture (m.p. ~640 °C). (a) Carbon dioxide and nitrogen fluxes (ml min^{-1} cm^{-2}) versus time (h) on the permeate side of a self-healing dual-phase membrane with an incorporated carbon fibre as the sacrificial defect-inducing material and 20:60:20 mole ratio as the carbonate mixture. **0-12h:** membrane tested for carbon dioxide permeation at 700 ºC, followed by temperature decrease to 600 ºC (12-14h). **14-17h:** carbonate solidification. **17-38h:** oxidation of the carbon fibre at 600 ºC. **38-46h:** permeation at 600 ºC. **46-52h:** permselectivity of the dual-phase membrane post-oxidation of the carbon fibre, at 700 ºC. (b) Carbon dioxide and nitrogen flux through a dual-phase Al_2O_3/carbon fibre membrane at 700 ºC prior to the oxidation of the carbon fibre. (c) Carbon dioxide and nitrogen flux through the aforementioned membrane post-

oxidation of the carbon fibre, at 700 º. (d) Digital images of an Al_2O_3/carbon fibre self-healing pellet after each experimental step: i) Al_2O_3/carbon fibre pellet mounted on an alumina tube, ii) Al_2O_3/carbon fibre pellet with a carbonate pellet on top, iii) infiltrated Al_2O_3/carbon fibre pellet, iv) infiltrated Al_2O_3 pellet after the oxidation of the carbon fibre.

ii. Non-autonomous self-healing in supported molten-salt membranes: dispersed glassy carbon as the sacrificial defect-inducing material

Subsequently to understanding how the molten carbonate phase can self-heal an operating membrane after a controlled-induced defect throughout the membrane's thickness, the ability of the molten phase to self-heal randomly created porosity in the form of voidage within the membrane's matrix was also investigated. In this case, the oxidation of the sacrificial defect-inducing material will result in significant increase in the membrane's porosity, ~18%, but the voidage created is not controlled, rather, it is dispersed throughout the membrane.

Region I: Membrane permselectivity *prior* to defect creation

Al_2O_3/20 wt% glassy carbon membranes infiltrated with the 20:60:20 carbonate mixture (m.p. ~ 640 °C) were initially tested towards carbon dioxide separation at 700 °C (1) using pCO_2=0.5 atm in nitrogen and pure argon as the feed and permeate-side gases respectively (Figure 5.12a: 0-10 h). The achieved carbon dioxide flux was 0.13 ml min^{-1} cm^{-2}, and the membrane showed a carbon dioxide to nitrogen selectivity of 350 at 700 °C (1). The temperature was then decreased to 600 °C (Figure 5.12a: 10-12 h), which is below the melting point of the 20:60:20 melt (m.p. ~ 640 °C). The decrease in temperature resulted in carbonate solidification, which resulted nitrogen and carbon dioxide leakage at 11h.

Region II: Defect creation

The glassy carbon was then oxidized at 600 °C (2) in an oxygen containing atmosphere (feed: pCO_2=0.01 atm, pO_2=0.196 atm in nitrogen, permeate: pO_2=0.2 atm in argon) (Figure 5.12a: 12-33h). A small amount of carbon dioxide (pCO_2=0.001 atm) was added on the feed side of the membrane to avoid any carbonate decomposition, as in the previous self-healing experiment (Figure 5.11). During the first three hours of glassy carbon oxidation (12-15 h, Figure 5.12a), nitrogen flux increased exponentially, as additional porosity was created in the Al_2O_3 pellet. At 28h (Figure 5.12a), glassy carbon appeared to have oxidised completely, with the permeating flux reaching a plateau at 0.63 ml min^{-1} cm^{-2} for nitrogen and

0.05 ml min^{-1} cm^{-2} for carbon dioxide. The higher nitrogen flux during the oxidation step is attributed to the significantly higher driving force for nitrogen during oxidation (pN_2 = 0.796 atm), compared to the significantly lower carbon dioxide driving force during oxidation (pCO_2 = 0.01 atm). Post-oxidation of the glassy carbon (33 h, Figure 5.12a), the feed and permeate-side inlets were switched back to a pCO_2 of 0.5 atm in nitrogen and pure argon, respectively (3) while the operating temperature remained at 600 °C. The additional porosity created from the oxidation of the glassy carbon inside the Al_2O_3 pellet, in addition to carbonate solidification at that temperature, led to a carbon dioxide and nitrogen transmembrane leakage of ~0.65 ml min^{-1} cm^{-2} (Figure 5.12a: 33-43h).

Region III: Self-healing of created defect

The temperature was then increased to 700 °C (43-45 h), allowing the carbonate to melt and fill the additional porosity created by the oxidation of the glassy carbon (4) (Figure 5.12a: 45-76h). The membrane did not regain its permselectivity towards carbon dioxide separation immediately after increasing the temperature to 700 °C, but instead, showed a nitrogen and carbon dioxide leakage from 45 to 70 h. The membrane regained its permselectivity towards carbon dioxide separation at 70 h (4) suggesting that self-healing of the membrane is delayed due to the increase in porosity from 40% to 58% after oxidation. The carbon dioxide flux achieved after the self-healing of the membrane was 0.14 ml min^{-1} cm^{-2} with a carbon dioxide to nitrogen selectivity of 300.

The resulting membrane after the oxidation of the glassy carbon, infiltrated with the 20:60:20 carbonate mixture (Figure 5.12a) was also cut in half and observed by SEM imaging after it was removed from the permeation apparatus. The glassy carbon was fully oxidised, creating sphere-like micro-voids (2-5 μm), and subsequently additional porosity, inside the membrane's matrix as can be seen in Figure 5.12a. The solidified carbonate is represented by the needle-shaped crystals escaping the micro-porosity of the Al_2O_3 and entering the sphere-like micro-voids. The SEM images were taken from the middle part of the Al_2O_3/glassy carbon pellet after oxidation.

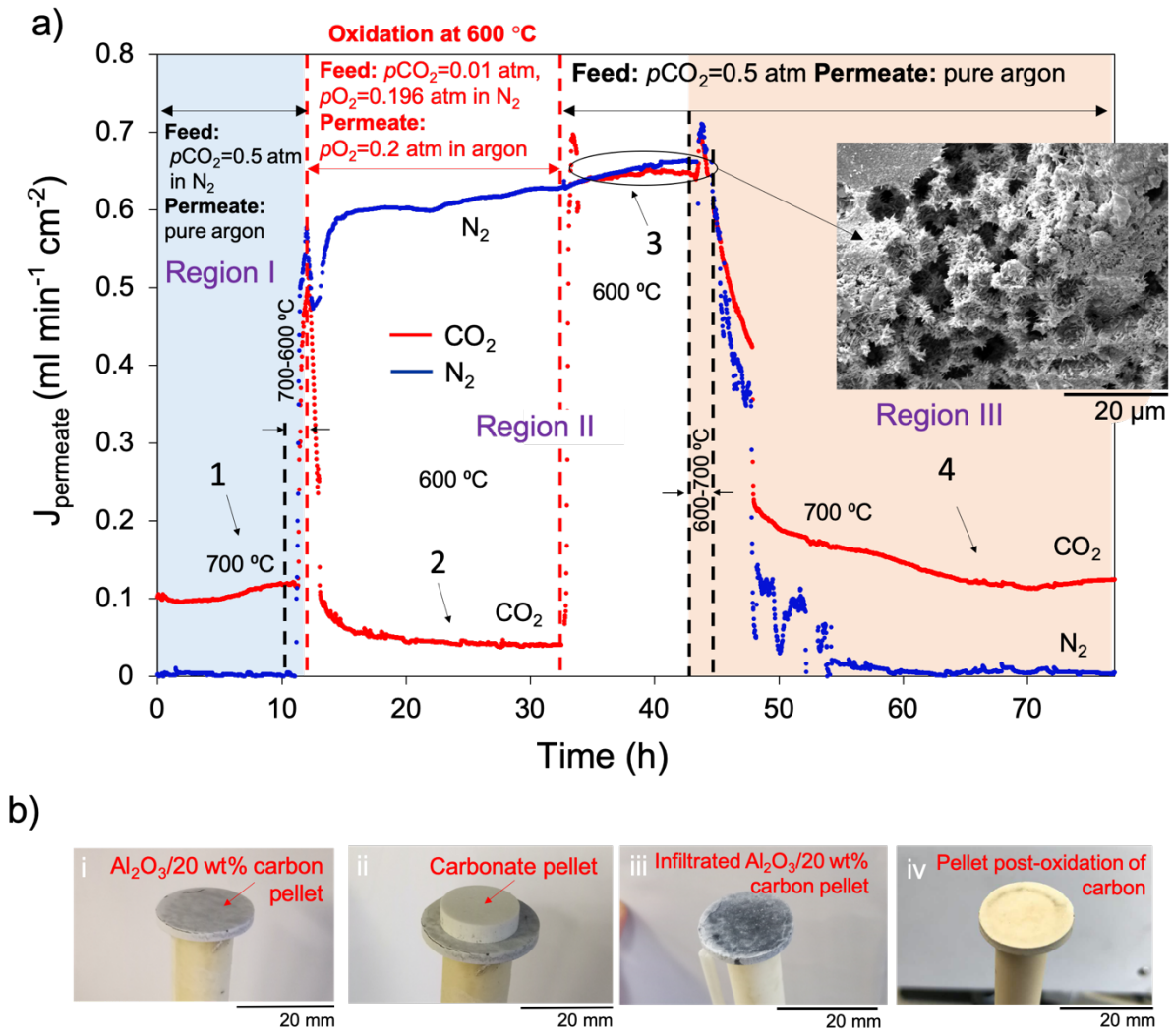

Figure 5.12: Non-autonomous intrinsic self-healing of Al_2O_3/20 wt% glassy carbon membranes infiltrated with the Li_2CO_3 : Na_2CO_3 : K_2CO_3 = 20 : 60 : 20 mole ratio carbonate mixture (m.p. ~640 °C). a) Carbon dioxide and nitrogen fluxes (ml min^{-1} cm^{-2}) versus time (h) on the permeate side of a self-healing dual-phase membrane with dispersed glassy carbon as the sacrificial defect-inducing material and 20:60:20 carbonate mixture as the molten salt phase. **0-10h:** membrane tested for carbon dioxide permeation at 700 ºC, followed by temperature decrease to 600 ºC (10-12 h). **12-33h:** oxidation of the glassy carbon at 600 ºC. **33-43h:** permeation at 600 ºC. **43-76h:** permselectivity of the dual-phase membrane post-oxidation of the glassy carbon, at 700 ºC. b) Digital images of an Al_2O_3/20 wt% glassy carbon pellet after each experimental step: a) Al_2O_3/20 wt% glassy carbon pellet mounted on an alumina tube, b) Al_2O_3/20 wt% glassy carbon pellet with a carbonate pellet on top, c) infiltrated Al_2O_3/20 wt% glassy carbon pellet, d) infiltrated Al_2O_3 pellet after the oxidation of the dispersed carbon.

iii. Autonomous self-healing in supported molten-salt membranes: carbon fibre as the sacrificial defect-inducing material

After investigating the self-healing capability of a 20:60:20 carbonate melt (m.p. ~ 640 °C), the process to determine the autonomous self-healing of a dual-phase ceramic molten-salt membrane was tested with the use of the eutectic carbonate mixture (m.p. ~400 °C). This way, the molten carbonate phase remains molten during the oxidation, and the redistribution and spreading of the melt, leading to self-healing within the membrane, occurs simultaneously with the oxidation process. Since the ternary eutectic carbonate mixture is molten during the oxidation process, no nitrogen leakage should be observed on the permeate side of the membrane during the oxidation. For the first autonomous self-healing membrane, an Al_2O_3/carbon fibre pellet, infiltrated with the eutectic mixture of carbonate was used (m.p. ~ 400 °C).

Region I: Membrane permselectivity *prior* to defect creation

As in the previous experiments, the temperature of the membrane was initially increased to 700 °C using pCO_2=0.5 atm in nitrogen on the feed and argon on the permeate side (1), to ensure the permselectivity of the membrane towards carbon dioxide separation (Figure 5.13: 0-9 h). The membrane reached a carbon dioxide flux of 0.012 ml min^{-1} cm^{-2}, and a carbon dioxide to nitrogen selectivity of 340.

Region II: Defect creation

With the decrease in temperature to 600 °C (oxidation temperature) no nitrogen or carbon dioxide leakage was expected to occur (Figure 5.13: 9-11 h), as the operating temperature is above the melting point of the eutectic carbonate mixture. Hence, the gas atmosphere was immediately switched to oxygen containing gases on both sides of the membrane (2), when decreasing the temperature to 600 °C (Figure 5.13: 11-41 h). As expected, the nitrogen flux decreased to ~0 ml min^{-1} cm^{-2} by the end of the oxidation process, as the membrane is permselective to carbon dioxide separation at 600 °C. Carbon dioxide flux was also ~0 ml min^{-1} cm^{-2} as the driving force for carbon dioxide decreases significantly during the oxidation process (pCO_2 = 0.5 atm in the permselective step, decreased to pCO_2 = 0.01 atm during oxidation). The membrane system remained under oxidative conditions for more than 24 h (Figure 5.13: 11-41 h) to ensure the full oxidation of the carbon fibre as suggested by the TGA results.

Region III: Self-healing of created defect

Post-oxidation of the carbon fibre, the feed and permeate-side inlets were switched back to the standard operating conditions for the membrane at 600 °C (3) (pCO_2 of 0.5 atm in nitrogen in the feed and pure argon in the permeate side), resulting in a 0.017 ml min^{-1} cm^{-2} carbon dioxide flux and a carbon dioxide to nitrogen selectivity of 210 (Figure 5.13: 41-62 h). The membrane continued exhibiting good permselectivity after increasing the temperature to 700 °C (62-64 h) with a carbon dioxide flux reaching 0.018 ml min^{-1} cm^{-2} and a selectivity of 280 (4) (Figure 5.13: 64-77 h). In order to investigate whether the membrane would regain its integrity after an additional cooling and heating cycle, the temperature was decreased to 350 °C (77-83 h), where both carbon dioxide and nitrogen leakage were observed (5), due to the solidification of the melt and the leak-pathway created by the oxidation of the carbon fibre (Figure 5.13: 83-94 h). Finally, the temperature was increased to 700 °C (6) (94-100 h), where carbon dioxide flux and selectivity were restored (Figure 5.13: 100-107 h). The final heating cycle shows that the redistribution and spreading of the carbonate after melting, can restore the membrane's permselectivity even when undergoing thermal cycling.

The oxidation of the carbon fibre was also confirmed by SEM imaging, as can be seen in Figure 5.13. The carbon fibre was fully oxidised in the presence of the eutectic carbonate mixture (membrane cut in half and polished after its removal from the permeation apparatus), creating a throughout membrane defect of approximately 350 μm diameter.

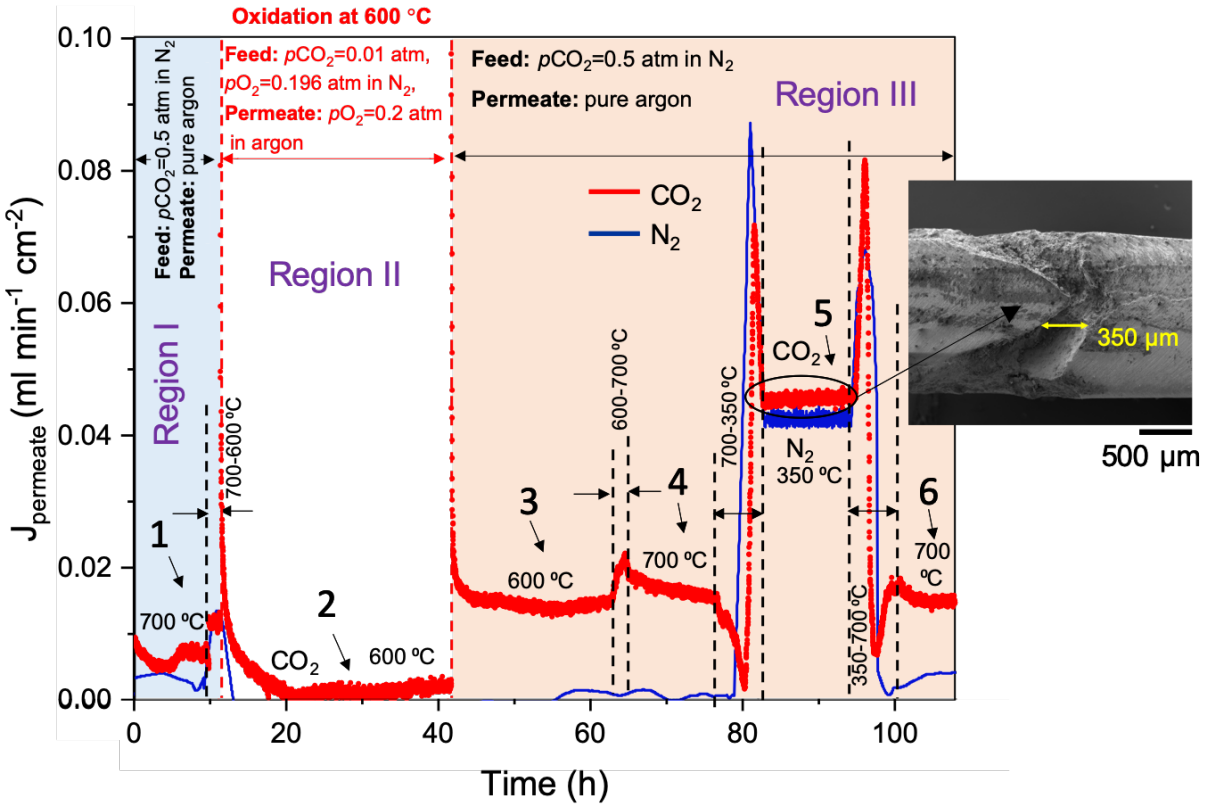

Figure 5.13: Intrinsic and autonomous self-healing of Al_2O_3/carbon fibre membrane infiltrated with the eutectic carbonate mixture (m.p. ~ 400 °C). (a) Carbon dioxide and nitrogen fluxes (ml min^{-1} cm^{-2}) versus time (h) on the permeate side of a self-healing dual-phase membrane with an incorporated carbon fibre as the sacrificial defect-inducing material and eutectic carbonate mixture as the molten salt phase. **0-9h:** membrane tested for carbon dioxide permeation at 700 ºC, followed by temperature decrease to 600 ºC (9-11h). **11-41h:** oxidation of the carbon fibre at 600 ºC. **41-62h:** permselectivity of the dual-phase membrane post-oxidation of the carbon fibre, at 600 ºC, followed by temperature increase to 700 ºC (62-64h). **64-77h:** permselectivity of the dual-phase membrane post-oxidation of the carbon fibre, at 700 ºC, followed by temperature decrease to 350 ºC (77-83h). **83-94h:** nitrogen and carbon dioxide flux when the membrane has cooled down to 350 ºC, carbonate solidification and defect from the oxidation of the carbon fibre, followed by temperature increase to 700 ºC (94-100). **100-107h:** permselectivity of the dual-phase membrane post-oxidation of the carbon fibre, at 700 ºC.

iv. Autonomous self-healing in supported molten-salt membranes: dispersed glassy carbon as the sacrificial defect-inducing material

Al_2O_3/20 wt% glassy carbon pellets infiltrated with the eutectic carbonate mixture (m.p. ~ 400 °C) were also used, in order to demonstrate intrinsic and autonomous self-healing of randomly created porosity inside the pellet, in the form of voidage.

Region I: Membrane permselectivity

During the first permselectivity step (1) (pCO_2 of 0.5 atm nitrogen in the feed side and pure argon in the permeate side), the carbon dioxide flux on the permeate side of the membrane reached 0.01 ml min^{-1} cm^{-2} at 700 °C (Figure 5.14b: 0-12 h) with a carbon dioxide to nitrogen selectivity>1000. The temperature was then decreased to 600 °C (12-14 h) for the oxidation of the glassy carbon (Figure 5.14a).

Region II: Defect creation

With the decrease in temperature to 600 °C (oxidation temperature) no nitrogen or carbon dioxide leakage was expected to occur, as the operating temperature is above the melting point of the eutectic carbonate mixture. Hence, the gas atmosphere was immediately switched to oxygen containing gases on both sides of the membrane (2) in order to oxidise the glassy carbon (Figure 5.14a: 14-36 h). At the start of the oxidation process, a nitrogen leakage was observed that reached a maximum of 1 ml min^{-1} cm^{-2} implying that even though the carbonate mixture was molten during that stage, the carbonate spreading did not happen fast enough to cover the newly created porosity from the oxidation of the glassy carbon. However, at 32 h (18 h after the start of the oxidation process) the nitrogen and carbon dioxide leak decreased to 0.009 and 0.006 ml min^{-1} cm^{-2} (detection limit: 0.001 ml min^{-1} cm^{-2}), respectively, suggesting that the molten carbonate phase had spread to infiltrate the additional randomly created voidage.

Region III: Self-healing of created defect

Post-oxidation of the glassy carbon, the temperature was increased to 700 °C (36-38 h), and the gases were switched back to a pCO_2 of 0.5 atm nitrogen in the feed side and pure argon in the permeate side (3). The membrane suffered from a carbon dioxide and nitrogen leak from 38 h to 50 h (Figure 5.14) but ultimately regained its permeselectivity towards carbon dioxide separation. Similar to the Al_2O_3/20 wt% glassy carbon membrane infiltrated with the 20:60:20 carbonate mixture, the volume of the

additional created porosity seems to delay the self-healing but does not prevent the membrane from regaining its permselectivity. The carbon dioxide flux after the self-healing reached 0.026 ml min^{-1} cm^{-2} with a carbon dioxide over nitrogen selectivity of 350 (Figure 5.14b: 38-52 h). It was also observed that the carbon dioxide flux increased by an order of magnitude after the autonomous self-healing of the created voidage, compared to its original flux when first tested towards carbon dioxide permselectivity. As mentioned earlier, the Al_2O_3/20 wt% glassy carbon pellet was initially infiltrated with the eutectic melt, aiming to fill the entire porosity of the pellet support, ~40 %, which was increased to ~58 % following the oxidation of the glassy carbon. Since the carbon dioxide permeselectivity of the membrane was not only restored after the autonomous self-healing process, but the carbon dioxide flux was also increased, it is implied that the molten carbonate reorganised during that period, resulting in a thinner carbonate layer inside the membrane support, which is expected to produce higher fluxes. Flux improvement due to the restriction of the molten phase in a thin layer inside the pellet support, due to carbonate wetting, has also been previously demonstrated in literature [132,133]. The membrane was also subjected to thermal cycling following the self-healing process (steps (4) and (5) in Figure 5.14), without losing its permselectivity. The operating temperature was decreased to 350 °C (52-58 h), where the non-selective permeation of carbon dioxide (7.5 ml min^{-1} cm^{-2}) and nitrogen (7.3 ml min^{-1} cm^{-2}) was observed (4), due to carbonate solidification and the oxidation of the glassy carbon (Figure 5.14: 58-70 h). With the increase of temperature to 700 °C (70-76 h) for a second time after the oxidation process, the membrane showed a carbon dioxide flux of 0.028 ml min^{-1} cm^{-2} and a carbon dioxide over nitrogen selectivity slightly above 350 (5) (Figure 5.14: 76-84 h).

The resulting membrane after the oxidation of the glassy carbon, infiltrated with the eutectic carbonate mixture (Figure 5.14) was also cut in half and observed by SEM imaging after it was removed from the permeation apparatus. The glassy carbon was fully oxidised, creating sphere-like micro-voids (2-5 μm), and subsequently additional porosity, inside the membrane's matrix as can be seen in Figure 5.14. The solidified carbonate is represented by the needle-shaped crystals escaping the micro-porosity of the Al_2O_3 and entering the sphere-like micro-voids. The SEM images were taken from the middle part of the Al_2O_3/glassy carbon pellet after oxidation.

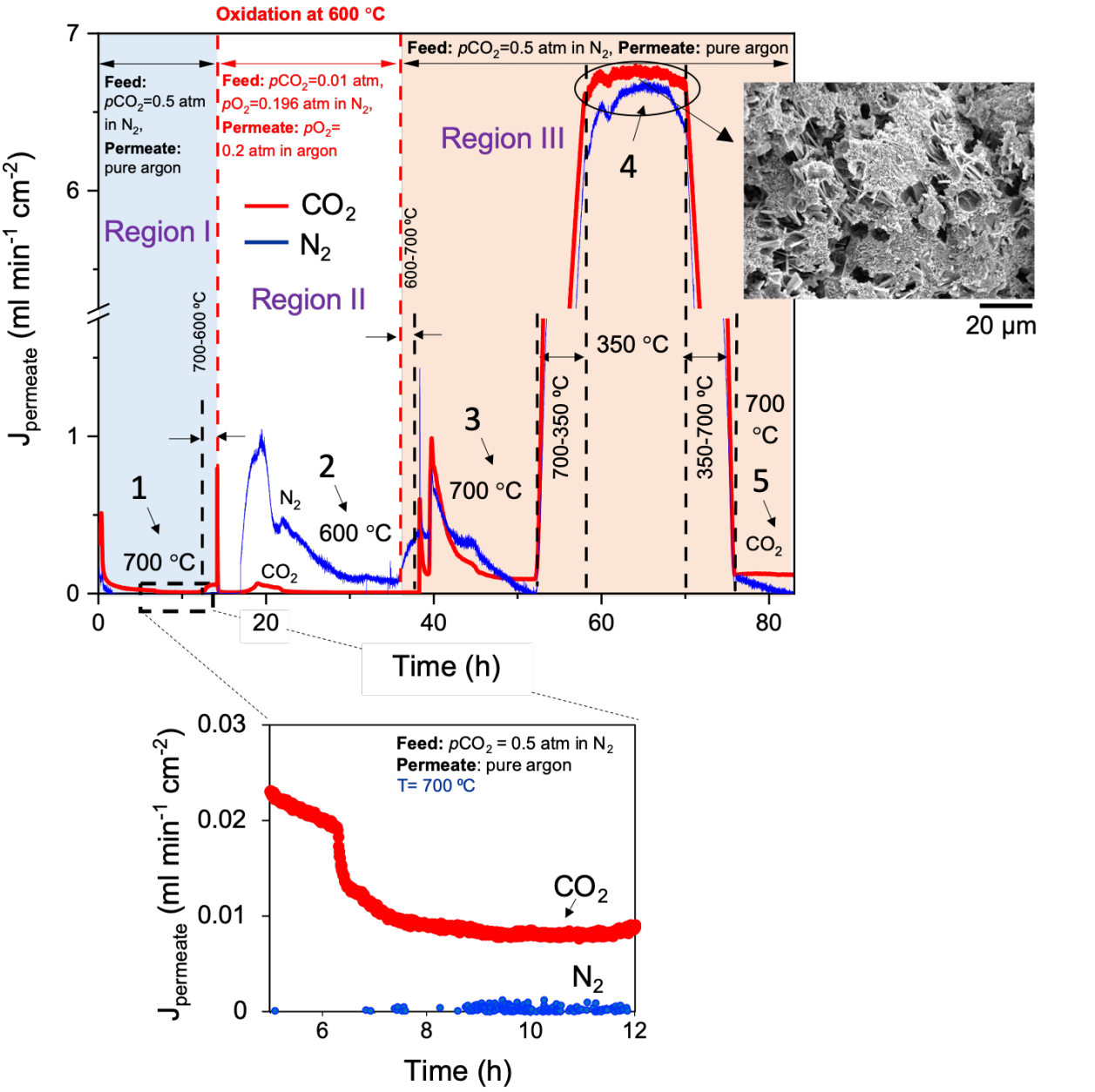

Figure 5.14: Autonomous self-healing experiment for Al_2O_3/20 wt% glassy carbon membranes infiltrated with the eutectic mixture of carbonate (m.p. ~ 400 °C). Carbon dioxide and nitrogen fluxes (ml min^{-1} cm^{-2}) versus time (h) on the permeate side of a self-healing dual-phase membrane with dispersed glassy carbon as the sacrificial defect-inducing material and the eutectic carbonates mixture as the molten salt phase. **0-12h:** membrane tested for carbon dioxide permeation at 700 ºC, followed by temperature decrease to 600 ºC (12-14h). **14-36h:** oxidation of the glassy carbon at 600 ºC. **36-38h:** temperature increase to 700 ºC. **38-52h:** permselectivity of the dual-phase membrane post-oxidation of the carbon fibre, at 700 ºC.**52-58h**: temperature decrease to 350 ºC. **58-70h:** carbonate solidification. **70-76h**: temperature increase to 700 ºC. **76-84h:** permselectivity of the dual-phase membrane post-oxidation of the carbon fibre, at 700 ºC.

5.4 Conclusions

By exploiting the wettability of molten carbonate on Al_2O_3 supports, the first intrinsic and autonomous self-healing dual phase membrane for carbon dioxide separation, with a pellet geometry, has been developed. The self-healing concept was initially investigated in a non-autonomously self-healing membrane where the Li_2CO_3:Na_2CO_3:K_2CO_3 =20:60:20 mole ratio carbonate mixture, with a melting point ~ 640 °C was employed as the molten phase. Oxidation of the sacrificial defect-inducing material, occurring at 600 °C, and self-healing of the dual-phase membrane were carried out in separate steps, due to the chosen carbonate mixture's melting point. When carbon fibre was used as the sacrificial defect-inducing material (~0.05% additional porosity and 350 μm defect diameter), membrane operation was immediately restored by re-melting of the carbonate phase after the increase in temperature to 700 °C post-oxidation. When glassy carbon was used as the sacrificial defect-inducing material, the membrane regained its permselectivity towards carbon dioxide separation ~25 h after increasing the temperature to 700 °C and re-melting the carbonate phase post-oxidation. This suggested that self-healing is delayed but is still successful when a substantial additional dispersed porosity, ~18%, is created inside the membrane (2 – 5 μm dispersed spherical void diameter). By using the ternary eutectic carbonate mixture (m.p. ~ 400 °C) as the self-healing phase infiltrated in the pellet, both the oxidation and autonomous self-healing of the membrane occurred at 600 °C. The membrane immediately regained its permselectivity toward carbon dioxide separation post-oxidation of the carbon fibre. Post-oxidation of dispersed glassy carbon, the membrane regained its permselectivity after ~18 h, confirming that the creation of a substantial additional dispersed porosity (~18%) delays self-healing. The ability of the molten phase to self-heal the dual-phase ceramic molten-salt membrane after the creation of a catastrophic defect, as well as thermal cycling, is encouraging for the application of these membranes for long-term carbon dioxide separation at high temperature.

Chapter 6

Conclusions and future work

The purpose of this chapter is to summarise the major findings of this work and make recommendations for future work related to these findings. Therefore, the conclusions from each of the results sections and their connectivity throughout this work, are discussed.

6.1 Conclusions

The preparation of dual-phase ceramic molten-salt hollow-fibre membranes in literature has so far been empirical and uncontrolled, *i.e.* carbonate infiltrated in both packed-pore network and micro-channels by immersion. The uncontrolled DPHFMs have successfully separated carbon dioxide, but due to their preparation method, the separation potential through a DPHFM with an asymmetric structure has not been realised. Moreover, the active surface area for separation in dual-phase membranes, has not been systematically quantified, resulting in inconsistencies in flux calculations amongst different membrane geometries. High carbon dioxide flux is important for the application of dual-phase membranes in NGCC and IGCC processes where a high carbon dioxide capture rate is required. Increasing the active permeate-side surface area in a surface-exchange-limited region, results in increased carbon dioxide flux, as mentioned in chapter 1, section 1.2.5.

To determine the parameters that would result in increased carbon dioxide flux through DPHFMs, a model crucible dual-phase membrane system with a nominally electrically insulating support, *i.e.* Al_2O_3, can be used. Establishing the rate-limiting steps for carbon dioxide flux over a range of operating temperatures, helped identify the temperature region where membrane operation is surface-exchange-limited. It was found that membrane operation was surface-exchange limited between 500 and 750 °C and bulk-diffusion-limited at temperatures above 750 °C, following a sigmoidal curve model. The flux *versus* temperature model also predicted the maximum flux that can be achieved through the model-crucible membranes. By varying the molten carbonate thickness in the model crucible membrane system, it was also possible to determine a critical length of 750 µm for this type of membrane.

To increase the active, permeate-side surface area for DPHFMs, a method to characterise and control the distribution of carbonate in the hollow fibre supports was developed. In this work, supports with a porosity of ~60% and a mechanical strength above 70 MPa were considered as the best candidates for the preparation of DPHFMs as they provide sufficient porous volume for the incorporation of the carbonate phase and sufficient mechanical strength in applications where the feed-side pressure is above atmospheric. The novel two-step coating method developed, allowed control over the quantity and distribution of carbonate infiltrated inside the hollow fibre supports. The quantity of carbonate required to fill the porosity of the packed-pore network without infiltrating the micro-channels of a hollow fibre support can be

identified through MIP analysis of the hollow fibre supports. To retain the carbonate in the packed-pore network of the hollow-fibre supports, carbonate infiltration occurred from the outer towards the inner/lumen side of the hollow fibre support. Due to the higher capillary forces (chapter 2, section 2.3.3, Eq. 2.17) developed in the packed-pore network (pore size: 0.05 to 0.4 μm), the micro-channels (pore size: 2 to 30 μm) were not infiltrated with carbonate. SEM and EDX analysis of hollow fibre supports infiltrated using the novel two-step coating method at room temperature, was then used to assess the homogeneity of the molten carbonate inside the packed-pore network of the hollow fibre supports. Overall, by developing a method that allows control over the distribution of carbonate inside hollow fibre supports, the micro-channels remain devoid of carbonate while the carbonate is homogeneously infiltrated in the packed-pore network of the hollow fibre supports. This was a significant diversion from current literature, where both micro-channels and packed-pore network were infiltrated with carbonate. The novel two-step method also showed good reproducibility for the preparation of controlled DPHFMs.

The effect of permeate-side surface area on carbon dioxide flux was also determined by comparing the flux of a controlled and uncontrolled distribution Al_2O_3-supported DPHFM operating in a surface-exchange-limited region. Using SEM imaging and X-ray micro-CT analysis, the active surface area of controlled Al_2O_3-supported DPHFMs in this work was calculated to be ~5 times higher than the surface area of uncontrolled Al_2O_3-supported DPHFMs. The five times higher surface area in controlled Al_2O_3-supported DPHFMs led to an 8-fold improvement in carbon dioxide flux. It was also determined that controlled 3% YSZ-supported DPHFMs achieved ~3.3 times higher flux than the YSZ-supported DPHFMs in literature where the distribution of carbonate inside the support was not controlled.

Furthermore, the dominant surface resistance for carbon dioxide separation can be established by changing the direction for carbon dioxide permeation in controlled Al_2O_3-supported DPHFMs. Carbon dioxide flux was four times higher when the lumen-side surface was used as the permeate-side surface for permeation compared to when the shell-side surface was used as the permeate-side surface for permeation. This confirmed that the permeate-side surface area is the dominant surface resistance for carbon dioxide separation. The sigmoidal curve model that derived from the model-crucible membranes was also found to successfully predict the flux *versus* temperature relationship in controlled Al_2O_3-supported DPHFMs.

The flux of controlled distribution dual-phase membranes over a range of partial pressures was also investigated at 600 °C, determining the relationship between applied pCO_2 and carbon dioxide flux in both controlled Al_2O_3-supported and controlled 3% YSZ-supported DPHFMs. In controlled Al_2O_3-supported DPHFMs, carbon dioxide flux increased linearly with the increase of the difference in pCO_2 between the feed and permeate side ($pCO_{2,feed} - pCO_{2,permeate}$). In controlled 3% YSZ-supported DPHFMs carbon dioxide flux increased linearly with the increase in $\ln(pCO_{2,feed}/pCO_{2,permeate})$.

Collectively, the results show that it is possible to overcome carbon dioxide flux limitations of conventional DPHFMs by controlling the distribution of the carbonate phase inside the hollow fibre supports.

Based on the good wettability of the molten carbonate phase on Al_2O_3 and the homogenous and controlled distribution of carbonate inside the hollow fibre supports, the potential of utilising the molten phase for self-healing defects in dual-phase membranes was also investigated. In chapter 5, the intrinsic and autonomous self-healing of a dual-phase membrane during operation was demonstrated for the first time in literature. A dual-phase pellet membrane with a sacrificial defect-inducing material was developed. Upon removal of the sacrificial defect-inducing material *via* oxidation, a controlled, throughout membrane defect, or additional porosity in the form of voidage was created inside the pellet. The high wettability and spreading of carbonate inside the ceramic support successfully self-healed the created defect, resulting in the membrane regaining its previous selectivity. The redistribution of carbonate inside the pellet during self-healing also increased the carbon dioxide flux, as a thinner layer was believed to be created inside the pellet. Theoretical and experimental evaluation confirmed that throughout defects with a diameter up to 350 μm and additional porosity up to 18% can be self-healed by the spreading of carbonate inside the pellet membranes.

Overall, it was clear that high wetting angles, high carbonate melt spreading, and high capillary forces, withholding the molten carbonate in the ceramic pellet supports, enable the membrane to regain its permselectivity after defect creation, while providing a selective layer for permeation. The ability of molten carbonate to self-heal potential defects in the membrane supports, results in longer lasting membranes which makes the membranes viable for industrial application in carbon dioxide separation processes

where the membranes need to showcase stability in their permeation performance under long-term operation.

This work mainly focuses on bringing the application of DPHFMs a step closer towards their application in CCS technologies. The use of cheap support materials such as Al_2O_3 and YSZ and the fabrication of the hollow fibre supports using a single-step viscous-fingering induced phase-inversion technique reduces the membrane production cost compared to higher cost multi-step fabrication methods, such as dry and wet spinning and polymer pyrolysis [178,179]. Moreover, the high mechanical strength of Al_2O_3 and 3% YSZ supports in this study (>70 MPa), allows their application in NGCC and IGCC processes, where the minimum requirement for membrane mechanical strength is 10 MPa [235]. Also, the method developed for controlled distribution of carbonate in the hollow fibre supports reduced the amount of carbonate needed for carbon dioxide separation and can be upscaled by using dry spraying. Dry spraying of hollow fibre supports with the carbonate mixture reduces process complexity which can be caused by the infiltration of hollow fibre supports when the carbonate mixture is molten. With the use of dry spraying, membrane preparation is less energy demanding as it occurs at room temperature instead of temperatures above the carbonate mixture's melting point (>400 °C) and process reactors and molten carbonate contact, which has shown a corrosive nature, is avoided. Finally, the self-healing work presented in this thesis, shows evidence that membrane operation can be resumed after a heating cycle and shows potential for the long-term application of dual-phase membranes in industry without requiring membrane replacement in case of defects below a 350 μm diameter. Therefore, the self-healing of created defects is important for the overall cost requirements of the separation process.

6.2 Future work

Further understanding the relationship between available surface area and carbon dioxide flux

This thesis has demonstrated that the controlled distribution of carbonate inside hollow fibre supports, results in DPHFMs with improved carbon dioxide flux while using less amount of carbonate for infiltration. This was attributed to the increased active permeate-side surface area for controlled DPHFMs compared to the low surface area of uncontrolled DPHFMs.

In order to develop a better understanding of the infiltration process and how the carbonates infiltrate and spread inside the hollow fibre supports under experimental gas conditions, *in-situ* X-ray micro-CT could be used. To further apply the controlled preparation method in other asymmetric structures and understand the contribution of active surface area in carbon dioxide flux, it would be useful to quantify the active permeate side surface area available in DPHFMs using X-ray micro-CT analysis. The active permeate-side surface area was only quantified by geometrical approximation in this work. X-ray micro-CT analysis would provide a more accurate calculation of the active permeate-side surface area and would also result in the calculation of the dead-end porosity inside the hollow fibre supports, which block pathways for permeation. At higher temperatures *in-situ* X-ray micro-CT under experimental gas conditions, could also be used to investigate whether the melt infiltrates the micro-channels due to carbonate volume expansion, and therefore decreases the available active permeate-side surface area for carbon dioxide permeation. Establishing a relationship between available surface area and carbon dioxide flux, is important for future material selection in the membrane fabrication process.

Establishing a flux versus driving force relationship for Al_2O_3-supported DPHFMs

In this work, the effect of a limited range of driving forces on carbon dioxide flux through controlled and uncontrolled Al_2O_3-supported DPHFMs has been investigated (chapter 4, section 4.3.2). Future work should investigate a wider range of driving forces at different feed-side and permeate-side pCO_2s. Additional datapoints in Figure 4.6 would improve upon the accuracy of the emperical relationships observed in this work and would facilitate prediction of carbon dioxide flux across a wider range of operating conditions, which is beneficial in planning membrane operating parameters.

Application of controlled DPHFMs in a wider scale

Future work on the application of dual-phase membrane technology in a wider scale will mainly focus on using controlled distribution DPHFMs membranes in modules, to improve carbon dioxide permeability. It is also worth investigating the long-term stability of the controlled DPHFMs membranes in conditions where simulated flue gas is used as the feed-side gas. The long-term stability of high-temperature sealing in the presence of simulated flue gas conditions, has also not been studied. An equimolar carbon dioxide and nitrogen mixture has predominately been used for carbon dioxide separation in dual-phase membranes as carbon dioxide separation is the main function these membranes need to accomplish. However, in IGCC and NGCC processes, carbon dioxide needs to be separated from flue gases that include hydrogen, carbon monoxide, carbon dioxide and nitrogen after the removal of hydrogen sulphide and other impurities.

Chemical stability of Al_2O_3-supported dual-phase membranes

XRD analysis of the Al_2O_3-supported DPHFMs after long-term operation would also be important for future work related to this thesis, as it can identify potential crystalline phases created at the Al_2O_3-molten carbonate interface. Interfacial reactions between Al_2O_3 and molten carbonate could decrease the high wettability of the molten carbonate on the Al_2O_3 support, increasing the wetting angle (decreasing the value of $\cos\theta$) and ultimately decreasing the capillary forces, which retain the molten carbonate inside the pores of the support (chapter 2, section 2.3.3, Eq. 2.17, capillary force). This could lead to molten carbonate creep (chapter 1, section 1.4.2) which is not desirable for the long-term operation of dual-phase membranes. The high wettability of the molten carbonate on the Al_2O_3 support is of particular importance in the case of self-healing, where the self-healing of the created defects is attributed to high wetting angles, high carbonate spreading and high capillary forces. XRD analysis would facilitate the identification of crystalline phases created by interfacial reactions, which could negatively impact membrane performance and self-healing. The objective of the studies would be to identify the conditions that will prevent potential interfacial reactions from impacting membrane performance.

Self-healing of dual-phase membranes

Even though autonomous self-healing of controlled membrane defects was successful, more work needs to be done in self-healing membranes systems where the defect

creation is not controlled. This could be accomplished by introducing self-healing agents inside the support material. It is essential, that the selection of the self-healing agents will not interrupt pathways for carbonate spreading and carbon dioxide separation. In addition, any reactions between the self-healing agents and the carbonate and/or the ceramic support must not hinder the permeation performance of the dual-phase membrane. *In-situ* X-ray micro-CT would be of interest in the case of self-healing dual-phase membranes, as the redistribution and spreading of carbonate to self-heal membrane defects would be possible to be observed *in-situ*.

Extending towards catalytic reactions

After confirming the long-term stability of the controlled DPHFMs, the devoid micro-channels of the DPHFMs can be further exploited for the incorporation of a catalyst or a promoter. With the addition of a catalyst, a separation and reaction system can be coupled together. Previous literature studies have shown that the incorporation of a palladium catalyst inside the micro-channels of an Al_2O_3 hollow fibre support resulted in separation of hydrogen with the presence of steam in the feed-side gas [280]. Hence, DPHFMs for carbon dioxide separation could be further investigated for the WGS reaction, as a two-stage process, separating both carbon dioxide and hydrogen from the flue gas with the use of a catalytic-DPHFM in stage one and carbon dioxide from hydrogen as a DPHFM in stage two. With the addition of a promoter, such as silver, inside the devoid micro-channels of the DPFHMs, an exceptionally high carbon dioxide permeable membrane could be achieved, benefiting from the high surface area for desorption and electrochemical reactions for carbon dioxide permeation [121].

Chapter 7

References

[1] S. Solomon, G.-K. Plattner, R. Knutti, P. Friedlingstein, Irreversible climate change due to carbon dioxide emissions, Proc. Natl. Acad. Sci. 106 (2009) 1704–1709. https://doi.org/10.1073/pnas.0812721106.

[2] M. Solomon, Susan, Qin Dahe, Manning, Climate Change 2007 The Physical Science Basis, 2007.

[3] C. Le Quéré, M.R. Raupach, J.G. Canadell, G. Marland, L. Bopp, P. Ciais, T.J. Conway, S.C. Doney, R.A. Feely, P. Foster, P. Friedlingstein, K. Gurney, R.A. Houghton, J.I. House, C. Huntingford, P.E. Levy, M.R. Lomas, J. Majkut, N. Metzl, J.P. Ometto, G.P. Peters, I.C. Prentice, J.T. Randerson, S.W. Running, J.L. Sarmiento, U. Schuster, S. Sitch, T. Takahashi, N. Viovy, G.R. van der Werf, F.I. Woodward, Trends in the sources and sinks of carbon dioxide, Nat. Geosci. 2 (2009) 831–836. https://doi.org/10.1038/ngeo689.

[4] E.G. Hertwich, G.P. Peters, Carbon Footprint of Nations: A Global, Trade-Linked Analysis, Environ. Sci. Technol. 43 (2009) 6414–6420. https://doi.org/10.1021/es803496a.

[5] M.C. Carbo, J. Boon, D. Jansen, H.A.J. van Dijk, J.W. Dijkstra, R.W. van den Brink, A.H.M. Verkooijen, Steam demand reduction of water–gas shift reaction in IGCC power plants with pre-combustion CO2 capture, Int. J. Greenh. Gas Control. 3 (2009) 712–719. https://doi.org/https://doi.org/10.1016/j.ijggc.2009.08.003.

[6] H. Yang, Z. Xu, M. Fan, R. Gupta, R.B. Slimane, A.E. Bland, I. Wright, Progress in carbon dioxide separation and capture: A review, J. Environ. Sci. 20 (2008) 14–27. https://doi.org/https://doi.org/10.1016/S1001-0742(08)60002-9.

[7] I.E. Agency, 20 Years of Carbon Capture and Storage, 2016. https://doi.org/https://doi.org/https://doi.org/10.1787/9789264267800-en.

[8] M. Bui, C.S. Adjiman, A. Bardow, E.J. Anthony, A. Boston, S. Brown, P.S. Fennell, S. Fuss, A. Galindo, L.A. Hackett, J.P. Hallett, H.J. Herzog, G. Jackson, J. Kemper, S. Krevor, G.C. Maitland, M. Matuszewski, I.S. Metcalfe, C. Petit, G. Puxty, J. Reimer, D.M. Reiner, E.S. Rubin, S.A. Scott, N. Shah, B. Smit, J.P.M. Trusler, P. Webley, J. Wilcox, N. Mac Dowell, Carbon capture and storage (CCS): the way forward, Energy Environ. Sci. 11 (2018) 1062–1176.

https://doi.org/10.1039/C7EE02342A.

[9] G.T. Rochelle, Amine Scrubbing for CO2 Capture, Science (80-.). 325 (2009) 1652–1654. https://doi.org/10.1126/science.1176731.

[10] D.P. Hagewiesche, S.S. Ashour, H.A. Al-Ghawas, O.C. Sandall, Absorption of carbon dioxide into aqueous blends of monoethanolamine and N-methyldiethanolamine, Chem. Eng. Sci. 50 (1995) 1071–1079. https://doi.org/https://doi.org/10.1016/0009-2509(94)00489-E.

[11] N. Ramachandran, A. Aboudheir, R. Idem, P. Tontiwachwuthikul, Kinetics of the Absorption of CO2 into Mixed Aqueous Loaded Solutions of Monoethanolamine and Methyldiethanolamine, Ind. Eng. Chem. Res. 45 (2006) 2608–2616. https://doi.org/10.1021/ie0505716.

[12] P. Luis, Use of monoethanolamine (MEA) for CO2 capture in a global scenario: Consequences and alternatives, Desalination. 380 (2016) 93–99. https://doi.org/https://doi.org/10.1016/j.desal.2015.08.004.

[13] M.E. Boot-Handford, J.C. Abanades, E.J. Anthony, M.J. Blunt, S. Brandani, N. Mac Dowell, J.R. Fernández, M.-C. Ferrari, R. Gross, J.P. Hallett, R.S. Haszeldine, P. Heptonstall, A. Lyngfelt, Z. Makuch, E. Mangano, R.T.J. Porter, M. Pourkashanian, G.T. Rochelle, N. Shah, J.G. Yao, P.S. Fennell, Carbon capture and storage update, Energy Environ. Sci. 7 (2014) 130–189. https://doi.org/10.1039/C3EE42350F.

[14] N. V Plechkova, K.R. Seddon, Applications of ionic liquids in the chemical industry, Chem. Soc. Rev. 37 (2008) 123–150. https://doi.org/10.1039/B006677J.

[15] S. Choi, J.H. Drese, C.W. Jones, Adsorbent Materials for Carbon Dioxide Capture from Large Anthropogenic Point Sources, ChemSusChem. 2 (2009) 796–854. https://doi.org/10.1002/cssc.200900036.

[16] B. Arias, M.E. Diego, J.C. Abanades, M. Lorenzo, L. Diaz, D. Martínez, J. Alvarez, A. Sánchez-Biezma, Demonstration of steady state CO2 capture in a 1.7MWth calcium looping pilot, Int. J. Greenh. Gas Control. 18 (2013) 237–245. https://doi.org/https://doi.org/10.1016/j.ijggc.2013.07.014.

[17] M.-H. Chang, C.-M. Huang, W.-H. Liu, W.-C. Chen, J.-Y. Cheng, W. Chen, T.-W. Wen, S. Ouyang, C.-H. Shen, H.-W. Hsu, Design and Experimental Investigation of Calcium Looping Process for 3-kWth and 1.9-MWth Facilities, Chem. Eng. Technol. 36 (2013) 1525–1532. https://doi.org/10.1002/ceat.201300081.

[18] S. Tonomura, Outline of Course 50, Energy Procedia. 37 (2013) 7160–7167. https://doi.org/https://doi.org/10.1016/j.egypro.2013.06.653.

[19] L.-S. Fan, L. Zeng, W. Wang, S. Luo, Chemical looping processes for CO2 capture and carbonaceous fuel conversion – prospect and opportunity, Energy Environ. Sci. 5 (2012) 7254–7280. https://doi.org/10.1039/C2EE03198A.

[20] S. Sircar, T.C. Golden, M.B. Rao, Activated carbon for gas separation and storage, Carbon N. Y. 34 (1996) 1–12. https://doi.org/https://doi.org/10.1016/0008-6223(95)00128-X.

[21] H.A.J. van Dijk, P.D. Cobden, M. Lundqvist, C.C. Cormos, M.J. Watson, G. Manzolini, S. van der Veer, L. Mancuso, J. Johns, B. Sundelin, Cost Effective CO2 Reduction in the Iron & Steel Industry by Means of the SEWGS Technology: STEPWISE Project, Energy Procedia. 114 (2017) 6256–6265. https://doi.org/https://doi.org/10.1016/j.egypro.2017.03.1764.

[22] C.C. Dean, J. Blamey, N.H. Florin, M.J. Al-Jeboori, P.S. Fennell, The calcium looping cycle for CO2 capture from power generation, cement manufacture and hydrogen production, Chem. Eng. Res. Des. 89 (2011) 836–855. https://doi.org/https://doi.org/10.1016/j.cherd.2010.10.013.

[23] J. Owen-Jones, Grand opening of Climeworks commercial DAC plant, Gasworld. (2017).

[24] D.Y. Lu, R.W. Hughes, E.J. Anthony, Ca-based sorbent looping combustion for CO2 capture in pilot-scale dual fluidized beds, Fuel Process. Technol. 89 (2008) 1386–1395. https://doi.org/https://doi.org/10.1016/j.fuproc.2008.06.011.

[25] C. Hawthorne, H. Dieter, A. Bidwe, A. Schuster, G. Scheffknecht, S. Unterberger, M. Käß, CO2 capture with CaO in a 200 kWth dual fluidized bed pilot plant, Energy Procedia. 4 (2011) 441–448. https://doi.org/https://doi.org/10.1016/j.egypro.2011.01.073.

[26] M.-H. Chang, W.-C. Chen, C.-M. Huang, W.-H. Liu, Y.-C. Chou, W.-C. Chang, W. Chen, J.-Y. Cheng, K.-E. Huang, H.-W. Hsu, Design and Experimental Testing of a 1.9MWth Calcium Looping Pilot Plant, Energy Procedia. 63 (2014) 2100–2108. https://doi.org/https://doi.org/10.1016/j.egypro.2014.11.226.

[27] H. Anselmi, O. Mirgaux, R. Bounaceur, F. Patisson, Simulation of Post-Combustion CO2 Capture, a Comparison among Absorption, Adsorption and Membranes, Chem. Eng. Technol. 42 (2019) 797–804. https://doi.org/10.1002/ceat.201800667.

[28] R.W. Baker, K. Lokhandwala, Natural Gas Processing with Membranes: An

Overview, Ind. Eng. Chem. Res. 47 (2008) 2109–2121. https://doi.org/10.1021/ie071083w.

[29] H. Lin, E. Van Wagner, R. Raharjo, B.D. Freeman, I. Roman, High-Performance Polymer Membranes for Natural-Gas Sweetening, Adv. Mater. 18 (2006) 39–44. https://doi.org/10.1002/adma.200501409.

[30] MTR, PolarisTM membrane: CO2 removal from syngas, Membrane Technology & Research, (n.d.).

[31] H. Strathmann, L. Giorno, E. Drioli, An Introduction to Membrane Science and Technology, Cons. Naz. Delle Ric. (2011).

[32] M. Mulder, Basic principles of membrane technology, 2nd ed., Kluwer Academic Publishers, Dordrecht, 1996.

[33] M. Knudsen, No Title, Ann Phys. 28 (1908) 75.

[34] H.P. Bonzel, A surface diffusion mechanism at high temperature, Surf. Sci. 21 (1970) 45–60. https://doi.org/https://doi.org/10.1016/0039-6028(70)90062-2.

[35] A. Iulianelli, A. Basile, H. Li, R.W. Van den Brink, 7 - Inorganic membranes for pre-combustion carbon dioxide (CO2) capture, in: A. Basile, S.P. Nunes (Eds.), Adv. Membr. Sci. Technol. Sustain. Energy Environ. Appl., Woodhead Publishing, 2011: pp. 184–213. https://doi.org/https://doi.org/10.1533/9780857093790.2.184.

[36] P.B. Balbuena, K.E. Gubbins, Theoretical interpretation of adsorption behavior of simple fluids in slit pores, Langmuir. 9 (1993) 1801–1814. https://doi.org/10.1021/la00031a031.

[37] P. Pandey, R.S. Chauhan, Membranes for gas separation, Prog. Polym. Sci. 26 (2001) 853–893. https://doi.org/https://doi.org/10.1016/S0079-6700(01)00009-0.

[38] J.G. Wijmans, R.W. Baker, The solution-diffusion model: a review, J. Memb. Sci. 107 (1995) 1–21. https://doi.org/https://doi.org/10.1016/0376-7388(95)00102-I.

[39] D. Shekhawat, D.R. Luebke, H.W. Pennline, A Review of Carbon Dioxide Selective Membranes: A Topical Report, (n.d.). https://doi.org/10.2172/819990.

[40] C. Scholes, S. Kentish, G. Stevens, Carbon Dioxide Separation through Polymeric Membrane Systems for Flue Gas Applications, Recent Patents Chem. Eng. 1 (2010). https://doi.org/10.2174/1874478810801010052.

[41] H.B. Park, J. Kamcev, L.M. Robeson, M. Elimelech, B.D. Freeman, Maximizing the right stuff: The trade-off between membrane permeability and selectivity,

Science (80-.). 356 (2017). https://doi.org/10.1126/science.aab0530.

[42] P.S. Manning, J.D. Sirman, J.A. Kilner, Oxygen self-diffusion and surface exchange studies of oxide electrolytes having the fluorite structure, Solid State Ionics. 93 (1996) 125–132. https://doi.org/https://doi.org/10.1016/S0167-2738(96)00514-0.

[43] E. Ruiz-Trejo, J.D. Sirman, Y.M. Baikov, J.A. Kilner, Oxygen ion diffusivity, surface exchange and ionic conductivity in single crystal Gadolinia doped Ceria, Solid State Ionics. 113–115 (1998) 565–569. https://doi.org/https://doi.org/10.1016/S0167-2738(98)00323-3.

[44] J.A. Lane, J.A. Kilner, Oxygen surface exchange on gadolinia doped ceria, Solid State Ionics. 136–137 (2000) 927–932. https://doi.org/https://doi.org/10.1016/S0167-2738(00)00530-0.

[45] Z.F. Cui, Y. Jiang, R.W. Field, Chapter 1 - Fundamentals of Pressure-Driven Membrane Separation Processes, in: Z.F. Cui, H.S. Muralidhara (Eds.), Membr. Technol., Butterworth-Heinemann, Oxford, 2010: pp. 1–18. https://doi.org/https://doi.org/10.1016/B978-1-85617-632-3.00001-X.

[46] R. Anantharaman, T. Peters, W. Xing, M.-L. Fontaine, R. Bredesen, Dual phase high-temperature membranes for CO2 separation – performance assessment in post- and pre-combustion processes, Faraday Discuss. 192 (2016) 251–269. https://doi.org/10.1039/C6FD00038J.

[47] M.I. Khan, M.R. Islam, Chapter 8 - Transportation, Processing, and Refining Operations, in: M.I. Khan, M.R. Islam (Eds.), Pet. Eng. Handb. Sustain. Oper., Gulf Publishing Company, 2007: pp. 295–364. https://doi.org/https://doi.org/10.1016/B978-1-933762-12-8.50015-5.

[48] H. Hassanzadeh, J. Abedi, M. Pooladi-Darvish, A comparative study of flux-limiting methods for numerical simulation of gas–solid reactions with Arrhenius type reaction kinetics, Comput. Chem. Eng. 33 (2009) 133–143. https://doi.org/https://doi.org/10.1016/j.compchemeng.2008.07.010.

[49] J.R. Couper, W.R. Penney, J.R. Fair, S.M.B.T.-C.P.E. (Second E. Walas, eds., Chapter 19 - Membrane Separations, in: Gulf Professional Publishing, Burlington, 2005: pp. 665–692. https://doi.org/https://doi.org/10.1016/B978-075067510-9/50051-6.

[50] A. Arratibel, A. Labella, Y. Liu, N. Porras, D. Tanaka, M. Annaland, F. Gallucci, Mixed Ionic-Electronic Conducting Membranes (MIEC) for Their Application in Membrane Reactors: A Review, Processes. 7 (2019) 128.

https://doi.org/10.3390/pr7030128.

[51] J.H. Joo, K.S. Yun, J.-H. Kim, Y. Lee, C.-Y. Yoo, J.H. Yu, Substantial Oxygen Flux in Dual-Phase Membrane of Ceria and Pure Electronic Conductor by Tailoring the Surface, ACS Appl. Mater. Interfaces. 7 (2015) 14699–14707. https://doi.org/10.1021/acsami.5b03392.

[52] J.H. Joo, K.S. Yun, Y. Lee, J. Jung, C.-Y. Yoo, J.H. Yu, Dramatically Enhanced Oxygen Fluxes in Fluorite-Rich Dual-Phase Membrane by Surface Modification, Chem. Mater. 26 (2014) 4387–4394. https://doi.org/10.1021/cm501240f.

[53] S. Aasland, I.L. Tangen, K. Wiik, R. Ødegård, Oxygen permeation of SrFe0.67Co0.33O3−d, Solid State Ionics. 135 (2000) 713–717. https://doi.org/https://doi.org/10.1016/S0167-2738(00)00389-1.

[54] K. Scott, INTRODUCTION TO MEMBRANE SEPARATIONS, in: K. Scott (Ed.), Handb. Ind. Membr., Elsevier Science, Amsterdam, 1995: pp. 3–185. https://doi.org/https://doi.org/10.1016/B978-185617233-2/50004-0.

[55] J.M. Whiteley, P. Taynton, W. Zhang, S.-H. Lee, Ultra-thin Solid-State Li-Ion Electrolyte Membrane Facilitated by a Self-Healing Polymer Matrix, Adv. Mater. 27 (2015) 6922–6927. https://doi.org/10.1002/adma.201502636.

[56] H. Li, A. Goldbach, W. Li, H. Xu, PdC formation in ultra-thin Pd membranes during separation of H2/CO mixtures, J. Memb. Sci. 299 (2007) 130–137. https://doi.org/https://doi.org/10.1016/j.memsci.2007.04.034.

[57] S.J. Zaidi, K.A. Mauritz, M.K. Hassan, Membrane Surface Modification and Functionalization, in: M.A. Jafar Mazumder, H. Sheardown, A. Al-Ahmed (Eds.), Funct. Polym., Springer International Publishing, Cham, 2018: pp. 1–26. https://doi.org/10.1007/978-3-319-92067-2_11-1.

[58] J. Gilron, S. Belfer, P. Väisänen, M. Nyström, Effects of surface modification on antifouling and performance properties of reverse osmosis membranes, Desalination. 140 (2001) 167–179. https://doi.org/https://doi.org/10.1016/S0011-9164(01)00366-6.

[59] A.S. Yu, T.-S. Oh, R. Zhu, A. Gallegos, R.J. Gorte, J.M. Vohs, Surface modification of La0.8Sr0.2CrO3−δ–YSZ dual-phase membranes for syngas production, Faraday Discuss. 182 (2015) 213–225. https://doi.org/10.1039/C5FD00007F.

[60] B.T. Na, J.H. Park, J.H. Park, J.H. Yu, J.H. Joo, Elucidation of the Oxygen Surface Kinetics in a Coated Dual-Phase Membrane for Enhancing Oxygen

Permeation Flux, ACS Appl. Mater. Interfaces. 9 (2017) 19917–19924. https://doi.org/10.1021/acsami.7b04685.

[61] N. Bryan, E. Lasseuguette, M. van Dalen, N. Permogorov, A. Amieiro, S. Brandani, M.-C. Ferrari, Development of Mixed Matrix Membranes Containing Zeolites for Post-combustion Carbon Capture., Energy Procedia. 63 (2014) 160–166. https://doi.org/https://doi.org/10.1016/j.egypro.2014.11.016.

[62] B. Comesaña-Gándara, J. Chen, C.G. Bezzu, M. Carta, I. Rose, M.-C. Ferrari, E. Esposito, A. Fuoco, J.C. Jansen, N.B. McKeown, Redefining the Robeson upper bounds for CO2/CH4 and CO2/N2 separations using a series of ultrapermeable benzotriptycene-based polymers of intrinsic microporosity, Energy Environ. Sci. 12 (2019) 2733–2740. https://doi.org/10.1039/C9EE01384A.

[63] Y. Huang, T.C. Merkel, R.W. Baker, Pressure ratio and its impact on membrane gas separation processes, J. Memb. Sci. 463 (2014) 33–40. https://doi.org/https://doi.org/10.1016/j.memsci.2014.03.016.

[64] R. Khalilpour, K. Mumford, H. Zhai, A. Abbas, G. Stevens, E.S. Rubin, Membrane-based carbon capture from flue gas: a review, J. Clean. Prod. 103 (2015) 286–300. https://doi.org/https://doi.org/10.1016/j.jclepro.2014.10.050.

[65] Z.Y. Yeo, T.L. Chew, P.W. Zhu, A.R. Mohamed, S.-P. Chai, Conventional processes and membrane technology for carbon dioxide removal from natural gas: A review, J. Nat. Gas Chem. 21 (2012) 282–298. https://doi.org/https://doi.org/10.1016/S1003-9953(11)60366-6.

[66] M. Songolzadeh, M. Soleimani, M. Takht Ravanchi, R. Songolzadeh, Carbon dioxide separation from flue gases: a technological review emphasizing reduction in greenhouse gas emissions, ScientificWorldJournal. 2014 (2014) 828131. https://doi.org/10.1155/2014/828131.

[67] P.S. Tin, T.-S. Chung, Y. Liu, R. Wang, Separation of CO2/CH4 through carbon molecular sieve membranes derived from P84 polyimide, Carbon N. Y. 42 (2004) 3123–3131. https://doi.org/https://doi.org/10.1016/j.carbon.2004.07.026.

[68] L.M. Robeson, The upper bound revisited, J. Memb. Sci. 320 (2008) 390–400. https://doi.org/https://doi.org/10.1016/j.memsci.2008.04.030.

[69] L.M. Robeson, Correlation of separation factor versus permeability for polymeric membranes, J. Memb. Sci. 62 (1991) 165–185. https://doi.org/https://doi.org/10.1016/0376-7388(91)80060-J.

[70] C.A. Trickett, A. Helal, B.A. Al-Maythalony, Z.H. Yamani, K.E. Cordova, O.M. Yaghi, The chemistry of metal–organic frameworks for CO2 capture, regeneration and conversion, Nat. Rev. Mater. 2 (2017) 17045.

[71] S.R. Venna, M.A. Carreon, Metal organic framework membranes for carbon dioxide separation, Chem. Eng. Sci. 124 (2015) 3–19. https://doi.org/https://doi.org/10.1016/j.ces.2014.10.007.

[72] S.J. Doong, 7 - Membranes, adsorbent materials and solvent-based materials for syngas and hydrogen separation, in: J.A. Kilner, S.J. Skinner, S.J.C. Irvine, P.P. Edwards (Eds.), Funct. Mater. Sustain. Energy Appl., Woodhead Publishing, 2012: pp. 179–216. https://doi.org/https://doi.org/10.1533/9780857096371.2.179.

[73] L.C. Tomé, D. Mecerreyes, C.S.R. Freire, L.P.N. Rebelo, I.M. Marrucho, Pyrrolidinium-based polymeric ionic liquid materials: New perspectives for CO2 separation membranes, J. Memb. Sci. 428 (2013) 260–266. https://doi.org/https://doi.org/10.1016/j.memsci.2012.10.044.

[74] M. Teramoto, K. Nakai, N. Ohnishi, Q. Huang, T. Watari, H. Matsuyama, Facilitated Transport of Carbon Dioxide through Supported Liquid Membranes of Aqueous Amine Solutions, Ind. Eng. Chem. Res. 35 (1996) 538–545. https://doi.org/10.1021/ie950112c.

[75] A. Kayvani Fard, G. McKay, A. Buekenhoudt, H. Al Sulaiti, F. Motmans, M. Khraisheh, M. Atieh, Inorganic Membranes: Preparation and Application for Water Treatment and Desalination, Mater. (Basel, Switzerland). 11 (2018) 74. https://doi.org/10.3390/ma11010074.

[76] D.F. Sanders, Z.P. Smith, R. Guo, L.M. Robeson, J.E. McGrath, D.R. Paul, B.D. Freeman, Energy-efficient polymeric gas separation membranes for a sustainable future: A review, Polymer (Guildf). 54 (2013) 4729–4761. https://doi.org/https://doi.org/10.1016/j.polymer.2013.05.075.

[77] A. Basile, F. Gallucci, Membranes for Membrane Reactors: Preparation, Optimization and Selection, 2011. https://doi.org/10.1002/9780470977569.

[78] S. Uemiya, T. Matsuda, E. Kikuchi, Hydrogen permeable palladium-silver alloy membrane supported on porous ceramics, J. Memb. Sci. 56 (1991) 315–325. https://doi.org/https://doi.org/10.1016/S0376-7388(00)83041-0.

[79] S. Smart, J. Beltramini, J.C.D. da Costa, S.P. Katikaneni, T. Pham, 9 - Microporous silica membranes: fundamentals and applications in membrane reactors for hydrogen separation, in: A. Basile (Ed.), Handb. Membr. React.,

Woodhead Publishing, 2013: pp. 337–369. https://doi.org/https://doi.org/10.1533/9780857097330.2.337.

[80] Y. Delft, L. Correia, J. Overbeek, D. Meyer, Palladium membrane reactors for large scale production of hydrogen, (2007).

[81] Y.S. Lin, Microporous and dense inorganic membranes: Current status and prospective, Sep. Purif. Technol. 25 (2001) 39–55. https://doi.org/10.1016/S1383-5866(01)00089-2.

[82] J. Petersen, M. Matsuda, K. Haraya, Capillary carbon molecular sieve membranes derived from Kapton for high temperature gas separation, J. Memb. Sci. 131 (1997) 85–94. https://doi.org/https://doi.org/10.1016/S0376-7388(97)00041-0.

[83] M.B. Rao, S. Sircar, Nanoporous carbon membrane for gas separation, Gas Sep. Purif. 7 (1993) 279–284. https://doi.org/https://doi.org/10.1016/0950-4214(93)80030-Z.

[84] M. Anderson, H. Wang, Y.S. Lin, Inorganic membranes for carbon dioxide and nitrogen separation, Rev. Chem. Eng. 28 (2012) 101–121. https://doi.org/10.1515/revce-2012-0001.

[85] M. Llosa Tanco, D. Tanaka, Recent Advances on Carbon Molecular Sieve Membranes (CMSMs) and Reactors, Processes. 4 (2016) 29. https://doi.org/10.3390/pr4030029.

[86] K. Kusakabe, S. Gohgi, S. Morooka, Carbon Molecular Sieving Membranes Derived from Condensed Polynuclear Aromatic (COPNA) Resins for Gas Separations, Ind. Eng. Chem. Res. 37 (1998) 4262–4266. https://doi.org/10.1021/ie9804024.

[87] A.B. Fuertes, T.A. Centeno, Preparation of supported asymmetric carbon molecular sieve membranes, J. Memb. Sci. 144 (1998) 105–111. https://doi.org/https://doi.org/10.1016/S0376-7388(98)00037-4.

[88] Y. Kusuki, H. Shimazaki, N. Tanihara, S. Nakanishi, T. Yoshinaga, Gas permeation properties and characterization of asymmetric carbon membranes prepared by pyrolyzing asymmetric polyimide hollow fiber membrane, J. Memb. Sci. 134 (1997) 245–253. https://doi.org/https://doi.org/10.1016/S0376-7388(97)00118-X.

[89] J.C. Poshusta, V.A. Tuan, E.A. Pape, R.D. Noble, J.L. Falconer, Separation of light gas mixtures using SAPO-34 membranes, AIChE J. 46 (2000) 779–789. https://doi.org/10.1002/aic.690460412.

[90] O. Cheung, N. Hedin, Zeolites and related sorbents with narrow pores for CO2 separation from flue gas, RSC Adv. 4 (2014) 14480–14494. https://doi.org/10.1039/C3RA48052F.

[91] K. Kusakabe, T. Kuroda, A. Murata, S. Morooka, Formation of a Y-Type Zeolite Membrane on a Porous α-Alumina Tube for Gas Separation, Ind. Eng. Chem. Res. 36 (1997) 649–655. https://doi.org/10.1021/ie960519x.

[92] A. Dyer, An introduction to zeolite molecular sieves, (n.d.).

[93] K. Kusakabe, K. Ichiki, S. Morooka, Separation of CO2 with BaTiO3 membrane prepared by the sol—gel method, J. Memb. Sci. 95 (1994) 171–177. https://doi.org/https://doi.org/10.1016/0376-7388(94)00109-X.

[94] G.A. Mutch, L. Qu, G. Triantafyllou, W. Xing, M.-L. Fontaine, I.S. Metcalfe, Supported molten-salt membranes for carbon dioxide permeation, J. Mater. Chem. A. 7 (2019) 12951–12973. https://doi.org/10.1039/C9TA01979K.

[95] A. Thursfield, I.S. Metcalfe, High temperature gas separation through dual ion-conducting membranes, Curr. Opin. Chem. Eng. 2 (2013) 217–222. https://doi.org/https://doi.org/10.1016/j.coche.2013.02.001.

[96] R.P.T. Janz, G. J.; Allen, C. B.; Bansal, N. P.; Murphy, R. M.; Tomkins, Physical Properties Data Compilations Relevant to Energy Storage; Molten Salts: Data on Single and Multi Component Salt System, National Bureau of Standards: Washington, DC, 1979.

[97] X. Dong, J. Ortiz Landeros, Y.S. Lin, An asymmetric tubular ceramic-carbonate dual phase membrane for high temperature CO2 separation, Chem. Commun. 49 (2013) 9654–9656. https://doi.org/10.1039/C3CC45949G.

[98] C. Appleby, A. J. , Van Drunen, Solubilities of Oxygen and Carbon Monoxide in Carbonate Melts, J. Electrochem. Soc. 127 (1980) 1655–1659. https://doi.org/10.1149/1.2129975.

[99] P. Claes, D. Moyaux, D. Peeters, Solubility and Solvation of Carbon Dioxide in the Molten Li2CO3/Na2CO3/K2CO3 (43.5:31.5:25.0 mol-%) Eutectic Mixture at 973 K I. Experimental Part, Eur. J. Inorg. Chem. 1999 (1999) 583–588. https://doi.org/10.1002/(SICI)1099-0682(199904)1999:4<583::AID-EJIC583>3.0.CO;2-Y.

[100] M.R. Cerón, L.S. Lai, A. Amiri, M. Monte, S. Katta, J.C. Kelly, M.A. Worsley, M.D. Merrill, S. Kim, P.G. Campbell, Surpassing the conventional limitations of CO2 separation membranes with hydroxide/ceramic dual-phase membranes, J. Memb. Sci. 567 (2018) 191–198.

https://doi.org/https://doi.org/10.1016/j.memsci.2018.09.028.
[101] J. Fang, X. Jin, K. Huang, Life cycle analysis of a combined CO2 capture and conversion membrane reactor, J. Memb. Sci. 549 (2018) 142–150. https://doi.org/https://doi.org/10.1016/j.memsci.2017.12.006.
[102] S.R. Sherman, J.R. Gray, K.S. Brinkman, K. Huang, Combustion-assisted CO2 capture using MECC membranes, J. Memb. Sci. 401–402 (2012) 323–332. https://doi.org/https://doi.org/10.1016/j.memsci.2012.02.024.
[103] E. van Grol, W. Yang, Evaluation of Alternate Water Gas Shift Configurations for IGCC Systems August, in: 2009.
[104] T. Chen, H.-C. Wu, Y. Li, Y.S. Lin, Poisoning Effect of H2S on CO2 Permeation of Samarium-Doped-Ceria/Carbonate Dual-Phase Membrane, Ind. Eng. Chem. Res. 56 (2017) 14662–14669. https://doi.org/10.1021/acs.iecr.7b03856.
[105] T. Chen, B. Yu, Y. Zhao, Y. Li, J. Lin, Carbon dioxide permeation through ceramic-carbonate dual-phase membrane-effects of sulfur dioxide, J. Membr. Sci. 540 (2017) 477–484. https://doi.org/10.1016/j.memsci.2017.06.063.
[106] M. Zuo, S. Zhuang, X. Tan, B. Meng, N. Yang, S. Liu, Ionic conducting ceramic–carbonate dual phase hollow fibre membranes for high temperature carbon dioxide separation, J. Memb. Sci. 458 (2014) 58–65. https://doi.org/https://doi.org/10.1016/j.memsci.2014.01.047.
[107] X. Dong, H.-C. Wu, Y.S. Lin, CO2 permeation through asymmetric thin tubular ceramic-carbonate dual-phase membranes, J. Memb. Sci. 564 (2018) 73–81. https://doi.org/https://doi.org/10.1016/j.memsci.2018.07.012.
[108] F. J. Varela-Gandía, A. Berenguer-Murcia, A. Linares-Solano, E. Morallon, D. Cazorla-Amorós, Membranes for Membrane Reactors: Preparation, Optimization and Selection, in: 2011: pp. 381–393. https://doi.org/10.1002/9780470977569.ch15.
[109] S. Smart, J.C. [Diniz Da Costa], S. Baumann, W.A. Meulenberg, 9 - Oxygen transport membranes: dense ceramic membranes for power plant applications, in: A. Basile, S.P. Nunes (Eds.), Adv. Membr. Sci. Technol. Sustain. Energy Environ. Appl., Woodhead Publishing, 2011: pp. 255–292. https://doi.org/https://doi.org/10.1533/9780857093790.2.255.
[110] G. Zhang, E.I. Papaioannou, I.S. Metcalfe, Selective, high-temperature permeation of nitrogen oxides using a supported molten salt membrane, Energy Environ. Sci. 8 (2015) 1220–1223. https://doi.org/10.1039/C4EE02256D.

[111] Z. Rui, M. Anderson, Y.S. Lin, Y. Li, Modeling and analysis of carbon dioxide permeation through ceramic-carbonate dual-phase membranes, J. Memb. Sci. 345 (2009) 110–118. https://doi.org/https://doi.org/10.1016/j.memsci.2009.08.034.

[112] S.B. Adler, Factors Governing Oxygen Reduction in Solid Oxide Fuel Cell Cathodes, Chem. Rev. 104 (2004) 4791–4844. https://doi.org/10.1021/cr020724o.

[113] W. Xing, T. Peters, M.-L. Fontaine, A. Evans, P.P. Henriksen, T. Norby, R. Bredesen, Steam-promoted CO2 flux in dual-phase CO2 separation membranes, J. Memb. Sci. 482 (2015) 115–119. https://doi.org/https://doi.org/10.1016/j.memsci.2015.02.029.

[114] J.L. Wade, K.S. Lackner, A.C. West, Transport model for a high temperature, mixed conducting CO2 separation membrane, Solid State Ionics. 178 (2007) 1530–1540. https://doi.org/https://doi.org/10.1016/j.ssi.2007.09.007.

[115] D.E. Anderson, D.L. Graf, Multicomponent Electrolyte Diffusion, Annu. Rev. Earth Planet. Sci. 4 (1976) 95–121. https://doi.org/10.1146/annurev.ea.04.050176.000523.

[116] F. Civan, CHAPTER 3 - PETROGRAPHICAL CHARACTERISTICS OF PETROLEUM-BEARING FORMATIONS, in: F. Civan (Ed.), Reserv. Form. Damage (Second Ed., Second Edi, Gulf Professional Publishing, Burlington, 2007: pp. 78–100. https://doi.org/https://doi.org/10.1016/B978-075067738-7/50004-X.

[117] S. Ahmad, A.K. Azad, K.F. Loughlin, Effect of the Key Mixture Parameters on Tortuosity and Permeability of Concrete, J. Adv. Concr. Technol. 10 (2012) 86–94. https://doi.org/10.3151/jact.10.86.

[118] A. Hunt, G. Dimitrakopoulos, A.F. Ghoniem, Surface oxygen vacancy and oxygen permeation flux limits of perovskite ion transport membranes, J. Memb. Sci. 489 (2015) 248–257. https://doi.org/https://doi.org/10.1016/j.memsci.2015.03.095.

[119] P.-M. Geffroy, M. Reichmann, T. Chartier, J. Bassat, J. Grenier, Oxygen diffusion, surface exchange and oxygen semi-permeation performances of Ln2NiO4+δ membranes (Ln = La, Pr and Nd), (2014).

[120] S.J. Chung, J.H. Park, D. Li, J.-I. Ida, I. Kumakiri, J.Y.S. Lin, Dual-Phase Metal−Carbonate Membrane for High-Temperature Carbon Dioxide Separation, Ind. Eng. Chem. Res. 44 (2005) 7999–8006.

https://doi.org/10.1021/ie0503141.

[121] N. Xu, X. Li, M.A. Franks, H. Zhao, K. Huang, Silver-molten carbonate composite as a new high-flux membrane for electrochemical separation of CO2 from flue gas, J. Memb. Sci. 401–402 (2012) 190–194. https://doi.org/https://doi.org/10.1016/j.memsci.2012.02.001.

[122] J. Tong, X. Lei, J. Fang, M. Han, K. Huang, Remarkable O2 permeation through a mixed conducting carbon capture membrane functionalized by atomic layer deposition, J. Mater. Chem. A. 4 (2016) 1828–1837. https://doi.org/10.1039/C5TA10105K.

[123] P. Zhang, J. Tong, Y. Jee, K. Huang, Stabilizing a high-temperature electrochemical silver-carbonate CO2 capture membrane by atomic layer deposition of a ZrO2 overcoat, Chem. Commun. 52 (2016) 9817–9820. https://doi.org/10.1039/C6CC04501D.

[124] J. Fang, J. Tong, K. Huang, A superior mixed electron and carbonate-ion conducting metal-carbonate composite membrane for advanced flue-gas carbon capture, J. Memb. Sci. 505 (2016) 225–230. https://doi.org/https://doi.org/10.1016/j.memsci.2016.01.041.

[125] J. Fang, N. Xu, T. Yang, P. Zhang, J. Tong, K. Huang, CO2 capture performance of silver-carbonate membrane with electrochemically dealloyed porous silver matrix, J. Memb. Sci. 523 (2017) 439–445. https://doi.org/https://doi.org/10.1016/j.memsci.2016.10.025.

[126] P. Zhang, J. Tong, K. Huang, A self-forming dual-phase membrane for high-temperature electrochemical CO2 capture, J. Mater. Chem. A. 5 (2017) 12769–12773. https://doi.org/10.1039/C7TA04096B.

[127] E.I. Papaioannou, H. Qi, I.S. Metcalfe, ‘Uphill’ permeation of carbon dioxide across a composite molten salt-ceramic membrane, J. Memb. Sci. 485 (2015) 87–93. https://doi.org/https://doi.org/10.1016/j.memsci.2015.03.013.

[128] T.T. Norton, J. Ortiz-Landeros, Y.S. Lin, Stability of La–Sr–Co–Fe Oxide–Carbonate Dual-Phase Membranes for Carbon Dioxide Separation at High Temperatures, Ind. Eng. Chem. Res. 53 (2014) 2432–2440. https://doi.org/10.1021/ie4033523.

[129] R.W. Trice, Y.J. Su, J.R. Mawdsley, K.T. Faber, A.R. De Arellano-López, H. Wang, W.D. Porter, Effect of heat treatment on phase stability, microstructure, and thermal conductivity of plasma-sprayed YSZ, J. Mater. Sci. 37 (2002) 2359–2365. https://doi.org/10.1023/A:1015310509520.

[130] L. Zhang, N. Xu, X. Li, S. Wang, K. Huang, W.H. Harris, W.K.S. Chiu, High CO2 permeation flux enabled by highly interconnected three-dimensional ionic channels in selective CO2 separation membranes, Energy Environ. Sci. 5 (2012) 8310–8317. https://doi.org/10.1039/C2EE22045H.

[131] J.L. Wade, C. Lee, A.C. West, K.S. Lackner, Composite electrolyte membranes for high temperature CO2 separation, J. Memb. Sci. 369 (2011) 20–29. https://doi.org/https://doi.org/10.1016/j.memsci.2010.10.053.

[132] B. Lu, Y.S. Lin, Synthesis and characterization of thin ceramic-carbonate dual-phase membranes for carbon dioxide separation, J. Memb. Sci. 444 (2013) 402–411. https://doi.org/https://doi.org/10.1016/j.memsci.2013.05.046.

[133] Z. Rui, M. Anderson, Y. Li, Y.S. Lin, Ionic conducting ceramic and carbonate dual phase membranes for carbon dioxide separation, J. Memb. Sci. 417–418 (2012) 174–182. https://doi.org/https://doi.org/10.1016/j.memsci.2012.06.030.

[134] B. Lu, Y.S. Lin, Asymmetric Thin Samarium Doped Cerium Oxide–Carbonate Dual-Phase Membrane for Carbon Dioxide Separation, Ind. Eng. Chem. Res. 53 (2014) 13459–13466. https://doi.org/10.1021/ie502094j.

[135] T.T. Norton, B. Lu, Y.S. Lin, Carbon dioxide permeation properties and stability of samarium-doped-ceria carbonate dual-phase membranes, J. Memb. Sci. 467 (2014) 244–252. https://doi.org/https://doi.org/10.1016/j.memsci.2014.05.026.

[136] M.-L. Fontaine, T.A. Peters, M.T.P. McCann, I. Kumakiri, R. Bredesen, CO2 removal at high temperature from multi-component gas stream using porous ceramic membranes infiltrated with molten carbonates, Energy Procedia. 37 (2013) 941–951. https://doi.org/https://doi.org/10.1016/j.egypro.2013.05.189.

[137] J.Y.S. Lin, Pre-Combustion Carbon Dioxide Capture by a New Dual Phase Ceramic-Carbonate Membrane Reactor, (n.d.). https://doi.org/10.2172/1172599.

[138] A. Lopez, N. G. Perez Rivera, A. Reyes Rojas, D. Lardizabal, Novel Carbon Dioxide Solid Acceptors Using Sodium Containing Oxides, SSTEDS. 39 (2005) 3559–3572. https://doi.org/10.1081/SS-200036766.

[139] D.J. Fauth, E.A. Frommell, J.S. Hoffman, R.P. Reasbeck, H.W. Pennline, Eutectic salt promoted lithium zirconate: Novel high temperature sorbent for CO2 capture, Fuel Process. Technol. 86 (2005) 1503–1521. https://doi.org/https://doi.org/10.1016/j.fuproc.2005.01.012.

[140] Q. Xu, D. Huang, W. Chen, J. Lee, B. Kim, H. Wang, R. Yuan, Influence of

sintering temperature on microstructure and mixed electronic–ionic conduction properties of perovskite-type La0.6Sr0.4Co0.8Fe0.2O3 ceramics, Ceram. Int. 30 (2004) 429–433. https://doi.org/https://doi.org/10.1016/S0272-8842(03)00127-5.

[141] X. Jiang, J. Zhu, Z. Liu, S. Guo, W. Jin, CO2-Tolerant SrFe0.8Nb0.2O3−δ–Carbonate Dual-Phase Multichannel Hollow Fiber Membrane for CO2 Capture, Ind. Eng. Chem. Res. 55 (2015) 150911122639002. https://doi.org/10.1021/acs.iecr.5b03036.

[142] M. Anderson, Y.S. Lin, Carbonate–ceramic dual-phase membrane for carbon dioxide separation, J. Memb. Sci. 357 (2010) 122–129. https://doi.org/https://doi.org/10.1016/j.memsci.2010.04.009.

[143] R. Lan, S.M.M. Abdallah, I.A. Amar, S. Tao, Preparation of dense La0.5Sr0.5Fe0.8Cu0.2O3−δ–(Li,Na)2CO3–LiAlO2 composite membrane for CO2 separation, J. Memb. Sci. 468 (2014) 380–388. https://doi.org/https://doi.org/10.1016/j.memsci.2014.06.030.

[144] S. Zhuang, Y. Li, M. Zuo, X. Tan, B. Meng, N. Yang, S. Liu, Dense composite electrolyte hollow fibre membranes for high temperature CO2 separation, Sep. Purif. Technol. 132 (2014) 712–718. https://doi.org/https://doi.org/10.1016/j.seppur.2014.06.025.

[145] L. Gao, J.R. Selman, P. Nash, Wetting of Porous α-LiAlO2 by Molten Carbonate, J. Electrochem. Soc. 165 (2018) F324–F333. https://doi.org/10.1149/2.0771805jes.

[146] J. Tong, F. Si, L. Zhang, J. Fang, M. Han, K. Huang, Stabilizing electrochemical carbon capture membrane with Al2O3 thin-film overcoating synthesized by chemical vapor deposition, Chem. Commun. 51 (2015) 2936–2938. https://doi.org/10.1039/C4CC09352F.

[147] L. Zhang, Y. Gong, J. Yaggie, S. Wang, K. Romito, K. Huang, Surface modified silver-carbonate mixed conducting membranes for high flux CO2 separation with enhanced stability, J. Memb. Sci. 453 (2014) 36–41. https://doi.org/https://doi.org/10.1016/j.memsci.2013.10.067.

[148] H.J.M. Bouwmeester, H. Kruidhof, A.J. Burggraaf, Importance of the surface exchange kinetics as rate limiting step in oxygen permeation through mixed-conducting oxides, Solid State Ionics. 72 (1994) 185–194. https://doi.org/https://doi.org/10.1016/0167-2738(94)90145-7.

[149] C. Li, J.J. Chew, A. Mahmoud, S. Liu, J. Sunarso, Modelling of oxygen

transport through mixed ionic-electronic conducting (MIEC) ceramic-based membranes: An overview, J. Memb. Sci. 567 (2018) 228–260. https://doi.org/https://doi.org/10.1016/j.memsci.2018.09.016.

[150] Y.-S. Lin, W. Wang, J. Han, Oxygen permeation through thin mixed-conducting solid oxide membranes, AIChE J. 40 (1994) 786–798. https://doi.org/10.1002/aic.690400506.

[151] T. Kojima, Y. Miyazaki, K. Nomura, K. Tanimoto, Density, Surface Tension, and Electrical Conductivity of Ternary Molten Carbonate System Li2CO3 – Na2CO3 – K2CO3 and Methods for Their Estimation, J. Electrochem. Soc. 155 (2008) F150–F156. https://doi.org/10.1149/1.2917212.

[152] K. Kinoshita, J.W. Sim, J.P. Ackerman, Preparation and characterization of lithium aluminate, Mater. Res. Bull. 13 (1978) 445–455. https://doi.org/https://doi.org/10.1016/0025-5408(78)90152-6.

[153] M.M. Martín, Chapter 4 - Water, in: M.M. Martín (Ed.), Ind. Chem. Process Anal. Des., Elsevier, Boston, 2016: pp. 125–197. https://doi.org/https://doi.org/10.1016/B978-0-08-101093-8.00004-5.

[154] T.T. Norton, Y.S. Lin, Ceramic–carbonate dual-phase membrane with improved chemical stability for carbon dioxide separation at high temperature, Solid State Ionics. 263 (2014) 172–179. https://doi.org/https://doi.org/10.1016/j.ssi.2014.06.005.

[155] Y. Zhang, Y. Chen, M. Yan, F. Chen, New formulas for the tortuosity factor of electrochemically conducting channels, Electrochem. Commun. 60 (2015) 52–55. https://doi.org/https://doi.org/10.1016/j.elecom.2015.08.009.

[156] C. Gaudillere, J.M. Serra, Freeze-casting: Fabrication of highly porous and hierarchical ceramic supports for energy applications, Boletín La Soc. Española Cerámica y Vidr. 55 (2016) 45–54. https://doi.org/https://doi.org/10.1016/j.bsecv.2016.02.002.

[157] W. He, H. Huang, J. Gao, L. Winnubst, C. Chen, Phase-inversion tape casting and oxygen permeation properties of supported ceramic membranes, J. Memb. Sci. 452 (2014) 294–299. https://doi.org/https://doi.org/10.1016/j.memsci.2013.09.063.

[158] R. Sondhi, R. Bhave, G. Jung, Applications and benefits of ceramic membranes, Membr. Technol. 2003 (2003) 5–8. https://doi.org/https://doi.org/10.1016/S0958-2118(03)11016-6.

[159] P.M. Biesheuvel, H. Verweij, Design of ceramic membrane supports:

permeability, tensile strength and stress, J. Memb. Sci. 156 (1999) 141–152. https://doi.org/https://doi.org/10.1016/S0376-7388(98)00335-4.

[160] L. Zhang, Y. Gong, K.S. Brinkman, T. Wei, S. Wang, K. Huang, Flux of silver-carbonate membranes for post-combustion CO2 capture: The effects of membrane thickness, gas concentration and time, J. Memb. Sci. 455 (2014) 162–167. https://doi.org/https://doi.org/10.1016/j.memsci.2013.12.077.

[161] L. Zhang, J. Tong, Y. Gong, M. Han, S. Wang, K. Huang, Fast electrochemical CO2 transport through a dense metal-carbonate membrane: A new mechanistic insight, J. Memb. Sci. 468 (2014) 373–379. https://doi.org/https://doi.org/10.1016/j.memsci.2014.06.028.

[162] R.M. Khattab, M.M.S. Wahsh, N.M. Khalil, Preparation and characterization of porous alumina ceramics through starch consolidation casting technique, Ceram. Int. 38 (2012) 4723–4728. https://doi.org/https://doi.org/10.1016/j.ceramint.2012.02.057.

[163] S. Li, C.-A. Wang, J. Zhou, Effect of starch addition on microstructure and properties of highly porous alumina ceramics, Ceram. Int. 39 (2013) 8833–8839. https://doi.org/https://doi.org/10.1016/j.ceramint.2013.04.072.

[164] T.C. Merkel, H. Lin, X. Wei, R. Baker, Power plant post-combustion carbon dioxide capture: An opportunity for membranes, J. Memb. Sci. 359 (2010) 126–139. https://doi.org/https://doi.org/10.1016/j.memsci.2009.10.041.

[165] K. Scott, AIR AND GAS FILTRATION AND CLEANING, in: K.B.T.-H. of I.M. Scott (Ed.), Elsevier Science, Amsterdam, 1995: pp. 309–327. https://doi.org/https://doi.org/10.1016/B978-185617233-2/50007-6.

[166] M. Shatat, S.B. Riffat, Water desalination technologies utilizing conventional and renewable energy sources, Int. J. Low-Carbon Technol. 9 (2012) 1–19. https://doi.org/10.1093/ijlct/cts025.

[167] L. Liu, E.S. Sanders, S.S. Kulkarni, D.J. Hasse, W.J. Koros, Sub-ambient temperature flue gas carbon dioxide capture via Matrimid® hollow fiber membranes, J. Memb. Sci. 465 (2014) 49–55. https://doi.org/https://doi.org/10.1016/j.memsci.2014.03.060.

[168] H. Kreulen, C.A. Smolders, G.F. Versteeg, W.P.M. van Swaaij, Microporous hollow fibre membrane modules as gas-liquid contactors. Part 1. Physical mass transfer processes: A specific application: Mass transfer in highly viscous liquids, J. Memb. Sci. 78 (1993) 197–216. https://doi.org/https://doi.org/10.1016/0376-7388(93)80001-E.

[169] S. Basu, A.L. Khan, A. Cano-Odena, C. Liu, I.F.J. Vankelecom, Membrane-based technologies for biogas separations, Chem. Soc. Rev. 39 (2010) 750–768. https://doi.org/10.1039/B817050A.

[170] S.A. Rackley, 8 - Membrane separation systems, in: S.A. Rackley (Ed.), Carbon Capture Storage (Second Ed., Second Edi, Butterworth-Heinemann, Boston, 2017: pp. 187–225. https://doi.org/https://doi.org/10.1016/B978-0-12-812041-5.00008-8.

[171] A.G. Gil, M.H.M. Reis, D. Chadwick, Z. Wu, K. Li, A highly permeable hollow fibre substrate for Pd/Al2O3 composite membranes in hydrogen permeation, Int. J. Hydrogen Energy. 40 (2015) 3249–3258. https://doi.org/https://doi.org/10.1016/j.ijhydene.2015.01.021.

[172] F.R. García-García, B.F.K. Kingsbury, M.A. Rahman, K. Li, Asymmetric ceramic hollow fibres applied in heterogeneous catalytic gas phase reactions, Catal. Today. 193 (2012) 20–30. https://doi.org/https://doi.org/10.1016/j.cattod.2012.01.006.

[173] X. Tan, Z. Wang, B. Meng, X. Meng, K. Li, Pilot-scale production of oxygen from air using perovskite hollow fibre membranes, J. Memb. Sci. 352 (2010) 189–196. https://doi.org/https://doi.org/10.1016/j.memsci.2010.02.015.

[174] A. Leo, S. Smart, S. Liu, J.C.D. da Costa, High performance perovskite hollow fibres for oxygen separation, J. Memb. Sci. 368 (2011) 64–68. https://doi.org/https://doi.org/10.1016/j.memsci.2010.11.002.

[175] T. Li, T.M.M. Heenan, M.F. Rabuni, B. Wang, N.M. Farandos, G.H. Kelsall, D. Matras, C. Tan, X. Lu, S.D.M. Jacques, D.J.L. Brett, P.R. Shearing, M. Di Michiel, A.M. Beale, A. Vamvakeros, K. Li, Design of next-generation ceramic fuel cells and real-time characterization with synchrotron X-ray diffraction computed tomography, Nat. Commun. 10 (2019) 1497. https://doi.org/10.1038/s41467-019-09427-z.

[176] M.H.D. Othman, Z. Wu, N. Droushiotis, U. Doraswami, G. Kelsall, K. Li, Single-step fabrication and characterisations of electrolyte/anode dual-layer hollow fibres for micro-tubular solid oxide fuel cells, J. Memb. Sci. 351 (2010) 196–204. https://doi.org/https://doi.org/10.1016/j.memsci.2010.01.050.

[177] D.Q. Vu, W.J. Koros, S.J. Miller, High Pressure CO2/CH4 Separation Using Carbon Molecular Sieve Hollow Fiber Membranes, Ind. Eng. Chem. Res. 41 (2002) 367–380. https://doi.org/10.1021/ie010119w.

[178] K.H. Lee, Y.M. Kim, Asymmetric Hollow Inorganic Membranes, in: Inorg.

Membr., Trans Tech Publications Ltd, 1992: pp. 17–22. https://doi.org/10.4028/www.scientific.net/KEM.61-62.17.

[179] J.E. Koresh, A. Sofer, Molecular Sieve Carbon Permselective Membrane. Part I. Presentation of a New Device for Gas Mixture Separation, Sep. Sci. Technol. 18 (1983) 723–734. https://doi.org/10.1080/01496398308068576.

[180] X. Tan, S. Liu, K. Li, Preparation and characterization of inorganic hollow fiber membranes, J. Memb. Sci. 188 (2001) 87–95. https://doi.org/https://doi.org/10.1016/S0376-7388(01)00369-6.

[181] S.P. Nunes, K.-V. Peinemann, Membrane Preparation, in: Membr. Technol., John Wiley & Sons, Ltd, 2001: pp. 6–11. https://doi.org/10.1002/3527600388.ch3.

[182] Membranes and Modules, in: Membr. Technol. Appl., John Wiley & Sons, Ltd, 2004: pp. 89–160. https://doi.org/10.1002/0470020393.ch3.

[183] F.R. García-García, K. Li, New catalytic reactors prepared from symmetric and asymmetric ceramic hollow fibres, Appl. Catal. A Gen. 456 (2013) 1–10. https://doi.org/https://doi.org/10.1016/j.apcata.2013.01.031.

[184] S. Liu, K. Li, R. Hughes, Preparation of porous aluminium oxide (Al2O3) hollow fibre membranes by a combined phase-inversion and sintering method, Ceram. Int. 29 (2003) 875–881. https://doi.org/https://doi.org/10.1016/S0272-8842(03)00030-0.

[185] T. Li, Z. Wu, K. Li, Single-step fabrication and characterisations of triple-layer ceramic hollow fibres for micro-tubular solid oxide fuel cells (SOFCs), J. Memb. Sci. 449 (2014) 1–8. https://doi.org/https://doi.org/10.1016/j.memsci.2013.08.009.

[186] X. Zhu, H. Liu, Q. Li, Y. Cong, W. Yang, Unsteady-state permeation and surface exchange of dual-phase membranes, Solid State Ionics. 185 (2011) 27–31. https://doi.org/https://doi.org/10.1016/j.ssi.2011.01.005.

[187] G.J. JANZ, M.A.X.R. LORENZ, Solid-Liquid Phase Equilibria for Mixtures of Lithium, Sodium, and Potassium Carbonates, J. Chem. Eng. Data. 6 (1961) 321–323. https://doi.org/10.1021/je00103a001.

[188] S. V Devyatkin, A.D. Pisanenko, V.I. Shapoval, Chemical and Electrochemical Behavior of Carbonate Melts Containing Silicon Oxide, Russ. J. Appl. Chem. 75 (2002) 562–564. https://doi.org/10.1023/A:1019504827943.

[189] X. An, J. Cheng, P. Zhang, Z. Tang, J. Wang, Determination and evaluation of the thermophysical properties of an alkali carbonate eutectic molten salt,

Faraday Discuss. 190 (2016) 327–338. https://doi.org/10.1039/C5FD00236B.
[190] R.I. Olivares, C. Chen, S. Wright, The Thermal Stability of Molten Lithium–Sodium–Potassium Carbonate and the Influence of Additives on the Melting Point, J. Sol. Energy Eng. 134 (2012) 41002–41008.
[191] P. L. Spedding, R. Mills, Trace-Ion Diffusion in Molten Alkali Carbonates, J. Electrochem. Soc. - J Electrochem SOC. 112 (1965). https://doi.org/10.1149/1.2423614.
[192] X. An, J.-H. Cheng, T. su, P. Zhang, Determination of thermal physical properties of alkali fluoride/carbonate eutectic molten salt, in: AIP Conf. Proc., 2017: p. 70001. https://doi.org/10.1063/1.4984415.
[193] G.J. Janz, T. Yamamura, M.D. Hansen, Corresponding-states data correlations and molten salts viscosities, Int. J. Thermophys. 10 (1989) 159–171. https://doi.org/10.1007/BF00500716.
[194] V. Daněk, Chapter 6 - Surface Tension, in: V. Daněk (Ed.), Physico-Chemical Anal. Molten Electrolytes, Elsevier Science, Amsterdam, 2006: pp. 271–312. https://doi.org/https://doi.org/10.1016/B978-044452116-3/50007-6.
[195] M.E. Schrader, Young-Dupre Revisited, Langmuir. 11 (1995) 3585–3589. https://doi.org/10.1021/la00009a049.
[196] H. Dobbs, D. Bonn, Predicting Wetting Behavior from Initial Spreading Coefficients, Langmuir. 17 (2001) 4674–4676. https://doi.org/10.1021/la001668u.
[197] W.A. ZISMAN, Relation of the Equilibrium Contact Angle to Liquid and Solid Constitution, in: Contact Angle, Wettability, Adhes., AMERICAN CHEMICAL SOCIETY, 1964: p. 1. https://doi.org/doi:10.1021/ba-1964-0043.ch001.
[198] S.K. Ghosh, Self-Healing Materials: Fundamentals, Design Strategies, and Applications, in: Self-Healing Mater., John Wiley & Sons, Ltd, 2009: pp. 1–28. https://doi.org/10.1002/9783527625376.ch1.
[199] R.P.T. Tomkins, N.P. Bansal, eds., Solubility data series, in: Gases in Molten Salts, 1991.
[200] W.R. Carper, P.G. Wahlbeck, T.R. Griffiths, DFT Models of Molecular Species in Carbonate Molten Salts, J. Phys. Chem. B. 116 (2012) 5559–5567. https://doi.org/10.1021/jp3016694.
[201] L. Zhang, X. Huang, C. Qin, K. Brinkman, Y. Gong, S. Wang, K. Huang, First spectroscopic identification of pyrocarbonate for high CO2 flux membranes containing highly interconnected three dimensional ionic channels, Phys.

Chem. Chem. Phys. 15 (2013). https://doi.org/10.1039/c3cp52362d.

[202] J.M.S. Henis, M.K. Tripodi, Composite hollow fiber membranes for gas separation: the resistance model approach, J. Memb. Sci. 8 (1981) 233–246. https://doi.org/https://doi.org/10.1016/S0376-7388(00)82312-1.

[203] J.M.S. Henis, M.K. Tripodi, The Developing Technology of Gas Separating Membranes, Science (80-.). 220 (1983) 11–17. https://doi.org/10.1126/science.220.4592.11.

[204] A.J. Brown, N.A. Brunelli, K. Eum, F. Rashidi, J.R. Johnson, W.J. Koros, C.W. Jones, S. Nair, Interfacial microfluidic processing of metal-organic framework hollow fiber membranes, Science (80-.). 345 (2014) 72–75. https://doi.org/10.1126/science.1251181.

[205] W.J. Koros, C. Zhang, Materials for next-generation molecularly selective synthetic membranes, Nat. Mater. 16 (2017) 289.

[206] N. Bhuwania, Y. Labreche, C.S.K. Achoundong, J. Baltazar, S.K. Burgess, S. Karwa, L. Xu, C.L. Henderson, P.J. Williams, W.J. Koros, Engineering substructure morphology of asymmetric carbon molecular sieve hollow fiber membranes, Carbon N. Y. 76 (2014) 417–434. https://doi.org/https://doi.org/10.1016/j.carbon.2014.05.008.

[207] L.-Z. Zhang, Chapter 8 - Heat and Mass Transfer in Hollow Fiber Membrane Bundles with Randomly Distributed Fibers, in: L.-Z. Zhang (Ed.), Conjug. Heat Mass Transf. Heat Mass Exch. Ducts, Academic Press, Boston, 2013: pp. 233–254. https://doi.org/https://doi.org/10.1016/B978-0-12-407782-9.00008-3.

[208] I. Voigt, H. Richter, M. Stahn, M. Weyd, P. Puhlfürß, V. Prehn, C. Günther, Scale-up of ceramic nanofiltration membranes to meet large scale applications, Sep. Purif. Technol. 215 (2019) 329–334. https://doi.org/https://doi.org/10.1016/j.seppur.2019.01.023.

[209] A.J. Burggraaf, Chapter 2 Important characteristics of inorganic membranes, in: A.J. Burggraaf, L. Cot (Eds.), Fundam. Inorg. Membr. Sci. Technol., Elsevier, 1996: pp. 21–34. https://doi.org/https://doi.org/10.1016/S0927-5193(96)80005-2.

[210] B.F.K. Kingsbury, K. Li, A morphological study of ceramic hollow fibre membranes, J. Memb. Sci. 328 (2009) 134–140. https://doi.org/https://doi.org/10.1016/j.memsci.2008.11.050.

[211] G.M. Homsy, Viscous Fingering in Porous Media, Annu. Rev. Fluid Mech. 19 (1987) 271–311. https://doi.org/10.1146/annurev.fl.19.010187.001415.

[212] J.A. Varela, J.A. Cerri, E.R. Leite, E. Longo, M. Shamsuzzoha, R.C. Bradt, Microstructural evolution during sintering of CoO doped SnO2 ceramics, Ceram. Int. 25 (1999) 253–256. https://doi.org/https://doi.org/10.1016/S0272-8842(98)00032-7.

[213] L.G. E. Drioli, Comprehensive Membrane Science and Engineering, in: Elsevier, Oxford, n.d.: pp. 253–273.

[214] B.F.K. Kingsbury, Z. Wu, K. Li, A morphological study of ceramic hollow fibre membranes: A perspective on multifunctional catalytic membrane reactors, Catal. Today. 156 (2010) 306–315. https://doi.org/https://doi.org/10.1016/j.cattod.2010.02.039.

[215] S. Liu, K. Li, Preparation TiO2/Al2O3 composite hollow fibre membranes, J. Memb. Sci. 218 (2003) 269–277. https://doi.org/https://doi.org/10.1016/S0376-7388(03)00184-4.

[216] M. Lee, Z. Wu, R. Wang, K. Li, Micro-structured alumina hollow fibre membranes – Potential applications in wastewater treatment, J. Memb. Sci. 461 (2014) 39–48. https://doi.org/10.1016/j.memsci.2014.02.044.

[217] R. Knitter, D. Göhring, P. Risthaus, J. Haußelt, Microfabrication of ceramic microreactors, Microsyst. Technol. 7 (2001) 85–90. https://doi.org/10.1007/s005420100107.

[218] P.L. Mills, D.J. Quiram, J.F. Ryley, Microreactor technology and process miniaturization for catalytic reactions—A perspective on recent developments and emerging technologies, Chem. Eng. Sci. 62 (2007) 6992–7010. https://doi.org/https://doi.org/10.1016/j.ces.2007.09.021.

[219] K. Jähnisch, V. Hessel, H. Löwe, M. Baerns, Chemistry in Microstructured Reactors, Angew. Chemie Int. Ed. 43 (2004) 406–446. https://doi.org/10.1002/anie.200300577.

[220] A. Gouveia Gil, Z. Wu, D. Chadwick, K. Li, Microstructured Catalytic Hollow Fiber Reactor for Methane Steam Reforming, Ind. Eng. Chem. Res. 54 (2015) 5563–5571. https://doi.org/10.1021/ie504953j.

[221] W. Zeng, L. Gao, L. Gui, J. Guo, Sintering kinetics of α-Al2O3 powder, Ceram. Int. 25 (1999) 723–726. https://doi.org/https://doi.org/10.1016/S0272-8842(99)00008-5.

[222] J.-S. Kim, R. A. Rudkin, X. Wang, A. Atkinson, Constrained Sintering Kinetics of 3YSZ Films, J. Eur. Ceram. Soc. - J EUR CERAM SOC. 31 (2011) 2231–2239. https://doi.org/10.1016/j.jeurceramsoc.2011.05.044.

[223] G. Suárez, N.M. Rendtorff, A.N. Scian, E.F. Aglietti, Isothermal sintering kinetic of 3YTZ and 8YSZ: Cation diffusion, Ceram. Int. 39 (2013) 261–268. https://doi.org/https://doi.org/10.1016/j.ceramint.2012.06.020.

[224] B.-N. Kim, T.S. Suzuki, K. Morita, H. Yoshida, Y. Sakka, H. Matsubara, Densification kinetics during isothermal sintering of 8YSZ, J. Eur. Ceram. Soc. 36 (2016) 1269–1275. https://doi.org/https://doi.org/10.1016/j.jeurceramsoc.2015.11.041.

[225] Ceramic Membrane Reactors, in: Ceram. Membr. Sep. React., John Wiley & Sons, Ltd, 2007: pp. 245–298. https://doi.org/10.1002/9780470319475.ch8.

[226] X. Tan, Y. Liu, K. Li, Mixed Conducting Ceramic Hollow Fiber Membranes for Air Separation, AIChE J. 51 (2005) 1991–2000. https://doi.org/10.1002/aic.10475.

[227] L. Moscou, S. Lub, Practical use of mercury porosimetry in the study of porous solids, Powder Technol. 29 (1981) 45–52. https://doi.org/https://doi.org/10.1016/0032-5910(81)85003-6.

[228] J.N. Cernica, Strength of Materials, 2nd editio, Holt, Rinehart, and Winston, New York, 1977.

[229] J.. Wachtman, Mechanical Properties of Ceramics, Wiley, New York, 1996.

[230] N. M. Terra, C. O. T. Lemos, F. da Silva, V. L Cardoso, M. H. M. Reis, Characterisation of asymmetric alumina hollow fibres: Application for hydrogen permeation in composite membranes, Brazilian J. Chem. Eng. 33 (2016) 567–576. https://doi.org/10.1590/0104-6632.20160333s20150074.

[231] X. Tan, N. Liu, B. Meng, S. Liu, Morphology control of the perovskite hollow fibre membranes for oxygen separation using different bore fluids, J. Memb. Sci. 378 (2011) 308–318. https://doi.org/https://doi.org/10.1016/j.memsci.2011.05.012.

[232] W. Yin, B. Meng, X. Meng, X. Tan, Highly asymmetric yttria stabilized zirconia hollow fibre membranes, J. Alloys Compd. 476 (2009) 566–570. https://doi.org/https://doi.org/10.1016/j.jallcom.2008.09.079.

[233] R.A. Page, Y.M. Pan, Miicrostructural Evolutiion Duriing Sinteriing, MRS Proc. 249 (1991) 449. https://doi.org/10.1557/PROC-249-449.

[234] J. Sunarso, S. Baumann, J.M. Serra, W.A. Meulenberg, S. Liu, Y.S. Lin, J.C.D. da Costa, Mixed ionic–electronic conducting (MIEC) ceramic-based membranes for oxygen separation, J. Memb. Sci. 320 (2008) 13–41. https://doi.org/https://doi.org/10.1016/j.memsci.2008.03.074.

[235] X. He, A review of material development in the field of carbon capture and the application of membrane-based processes in power plants and energy-intensive industries, Energy. Sustain. Soc. 8 (2018) 34. https://doi.org/10.1186/s13705-018-0177-9.

[236] L. Jiansheng, W. Lianjun, H. Yanxia, L. Xiaodong, S. Xiuyun, Preparation and characterization of Al2O3 hollow fiber membranes, J. Memb. Sci. 256 (2005) 1–6. https://doi.org/https://doi.org/10.1016/j.memsci.2004.07.014.

[237] C. Zhang, C.-J. Li, G. Zhang, X.-J. Ning, C.-X. Li, H. Liao, C. Coddet, Ionic conductivity and its temperature dependence of atmospheric plasma-sprayed yttria stabilized zirconia electrolyte, Mater. Sci. Eng. B. 137 (2007) 24–30. https://doi.org/https://doi.org/10.1016/j.mseb.2006.10.005.

[238] Q. Liu, R.A. Lange, New density measurements on carbonate liquids and the partial molar volume of the CaCO3 component, Contrib. to Mineral. Petrol. 146 (2003) 370–381. https://doi.org/10.1007/s00410-003-0505-7.

[239] X. Tan, Y. Liu, K. Li, Preparation of LSCF Ceramic Hollow-Fiber Membranes for Oxygen Production by a Phase-Inversion/Sintering Technique, Ind. Eng. Chem. Res. 44 (2005) 61–66. https://doi.org/10.1021/ie040179c.

[240] J.Y. Chong, N.F.D. Aba, B. Wang, C. Mattevi, K. Li, UV-Enhanced Sacrificial Layer Stabilised Graphene Oxide Hollow Fibre Membranes for Nanofiltration, Sci. Rep. 5 (2015) 15799.

[241] S. Liu, X. Tan, K. Li, R. Hughes, Preparation and characterisation of SrCe0.95Yb0.05O2.975 hollow fibre membranes, J. Memb. Sci. 193 (2001) 249–260. https://doi.org/https://doi.org/10.1016/S0376-7388(01)00518-X.

[242] D.W. Shin, S.H. Hyun, C.H. Cho, M.H. Han, Synthesis and CO2/N2 gas permeation characteristics of ZSM-5 zeolite membranes, Microporous Mesoporous Mater. 85 (2005) 313–323. https://doi.org/https://doi.org/10.1016/j.micromeso.2005.06.035.

[243] B.C.H. Steele, Interfacial reactions associated with ceramic ion transport membranes, Solid State Ionics. 75 (1995) 157–165. https://doi.org/https://doi.org/10.1016/0167-2738(94)00182-R.

[244] L.-Z. Zhang, Heat and mass transfer in a randomly packed hollow fiber membrane module: A fractal model approach, Int. J. Heat Mass Transf. 54 (2011) 2921–2931. https://doi.org/https://doi.org/10.1016/j.ijheatmasstransfer.2011.03.005.

[245] S.G. Patrício, E.I. Papaioannou, B.M. Ray, I.S. Metcalfe, F.M.B. Marques,

Composite CO2 separation membranes: Insights on kinetics and stability, J. Memb. Sci. 541 (2017) 253–261. https://doi.org/https://doi.org/10.1016/j.memsci.2017.07.008.

[246] T. Li, X. Lu, B. Wang, Z. Wu, K. Li, D.J.L. Brett, P.R. Shearing, X-ray tomography-assisted study of a phase inversion process in ceramic hollow fiber systems – Towards practical structural design, J. Memb. Sci. 528 (2017) 24–33. https://doi.org/https://doi.org/10.1016/j.memsci.2017.01.004.

[247] X. Zhu, H. Liu, Y. Cong, W. Yang, Permeation model and experimental investigation of mixed conducting membranes, AIChE J. 58 (2012) 1744–1754. https://doi.org/10.1002/aic.12710.

[248] C. Li, W. Li, J.J. Chew, S. Liu, X. Zhu, J. Sunarso, Rate determining step in SDC-SSAF dual-phase oxygen permeation membrane, J. Memb. Sci. 573 (2019) 628–638. https://doi.org/https://doi.org/10.1016/j.memsci.2018.12.044.

[249] J. Huang, Z. Mao, Z. Liu, C. Wang, Development of novel low-temperature SOFCs with co-ionic conducting SDC-carbonate composite electrolytes, Electrochem. Commun. 9 (2007) 2601–2605. https://doi.org/https://doi.org/10.1016/j.elecom.2007.07.036.

[250] M.D. Hager, P. Greil, C. Leyens, S. van der Zwaag, U.S. Schubert, Self-Healing Materials, Adv. Mater. 22 (2010) 5424–5430. https://doi.org/10.1002/adma.201003036.

[251] D. Bekas, K. Tsirka, D. Baltzis, A. Paipetis, Self-healing materials: A review of advances in materials, evaluation, characterization and monitoring techniques, Compos. Part B Eng. 87 (2015). https://doi.org/10.1016/j.compositesb.2015.09.057.

[252] H. Kausch, K. Jud, Molecular aspects of crack formation and healing in glassy polymers, Plast. Rubber Process. Appl. 2 (1982) 265–268.

[253] X. Chen, M.A. Dam, K. Ono, A. Mal, H. Shen, S.R. Nutt, K. Sheran, F. Wudl, A Thermally Re-mendable Cross-Linked Polymeric Material, Science (80-.). 295 (2002) 1698–1702. https://doi.org/10.1126/science.1065879.

[254] X. Chen, F. Wudl, A.K. Mal, H. Shen, S.R. Nutt, New Thermally Remendable Highly Cross-Linked Polymeric Materials, Macromolecules. 36 (2003) 1802–1807. https://doi.org/10.1021/ma0210675.

[255] P. Scardi, M. Sglavo, Relaxation of Indentation Residual Stress in Alumina : Experimental Observation by X-Ray Diffraction, 2219 (1998) 1663–1668.

[256] K. Ando, Y. Shirai, M. Nakatani, Y. Kobayashi, S. Sato, (Crack-healing+proof

test): a new methodology to guarantee the structural integrity of a ceramics component, J. Eur. Ceram. Soc. 22 (2002) 121–128. https://doi.org/https://doi.org/10.1016/S0955-2219(01)00236-9.

[257] T.K. GUPTA, Crack Healing and Strengthening of Thermally Shocked Alumina, J. Am. Ceram. Soc. 59 (1976) 259–262. https://doi.org/10.1111/j.1151-2916.1976.tb10949.x.

[258] G.M. Song, 11 - Self-healing of MAX phase ceramics for high temperature applications: evidence from Ti3AlC2, in: I.M. Low (Ed.), Adv. Sci. Technol. Mn+1AXn Phases, Woodhead Publishing, 2012: pp. 271–288. https://doi.org/https://doi.org/10.1533/9780857096012.271.

[259] A. Farle, C. Kwakernaak, S. Van Der Zwaag, W.G. Sloof, A conceptual study into the potential of M n + 1 AX n -phase ceramics for self-healing of crack damage, J. Eur. Ceram. Soc. 35 (2015) 37–45. https://doi.org/10.1016/j.jeurceramsoc.2014.08.046.

[260] W.G. Sloof, R. Pei, S.A. McDonald, J.L. Fife, L. Shen, L. Boatemaa, A.S. Farle, K. Yan, X. Zhang, S. Van Der Zwaag, P.D. Lee, P.J. Withers, Repeated crack healing in MAX-phase ceramics revealed by 4D in situ synchrotron X-ray tomographic microscopy, Sci. Rep. 6 (2016) 1–9. https://doi.org/10.1038/srep23040.

[261] S. Li, G. Song, K. Kwakernaak, S. Van Der Zwaag, W.G. Sloof, Multiple crack healing of a Ti 2 AlC ceramic, J. Eur. Ceram. Soc. 32 (2012) 1813–1820. https://doi.org/10.1016/j.jeurceramsoc.2012.01.017.

[262] G.M. Song, Y.T. Pei, W.G. Sloof, S.B. Li, J. Th, M. De Hosson, Oxidation-induced crack healing in Ti 3 AlC 2 ceramics, Scr. Mater. 58 (2008) 13–16. https://doi.org/10.1016/j.scriptamat.2007.09.006.

[263] H.J. Yang, Y.T. Pei, J.T.M. De Hosson, Oxide-scale growth on Cr 2 AlC ceramic and its consequence for self-healing, Scr. Mater. 69 (2013) 203–206. https://doi.org/10.1016/j.scriptamat.2013.04.013.

[264] Y. C. Yuan, Self healing in polymers and polymer composites. Concepts, realization and outlook: A review, Express Polym. Lett. - EXPRESS POLYM LETT. 2 (2008) 238–250. https://doi.org/10.3144/expresspolymlett.2008.29.

[265] S. Burattini, B.W. Greenland, D. Chappell, H.M. Colquhoun, W. Hayes, Healable polymeric materials: a tutorial review, Chem. Soc. Rev. 39 (2010) 1973–1985. https://doi.org/10.1039/B904502N.

[266] D.Y. Zhu, M.Z. Rong, M.Q. Zhang, Self-healing polymeric materials based on

microencapsulated healing agents: From design to preparation, Prog. Polym. Sci. 49–50 (2015) 175–220. https://doi.org/https://doi.org/10.1016/j.progpolymsci.2015.07.002.

[267] M. G. JENKINS, A. Kobayashi, K. White, R. C. BRADT, Crack Initiation and Arrest in a SiC Whisker/Al2O3 Matrix Composite, J. Am. Ceram. Soc. 70 (2005) 393–395. https://doi.org/10.1111/j.1151-2916.1987.tb05657.x.

[268] Y.-S. Chou, D.J. Green, Silicon Carbide Platelet/Alumina Composites: II, Mechanical Properties, J. Am. Ceram. Soc. 76 (1993) 1452–1458. https://doi.org/10.1111/j.1151-2916.1993.tb03925.x.

[269] K. Takahashi, M. Yokouchi, S.-K. Lee, K. Ando, Crack-Healing Behavior of Al2O3 Toughened by SiC Whiskers, J. Am. Ceram. Soc. 86 (2003) 2143–2147. https://doi.org/10.1111/j.1151-2916.2003.tb03622.x.

[270] S. Yoshioka, L. Boatemaa, S. van der Zwaag, W. Nakao, W.G. Sloof, On the use of TiC as high-temperature healing particles in alumina based composites, J. Eur. Ceram. Soc. 36 (2016) 4155–4162. https://doi.org/https://doi.org/10.1016/j.jeurceramsoc.2016.06.008.

[271] A. Farle, L. Boatemaa, L. Shen, S. Gövert, J.B.W. Kok, M. Bosch, S. Yoshioka, S. Van Der Zwaag, W.G. Sloof, Demonstrating the self-healing behaviour of some selected ceramics under combustion chamber conditions, Smart Mater. Struct. 25 (2016) 1–10. https://doi.org/10.1088/0964-1726/25/8/084019.

[272] D.Y. Wu, S. Meure, D. Solomon, Self-healing polymeric materials: A review of recent developments, Prog. Polym. Sci. 33 (2008) 479–522. https://doi.org/https://doi.org/10.1016/j.progpolymsci.2008.02.001.

[273] F. Pitsch, F.F. Krull, F. Agel, P. Schulz, P. Wasserscheid, T. Melin, M. Wessling, An Adaptive Self-Healing Ionic Liquid Nanocomposite Membrane for Olefi n-Paraffi n Separations, (2012) 4306–4310. https://doi.org/10.1002/adma.201201832.

[274] R. Olivares, Coupled Experimental Study and Thermodynamic Modeling of Melting Point and Thermal Stability of Li2CO3-Na2CO3-2CO3 Based Salts, Int. J. Sol. Energy. August 201 (2014) 031017–1: 031017.

[275] H. Ibrahim, Y. Temerk, Novel sensor for sensitive electrochemical determination of luteolin based on In2O3 nanoparticles modified glassy carbon paste electrode, Sensors Actuators B Chem. 206 (2015) 744–752. https://doi.org/https://doi.org/10.1016/j.snb.2014.09.011.

[276] A. Dash, R. Vaßen, O. Guillon, J. Gonzalez-Julian, Molten salt shielded

synthesis of oxidation prone materials in air, Nat. Mater. 18 (2019) 465–470. https://doi.org/10.1038/s41563-019-0328-1.

[277] A. Braun, M. Bärtsch, B. Schnyder, R. Kötz, O. Haas, A. Wokaun, Evolution of BET internal surface area in glassy carbon powder during thermal oxidation, Carbon N. Y. 40 (2002) 375–382. https://doi.org/https://doi.org/10.1016/S0008-6223(01)00114-2.

[278] J. Drelich, E. Chibowski, Superhydrophilic and Superwetting Surfaces: Definition and Mechanisms of Control, Langmuir. 26 (2010) 18621–18623. https://doi.org/10.1021/la1039893.

[279] G. Triantafyllou, G.N. Angelopoulos, P. Nikolopoulos, Surface and grain-boundary energies as well as surface mass transport in polycrystalline yttrium oxide, J. Mater. Sci. 45 (2010) 2015–2022. https://doi.org/10.1007/s10853-009-4013-7.

[280] A.G. Gil, Z. Wu, D. Chadwick, K. Li, A catalytic hollow fibre membrane reactor for combined steam methane reforming and water gas shift reaction, Chem. Eng. Sci. 137 (2015) 364–372. https://doi.org/https://doi.org/10.1016/j.ces.2015.06.051.

Chapter 8

Appendices

8.1 Appendix A for chapter 3

1) SEM images of Al_2O_3 and 3% YSZ hollow fibre supports sintered at 1200, 1250, 1300 and 1350 °C, used to calculate their inner (ID) and outer diameter (OD).

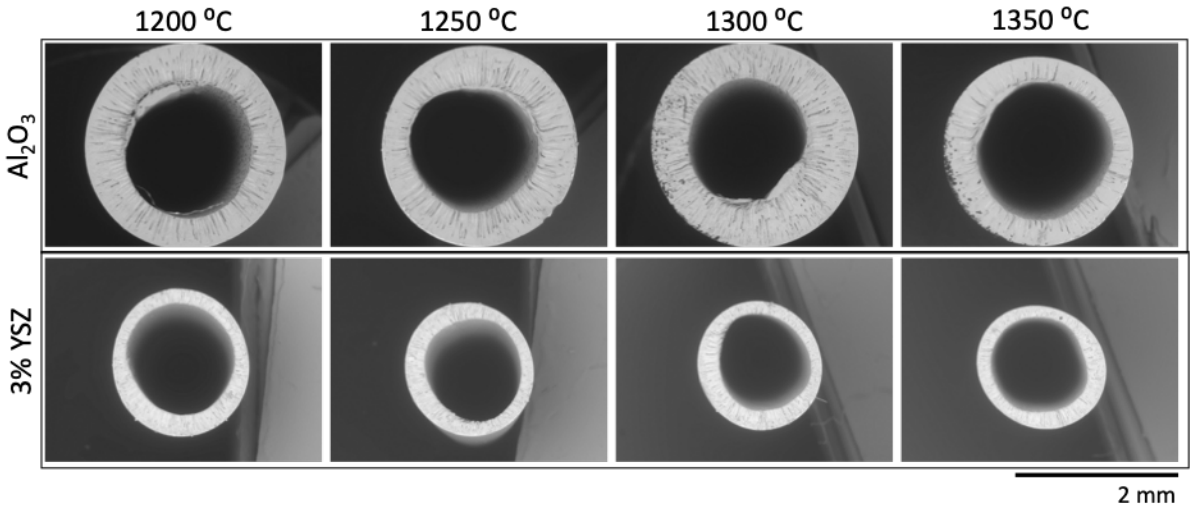

Figure A1: Cross-sectional SEM images of Al_2O_3 (1st row) and 3% YSZ (2nd row) hollow-fibre supports sintered at 1200, 1250, 1300 and 1350 °C.

2) Outer surface porosity of 3% YSZ infiltrated hollow fibre supports sintered at 1200 and 1250 °C.

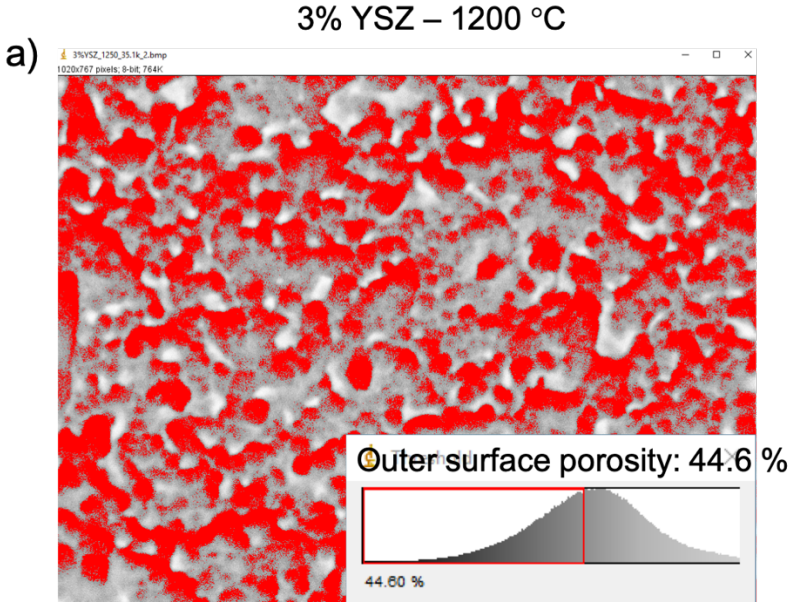

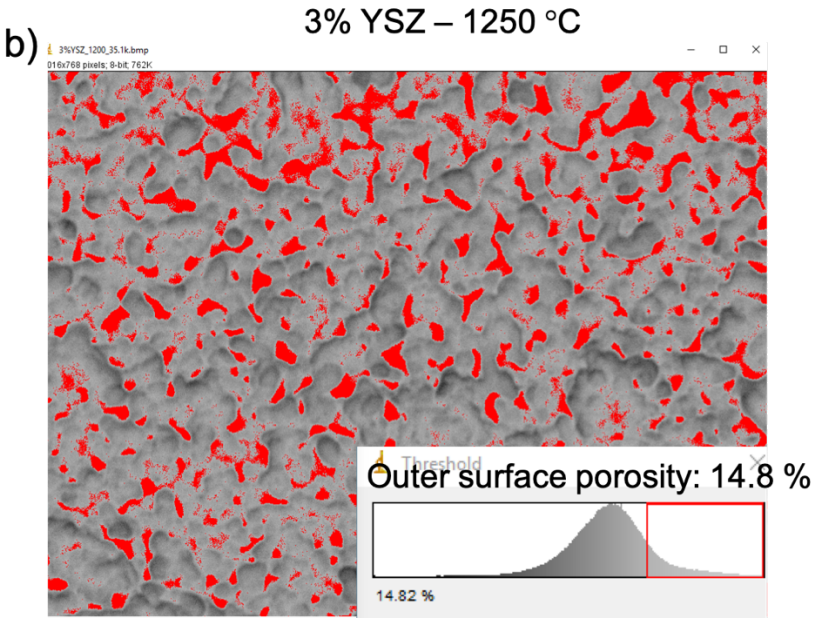

Figure A2: Outer surface porosity of 3% YSZ hollow fibre supports sintered at 1200 (a) and 1250 °C (b).

3) Outer surface porosity of 8% YSZ infiltrated hollow fibre supports sintered at 1200, 1250, 1300 and 1350 °C.

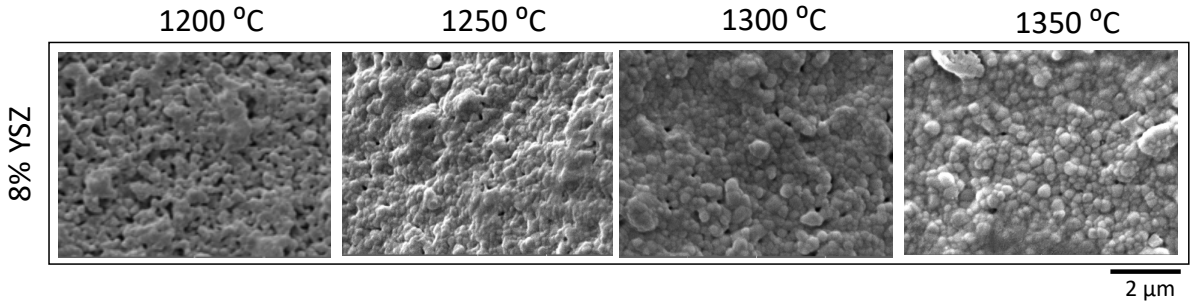

Figure A3: Outer surface porosity of 8% YSZ hollow fibre supports sintered at 1200, 1250, 1300 and 1350 °C.

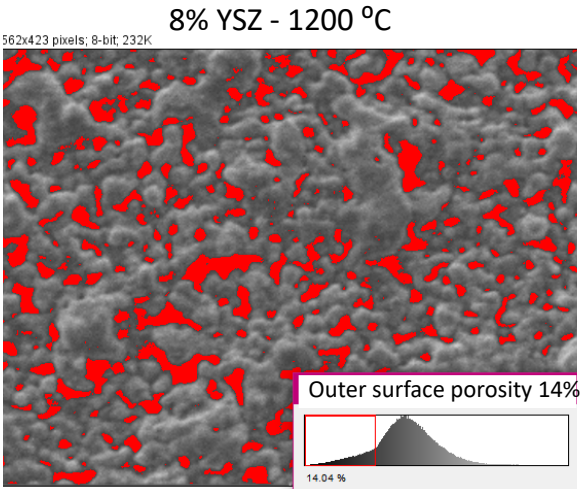

Figure A4: Outer surface porosity of 8% YSZ hollow fibre supports sintered at 1200 °C.

4) Carbonate particle size and carbonate particle size distribution in the carbonate suspension used for hollow fibre infiltration.

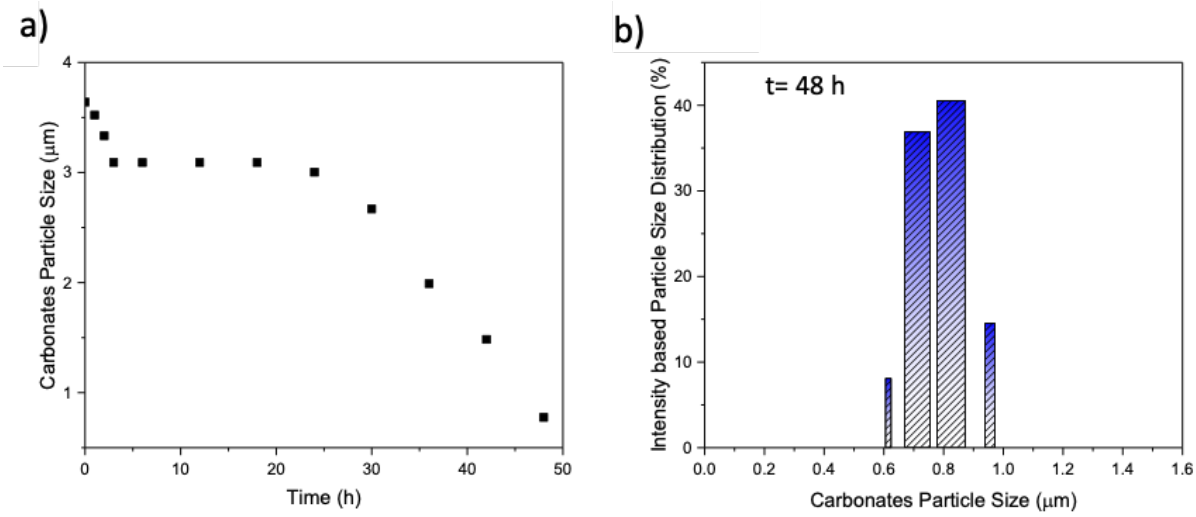

Figure A5: Carbonate particle size in carbonate suspension. a) Carbonate mean particle size (nm) versus time (h) during a 48 h milling period, and b) intensity based particle size distribution (%) versus carbonate particle size (nm) after milling the carbonate suspension for 48 h.

5) Calculation of gram of carbon per gram of hollow fibre support.

Carbonate density: $\rho = 2.36$ g cm^{-3}

Volume of packed-pore network: $V_{ppn} = 0.2$ ml g^{-1}

Mass of molten carbonate in the packed-pore network per gram of fibre:

$m = \rho V_{ppn} = 0.47$ g per gram of fibre

6) Actual infiltration percentage calculations for a hollow fibre support infiltrated with 100 vol% carbonate in its packed-pore network.

Original hollow fibre support weight, without any carbonate: 0. 3432 g

Weight of hollow fibre coated with carbonate: 0.5085 g

Weight of hollow fibre infiltrated with carbonate: 0.4168 g

% of packed-pore network infiltrated with carbonate: $\frac{0.4168\ g\ 100}{0.5088\ g}$%= 82%

7) SEM and EDX images of 3% YSZ hollow fibre supports with 75 and 100 vol% carbonate loading in their packed-pore network.

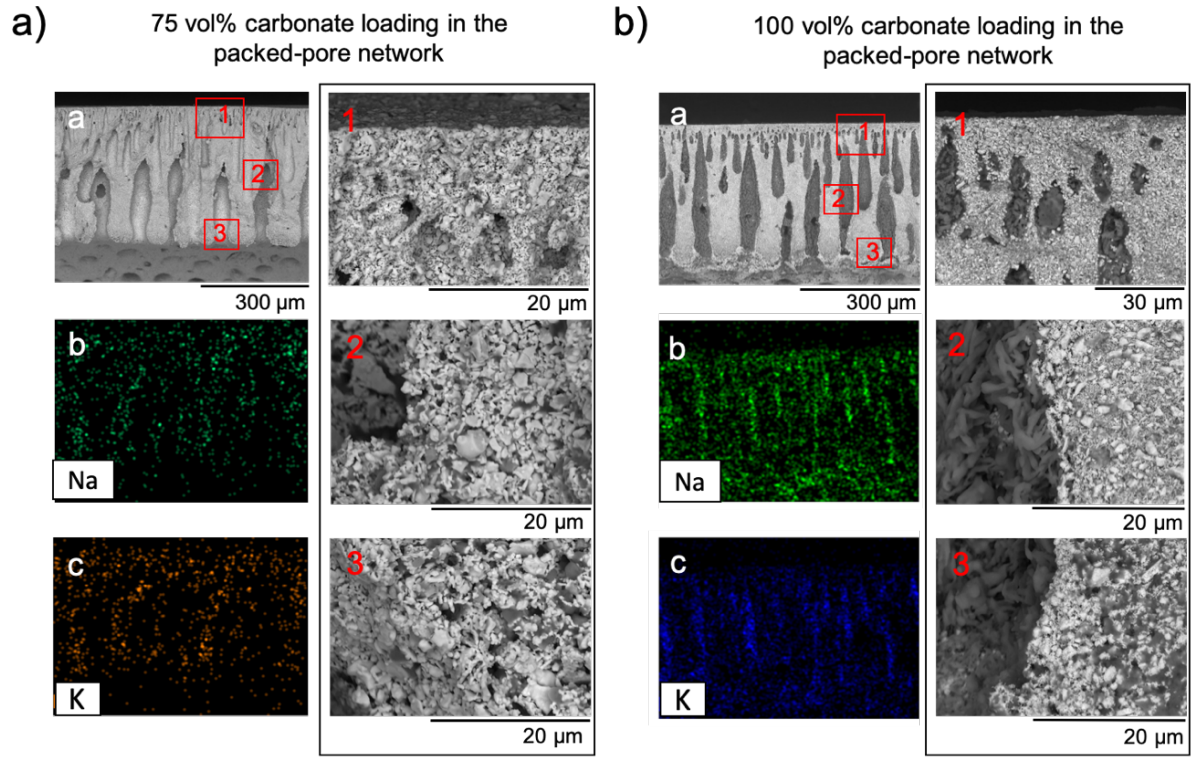

Figure A6: SEM and EDX analysis of the cross-sectional surface area of 75 and 100 vol% infiltrated 3%-YSZ hollow-fibre supports. Analysis of different regions across the 75 and 100 vol% infiltrated 3% YSZ hollow-fibre cross-section.

8) Carbonate tracing technique at room temperature.

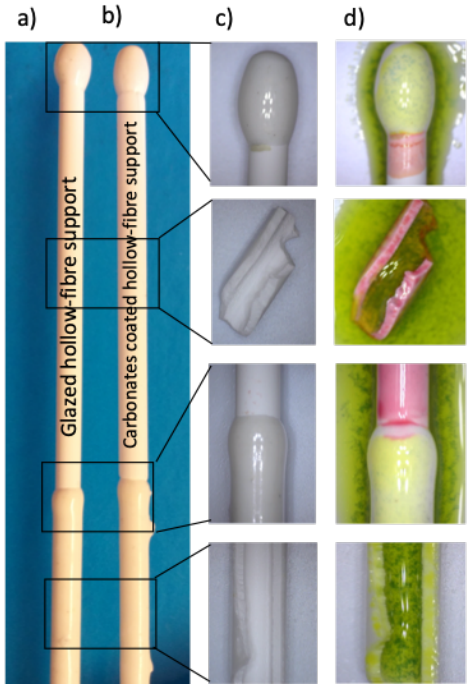

Figure A7: Carbonate detection on a glazed and infiltrated Al_2O_3 hollow-fibre support. Detection of carbonate on a glazed and infiltrated support with the use of green food die. The areas of the support that have been infiltrated with carbonate turn red, whereas the areas that there are no carbonate present remain green.

8.2 Appendix B for chapter 4

The permeate carbon dioxide flux data for dual-phase membranes were calculated based on mass spectrometry and infrared radiation (IR) measurements. The current carbon dioxide data of the mass spectrometer were translated into carbon dioxide concentration data by correlating known carbon dioxide sample concentration values with the equivalent carbon dioxide current; based on the following equation:

$$C_{CO_2} = \frac{I_{CO_2} - I_{CO_2,background}}{CF} \quad \text{(Eq. A1)}$$

where CF is the calibration factor expressed as:

$$CF = \frac{I_{CO_2} - I_{CO_2,background}}{C_{CO_2,known\ sample}} \quad \text{(Eq. A2)}$$

The same process was followed for converting current data to concentration data for the nitrogen gas on the permeate side of the membrane. The calibration curve for each gas, was obtained by a three-point calibration of both the mass spectrometer and the IR analyser, in line.

The permeate volumetric flux (ml min^{-1} cm^{-2}) for carbon dioxide and nitrogen was then obtained by the following equation:

$$J_{CO_2} = \frac{\varphi_{CO_2}\dot{V}}{A_S} \quad \text{(Eq. A3)}$$

where φ_{CO_2} is the volume fraction of carbon dioxide in the permeate-side outlet, $\dot{V}$ is the volumetric flow rate on the permeate side set at 50 ml min^{-1}, and A_s is the active lateral surface area of the membrane. For the IR data, the flux was calculated in the same way. For both mass spectrometer and IR data, the data point representing flux value, is the average flux of several experimental points of the recorded permeate carbon dioxide flux. The data points during the last hours of measurements for each experimental step, where the flux variation was below 3%, were used to calculate the average flux. Figure A6 a, b, c and d, show the carbon dioxide and nitrogen flux data for each experimental data point presented in Figure 4.5, in chapter 4 of the main thesis.

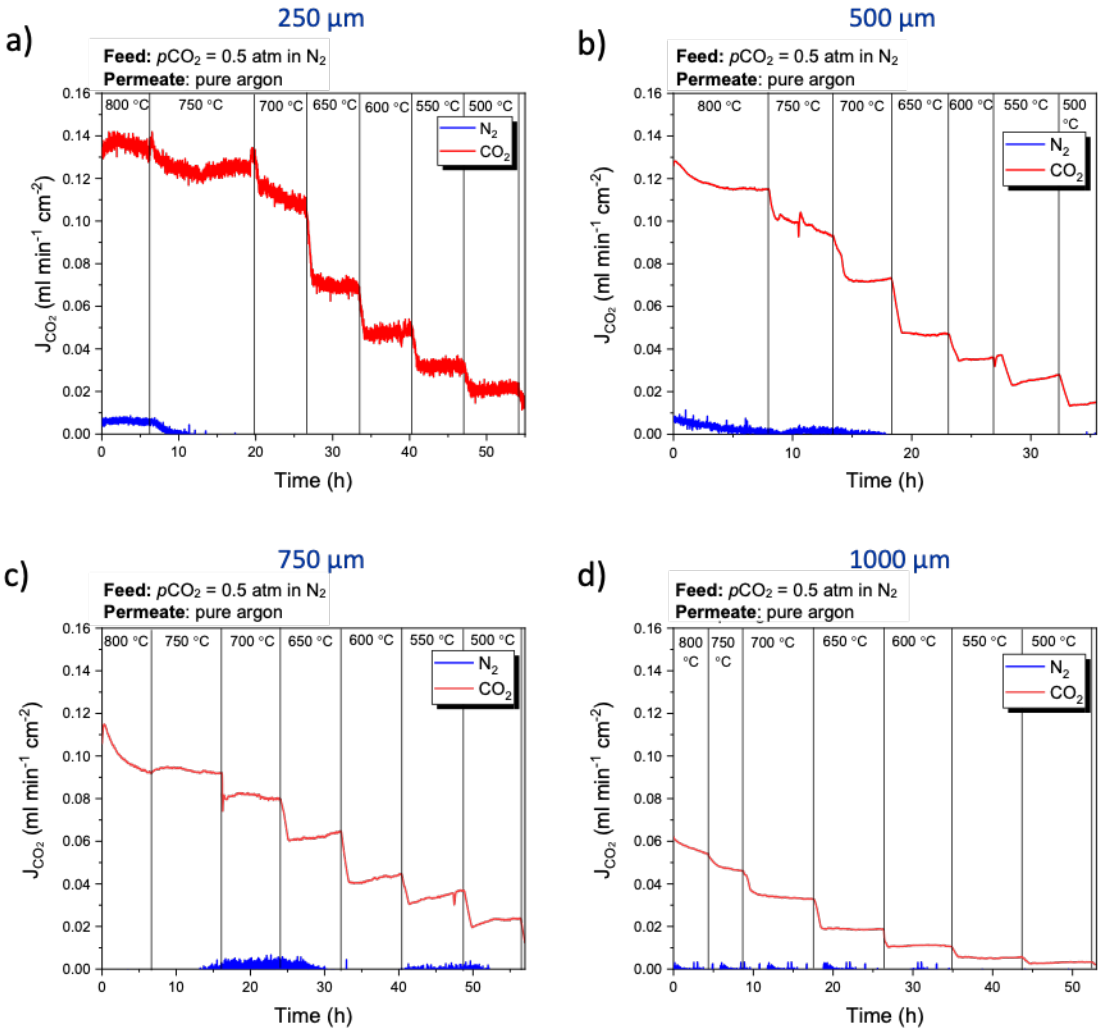

Figure A8: Carbon dioxide and nitrogen flux in model dual-phase crucible membranes with 250 (a), 500 (b), 750 (c) and 1000 (d) molten carbonate thickness on top of the 440 µm length drilled channels.

The same process was used to calculate flux in Al_2O_3-supported controlled and uncontrolled DPHFMs. For Al_2O_3-supported controlled DPHFMs presented in chapter 4, section 4.3.2, the flux values derived from the steady-state flux value of each experimental step, shown in Figure A7. Each flux value corresponds to the equivalent driving force in Figure 4.6 of the main thesis and is depicted by the equivalent data point.

a)

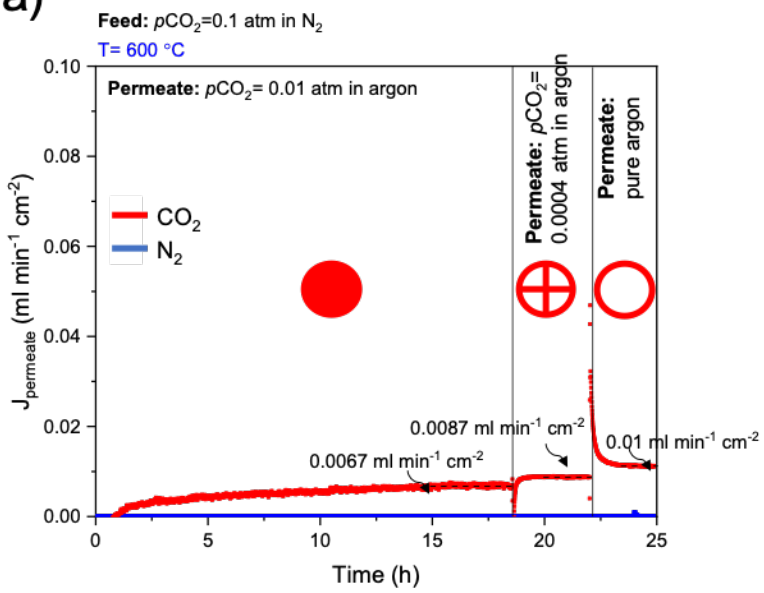
Feed: pCO2=0.1 atm in N2
T= 600 °C
Permeate: pCO2= 0.01 atm in argon
CO2
N2
Permeate: pCO2= 0.0004 atm in argon
Permeate: pure argon
0.0067 ml min-1 cm-2
0.0087 ml min-1 cm-2
0.01 ml min-1 cm-2
Jpermeate (ml min-1 cm-2)
Time (h)

b)

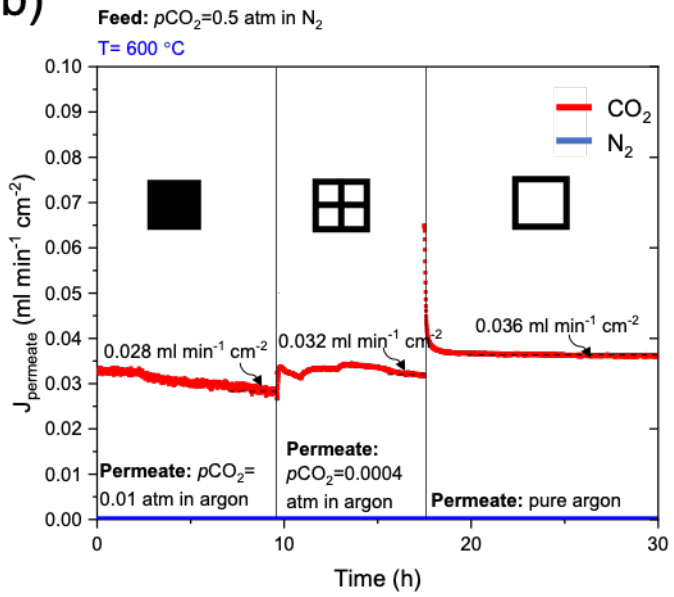
Feed: pCO2=0.5 atm in N2
T= 600 °C
CO2
N2
0.028 ml min-1 cm-2
0.032 ml min-1 cm-2
0.036 ml min-1 cm-2
Permeate: pCO2= 0.01 atm in argon
Permeate: pCO2=0.0004 atm in argon
Permeate: pure argon
Jpermeate (ml min-1 cm-2)
Time (h)

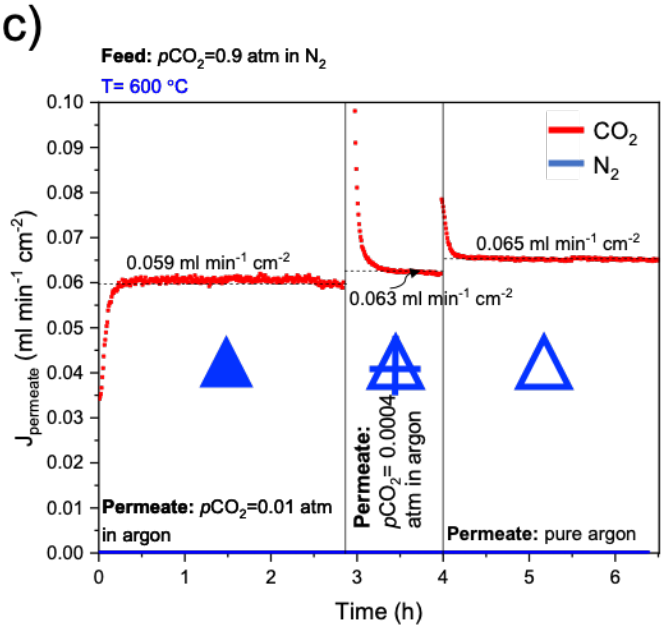

Figure A9: Effect of partial pressure difference on the carbon dioxide flux through Al_2O_3-supported controlled DPHFMs at T= 600 °C. a) for a feed-side pCO_2= 0.1 atm, b) a feed-side pCO_2= 0.5 atm, and c) a feed-side pCO_2= 0.9 atm.

For Al_2O_3-supported uncontrolled DPHFMs presented in chapter 4, section 4.3.2, the flux values derived from the steady-state flux value of each experimental step, shown in Figure A8. Each flux value corresponds to the equivalent driving force in Figure 4.6 of the main thesis and is depicted by the equivalent data point.

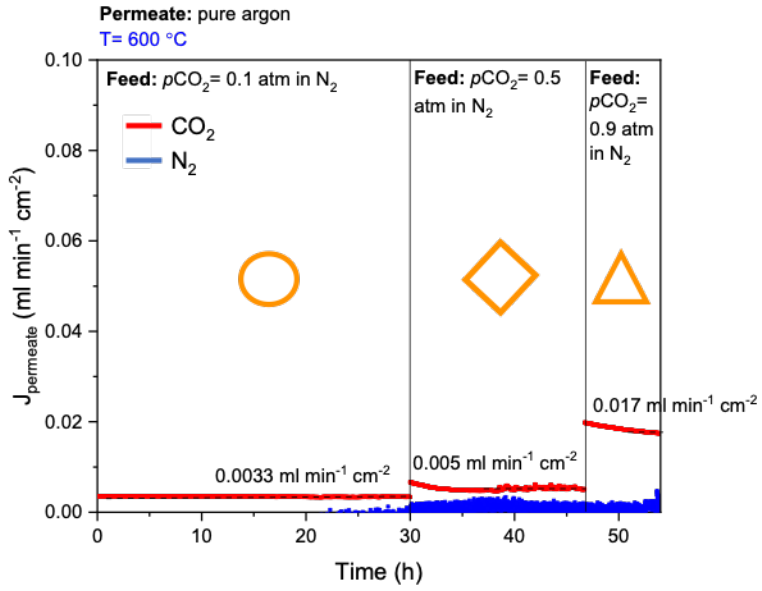

Figure A10: Effect of partial pressure difference on the carbon dioxide flux through Al_2O_3-supported uncontrolled DPHFMs at T= 600 °C.

For Al_2O_3-supported controlled DPHFMs presented in chapter 4, section 4.3.2, the flux values derived from the steady-state flux value of each experimental step, shown in Figure A9.

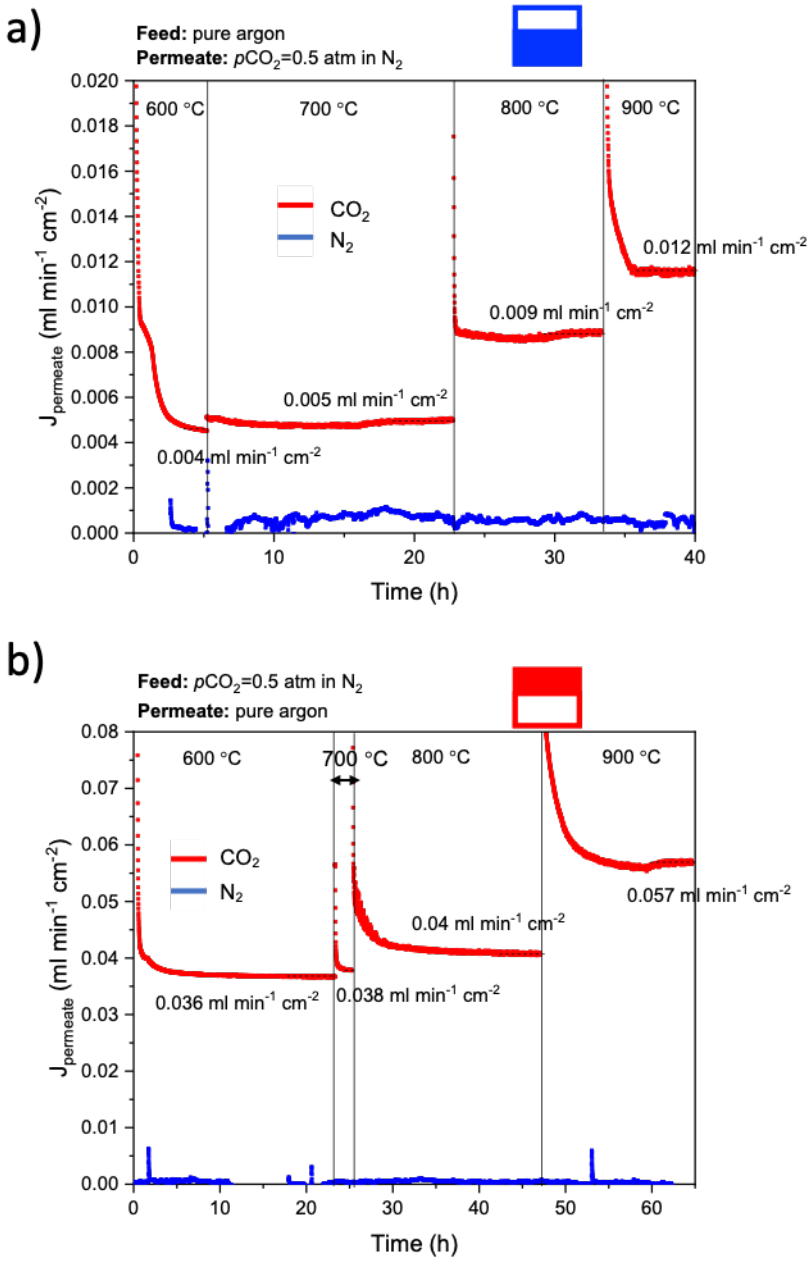

Figure A11: Impact of permeate side surface area for carbon dioxide sorption and desorption on carbon dioxide flux through a controlled DPHFM.

For 3% YSZ-supported controlled DPHFMs presented in chapter 4, section 4.3.2, the flux values derived from the steady-state flux value of each experimental step, shown in Figure A10. Each flux value corresponds to the equivalent driving force in Figure 4.9 of the main thesis and is depicted by the equivalent data point.

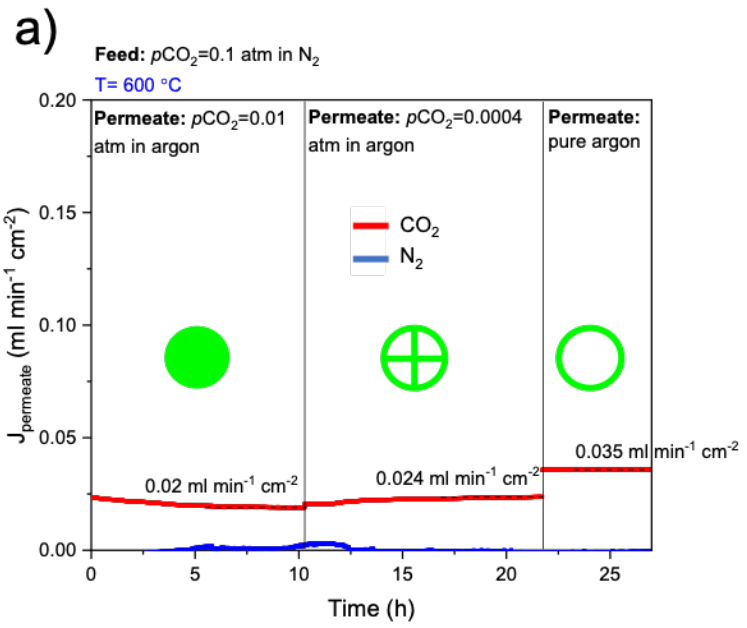
a)
Feed: pCO2=0.1 atm in N2
T= 600 °C
Permeate: pCO2=0.01 atm in argon
Permeate: pCO2=0.0004 atm in argon
Permeate: pure argon
CO2
N2
0.02 ml min-1 cm-2
0.024 ml min-1 cm-2
0.035 ml min-1 cm-2
Jpermeate (ml min-1 cm-2)
Time (h)

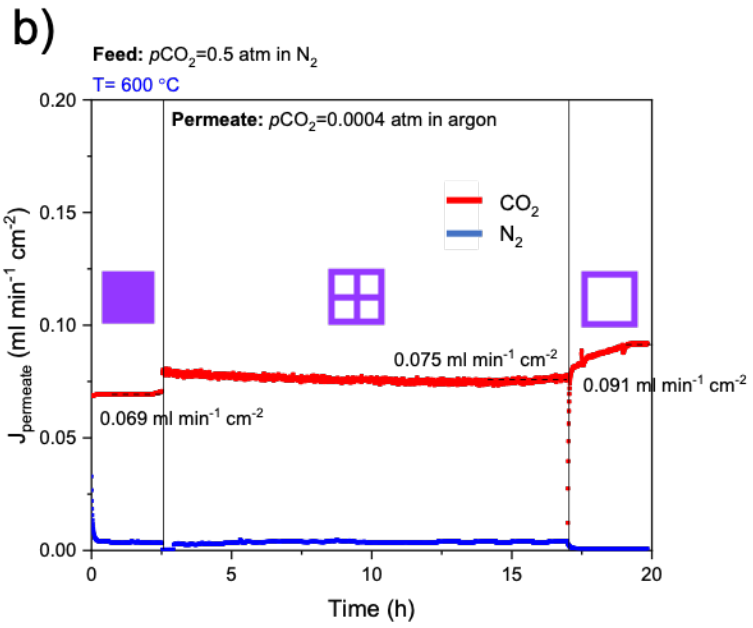
b)
Feed: pCO2=0.5 atm in N2
T= 600 °C
Permeate: pCO2=0.0004 atm in argon
CO2
N2
0.069 ml min-1 cm-2
0.075 ml min-1 cm-2
0.091 ml min-1 cm-2
Jpermeate (ml min-1 cm-2)
Time (h)

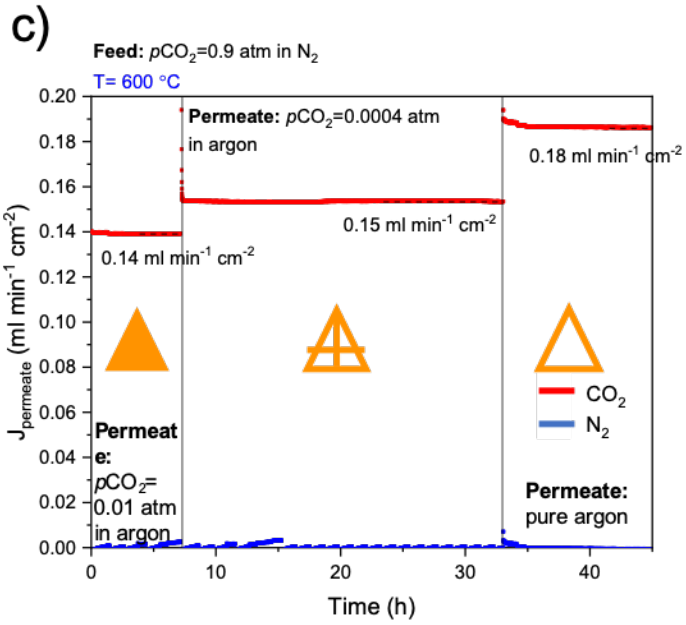

Figure A12: Effect of partial pressure difference on the carbon dioxide flux through 3% YSZ-supported controlled DPHFMs at T= 600 °C. a) for a feed-side pCO_2= 0.1 atm, b) a feed-side pCO_2= 0.5 atm, and c) a feed-side pCO_2= 0.9 atm.

8.3 Appendix C for chapter 5

1) Fabrication of asymmetric micro-structure ceramic pellets.

Asymmetric micro-structured ceramic pellets were prepared by viscous-fingering induced-phase inversion followed by a high-temperature sintering technique [210,214,216,220]. The ceramic suspension for their preparation consisted of 60 wt% Al_2O_3 as the ceramic powder, 33.3 wt% DMSO as the solvent, 0.4 wt% Arlacel P135 as the dispersant and 6.3 wt% PESf as the polymer binder (Figure A11: a). The ceramic suspension was mixed *via* ball milling (Planetary Ball Mill PM 100, Retsch) with the use of 30 zirconia balls (Inframat advanced materials, grinding media spherical, 10.0 mm, D) for 24 h (Planetary Ball Mill PM 100, Retsch) at 350 rpm (b) and was then placed inside a vacuum chamber (10L, manufactured) for 4 h in order to remove remaining air bubbles (c). After degassing, the ceramic suspension was transferred into 200 ml plastic syringes (d) and poured into stainless-steel molds (D= 2 cm, H= 2 mm) (e). The molds were then horizontally immerged into a water bath of deionized water (DI) (H_{water}=15 cm) and remained submerged for 24h (f). The DI water in the bath was replaced with fresh DI water after 12h to ensure the full removal of the excess solvent. The precursor pellets were finally removed from the stainless-steel molds and were dried in a drying oven at 50 °C before sintering in a tubular furnace at 1300 °C in air [171]. The sintering profile for the micro-structured Al_2O_3 phase-inversed pellets was the same as the sintering profile used for the Al_2O_3 hollow fibre supports, described in chapter 3, section 3.2.2.

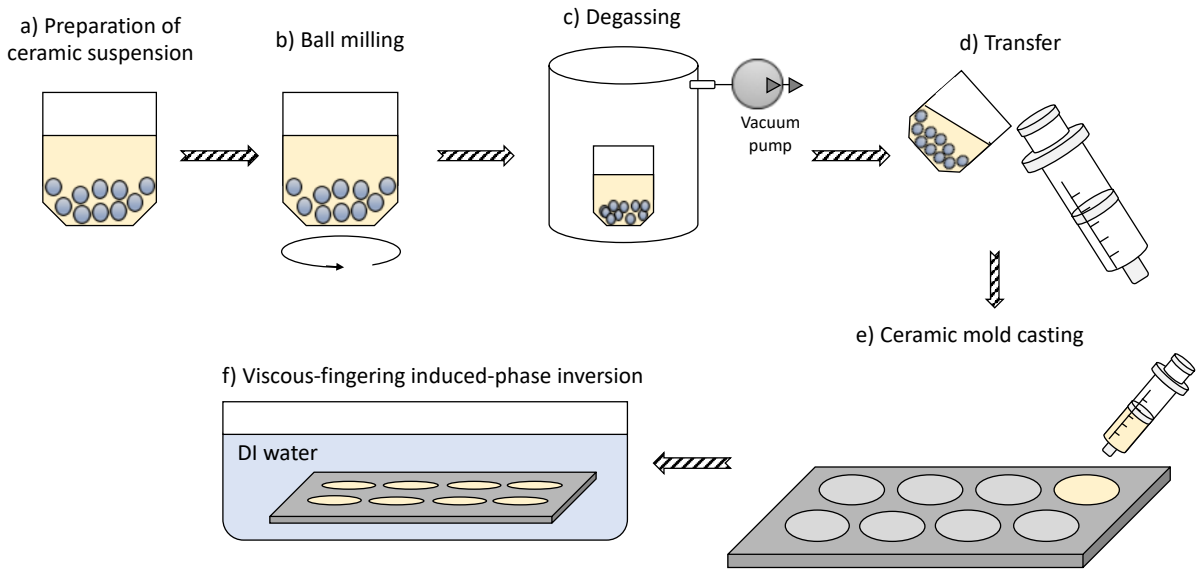

Figure A13: Preparation of micro-structured Al_2O_3 pellets by viscous-fingering induced-phase inversion.

Micro-structured pellet precursors fabricated in this work were originally 2 mm thick with the channel formation originating from the top of the pellet surface, which was exposed to the bulk volume of deionised water (non-solvent), towards the bottom surface of the pellets (bottom of stainless-steel moulds, Figure A11: f). After removing the pellets from the stainless-steel moulds, they were sanded down a desired thickness using a silicon carbide sandpaper sheet (P600 Wetordry, 3M).

2) Analysis of self-healing permeate flux data.

The permeate flux data for carbon dioxide for the self-healing membranes were calculated based on mass spectrometry and infrared radiation (IR). The current carbon dioxide data of the mass spectrometer were translated into carbon dioxide concentration data by correlating known carbon dioxide sample concentration values with the equivalent carbon dioxide current, as analysed in Appendix B.

The same process was followed for converting current data to concentration data for the nitrogen gas on the permeate side of the membrane. The ion current of nitrogen from the permeate outlet stream was also calibrated based on the ion current of argon in order to minimize its relative changes resulted from experimental condition variation, such as temperature and pressure, in the reactor throughout the experiment. The concentration of nitrogen was calculated based on linear regression equation of concentration against ion intensity using argon and 0.95%N_2-0.99%CO_2-argon. The calibration curve for each gas, during the rest of the experimental values, was obtained by a three-point calibration of the mass spectrometer and the IR analyser.

For the mass spectrometry and IR data, the flux was calculated by Eq. A3, as analysed in Appendix B.

For both mass spectrometer and IR data, the data point representing flux value, is the average flux of several experimental points of the recorded permeate carbon dioxide. The data points during the last hour of measurements, where the flux variation was below 3%, were used to calculate the average flux.